



1949

**THE ATLANTIC FORCING ON ECUADORIAN PALEORECORDS:
SPELEOTHEMS AND TREE-RINGS**

Thesis for the Degree of Doctor of Philosophy (PhD)

Danny Fernando Vargas Espin

Supervisor

Dr. László Palcsu, PhD

UNIVERSITY OF DEBRECEN

Doctoral Council of Natural Sciences and Information Technology

Doctoral School of Physics

Debrecen, 2023

Prepared at
the Doctoral School of Physics, University of Debrecen
and the Institute for Nuclear Research

Hereby I declare that I prepared this thesis within the Doctoral Council of Natural Sciences and Information Technology, Doctoral School of Physics, University of Debrecen in order to obtain a PhD Degree in Natural Sciences at Debrecen University.

The results published in the thesis are not reported in any other PhD theses.

Debrecen, 2023.

.....
Danny Fernando Vargas Espin

Candidate

Hereby I confirm that Danny Fernando Vargas Espin conducted his studies with my supervision within the Physical Methods in Interdisciplinary Research Doctoral Program of the Doctoral School of Physics between 2017 and 2022. The independent studies and research work of the candidate significantly contributed to the results published in the thesis.

I also declare that the results published in the thesis are not reported in any other theses.

I support the acceptance of the thesis.

Debrecen, 2023.

.....
Dr. László Pálcsu

Supervisor

**THE ATLANTIC FORCING ON ECUADORIAN PALEORECORDS:
SPELEOTHEMS AND TREE-RINGS**

Dissertation submitted in partial fulfillment of the requirements for the doctoral
(PhD) degree in **Physics**

Written by **Danny Fernando Vargas Espin**
certified MSc. in Environmental Management on Agricultural Engineering

Prepared in the framework of the doctoral school of Physics of the
University of Debrecen
Physical Methods in Interdisciplinary Research program

Dissertation advisor: **Dr. László Palcsu**

The official opponents of the dissertation:

Dr.
Dr.

The evaluation committee:

Chairperson: Dr.
members: Dr.
Dr.
Dr.

The date of the dissertation defense: 202.....

TABLE OF CONTENTS

LIST OF ABBREVIATIONS	x
ABSTRACT.....	xi
INTRODUCTION.....	1
 1.1 Tropical climatology	1
 1.2 Monsoonal circulations.....	3
 1.3 ITCZ and SAMS dichotomy	4
 1.4 Paleoclimate studies	6
 1.4.1 Stable isotopes of water	7
 1.4.2 Terrestrial archives.....	9
 1.4.3 Statistical analysis of paleoclimate records	14
 1.5 General overview of Ecuador on Paleoclimate	16
 1.6 Aims and objectives of this study	24
MATERIALS AND METHODS	26
 2.1 General overview of the study site.....	26
 2.2 Sample collection.....	26
 2.2.1 Rainwater sampling	26
 2.2.2 Tree-rings identification and sampling.....	29
 2.2.3 Surveying and monitoring of caves	31
 2.3 Sample preparation	33
 2.3.1 Dendrochronological work.....	33
 2.3.2 Speleothems slabs	34
 2.4 Analytical measurements	35
 2.4.1 Stable isotopes	35
 2.4.1.1 Water stable isotopes in precipitation.....	35
 2.4.1.2 Cellulose-based tree-ring oxygen and carbon isotopes.....	35
 2.4.1.3 Carbon and oxygen isotopes in calcite speleothem and Hendy test	36
 2.4.2 Radioisotopes.....	37
 2.4.2.1 Radiocarbon and annual ring validation.....	37
 2.4.2.2 U-Th dating.....	37
 2.5 Climate datasets and gridded products	39
 2.5.1 Stable isotopes of water	39
 2.5.1.1 Stable isotopes database	39
 2.5.1.2 Lagrangian back trajectories.....	40
 2.5.1.3 Cross-equatorial flow over western Amazon and gridded precipitation.....	40
 2.5.2 Statistical analysis	41
 2.5.2.1 <i>Cedrela nebulosa</i> tree-rings and regional records.....	41
 2.5.2.2 Dino-1 speleothems and regional records	41

2.5.2.3	Spectral analysis.....	41
2.5.2.4	Mid-Holocene Earth System model.....	42
2.6	Reproducibility.....	42
RESULTS	43
3.1	Water stable isotopes	43
3.1.1	OLR decomposition and moisture trajectories	43
3.1.2	Local Meteoric Water Line (LMWL) and “amount” effect	45
3.1.3	Local “altitude” effect.....	47
3.1.4	Regional “amount” effect at the V-index.....	48
3.2	Tree-rings and modern climate	52
3.2.1	Annual ring periodicityd	52
3.2.2	Tree-ring chronologies.....	53
3.2.3	Oxygen isotopes and western Amazon precipitation	56
3.2.4	Carbon isotopes and temperature controls	58
3.3	Dino-1 stalagmite and mid-Holocene climate.....	60
3.3.1	Cave monitoring.....	60
3.3.1.1	Temperature.....	60
3.3.1.2	Dripwater.....	63
3.3.2	Dino-1 speleothem	64
3.3.2.1	Mineralogy, U-Th dating and spectral analysis	64
3.3.2.2	Mid-Holocene climate	66
Precipitation simulations.....	66	
Water isotopes in the MPI-ESM model	67	
Holocene regional paleoclimate records	68	
DISCUSSION	72	
4.1	Rainwater stable isotopes	72
4.1.1	Local temperature and precipitation amount	72
4.1.2	Altitude effect	73
4.1.3	Low Level-Jets (LLJs)	73
4.1.4	V-index and monsoon trough.....	74
4.2	Modern climate (centennial-scale).....	77
4.2.1	Cedrela nebulosa growth.....	77
4.2.2	Tree-ring oxygen isotopes and western Amazonian precipitation .	78
4.2.3	Tree-ring carbon isotopes and role of cloud cover	80
4.3	Mid-Holocene climate (millennial-scale).....	81
4.3.1	$\delta^{18}\text{O}$ values in the cave system	81
4.3.2	Kinetic fractionation between water and carbonate.....	82
4.3.3	Holocene rainfall changes.....	83
SUMMARY AND CONCLUSIONS	88	
NEW SCIENTIFIC FINDINGS	90	

REFERENCES.....	91
ACKNOWLEDGMENTS	116
APPENDIX A – MERA STUDY SITE SURVEY.....	117
APPENDIX B – SPELEOTHEMS	124

LIST OF ABBREVIATIONS

BP	Before AD 1950
CHIRPS	Climate Hazards Group InfraRed Precipitation with Station data
DJF	December-February (austral summer)
ENSO	El Niño Southern Oscillation
GMWL	Global Meteoric Water Line
GNIP	Global Network of Isotopes in Precipitation
IAEA	International Atomic Energy Agency
ITCZ	Intertropical Convergence Zone
JJA	June-August (austral winter)
LMWL	Local Meteoric Water Line
MAM	March-May (austral autumn)
MT	Monsoon trough
OLR	Outgoing longwave radiation
SACZ	South Atlantic Convergence Zone
SAMS	South American Monsoon System
SON	September-November (austral spring)
SST	Sea Surface Temperature
SISAL	Speleothem Isotopes Synthesis and Analysis

ABSTRACT

Paleoclimate reconstructions in tropical regions (30°N - 30°S) are scarce and hindered due to the small temperature fluctuations and continuous precipitation regimes that mask the climate seasonality. However, the physical climate processes occurring at these low latitudes provide the missing elements in our understanding of the thermodynamic cycle of the Earth's past climate at high latitudes. In South America, the small number of available records are interpreted based on the changes in hydrology and not due to temperature. Most are biased towards the South American Monsoon System (SAMS), which occurs during the austral summer (DJF) and feeds the continent's central and southern parts, marking a defined onset of wet and dry seasons. However, at regions close to the equator, the paleoclimatological potential that can be obtained has been unexplored, perhaps due to complex seasonality dictated by the Andes topography, the rainwater bimodality brought by the Intertropical Convergence Zone (ITCZ) excursions, and lack of continuous instrumental records for the calibration of archives.

Nevertheless, these intricacies are precisely what bring the novelty and focus of this dissertation. There is an evident ambiguity in the climate literature regarding the ITCZ and SAMS boundaries, especially in Northern South America, and frequently this differentiation is vaguely stated. Long-term records harboring climate signals are required to address this ambivalence of terms, so a systematic evaluation of these systems during centennial to millennial scales should be undertaken.

The aims of the current thesis are:

1. To evaluate the amount effect and identify the local or regional controller of the rainwater stable isotopic composition in the Ecuadorian Andes and Amazon
2. To reconstruct modern centennial hydrology using $\delta^{18}\text{O}$ and $\delta^{13}\text{C}$ in cellulose from tree species
3. To reconstruct past millennial hydrology using $\delta^{18}\text{O}$ from speleothems

To accomplish this task, I employ standard dendrochronological techniques and karstological principles to study two terrestrial archives: speleothems and tree-rings in Central Ecuador supported by a 4-year monthly collection of precipitation for determination of its seasonal stable isotopic composition. This work employs well-established analytical techniques, including stable isotopes (^2H , ^{18}O , ^{13}C) and radioisotopes (^{14}C , ^{238}U - ^{230}Th). It harnesses the vast amounts of remote and satellite data from the ERA5, CHIRPS, NCEP-NCAR, and CRU for bridging climate data gaps, along with available instrumental datasets from the GNIP and local meteorological stations. Furthermore, datasets from the PMIP4-CMIP6 and MPI-ESM-wiso for precipitation and stable isotope modeling, respectively, are utilized for mid-Holocene comparison. Pearson's moment correlation and spectral analysis techniques are employed for the statistical treatment of time-series.

Results showed that there is a coherent seasonality. The lowest precipitation $\delta^{18}\text{O}$ values occurred during austral autumn (AMJ) and spring (ON), while higher values were found in summer (DJFM) and winter (JAS). The $\delta^{18}\text{O}$ variability is a complex process that starts upstream at the Tropical North and South Atlantic. The generated water vapor in these regions is seasonally advected by the easterlies and transported by the Orinoco and the Equatorial mid-tropospheric easterly jet, to be finally modulated at the convective V-index region (an aerial lake at 5°S-5°N, 65°-75°W) that generates the characteristic “W-shape” rainfall isotopic pattern in the Ecuadorian stations. Regarding the paleoclimate work, three (3) *Cedrela nobulosa* tree-ring chronologies were constructed: tree-ring width (TRW, 1860-2018) and oxygen and carbon stable isotopes from cellulose (1864-2018). The dendro-records showed that the ITCZ rainfall and cloudiness are the chief factors modulating the $\delta^{18}\text{O}$ and $\delta^{13}\text{C}$ with minimal SAMS influence in the modern climate. At the millennial scale, the Dino-1 speleothem was dated from 6856 to 5313 a (1.5 ka) and showed a coherent variability with Bond event 4, suggesting the influence of abrupt cold North Atlantic pulses. On a regional scale, a consistent unison pattern of wetness developed from early, mid-Holocene, and pre-Industrial times is observed in climate models and northeastern and northwestern regional speleothem, sediments, and glacier records owing to increment in solar insolation during the Holocene in the Southern Hemisphere.

In summary, I conclude that the ITCZ has been the main factor modulating the climatology in South America. For paleoclimate studies, the systems should be addressed separately during the mid-Holocene. For calibration of modern archives at latitudes near the equator, I found evidence to lock them between ITCZ and SAMS systems in the so-called monsoon trough. Overall, this work provides evidence of the ITCZ's role in determining paleohydrology in the western Amazon and contributes to advancing and expanding the geographic frontier of tropical paleoclimatology.

CHAPTER 1

INTRODUCTION

1.1 Tropical climatology

The tropical regions located between the Tropic of Cancer (23.5°N) and the Tropic of Capricorn (23.5°S) receive approximately 56% of the total precipitation on Earth (Wang and Ding, 2008; Xie and Arkin, 1997). This considerable amount of rainfall is accompanied by latent heat release during phase changes, an important energy source that drives the tropical circulation and supplies moisture to the high and middle latitudes (Wang and Ding, 2008; Zhang et al., 2019). These atmospheric processes are particularly enhanced at the climatological equator, where the trade winds of the two hemispheres converge (Goosse, 2015; Waliser and Jiang, 2015). These winds are laden with heat, moisture and meet to form a belt of higher convection, cloudiness, and rainfall. In meteorology, vertical heat exchange is called convection and occurs due to mass movement. In the troposphere, rising air will expand and cool, whereas sinking air will compress and warm (Ahrens, 2019; Stull, 2020).

This tropical belt, located within 10° of the equator, is known as the Intertropical Convergence Zone (ITCZ) and is the primary system within the tropical atmosphere where precipitation is maximal (Figure 1.1) (Schneider et al., 2014; Waliser and Jiang, 2015). However, the ITCZ does not extend across the continental masses because this is primarily a marine phenomenon (Ancapichún et al., 2022, 2021; Baker and Fritz, 2015; Cook, 2009; Hua et al., 2022; Marsh et al., 2018). Nevertheless, in the climate literature, the ITCZ boundaries are often extended over the continents (e.g., Hogg et al., 2020; Veblen et al., 2015). This is not surprising because tropical boundaries (and hence the ITCZ) vary among scientific disciplines. For instance, in astronomy and cartography, the edges of the tropical belt are the Tropics of Cancer and Capricorn ($\sim 23.5^{\circ}$ North and South) associated to the insolation and Earth axial tilt (Seidel et al., 2008). In climatology and geography, the tropics have been identified using Köppen classification (Beck et al., 2018; Seidel et al., 2008). The atmospheric equivalent of the marine ITCZ is a tropical low-pressure belt (TLPB) also known as “equatorial low” characterized by low atmospheric pressure (Ancapichún et al., 2021). The TLPB is formed in the tropics due to the heating of air by direct insolation causing the air to warm, rise (lower buoyancy), expand and ascend to the upper troposphere, establishing lower pressure at the surface (Figure 1.1d) (Ancapichún et al., 2021; Cook, 2009; Goosse, 2015; Hastenrath, 1991; Stull, 2020; Waliser and Jiang, 2015). Due to the decrease of temperature with altitude in the troposphere, the rising warm air cools and begins to condense forming clouds and rainfall (Bony et al., 2008; Clark, 2015; Goosse, 2015; Sodemann, 2006). This process leads to the formation of a band of convective clouds and increase precipitation, complementing the process carried out by the marine ITCZ in the oceans (Araguás-

Araguás et al., 2000; Schneider et al., 2014). In this dissertation, I describe the ITCZ as the compound phenomenon involving the marine and terrestrial (TLPB) components, confident that this provides a more holistic understanding. It is now well established that the trade winds are the low-level part of the Hadley cells, which rise near the ITCZ due to buoyancy, sink in the subtropics, and return with a flow at upper levels from the poles towards the equator (Lu and Vecchi, 2015) (Figure 1.1). The Hadley circulation corresponds to the zonally averaged meridional overturning motions in the low-latitude troposphere. It plays a crucial role in transporting heat, moisture, and momentum meridionally (parallel to a line of longitude), and its descending branch marks the position of the subtropical regions (deserts) (Lu and Vecchi, 2015). Globally, the ITCZ mean position resides in the Northern Hemisphere (NH) for most of the year at around 6° due to the cross-equatorial transport of energy by the Atlantic Ocean. This makes the NH warmer than the SH (Southern Hemisphere), except during glacial times (Arbuszewski et al., 2013; Schneider et al., 2014).

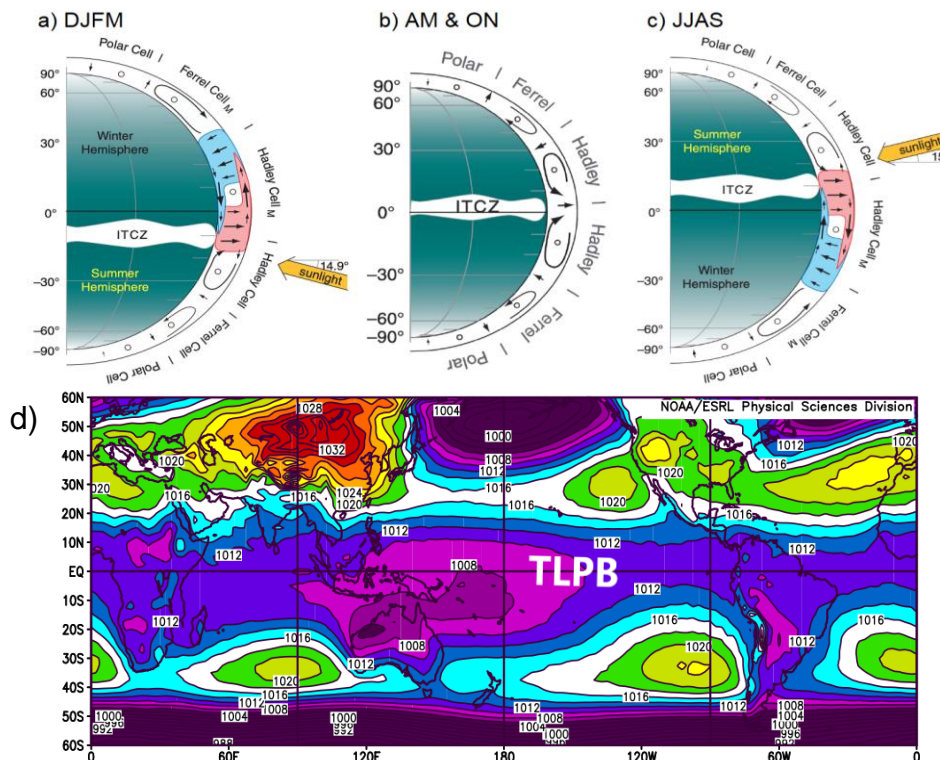


Figure 1.1 Cross section of the Earth's global circulation in the troposphere **a)** Southern Hemisphere summer (DJFM), **b)** transition (shoulder) months (AM and ON), and **c)** Northern Hemisphere summer (JJAS). The major Hadley cell is colored in red and blue and is indicated by the subscript M. Note the intra-annual ITCZ excursions (horizontal white cloud along the equator) following the annual insolation. Adapted from Stull (2020) under Creative Commons license CC BY-NC-SA 3.0 US. **d)** Location of the Tropical Low Pressure Belt (TLPB; purple-magenta contour) during austral summer (DJF) where its features are enhanced. Sea Level Pressure (mb) data from NCAR/NCEP reanalysis for the period 1949-2019 (70 years).

1.2 Monsoonal circulations

In the last decades, there has been a surge in interest in the role of tropical circulations and its global climate influence (e.g., El Niño-Southern Oscillation (ENSO) cycle, Madden-Julian Oscillation, Pacific double ITCZ) (Chiang, 2009; Hwang and Frierson, 2013; Zhang, 2001; Zhang and Delworth, 2005). In particular, attention has focused on studying the Global Monsoon systems, which besides the ITCZ, is the dominant mode that brings annual precipitation in the tropics (Rojas et al., 2016; Wang and Ding, 2008; Wang et al., 2014) (Figure 1.2).

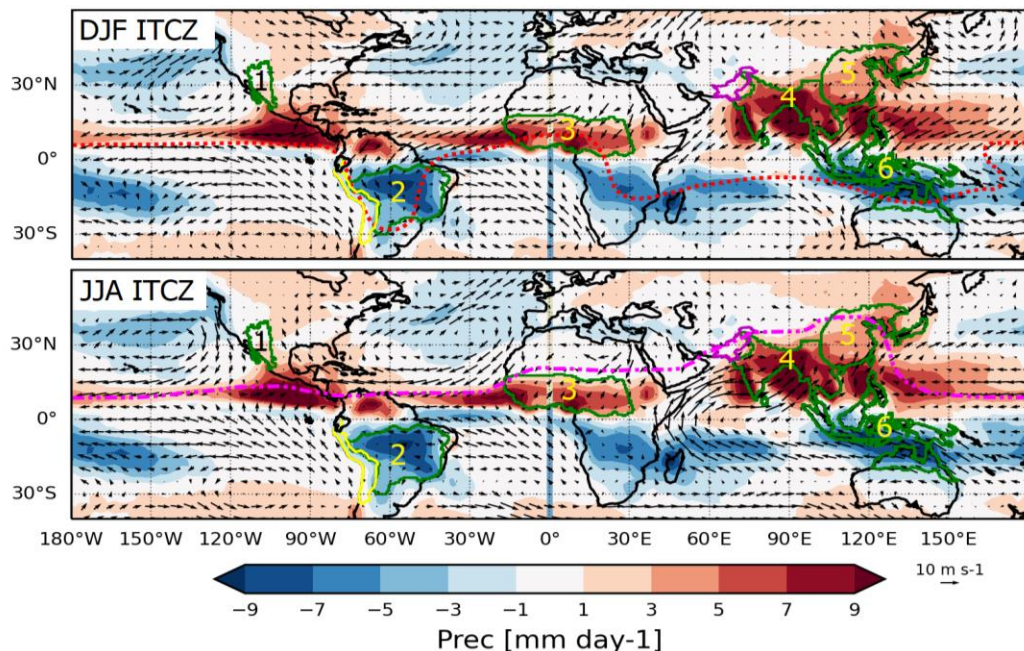


Figure 1.2 World map showing the monsoon areas according to the criteria of Wang and Ding (2008), where the local summer minus winter precipitation exceeds 2 mm day^{-1} , and summer accounts for at least 55% percent of the annual total rainfall (red and blue zones). Green areas with numbers (1-6) indicate the Global Monsoon regions defined by the Intergovernmental Panel on Climate Change (IPCC) Six Assessment Report (Douville et al., 2021). 1-North American Monsoon, 2-South American Monsoon, 3-West African Monsoon, 4-South and Southeast Asian Monsoon, 5-East Asian Monsoon, 6-Australian and Maritime Continent Monsoon. The means of low winds (1959-2021; 925 hPa) for DJF (top panel) and JJA (bottom panel) are depicted by the black arrows with corresponding velocity scale at the bottom right. Red and magenta dotted and dashed lines represent the present day ITCZ mean positions during the annual excursions in DJF and JJA respectively according to Hogg et al. (2020) and used as boundary for global ^{14}C distribution. In South America, the borders of modern Ecuador (black) and past Inca Empire (Tawantinsuyu 1438–1533/1572, Marsh et al. (2017); yellow) are highlighted. Similarly, in Asia the borders of Pakistan (magenta) illustrate the monsoonal influence during JJA. The enhanced monthly averaged precipitation values (mm day^{-1}) were obtained from CPC Merged Analysis of Precipitation (CMAP) (Xie and Arkin, 1997). The uv wind components at 925 hPa pressure levels correspond to ERA5 reanalysis (Hersbach et al., 2019).

Monsoons are seasonal phenomena with a well-established onset, mature phase, and demise rainfall periods (Vuille et al., 2012). They are characterized by an annual rainfall cycle with a wet summer and drier winter showing an annual reversal of surface winds, except in the South American Monsoon System (SAMS; number 2 in Figure 1.2), where wind reversal is observed once the annual mean is removed from the winter and summer mean circulation (Garcia and Kayano, 2010; Zhou and Lau, 1998). The principal Global Monsoon systems correspond to the North and South American Monsoon, West African Monsoon, South and Southeast Asian Monsoon, East Asian Monsoon, and the Australian and Maritime Continent Monsoon (IPCC, 2021; Wang and Ding, 2008).

The study of monsoons is an increasingly important area in meteorology and climatology because their anomalies are associated with droughts, floods, and extreme events affecting millions of people settled over these areas especially in developing countries. That is the case of the extreme floods registered in Pakistan during the boreal summer in 2022, which besides the glacial melt due to extreme heatwaves had an earlier and prolonged monsoonal component (number 4 in Figure 1.2) (Mallapaty, 2022; Zhisheng et al., 2015).

1.3 ITCZ and SAMS dichotomy

Earlier research has established that the ITCZ and the monsoonal circulation are two separate precipitation systems (Baker and Fritz, 2015; Cook, 2009; Marsh et al., 2018; Rojas et al., 2016; Vuille et al., 2012; Zhou and Lau, 1998). On the contrary, recent literature suggests that the monsoon is just an extension of the ITCZ but shifted southwards during the summer season, when the insolation is maxima (Chao and Chen, 2001; Gadgil, 2018; Garcia and Kayano, 2010). In South America, the delayed recognition of the SAMS as monsoon has led to some confusion with the ITCZ. The terms have been used interchangeably in some cases; however, their spatiotemporal characteristics are quite different (Vuille et al., 2012). Although the SAMS controls a significant part of the seasonal precipitation variability, its modern influence is limited to 10° away from the equator, because at latitudes between 10°N - 10°S , the annual mean wind and velocity potential fields are approximately symmetric and do not reflect any monsoonal character (Chao and Chen, 2001; Douville et al., 2021; Murakami and Nakazawa, 1985). Despite this apparent difference between the systems, there are several statements that are not consistent. For instance, Cook (2009) suggests that in some parts in South America, the ITCZ and SAMS are related or even overlap at times. Wang and Fu (2002) showed that the onset of the wet (monsoon) season in South America starts during austral spring (SON) in the northwestern Amazon basin (10°N - 10°S ; their Figure 1) and distribute rainfall southward along the Andes foothills and eastward to central Amazon, hence feeding the SAMS. In other words, the onset of the SAMS occurs within the ITCZ domain, which is quite paradoxical. Furthermore, by means of an Empirical

Orthogonal Function (EOF) analysis of the Outgoing Longwave Radiation (OLR), a proxy for convective precipitation, Garcia and Kayano (2010) showed that the ITCZ (EOF1, 69.1%) and ITCZ (EOF2, 17.9%) modes evolve into each other within a period of one year. This brings evidence of the tight relationship between these two systems.

The clarification of the ITCZ and SAMS boundaries is not a trivial issue. The ITCZ position, structure and migration play a role on the local, regional and global scale permitting the interaction between land and ocean with the atmosphere (Waliser and Jiang, 2015). For instance, one of the main direct applications comes from the field of Radiocarbon (^{14}C), in particular South America, whose territory spans both hemispheres and experiences atmospheric mixing near the equator (Hogg et al., 2020; Marsh et al., 2018). Surprisingly, the available ^{14}C calibration curves for the Southern Hemisphere (SH Zone 1-2, SH Zone 3) are constructed based on seasonal biased temperate trees (Figure 1.3) (Hua et al., 2022; Reimer and Reimer, 2004). This is due to the fact that there are few tropical chronologies constructed at low latitudes, bolstered by the misconception that there is no formation of visible rings at the tropics (Hogg et al., 2020; Worbes, 2002)

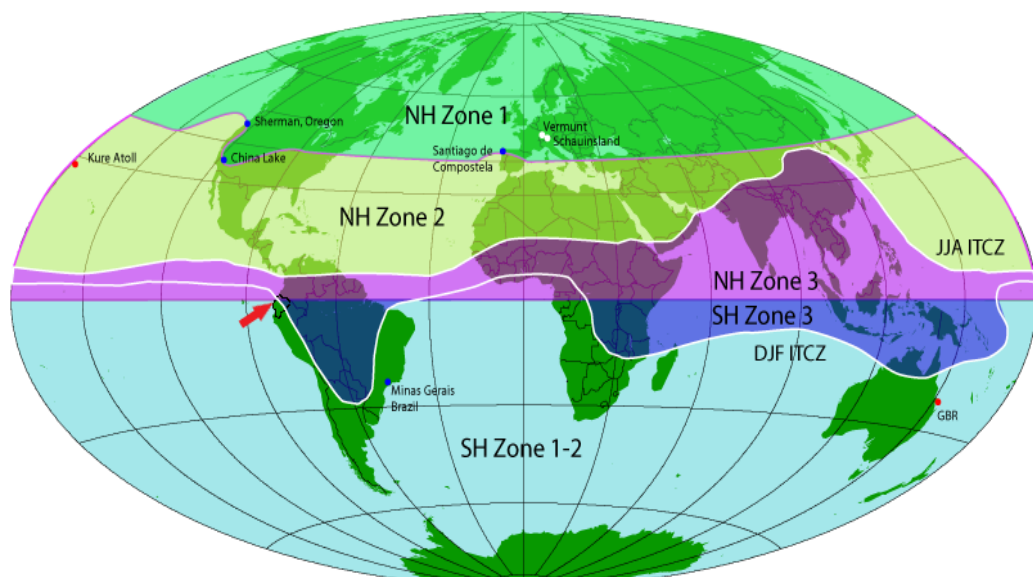


Figure 1.3 Radiocarbon zones around the globe indicating the distribution of ^{14}C and their corresponding calibration curves. Note that continental Ecuador (indicated by the red arrow) is geographically located in the intersection of three zones NH Zone 3, SH Zone 1-2 and SH Zone 3. Figure from Reimer et al. (2004) available at <http://calib.org/CALIBomb/>.

Up to now, the closest chronology to the equatorial line ($0^\circ 0' 0''$) used for the construction of the ^{14}C calibration curves comes from Indonesia (5°S , 122°E ; 1950–1972). In South America, the closest tree-ring record relative to the equator is from Chile (20°S , 68°W ; 1950–1972) and Camanducaia, Brazil ($22^\circ 50'\text{S}$, $46^\circ 04'\text{W}$; 1950–1972) (See

Table 1 in Hua et al. (2022)). Despite the fact that the SH ^{14}C calibration curves differ less than a century and are useful for paleoenvironmental studies, they are not robust for establishing reliable ages of past human activities like the Inca Empire, whose territory was influenced by the ITCZ excursions during austral summer (DJF) (Figure 1.2 and 1.3). In fact, some dated Inca artifacts have shown that ^{14}C error is bigger than the lifespan of an Inca ruler and does not agree with the written Spanish chronologies (Ancapichún et al., 2022, 2021; Marsh et al., 2018; Ogburn, 2012). Therefore, more tree-ring chronologies close to the equator are necessary for improving the ^{14}C calibration curve to expand the geographic frontiers of dendrochronology and revisit some of the preconceived history of the American continent as recently done by Kuitems et al. (2022).

1.4 Paleoclimate studies

Another field where the ITCZ-SAMS boundaries have not been thoroughly studied is paleoclimatology. The study of past climates has become crucial for improving our understanding of the effects of past natural forcings and validating numerical climate models representing physical processes on Earth (Goosse, 2015). It provides a valuable bridge between past trends and future global climate change scenarios affecting human development and socio-economic growth (Bradley, 2015). For paleoclimate studies, a detailed understanding of the system under study and its complex interactions is key for an accurate interpretation of the records (Fairchild and Baker, 2012; Kwiecien et al., 2021; Lachniet, 2009). Recent work has established that any past environmental system can be decomposed into three components: sensor, archive, and observation (Evans et al., 2013), and is indicated in Figure 1.4. This framework is called Proxy System Model and captures the complexities of the natural systems (Dee et al., 2015; Evans et al., 2013).

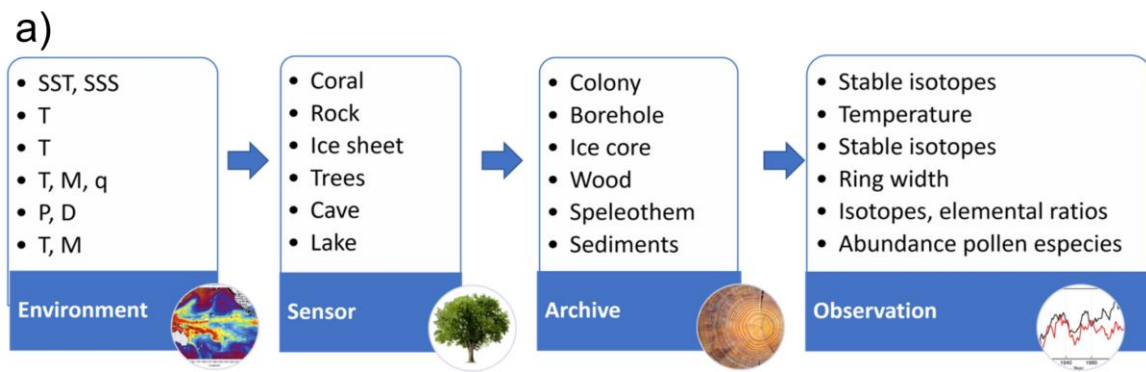


Figure 1.4 a) Conceptual proxy system model in paleoclimatology. Adapted from Evans et al. (2013). The acronyms in the *Environment* box correspond to Sea Surface Temperature (SST), Sea Surface Salinity (SSS), Air Temperature (T), Soil Moisture (M), Humidity (q), Precipitation (P), and Drip rate (D).

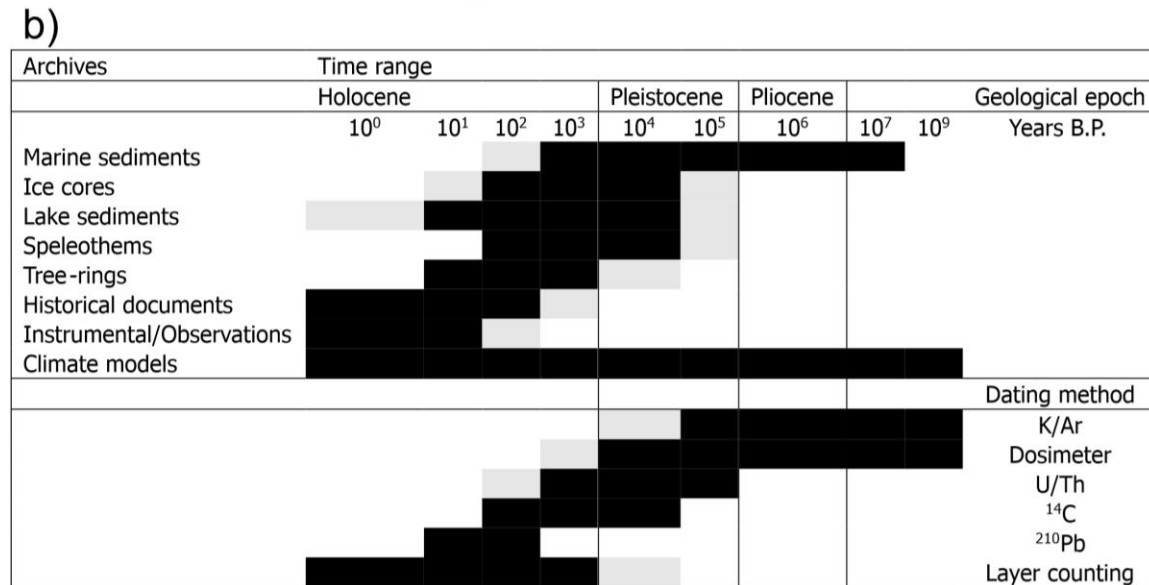


Figure 1.4 (continued) b) Most common archives used in past climate studies, epochs and their absolute dating methods. The “frequently” and “occasionally” used archives for reconstructing a specific epoch are shown in dark and light shading respectively. Adapted from Mudelsee (2014).

Consequently, an archive is only a medium where the response of a sensor to an environmental forcing is recorded, thus it becomes a natural element that harbors paleodata in form of a time-series (Dee et al., 2015; Evans et al., 2013; Mudelsee, 2014). For example, past hydrology can be reconstructed using stable isotopes (observation) in calcite from speleothems (archive), which is the long-term response of a karstic cave (sensor) to changes in the regional to global climatology (environment).

1.4.1 Stable isotopes of water

The stable isotopes of water, oxygen-18 (^{18}O), and deuterium (^2H), are some of the most common environmental tracers of relevance for climatological, glaciological, oceanographic, and hydrological studies (Araguás-Araguás et al., 2000; Clark, 2015). They are expressed in delta notation, and in the case of precipitation, the observed isotopic variations in oxygen and hydrogen will be expressed as $\delta^{18}\text{O}_p$ and $\delta^2\text{H}_p$ according to the formula:

$$\delta^{18}\text{O} (\text{\textperthousand}) = \left[\frac{(^{18}\text{O}/^{16}\text{O})_{sample}}{(^{18}\text{O}/^{16}\text{O})_{standard}} - 1 \right] \times 1000 \quad (1)$$

where the standard corresponds to the Vienna Standard Mean Ocean Water (VSMOW), and the final results are given in per mil (‰) (Araguás-Araguás et al., 2000; Araguas et al., 1996; Clark, 2015).

In an isotopic system, physical or chemical transformations produce a product pool with a specific isotopic signal that presents the signal of the starting isotopic pool

but altered by subsequent fractionation (Bowen, 2010). A change in the ratio from a source to a final product is called fractionation (McCarroll and Loader, 2004). The degree of isotopic fractionation depends on whether the system is governed by equilibrium or kinetic fractionation (Clark, 2015; Sharp, 2017). In the case of precipitation, isotopologues of water are sensitive to phase transition (Clark, 2015; Sharp, 2017; Tada et al., 2021). The ^{18}O and ^2H -rich rainwater preferentially condense and less preferentially evaporate, compared to the ^{16}O and ^1H isotopes (Araguas et al., 1996; Clark, 2015; Tada et al., 2021). Dansgaard (1964) formulated several empirical relationships between $\delta^{18}\text{O}_p$, $\delta^2\text{H}_p$ and the environmental parameters (e.g., surface air temperature, amount of precipitation, latitude, altitude, distance from the coast), which are known as fractionation “effects”. At mid and high latitudes, the gradual lowering of $\delta^{18}\text{O}_p$ and $\delta^2\text{H}_p$ values corresponds to the progressive cooling of air masses transporting moisture from the tropics towards the poles and the pronounced seasonal air temperature variations (Araguás-Araguás et al., 2000; Clark, 2015). For tropical regions, characterized by minimal temperature fluctuations, $\delta^{18}\text{O}_p$ and $\delta^2\text{H}_p$ changes are not associated with temperature, but there is a noticeable negative correlation with the amount of precipitation, coined as the “amount effect” (Dansgaard, 1964; Kurita et al., 2009; Rozanski and Araguás-Araguás, 1995). Although the rest of the effects might also play a role modifying the isotopic signal, this will ultimately depend on the site’s location.

The suitability of $\delta^{18}\text{O}_p$ and $\delta^2\text{H}_p$ in paleoclimatology relies on their ability to encode information about the source of the precipitation and its evaporation and condensation history (Guy et al., 2019; Sodemann et al., 2008). Nevertheless, the quantitative interpretation of isotopic signals from archives to past climate can sometimes be intricate. Processes associated to changes in evaporation conditions, moisture sources, atmospheric transport pathways or rainfall seasonality might play a crucial role in the final isotopic imprint (Cauquoin et al., 2019). This becomes even more challenging at tropical latitudes, where convective processes are connected to numerous phase changes within the cloud (cumuliform) such as unsaturated downdrafts, rainfall re-evaporation, and subcloud processes (Bony et al., 2015, 2008; Risi et al., 2010). Traditionally, the isotopic signal from archives have been calibrated based on a modern analog approach; which means modern observed surface temperature, precipitation amount or salinity are used to interpret changes in the observed isotopic values (Cauquoin et al., 2019). Another option is to represent the evolution of the remaining water vapor in a cloud using a Rayleigh distillation model (Cauquoin et al., 2019; Clark, 2015). A third alternative is to employ Earth System Models (ESM; previously known as General Circulation Models) which take into account numerous physical processes nudged with stable isotopes (Cauquoin et al., 2019; Werner et al., 2011).

1.4.2 Terrestrial archives

Based on their growing environment, most archives could be classified as aquatic, terrestrial and anthropogenic (Figure 1.4b). For aquatic environments, marine and lake sediment cores along with coral reefs are the most representative. In case of terrestrial, the most frequently used are ice cores, tree rings, speleothems, pollen, boreholes, loess, paleosols and plant macrofossil (Bradley, 2015; Fairchild and Baker, 2012; Speer, 2010). Lastly, historical records and past climate models fit into the category of anthropogenic archives (Mudelsee, 2014; Valdes et al., 2021). The longest records have been constructed with the use of marine sediments and ice cores (Lambert et al., 2008; Petit et al., 1999). In particular, the stratigraphy of marine records provides a Pliocene-Pleistocene stack of 57 globally distributed benthic $\delta^{18}\text{O}$ records denominated Marine Isotope Stages and cover the last 5.3 Ma (Lisiecki and Raymo, 2005; Railsback et al., 2015). Regarding ice cores, the Antarctica Vostok and EPICA-C cores have provided valuable data for the last 400 and 800 ka respectively (Lambert et al., 2008; Petit et al., 1999). They compare well with the distant Greenland ice records (Alley et al., 2010), and indicate global ocean-cryosphere changes. However, despite of giving the longest records, both marine records and ice cores are either spatially bias towards the poles or do not register climatic variations in land. Additionally, the chronologies of the marine records often depend on orbital tuning, or they have large uncertainties (Bradley, 2015). Similarly, ice cores might suffer from postdepositional length distortions such as compressing affecting the spacing of the record (Mudelsee, 2014). Furthermore, usually radiometric dating cannot be carried out in the complete ice core, but on sections with trapped material leaving many segments to be fitted by wiggle matching, orbital tunning or mathematical models (Fernández Sánchez, 2016; Ramirez, 2003; Thompson et al., 2000; Thompson and Davis, 2007).

On the contrary, tree-rings and speleothems are two of the most ubiquitous and versatile archives on Earth. Their worldwide presence, accessibility, exploration costs, novel analytical techniques for sampling and measuring, but especially their dating precision (up to yearly resolution) have made them particularly attractive (Betancourt et al., 2002; Cheng et al., 2013a; Fairchild et al., 2006; Fairchild and Baker, 2012; Grissino-Mayer, 2001; Holmes, 1983; McCarroll and Loader, 2004; Schwarcz, 2013; Siegwolf et al., 2022; Speer, 2010). Indeed, tree-rings and speleothems are some of the few archives whose sampling can be accomplished at time-equidistant points, avoiding interpolation which increases serial dependence (persistence) to the climate time-series (Mudelsee, 2014). Dendrochronology (from Greek: *dendros*, tree; *chronos*, time, and *logos*, science) examines events using patterns of tree-ring width, wood density, element content, and other tree features (e.g. cellulose, phytoliths) (Lisztes-Szabó et al., 2019; Speer, 2010; Worbes, 2002; Zuidema et al., 2022). The main subdivisions are dendrochemistry, dendroecology, dendrogeomorphology, dendroarchaeology, and dendroclimatology (Speer, 2010). A clear aim at the beginning of the project is crucial for tackling a tree-

ring sampling campaign. Although obvious, it is easy to make a mistake sampling tree cores that are not suitable for one subfield but useful for others. For instance, tree trunks which are injured or tilted must not be employed for dendroclimatic studies but might serve as raw material for solving dendrogeomorphological questions (Speer, 2010; Stokes and Smiley, 1968). Sampling a representative number of trees is also vital for research. Usually, robust tree-ring chronologies are built employing 15-30 trees, and from each individual tree, 2-4 cores are taken following the cardinal points. Hence, at the end, one might end up collecting 30-120 cores from a new study site (Cook and Kairiukstis, 1990; Phipps, 1985; Stokes and Smiley, 1968). After a meticulous sanding of the samples, the ring width is measured employing a tree-ring station or digitally on scanned high resolution images, where patterns are compared among the cores assigning a calendar year to each ring in a process called cross-dating (Cook and Kairiukstis, 1990; Larsson, 2016). In fact, cross-dating is what makes dendrochronology a science and not mere ring counting, and it is the common phase in any dendro-study.

In dendroclimatology, the use of stable isotopes takes advantage of the systematic way some specific isotopes behave in nature, exploiting the small mass differences in the isotopic ratios which are redistributed after going through physical or chemical reactions (fractionation) (Saurer et al., 2022; Siegwolf et al., 2022). In the wood, there is a tendency of the isotopes to redistribute sequentially from the beginning to end of a ring. In case that trees uptake soil water dominated by precipitation, the water has an isotopic signature related to local air-mass characteristics carrying a specific atmospheric ^{18}O imprint (Figure 1.5). Hence, it is assumed that the obtained oxygen isotopic signal in tree-rings ($\delta^{18}\text{O}_{\text{TR}}$) will mainly reflect the $\delta^{18}\text{O}_{\text{p}}$ (Loader et al., 2007; McCarroll and Loader, 2004; Treydte et al., 2014). In tropical regions, $\delta^{18}\text{O}_{\text{TR}}$ has been primarily used as a proxy for reconstructing past precipitation and identifying annual rings in ring-less wood (Baker et al., 2016; Brienen et al., 2012; van der Sleen et al., 2017). As a complement to $\delta^{18}\text{O}_{\text{TR}}$, carbon isotopes in tree-rings ($\delta^{13}\text{C}_{\text{TR}}$) have been shown to reflect changes in the internal concentration of CO_2 within the leaf space compared to ambient CO_2 (McCarroll and Loader, 2004). Approximately, the $\delta^{13}\text{C}$ value in the atmospheric CO_2 is around -8‰ (<https://gml.noaa.gov/ccgg/isotopes/c13tellus.html>, last access: 16 April 2023). Once diffused through the leaves stomata, it is distributed to the tree trunk in form of sugars with a $\delta^{13}\text{C}$ value ranging between -25 to -30‰ (Siegwolf et al., 2022). The amount of CO_2 in leaves is actively regulated by the stomatal conductance and photosynthetic rate. The climatic controls regulating photosynthetic rate are irradiance (light availability) and temperature. For stomatal conductance, air humidity and soil moisture are the main modifiers of the carbon signal (Loader et al., 2007; van der Sleen et al., 2017).

Usually, $\delta^{13}\text{C}_{\text{TR}}$ is expressed relative to a pre-industrial standard value by adding a correction factor. This value corrects the atmospheric decline in the atmospheric $\delta^{13}\text{C}$ signal due to an increase in ambient CO_2 of anthropogenic origin (McCarroll and Loader, 2004).

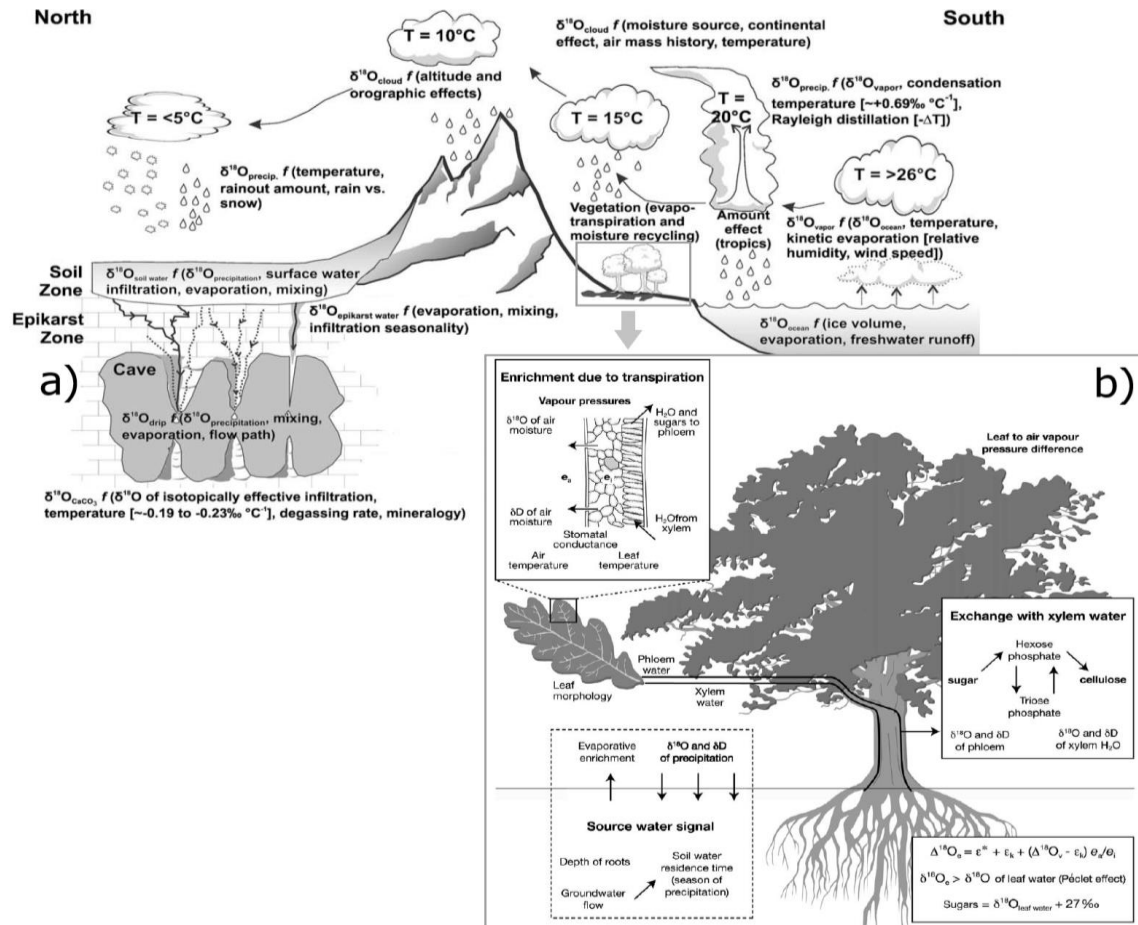


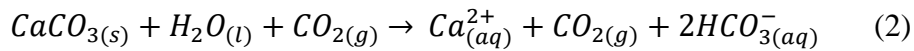
Figure 1.5 Main processes related to tree-ring and speleothem paleoclimatology modified from Figure 1 in Lachniet (2009) and Figure 3 in McCarroll et al. (2004). **a)** The $\delta^{18}\text{O}$ variations correspond to phase changes starting at the ocean, atmosphere, soil, epikarst zone and finally deposited in cave speleothems. **b)** Once in the soil, the $\delta^{18}\text{O}$ signal from precipitation is incorporated through the tree root zone for the physiological internal non-fractionating processes except during transpiration, which can enrich the isotopic signal in the wood. For a detailed explanation of the symbols and equations, the reader is referred to the original cited authors.

On the other hand, speleothems, found in karst environments, are secondary mineral deposits formed in caves (Figure 1.5). Speleothem is a generic term that encompasses a broad myriad of shapes as a result of combination of different flow regimes and growth habits inside the cave atmosphere as illustrated in Table 1.

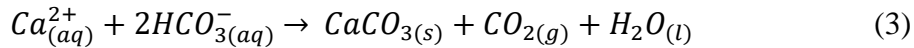
Table 1. Classification of speleothems according to White (2019).

A. Forms created by dripping water
Stalactites
Stalagmites
Draperies
Shields
B. Forms created by flowing water
Flowstone
Rimstone Dams
Coralloid Forms (globulites, cave popcorn, cave beads, cave coral)
C. Forms created by seeping water
Crusts and Coatings
Helictites
Oulopholites (Gypsum Flowers)
Anthodites/Frostwork
D. Forms created in standing water
Cave Pearls and other concretions
Shelfstone
Pool Spar
Pool Fingers

In paleoclimatology, stalagmites are the most common employed speleothems due to their simple internal structure (Fairchild and Baker, 2012). The path towards stalagmite formation starts when meteoric water percolates through the soil, that has high pCO₂ due to aerobic respiration, obtaining aqueous carbonic acid which dissolves the limestone bedrock traveling downwards in the vadose zone until mineral saturation (Fairchild and Baker, 2012; White, 2019) (Equation 2).



Upon reaching the cave void, having lower pCO₂, secondary carbonate mineral deposition occurs through the degassing of saturated cave drip water, that is controlled by the cave background CO₂ pressure and ventilation (geometry) (Dreybrodt et al., 2005; Fairchild et al., 2006; Fairchild and Baker, 2012; White, 2019).



Calcite, aragonite, and in different chemical processes gypsum are the most common deposited minerals occurring in speleothems (White, 2019), of which calcite and aragonite composed speleothems are the most useful for paleoclimate purposes (Fairchild and Baker, 2012). Their oxygen isotope composition ($\delta^{18}O_{cc}$), assuming equilibrium fractionation of isotopes between water and carbonate, depends on the temperature during precipitation and oxygen isotope composition of the dripwater

($\delta^{18}\text{O}_{\text{drip}}$). However, various processes (e.g., rates of CO_2 degassing, and mineral precipitation, evaporation, prior calcite precipitation, etc.), can induce kinetic fractionation, masking the original climate-control $\delta^{18}\text{O}_{\text{drip}}$ signal (Fairchild and Baker, 2012; Hendy, 1971). The presence of equilibrium CaCO_3 precipitation are frequently evaluated through a Hendy test (Hendy, 1971). The test consists of the selection of few laminae from which several points away from the axial zone are sampled and their $\delta^{13}\text{C}_{\text{cc}}$ and $\delta^{18}\text{O}_{\text{cc}}$ measured. If there is a strong covariation between the isotopic values, this would indicate that deposition occurred under kinetic fractionation (Fairchild and Baker, 2012). The Hendy test has been recently challenged (Dorale and Liu, 2009; Fairchild and Baker, 2012) especially because:

1. Equilibrium might be present in the central axis but not in the flanks.
2. Difficulties for targeting and correctly sampling the same lamina.
3. The strong correlation between $\delta^{13}\text{C}_{\text{cal}}$ and $\delta^{18}\text{O}_{\text{cal}}$ might be caused by processes during calcite precipitation and not related to climatic or hydrological processes.

In addition, the recent findings of Daëron et al. (2019) have established that most carbonates on Earth deposit out of isotopic equilibrium. Nevertheless, it is still the most common method to ascertain possible kinetic effects in a speleothem record (e.g., Wendt et al., 2021).

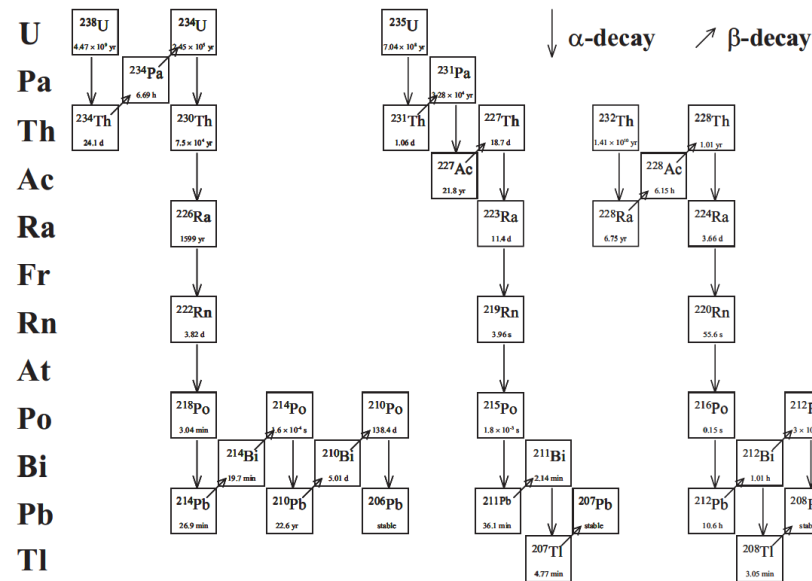


Figure 1.6 The three ^{238}U , ^{235}U and ^{232}Th decay chains which end up in different Pb stable isotopes. Their half-lives are shown in each box. Alpha (α) and beta (β) decay are represented by the vertical and diagonal arrows respectively. During α -decay there is an emission of an alpha particle (${}^4\text{He}$) and gamma ray (γ). In case of a β -decay, a neutron turns into a proton plus a β -particle (accompanied with a neutrino) and γ -ray (Challoner, 2018). Diagram obtained from Figure 1 in Scholz and Hoffmann (2008).

U-Th (or ^{230}Th) dating of speleothems is based on the extreme fractionation of U and Th in groundwater, with U being easily soluble and Th having extremely low

solubility (Figure 1.6). Indeed, taking into account the chemical characteristics of U and Th in aqueous environments, the U^{+6} rapidly forms aqueous uranyl ions, whereas Th^{+4} is insoluble (Fairchild and Baker, 2012; Nissen, 2018). As a result, the crystal lattice of the speleothems incorporates U, but only negligible amounts of ^{230}Th . Thus, if the crystal lattice remains a closed system, the time passed since speleothem deposition can be determined based on the radioactive evolution of ^{238}U , ^{234}U , and ^{230}Th (Cheng et al., 2013a; Dorale et al., 2007; Edwards et al., 1987). In other words, carbonate deposits formed in aqueous environments have low initial ^{230}Th and its presence is indicative of radioactive decay from ^{238}U which allow the radiometric dating (Fairchild and Baker, 2012; Nissen, 2018; Scholz and Hoffmann, 2008).

To utilize the $\delta^{18}\text{O}_{\text{cc}}$ as climate proxy, a calibration of the stalagmite has to be carried out. This is typically accomplished by monitoring the processes above ($\delta^{18}\text{O}_{\text{p}}$) and beneath the epikarst zone in the cave drip water ($\delta^{18}\text{O}_{\text{drip}}$) (Baker et al., 2019; Dreybrodt et al., 2005; Dreybrodt and Gabrovsek, 2003; Kogovšek, 2010). In monsoonal regions with cooler mean annual temperature (MAT), it was found that it is likely for the $\delta^{18}\text{O}_{\text{drip}}$ to be similar to the amount-weighted $\delta^{18}\text{O}_{\text{p}}$ (Baker et al., 2019). In warmer monsoonal environments, with $\text{MAT}>16\ ^\circ\text{C}$, the authors suggested that the $\delta^{18}\text{O}_{\text{drip}}$ presents a seasonal bias towards the $\delta^{18}\text{O}_{\text{p}}$ of recharged periods, due to the combined effect of the selective recharge and the evaporative fractionation at such temperatures of stored karst water. These findings are in agreement with previous studies suggesting that speleothems from low-latitudes are useful for paleohydrological studies (Apaéstegui et al., 2014; Fairchild and Baker, 2012; Kanner et al., 2013; Wolf et al., 2020).

1.4.3 Statistical analysis of paleoclimate records

In climatology, time-series which are stationary (constant mean and variance) are usually the exception rather than the rule (Bisgaard and Kulahci, 2011; Fairchild and Baker, 2012). There are two approaches to examine patterns and properties in the records. They are associated with the time and the spectral domain (Ghil, 1997; Ghil et al., 2002; Mudelsee, 2014; Percival and Walden, 1993; Wilks, 2019). The time domain analysis focuses on the behavior of the signal over time, where quantifying the first statistical moments (e.g., mean, variance, skewness, kurtosis), autocorrelation, trends and patterns over time are the target (Storch and Zwiers, 1999; Wilks, 2019). On the other hand, spectral domain analysis requires transforming the datasets into a frequency domain using techniques like the Fourier transform, facilitating the location and strength of the different frequency components in the signal (Schulz and Stattegger, 1997; Trauth, 2021). A spectral analysis becomes particularly useful in paleoclimatology when two or more records are to be compared. Contrary to datasets in other fields, such as economy or engineering where the time-series are evenly spaced, most of the paleoclimate records are not equidistant and their spacing usually depends on their radiometric dating and sampling resolution (e.g., ^{14}C , U-Th, U-Pb) (Mudelsee, 2014, 2001; Schulz and

Mudelsee, 2002). Unfortunately, an interpolation in the time domain to make the series evenly spaced is not recommended (Mudelsee, 2014; Schulz and Stattegger, 1997). In fact, Schulz and Stattegger (1997) have shown that interpolation affects the spectral domain by enhancing the low-frequency components in the time-series in detriment of the high-frequency making the spectrum too “red” by adding this so called red-noise (Gilman et al., 1963; Schulz and Mudelsee, 2002). Red-noise and white-noise are two types of signals within the time-series that have different characteristics. The red-noise signal changes slowly over time due to the presence of more energy at lower-frequencies, whereas white noise has equal amount of energy across all frequencies and therefore has equal probability of depicting a random signal of uncorrelated variables (Shumway and Stoffer, 2017). These characteristics affect their long-term correlations and persistence (serial dependence) properties. Nearby values in a time-series with red-noise will show strong correlation (memory) contrary to one with white-noise, with no memory and random past values. The reason for the memory effect might come from innate characteristic of the sensor transferring climatic fluctuations into the archive or induced by sampling resolution of the data (higher resolution = stronger persistence) (Mudelsee, 2014, 2002).

A novel approach to analyze paleoclimate time-series has been proposed by Mudelsee (2014), and consist in the decomposition of a discrete time-series $X(T(i)) \equiv X(i)$ as the sum of the trend, outliers, and noise scaled by its variability according to Equation 4:

$$X(i) = X_{trend}(i) + X_{out}(i) + S(i) \cdot X_{noise}(i) \quad (4)$$

The trend $X_{trend}(T)$ can be determined by linear, nonlinear and nonparametric methods (Mudelsee, 2019). The noise component $X_{noise}(T)$ is usually obtained through spectral analysis, and the variability $S(T)$ by detrending or normalizing the time series as presented in Figure 1.7. These parameters are important to quantify in order to determine the “true” signal, because a recurrent issue in climate analysis is that the observation values superimpose on the climatic processes. For instance, non-climatic trends, outliers, and noise might be embedded into the data due to changes in the recording resolution affecting the trend. Noise might come from instrument measurements and dating errors. Finally, the provenance of outliers might be power loss in the recording instrument (Mudelsee, 2014, 2002).

Trend $X_{trend}(T)$	Noise $X_{noise}(T)$	Variability $S(T)$	Outliers $X_{out}(T)$
<ul style="list-style-type: none"> •Linear •Nonlinear <ul style="list-style-type: none"> •Break •Ramp •Piecewise linear •Trapezoidal •Parabolic •Saturation •Continuos nonlinear •Abrupt constant •Abrupt linear •Abrupt nonlinear •Nonparametric •Kernel 	<ul style="list-style-type: none"> •Statistical noise distribution •Persistance •Red noise 	<ul style="list-style-type: none"> •Detrending •Normalization 	<ul style="list-style-type: none"> •Probability Density Function (PDF) estimation •Generalized Extreme Value distribution •Generalized Pareto distribution

Figure 1.7 Statistical analysis of climate time-series $X(t)$ proposed by Mudelsee (2014).

1.5 General overview of Ecuador on Paleoclimate

Historically, the location of Ecuador has been of particular interest to the scientific community. In the eighteen-century, the impact of Newtonian gravitational theory on ideas about the shape of the Earth was a heated debate at the French Academy of Sciences (Ferreiro, 2011). To settle the matter, two geodesic missions were launched to provide an accurate measurement of the length of a degree of latitude at the Artic Circle (Meänmaa in Lapland, 1736-1737; currently Finland), and at the equator (Spanish American province of Quito, 1736-1744; currently Ecuador) (Capello, 2018; Robinson, 2011). As a result, both expeditions determined that a degree of latitude is shorter at the equator (56753 toises \sim 110.54 km) than at Paris (57060 toises \sim 111.20 km) or towards the North Pole (57,437 toises \sim 111.94 km), and hence confirmed that the Earth's shape is an oblate spheroid (i.e., flattened at the poles) (Robinson, 2011). Although these findings enhanced our understanding of the Earth's shape and improved the navigation systems, the use of the geographical equator for climatological studies offers little help in explaining some of the features and complexity of climate and weather at low latitudes (Hastenrath, 1991).

1.5.1 Climatology (ITCZ, low-level jets and isotopologues of water)

In South America, there has been little discussion about precipitation outside the SAMS spanning the equator, especially in Northern Amazon (NAMZ) where the Ecuadorian Andes and Amazon are situated (Figure 1.8a). This region is characterized by complex local topography interacting with the annual migration of the ITCZ (Bendix and Lauer, 1992; Garcia et al., 1998; Ilbay-Yupa et al., 2021; Vuille et al., 2012). Curiously, this continental configuration spanning the equator presents two rainfall maxima

occurring with the equinoxes, while the dry seasons are demarcated by solstices (Webster and Fasullo, 2015), making the transfer to the paleoclimate proxy material and subsequent interpretation challenging. Previous research has established that the climate of Ecuador is indeed controlled by the ITCZ seasonal excursions and complex Andean orography (Garcia et al., 1998; Ilbay-Yupa et al., 2021; Slingo, 2015). Indeed, crossing the equator and located in both hemispheres (Figure 1.2 and 1.8), Ecuador is influenced by modes of precipitation variability occurring in Colombia and Peru. For these latter countries, the rainfall seasonality responds to the ITCZ and SAMS, respectively, making Ecuador a transition zone between these climatic systems (Garreaud et al., 2009; Ilbay-Yupa et al., 2021; Poveda et al., 2006; Wang and Fu, 2002). In the first case, the ITCZ excursions throughout the year determine the provenance of air masses with different humidity and temperature condition (Araguás-Araguás et al., 2000; Garcia et al., 1998; Ilbay-Yupa et al., 2021). When the ITCZ is at its northernmost position (JJA), cold westerlies flow into Ecuador, whereas during austral summer (DJF), moist winds from easterly directions reach the country (Ilbay-Yupa et al., 2021). Regarding the Andes, they act as a weather divide between the Pacific coast and the western Amazon due to its high elevation (>4000 m a.s.l.).

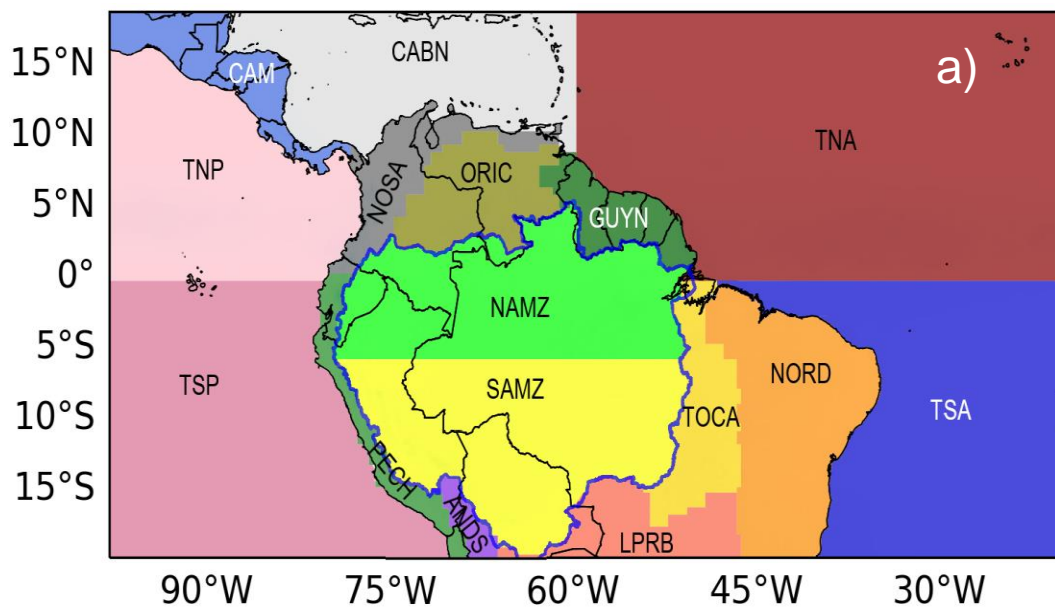


Figure 1.8 a) South American domains: Central America (CAM), northern South America (NOSA), Orinoco basin (ORIC), Guyanas (GUYN), Peru–Chile (PECH), Northern Amazon (NAMZ), Southern Amazon (SAMZ), subtropical Andes (ANDS), Tocantins basin (TOCA), La Plata River basin (LPRB), Brazil’s Northeast (NORD), tropical North Pacific (TNP), tropical South Pacific (TSP), Caribbean Sea (CABN), tropical North Atlantic (TNA), and tropical South Atlantic (TSA). Figure adapted from Ruiz-Vásquez et al. (2020).

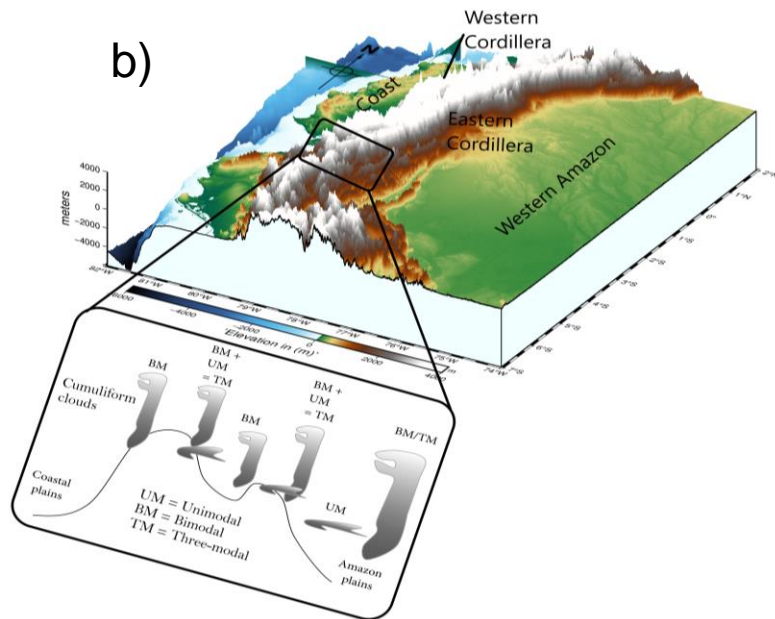


Figure 1.8 (continued) b) 3D perspective of the topography of Ecuador. The western and eastern Andean cordillera clearly stands out and modulates the country's rainfall and temperature variations. The inset at the bottom shows the diverse precipitation regimes: uni, bi and three-modal (peaks in precipitation) occurring at the inter-Andean valley adapted from Campozano et al. (2016).

The influence of the Andes is evident in the diverse unimodal, bimodal, and three-modal rainfall regimes (Figure 1.8b). The most common is the bimodal regime (two peaks in precipitation) showing typical convective character during the equinoxes (March and September), whereas the three-modal (three peaks in precipitation) is due to an advective barrage effect (Campozano et al., 2016; Ilbay-Yupa et al., 2021). Although the Ecuadorian climate is not monsoonal per se (see Figure 1.2 white gap at the equator), its unique location at the geographical equator permits investigating the interhemispheric moisture transport linking the Southern to the Northern Hemisphere fluxes (Martinez et al., 2022; Murakami and Nakazawa, 1985). This transport of moisture, mass, momentum, and energy is called the cross-equatorial flow of air masses (Hu et al., 2018).

The cross-equatorial flow plays a crucial role in the advection of moist and warm air from tropical regions toward the poles (Sturm et al., 2007b; Wang and Fu, 2002). Wang and Fu (2002) showed that precipitation variability over South America involves significant meridional migration and reversal of low-level winds between the south and north of the equator. These wind corridors in the lower atmosphere are low-level jets (LLJs) and transport water vapor that modulates weather and climate (Builes-Jaramillo et al., 2021; Gimeno et al., 2016; Martinez et al., 2022). Hence, LLJs are vital structures in the water vapor transport in the atmosphere, feeding the precipitation systems (Gimeno et al., 2016). In particular, a region where the cross-equatorial flow is enhanced corresponds to the V-Index region (5°S - 5°N , 65°W - 75°W ; black squares in Figure 1.9) that presents a

LLJ like structure that effectively captures the seasonal reversal of the circulation in the continent (contrary to the eastern Amazon) and is strongly associated with the SAMS transitions in the equinox and solstice seasons (Fu et al., 2016; Martinez et al., 2022; Wang and Fu, 2002). This monsoon index (V-Index) was constructed to represent the cross-equatorial flow variability, where positive (negative) values indicate southerly (northerly) winds (Arias et al., 2015; Ruiz-Vásquez et al., 2020; Wang and Fu, 2002). Northerly winds dominate the cross-equatorial flow in austral summer (DJF) and southerly winds in winter (JJA), with a transition from northerly to southerly winds in autumn (MAM) and southerly to northerly winds in spring (SON) (Wang and Fu, 2002) (Figure 1.9). A critical role of this atmospheric structure is the advection of moist, warm air poleward (Martinez et al., 2022). Bendix and Lauer (1992) already indicated the passage of a LLJ at the eastern Andean slope from February to March in the Ecuadorian territory, which most likely corresponds to this low-level cross-equatorial flow. Unfortunately, direct and continuous rawin (winds-aloft) observations are scarce in the country and have delayed the investigation of these essential meteorological structures.

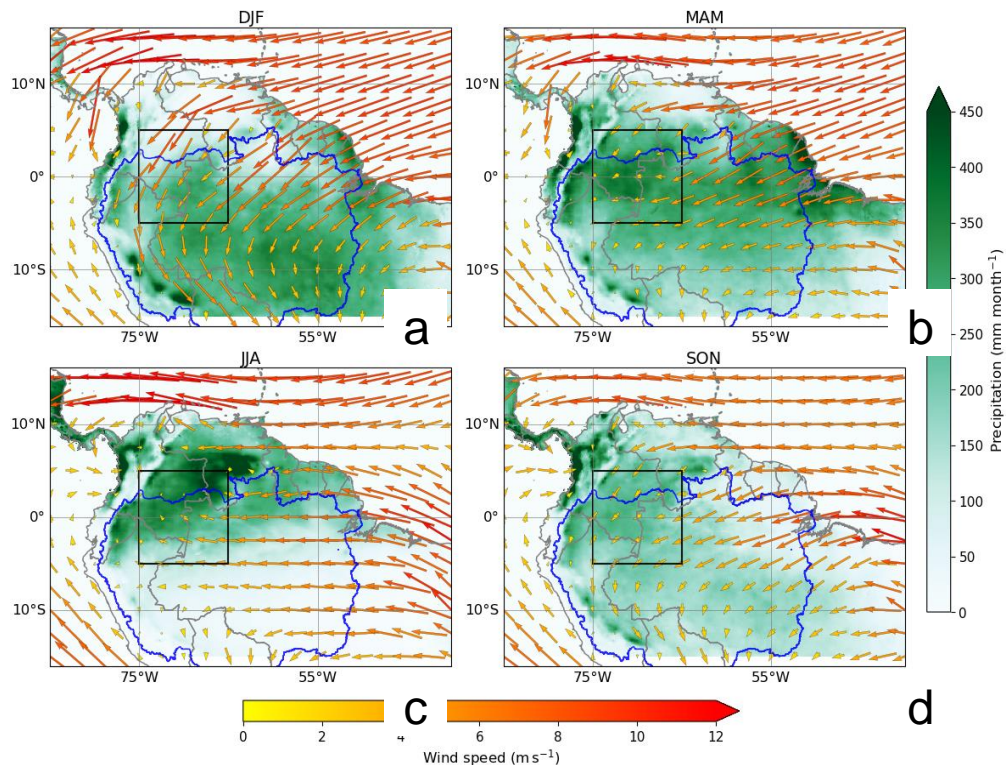


Figure 1.9 Plot of the 950-850 hPa ERA5 wind vectors (arrows) and mean precipitation of the Climate Hazards Group InfraRed Precipitation with Station data (CHIRPS) for austral (a) summer (b) autumn (c) winter (d) spring. The black box indicates the monsoon V-Index region over the western Amazon (5°S - 5°N , 65°W - 75°W), an area where the seasonal reversal of the cross-equatorial flow over South America is observed, according to Wang and Fu (2002). The blue line indicates the limits of the Amazon basin.

The seminal work of Garcia et al. (1998) investigated the $\delta^2\text{H}_p$ and $\delta^{18}\text{O}_p$ patterns in Ecuador by establishing two latitudinal northern and southern transects from the Coastal to the Amazon regions in the country. The authors showed that the Andes complex orography and the ITCZ precipitation in austral autumn (Mar-May) and spring (Oct-Nov) at these latitudes were responsible for the lowest $\delta^{18}\text{O}_p$ values, representing an amount effect. In addition, the surprisingly high $\delta^2\text{H}_p$ and $\delta^{18}\text{O}_p$ values in the Ecuadorian Amazon (>2000 km from the Atlantic) were due to the intense recycling of water vapor in the Amazon Basin, which is not fractionated during evapotranspiration and hence enriched the signal (Garcia et al., 1998; Salati et al., 1979). However, questions have been raised about the inadequacy of the local amount effect to capture the observed isotopic variation in the country. For instance, Villacís et al. (2008) found that the local amount of precipitation in Nuevo Rocafuerte station (Figure 1.10, right column) poorly explained the $\delta^{18}\text{O}_p$ variability. In contrast, correlation with convection using OLR (a proxy for convective precipitation) at northeastern South America resulted in a better predictor of monitored isotopic values.

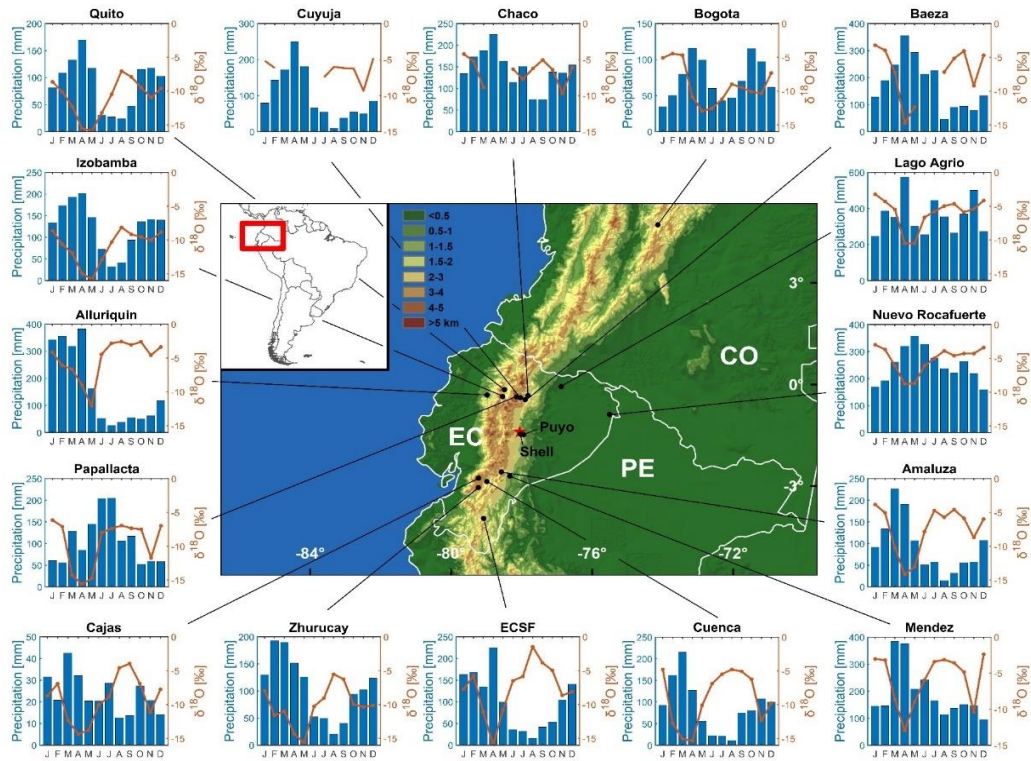


Figure 1.10. Rainfall climatology and $\delta^{18}\text{O}_p$ seasonality for stations along Ecuador's Amazon and Andean region. Datasets correspond to the GNIP stations (IAEA/WMO, 2020). Data for ECSF from Goller et al. (2005) and Timbe et al. (2014). Values for Zhurucay are from Mosquera et al. (2016), Cajas from Esquivel-Hernández et al. (2019) and for Nuevo Rocafuerte from Bowen (2022). The Mera study site is marked by a red star, whereas the nearby Shell and Puyo instrumental stations are also indicated.

Similarly Lima (2019) monitored the rainfall and runoff in the Ecuadorian Andes and noted the discrepancy in the precipitation regime between the Papallacta and the Izobamba Andean stations (Figure 1.10; left column). The former shows a unimodal rainfall regime (one peak of precipitation from Apr-Aug) while the second displays a bimodal pattern (two peaks of precipitation from Mar-May and Oct-Nov). Nevertheless, both stations presented similar isotopic seasonality bringing up doubts about the efficacy of the local amount of precipitation to capture the $\delta^2\text{H}_p$ and $\delta^{18}\text{O}_p$ variability. The issue has also been addressed by simulating stable water isotopes using regional and global circulation models, resulting in underestimation (Vuille et al., 2003), overestimation (Sturm et al., 2007a), or a slight improvement of rainfall isotopic values compared to the northern hemisphere (Yoshimura et al., 2008). Overall, previously published studies are limited to local surveys, and the existing literature has not successfully resolved the contradiction between the various rainfall regimes (Figure 1.8b) and the common inter-annual variability of $\delta^{18}\text{O}_p$ over the Ecuadorian inter-Andean valley and Amazon.

1.5.2 Dendroclimatological studies

Few studies have systematically investigated the ITCZ and SAMS actual boundaries, which has been amplified by climate data shortcomings and the lack of extended local records of $\delta^{18}\text{O}_p$ in the country (Vuille et al., 2012). Studies employing tree-ring width and their correlations with climate variables in Ecuador have principally focused on dry forest and their possible teleconnections with ENSO, especially in the country's south (Figure 1.11). For instance, TRW chronologies from the southwest at Laipuna Nature Reserve have employed *Bursera graveolens* (203 years/1809-2011, 590-1480 m a.s.l.) and *Maclura tinctoria* (87 years/1926-2012, 590-1480 m a.s.l.) (Puchac-Cofrep et al., 2015). In the Tumbesian forest, the species *Geoffroea spinosa* (28 years/1985-2012, 730 m a.s.l.) and *Handroanthus chrysanthus* (79 years/1934-2012, 230 m a.s.l.) were utilized (Espinosa et al., 2018). These studies found robust tree-ring growth responses to precipitation, especially during the wet season (January-May), whereas diverse growth responses were determined for ENSO events across sites. On the other hand, studies at southeast in Bellavista and Malacatos towns (Loja) with *Acacia macracantha* (72 years/1948-2019, 1500-2300 m a.s.l.) observed that the annual dry period is not a limiting growth factor for this species, and stronger correlations were obtained at five-year intervals (Chalán, 2019).

At the Pacific coast in Santa Elena, Suntaxi and Jiménez (2011) employed *Guazuma ulmifolia* (30 years/1978-2007, 101 m a.s.l.). They concluded that precipitation amount is highly correlated with tree-ring growth, particularly illustrated during intense ENSO wet events in 1983 and 1998, which produced the highest growth peaks in the time series for this species.

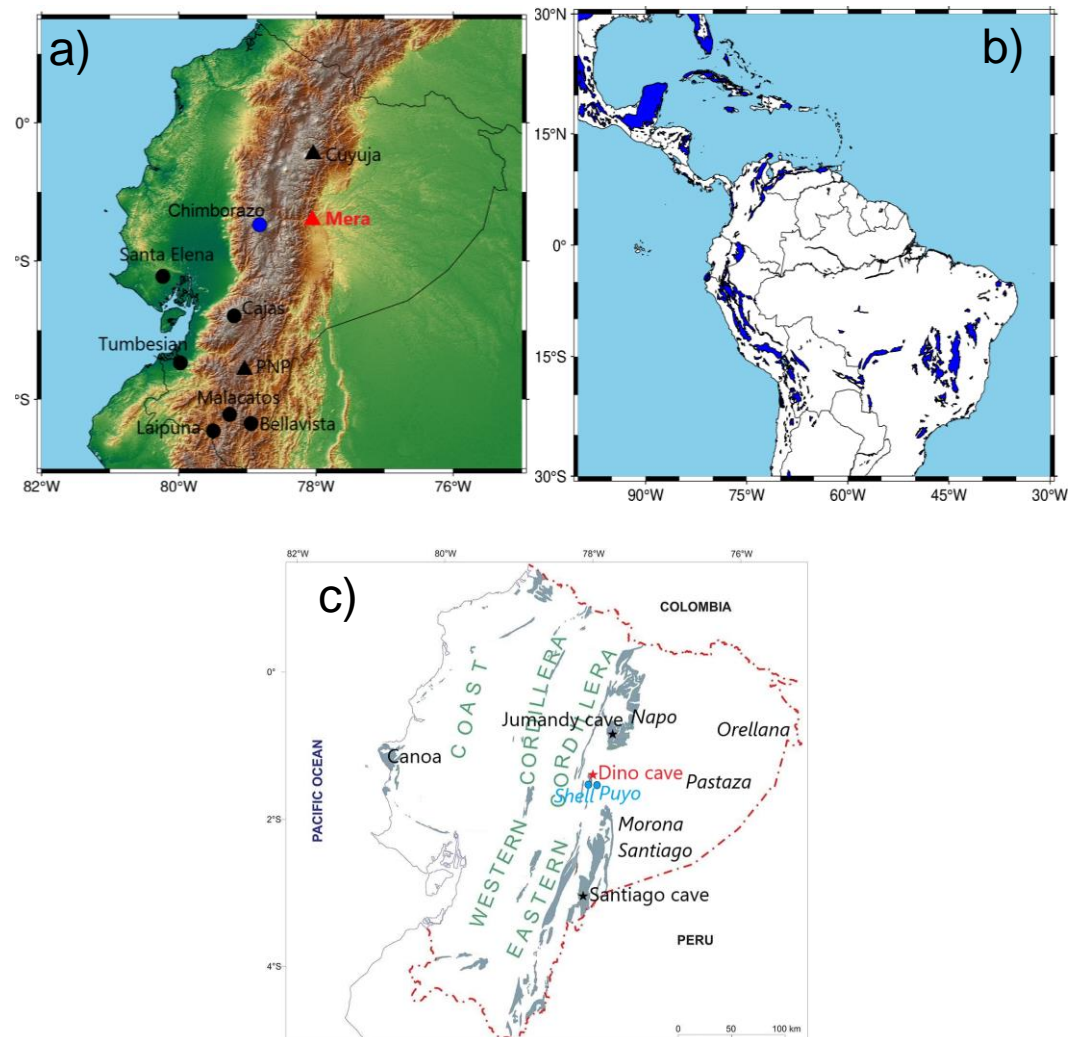


Figure 1.11 a) Map of continental Ecuador showing previous published records on tree-ring width (TRW; black dots), $\delta^{18}\text{O}_{\text{TR}}$ (black triangles), and ice core $\delta^{18}\text{O}$ from Chimborazo glacier (blue dot). The location of the Mera cedar forest (this study, red triangle) used for the construction of TRW, $\delta^{18}\text{O}_{\text{TR}}$ and $\delta^{13}\text{C}_{\text{TR}}$ is also shown. b) Karst rocks in South America obtained from https://www.whymap.org/whymap/EN/Maps_Data/Wokam/wokam_node_en.html. c) Map of karst rocks in continental Ecuador (gray patches) adapted from Constantin et al. (2019). Jumandy and Santiago caves are indicated with a black star (Jiménez-Iñiguez et al., 2022; Mosblech et al., 2012). In this dissertation a speleothem from Dino cave (Dino-1) is analyzed and its location is indicated by a red star. The blue dots correspond to the Puyo and Shell instrumental stations near to the Dino cave.

Recently, the responses of seasonal climatic factors and TRW of the endemic *Polylepis reticulata* in three sites at the Andean Cajas National Park were evaluated. Although both precipitation and temperature affected tree growth in the built chronologies (195 years/1821-2015, 3990 m a.s.l.), their responses were different and possibly associated with multiple factors, including, for example, soil traits, evaporative

demand, precipitation regimes, tree age and leaf phenology (Alvites et al., 2019). Overall, most of the chronologies have principally focused on the coast and the southern Andes, whereas limited records exist that explore the dendrochronological potential at the eastern Ecuadorian lowland Amazon.

On the other hand, studies on stable isotopes in tree-rings, especially $\delta^{18}\text{O}_{\text{TR}}$, have recently contributed to counteract the sparsity of climate data in Ecuador. The cedar tree *Cedrela* (*Meliaceae*) has been the preferred genus due to its diversification, spread, and annual ring formation (Pennington and Muellner, 2010; Figure 1.11a black triangles). The records primarily come from two montane Andean forests of *Cedrela montana* from southern Podocarpus National Park (PNP) (126 years/1885-2011, 1800-3180 m a.s.l.) and northern Cuyuja (213 years/1799-2012, 2950 m a.s.l.) (Baker et al., 2018; Volland et al., 2015). The meridional PNP $\delta^{18}\text{O}_{\text{TR}}$ record has shown positive correlations with seasonal precipitation from January to April, frequency of wet days, and cloud cover over the Andean Cordillera Real. Spatially it has given strong correlations with the El Niño-Southern Oscillation (ENSO), which influences its $\delta^{18}\text{O}_{\text{TR}}$. On the other hand, $\delta^{18}\text{O}_{\text{TR}}$ from Cuyuja resulted in a good proxy for studying the Amazon hydro-climatic variability in the past centuries. The observed change in the $\delta^{18}\text{O}_{\text{TR}}$ trend was interpreted as a reduction in rainout fraction over the Amazon basin, probably driven by the warming of the Sea Surface Temperature (SST) in the North Atlantic (Baker, 2017). These studies of $\delta^{18}\text{O}_{\text{TR}}$ have indicated direct Pacific and Atlantic Oceanic influence, respectively. However, the influence of either the ITCZ or the SAMS controlling the isotopic signals feeding the forests has not been evaluated thoroughly.

1.5.3 Speleothem research

Regionally, the more extended karst areas in South America are in the southeastern part of the continent, concentrated in Brazil, Bolivia, Peru, Ecuador and Colombia (Figure 1.11b). In the Ecuadorian Amazon, Cretaceous limestones of the Napo, Orellana, Pastaza, and Morona Santiago provinces host most of the current 400 caves known so far (Gunn, 2004; Figure 1.11c). The Ecuadorian coast also presents caves of karstic origin, primarily within the Canoa Formation, which is approximately 1.8 Ma old, but most of the landscapes are not extensive (Constantin et al., 2019). Nevertheless, Ecuador's oldest and denser karst systems are concentrated principally in the western Amazon with difficult access where even the protruding karren is frequently unseen by the dense rainforest (Constantin et al., 2019). Unfortunately, there is little knowledge of karst hydrological systems and their dynamics, reflected also in the low number of published speleothem chronologies. In fact, the unique speleothem record comes from the Santiago cave in southeast Ecuador (Figure 1.11c), where the authors reconstructed the precipitation over the past 94 ka employing $\delta^{18}\text{O}_{\text{cc}}$ tuned with the precessional changes in the Earth's orbit (Mosblech et al., 2012). Most recently, the first monitoring cave study of $\delta^{18}\text{O}_{\text{p}}$ and $\delta^{18}\text{O}_{\text{drip}}$ of Jumandy cave in north-central Ecuador indicates that the system has

an Atlantic signal whose infiltrated rainwater resides three weeks in the epikarst (Jiménez-Iñiguez et al., 2022).

In a broader regional context, speleothems studies in northwestern South America have not dealt with the distinction between the ITCZ and SAMS as drivers of rainfall seasonality. Variations in the $\delta^{18}\text{O}_p$ have been placed mainly into the SAMS context (e.g., see Figure 1 in Cheng et al., 2013) although regions close to the equator showed two rainy seasons contrary to the single wet season described during the SAMS (Slingo, 2015). However, the evidence for their demarcation has not been examined with terrestrial archives; hence ambiguity still exists for paleoclimate studies in Ecuador.

1.6 Aims and objectives of this study

At the heart of this work is therefore the development of paleoclimate reconstructions in Ecuador using terrestrial archives: speleothems and tree-rings, presenting the following objectives:

4. To evaluate the amount effect and identify the local or regional controller of the rainwater stable isotopic composition in the Ecuadorian Andes and Amazon

The variability of the rainfall stable isotopic values ($\delta^2\text{H}_p$, $\delta^{18}\text{O}_p$) in Ecuador presents a marked local “altitude” effect. At the same time, this complex orography creates diverse precipitation regimes (unimodal, bimodal, and three-modal) that make it difficult to establish a relationship with the local amount. Nevertheless, stations along these regions show a similar intra-annual isotopic variability. I evaluate the hypothesis of the presence of a regional controller which determines the main isotopic variability which is then tuned by the local components. This is accomplished using Lagrangian back-trajectories and Outgoing Longwave Radiation (OLR). I also evaluate the possibility of not tagging the Ecuadorian Amazon and Andean regions as ITCZ or SAMS, but as transition zone between these systems in what is called a monsoon trough (Wang et al., 2017).

5. To reconstruct modern centennial hydrology using $\delta^{18}\text{O}$ and $\delta^{13}\text{C}$ in cellulose from tree species

Employing dendrochronological standard methods, TRW, and cellulose-based $\delta^{18}\text{O}_{\text{TR}}$ and $\delta^{13}\text{C}_{\text{TR}}$ records are constructed using for the first time *Cedrela nebulosa* tree-ring species from the Amazonian lowlands. I show through spatial and spectral analysis that the wood oxygen isotopes capture a rainfall signal spatially extended in a convective hub (V-index) within the monsoon trough area, while the carbon isotopic signal is tuned to the cloudiness associated with the ITCZ excursions. These results permit to infer the chief rainfall system exerting control over Ecuador, the SAMS or the ITCZ, terminology often used interchangeably when describing precipitation in northwestern South America.

6. To reconstruct past millennial hydrology using $\delta^{18}\text{O}$ from speleothems

High resolution paleo-precipitation during the mid-Holocene is scarce in northwestern South America. Hence, a U-Th dated speleothem from Dino cave (Dino-1) is analyzed and its record compared to regional records and available climate models for the epoch. This work is complemented with a cave monitoring campaign on the site. Overall, these records permit us to assess whether recent climate patterns have also been present at the millennial scale.

CHAPTER 2

MATERIALS AND METHODS

2.1 General overview of the study site

The study area for both tree-rings and speleothems is located in the Mera, Province of Pastaza ($1^{\circ}24'S$, $78^{\circ}03'W$, 1200 m a.s.l.) in the eastern foothills of the Ecuadorian Andes. The site is distinctive because it is a transition zone from the Amazon lowlands to the Andes with elevations above 4000 m a.s.l. (Figure 2.1a). This latter has a significant influence on the regular moisture transport due to its role as an orographic barrier that enhances condensation and, therefore, precipitation making this site perhumid (Ilbay-Yupa et al., 2021; Insel et al., 2010). The Mera site is covered by the Napo Formation (Middle-Late Cretaceous limestone, sandstone, black shale) with marine deposits of Upper Albian-Upper Cenomanian age (100.5 – 93.9 Ma) (Chamba Vásquez, 2020). It corresponds to the recently identified Mera-Upano morphological marker with high tectonic uplift and fluvial incision (Bés de Berc et al., 2004). The mean annual rainfall for Puyo (1965-2018) and Shell (1981-2018) stations is 4586 and 5357 mm, respectively. The rainfall regime has been described as bimodal and consists of two minor (Dec-Feb and Jul-Sep) and two main rainy seasons (Apr-Jun and Oct-Nov) (Ilbay-Yupa et al., 2021) (Fig. 2.1b). It is noteworthy to mention that these thresholds serve as a reference, and sometimes the seasons may be shorter or longer, but the bimodality is preserved. On the other hand, the mean monthly temperature presents small variations between 21 and 23 °C during the year. Nevertheless, the months with the lowest temperature occur from June to August, where the mean temperature drops to values below 21.0 °C (Fig. 2.1c). The mean annual temperature for Puyo (1965-2018) and Shell (1981-2018) was 21.7 °C and 22.4 °C, respectively.

2.2 Sample collection

2.2.1 Rainwater sampling

The Mera site is an optimal location for stable isotopic monitoring of rainwater. It fills the isotopic data gap in precipitation between the northern and southern transects in the country (Figure 1.10). It displays a transition between the Amazon lowland and the eastern Andean foothills, which is essential to evaluate a potential "altitude" effect. Rainwater samples were continuously collected over 48 months. The monitoring campaign started on February 2019 until January 2023 storing rainwater in a 12 L plastic container to which 300 ml of paraffin oil was added to prevent evaporation according to standard procedures for the totalizer paraffin-based method (IAEA/WMO, 2014) (Figure 2.2). Due to logistical reasons, the collector was installed in an open area ($1^{\circ} 25' 05'' S$, $78^{\circ} 02' 58'' W$), at 1.7 km from the tree-ring sampling site and 0.96 km far from the Dino cave.

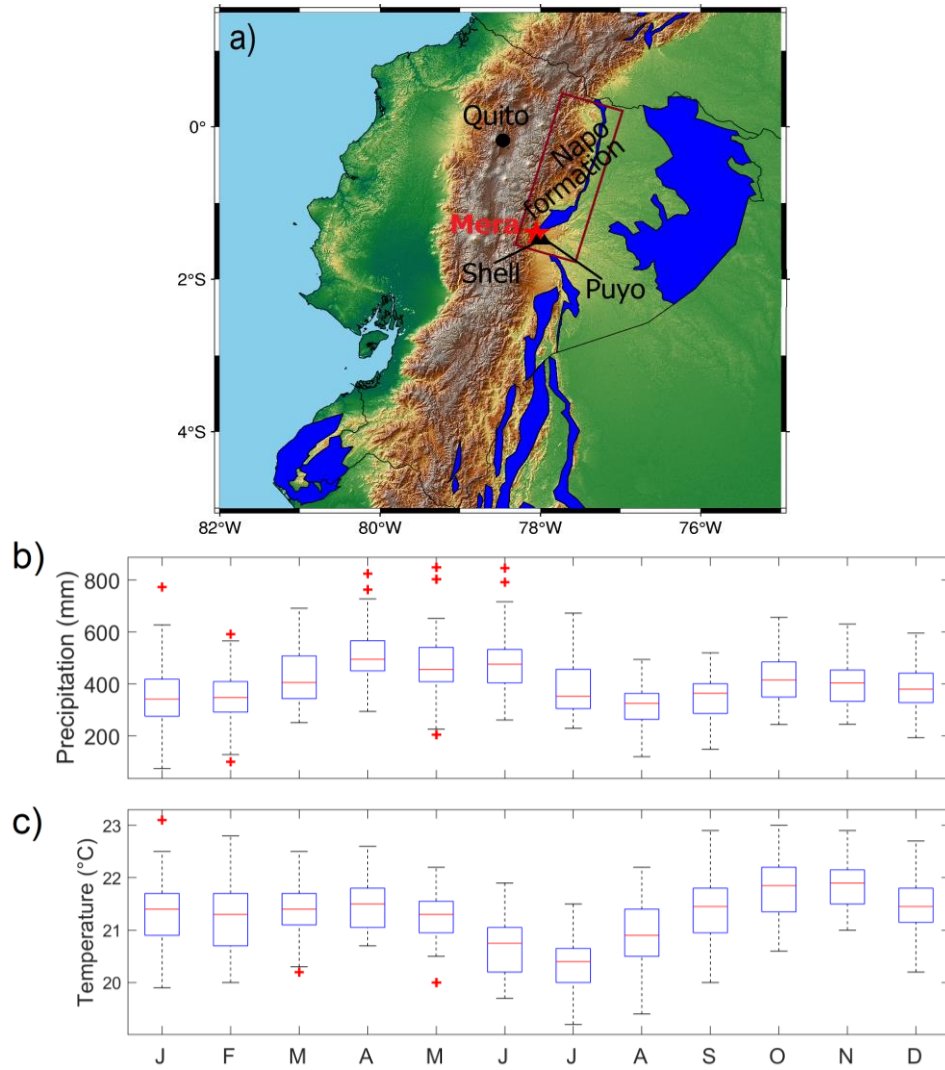


Figure 2.1 a) Location of the Mera study site (red star) positioned in the eastern Andean foothills (northwestern Amazon basin), central Ecuador. The instrumental stations Shell ($1^{\circ}29'S$, $78^{\circ}02'W$, 1043 m a.s.l.) and Puyo ($1^{\circ}30'S$, $77^{\circ}57'W$; 956 m a.s.l.) are located 10 and 15 km away from the study site and are shown in black triangles. Areas in blue correspond to the karst landscape obtained from the World Karst Aquifer Map. Climographs showing distribution of monthly b) precipitation and c) temperature averaged between the Puyo and Shell stations (1965-2018). Boxplots show the location of the middle quartile of monthly observations with their median (horizontal red line). The whiskers extend to the two extreme data values. Outliers are any data value more than $1.5 \times \text{IQR}$, where IQR is the interquartile range (red cross marker). Datasets correspond to the National Institute of Meteorology and Hydrology (INAMHI) and the Civil Aviation Directorate (DAC) of Ecuador.

Monthly rainfall samples were collected by research collaborators (BSc. students) from the Universidad Politécnica Salesiana. Containers were replaced at the beginning of each month for $\delta^{2}\text{H}_p$ and $\delta^{18}\text{O}_p$ measurements. After each collection, precipitation was preserved in polyethylene terephthalate (PET) bottles, tightly sealed to avoid

contamination and evaporation. Rainwater samples were immediately transported to the Chemistry laboratory of the University in Quito for monthly volume measurement, packing, and shipping to Institute for Nuclear Research (ATOMKI) in Debrecen. However, due to the coronavirus pandemic, the amount of precipitation could not be measured continuously at the laboratory, and therefore the samples were directly dispatched. Hence, the amount of precipitation (Mar-Dec 2020) was obtained from Shell and Puyo stations located 10 and 15 km from the rainwater collector to fill data gaps (Figure 2.2). The correlation between Puyo (956 m) and Shell (1043 m) stations for their common 1981-2021 precipitation period is $r = 0.72$ ($p < 0.01$), and for the gap Mar-Dec 2020 is $r = 0.89$ ($p < 0.01$). For the statistical analysis, all the monthly amount values were used, including any extreme value.

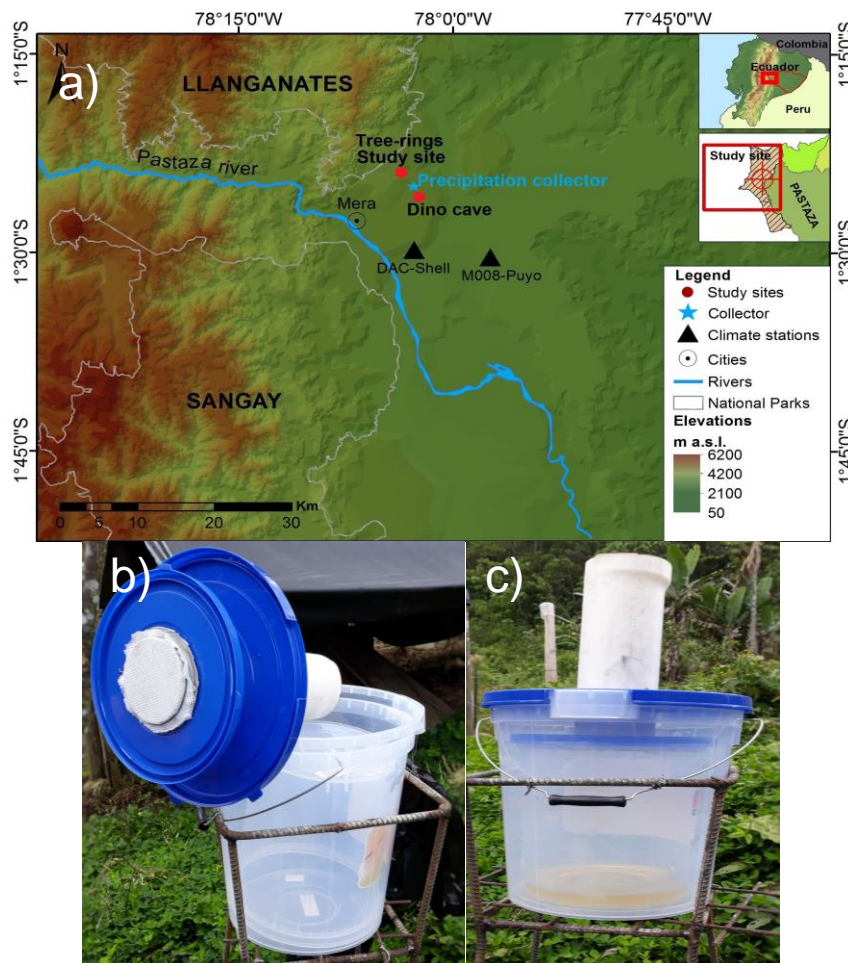


Figure 2.2. **a)** Location of the tree-rings, speleothem, and rainwater sampling sites in Mera, central Ecuador for paleoclimate studies **b-c)** HDPE plastic precipitation collector installed with a two-inches collection pipe and mesh for sorting impurities. Note the paraffin oil at the bottom of the bucket in c) for prevention of evaporation in the monthly composite sample.

2.2.2 Tree-rings identification and sampling

Initially, a field campaign in February 2019 was undertaken to identify potential species for dendroclimatic purposes surveying a total area of 2000 m² (0.2 ha) (See Appendix A.1). The *Cedrela nebulosa* species (cedar) was the most appropriate of all collected specimens due to its prominence and visible display of rings. It was identified by Dr. Walter Palacios who is the expert on the *Meliaceae* family in Ecuador. Unfortunately, this species is a deciduous broad-leaved tree in a current vulnerable status and only grows in a narrow altitudinal range (~800-12000 m a.s.l.) on the eastern flank of the Andes (Figure 2.3) (CITES, 2021; Layme-Huaman et al., 2018; Palacios, 2016, 2007; Palacios et al., 2019; Tropicos.org, 2020). With this preliminary information, the subsequent focus of the work was on a *Cedrela nebulosa* forest located in the Colonia 24 de Mayo parish, in the Mera site. This is an open canopy forest positioned between the biocorridor of two National Parks, Sangay and Llanganates (Figure 2.2a). The field campaign on September 2019 permitted the sampling of 33 individuals (3 cross-sections and 67 cores) as described in Table 2 and Appendix A.2.

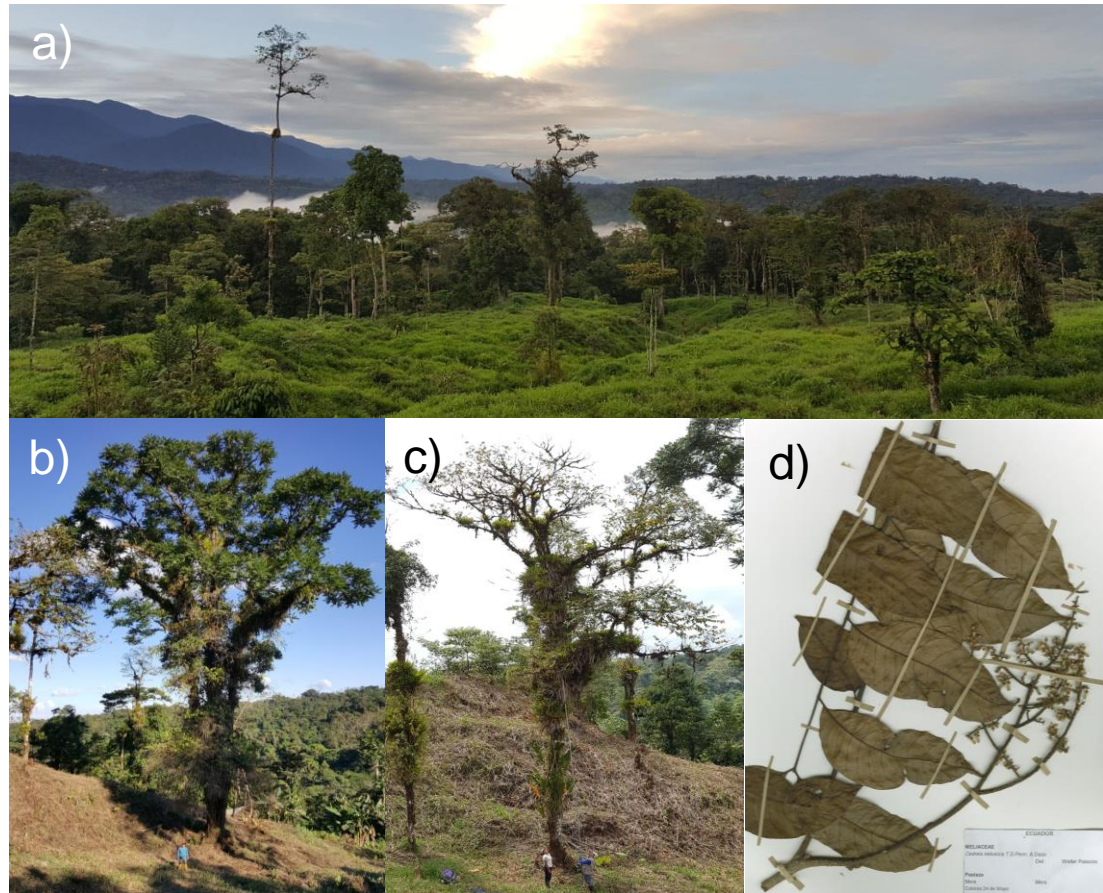


Figure 2.3 a) *C. nebulosa* forest in Mera, central Ecuador. b) *C. nebulosa* during growing period (Feb/Mar-Aug/Sep) and c) cambial dormancy (Oct-Dec/Jan). d) Botanical sample used for identification and registration of the species at the Herbarium of the Universidad Nacional de Loja, Ecuador.

Table 2 Sampled *C. nebulosa* trees in the field campaign on September 2019

Code	Latitude	Longitude	Elevation (m a.s.l.)	[†] DBH (cm)	Foliage (%)
MECE01	1° 24' 25.8300" S	78° 03' 10.8493" W	1211	41.38	90
MECE02	1° 24' 25.2108" S	78° 03' 09.7836" W	1195	51.38	95
MECE03	1° 24' 01.1196" S	78° 03' 10.7187" W	1183	32.79	0
MECE04	1° 24' 23.7492" S	78° 03' 10.7226" W	1210	32.15	70
MECE05	1° 24' 23.6520" S	78° 03' 10.0441" W	1241	42.65	30
MECE06	1° 24' 23.3928" S	78° 03' 10.0767" W	1163	33.1	10
MECE07	1° 24' 22.4496" S	78° 03' 10.5950" W	1179	35.01	10
MECE08	1° 24' 22.6040" S	78° 03' 11.2088" W	1203	26.41	40
MECE09	1° 24' 21.6648" S	78° 03' 07.1702" W	1221	48.7	90
MECE10	1° 24' 19.4544" S	78° 03' 07.1406" W	1214	61.43	100
MECE11	1° 24' 20.3976" S	78° 03' 07.9151" W	1210	38.52	60
MECE12	1° 24' 17.0100" S	78° 03' 02.3605" W	1244	25.78	40
MECE13	1° 24' 16.4232" S	78° 03' 01.7795" W	1214	50.29	75
MECE14	1° 24' 17.7876" S	78° 03' 01.7132" W	1229	36.61	95
MECE15	1° 24' 17.2044" S	78° 03' 01.5523" W	1205	37.56	15
MECE16	1° 24' 18.2448" S	78° 03' 01.5510" W	1225	41.1	95
MECE17	1° 24' 16.6176" S	78° 03' 00.7451" W	1339	31.51	80
MECE18	1° 24' 16.0632" S	78° 03' 00.0671" W	1227	51.56	80
MECE19	1° 24' 16.9416" S	78° 03' 00.1952" W	1208	41.38	75
MECE20	1° 24' 17.8776" S	78° 02' 56.4451" W	1218	93.27	85
MECE21	1° 24' 16.2900" S	78° 02' 59.3234" W	1235	29.13	10
MECE22	1° 24' 07.0812" S	78° 02' 53.6146" W	1152	53.16	85
MECE23	1° 24' 18.0792" S	78° 03' 00.0969" W	1214	30.56	45
MECE24	1° 24' 16.0632" S	78° 03' 00.0671" W	1227	44	85
MECE25	1° 24' 06.4224" S	78° 02' 48.0566" W	1186	44.56	90
MECE26	1° 24' 04.6656" S	78° 02' 46.8307" W	1167	48.38	80
MECE27	1° 24' 18.2160" S	78° 03' 05.2677" W	1254	38.2	0
MECE28	1° 24' 17.9208" S	78° 03' 04.5247" W	1253	38.2	0
MECE29	1° 24' 14.7024" S	78° 03' 03.9793" W	1221	31.83	80
MECE30	1° 24' 14.9292" S	78° 03' 04.5608" W	1222	28.65	90
*MECE31	1° 27' 36.1944" S	78° 06' 50.6442" W	1198	34.06	0
*MECE32	---	---	572	38.21	0
*MECE33	1° 24' 17.9316" S	78° 03' 13.2185" W	1158	48.7	0
[†] Diameter at breast height		Mean	1194	41.00	55
*Cross sections (wood disks)		Median	1214	38.21	75
		Maximum	1339	93.27	100
		Minimum	572	25.78	0

Increment cores were extracted at breast height (1.3 m) using a Haglöf 5 mm Pressler borer. During coring, when possible, four cores per cedar tree were collected in the four cross directions of the trunk. The increment cores were then mounted in wooden grooved holders with the direction of vessels vertically aligned and then transported to the Laboratory of Dendrochronology at the Universidad Nacional de Loja, Ecuador to be air-dried and proceed with the subsequent dendrochronological standard methods (Cook and Kairiukstis, 1990; Stokes and Smiley, 1968; van der Sleen et al., 2017).

2.2.3 Surveying and monitoring of caves

In addition to the tree-ring sampling, three caves part of the Napo formation, locally known as the Anzu River caves, were explored (Figure 2.4). The caves are “Unión de los Continentes” ($01^{\circ} 24.4' S$, $78^{\circ} 2.7' W$, Union hereafter), “Garganta del Dino” ($01^{\circ} 25.5' S$, $78^{\circ} 2.4' W$, Dino hereafter) and “Copa del Mundo” ($01^{\circ} 24.3' S$, $78^{\circ} 2.6' W$, Copa hereafter).

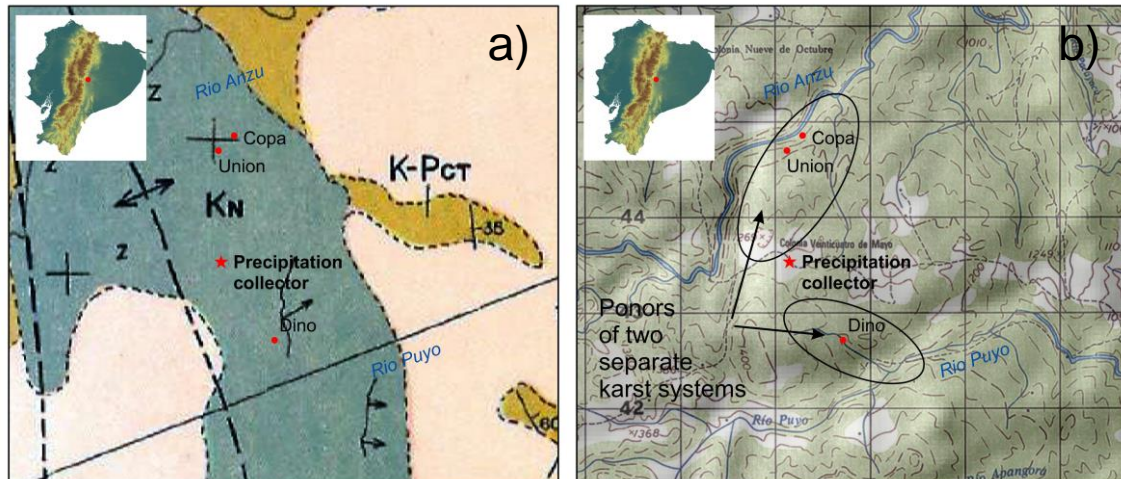


Figure 2.4 a) Geological and b) topographical maps showing the location of Copa, Union and Dino caves within the Napo formation (Cretaceous) and the Anzu river above them. The precipitation collector almost equidistant to the caves is marked by a red star. The three caves present a ponor configuration and are part of two separate karst systems. Dino cave is separated ~ 2.5 km from Copa and Union. The latter are separated 245 m from each. For a sketch of the cave's morphology, see Appendix B.1.

The morphology of Copa and Union caves is simple, presenting a long straight passage and a lithology with bituminous limestone/claystone embedded into gray limestone (Appendix B.1). Furthermore, the abundance of broken stalagmites pointed to unstable inner cave structure with fast drip rate, which was measured at one location in Copa cave. On the other hand, Dino cave also presents a ponor morphology with two entrances and a river coming from the covering claystone layers sinking in contact with the underlying limestone. In a dry speleothem-filled room inside Dino cave (Figure 2.5a-b), one complete and inactive suitable stalagmite was found on a boulder in the middle of

the room and was detached by hammering (Dino-1 hereafter, Appendix B.1). Dripwater samples were collected in the three caves on a point-event frequency according to the availability of people or meteorological conditions. This thesis focuses principally on Dino cave and its associated Dino-1 stalagmite. However, the dripwater data from Union and Copa cave is used for complementing the later-established dripwater monitoring at Dino cave (Figure 2.5c), useful for analyzing the transfer of the meteoric water signal to the cave system. All dripwater samples were collected in 50 ml HDPE CITOTEST centrifuge tubes, labelled, packed and shipped along with the rainwater samples (see Section 2.2.1).

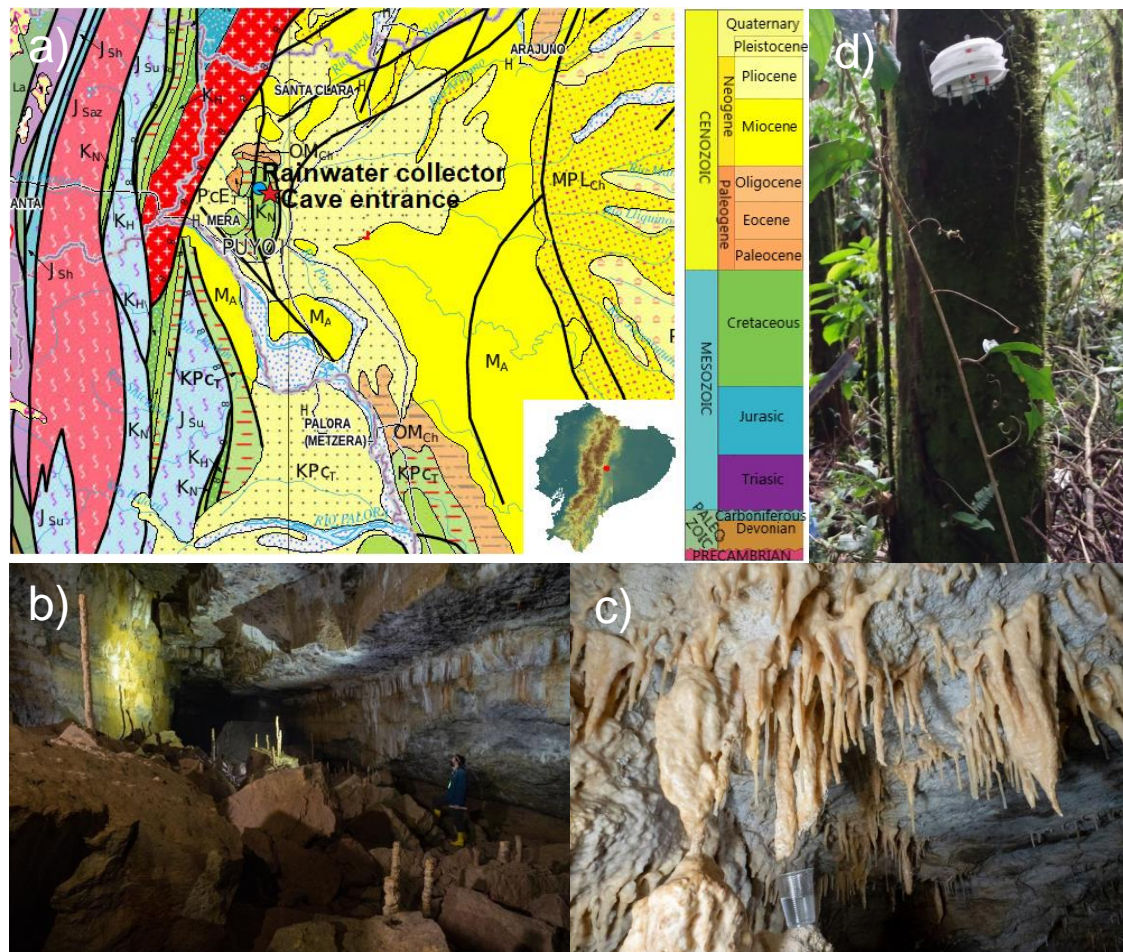


Figure 2.5 **a)** Geological map of Ecuador showing the Dino cave entrance (red star) and the rainwater collector from Figure 2.2 (blue dot) in the Napo formation (Cretaceous 145-66 Ma) composed of sandstones, limestones, and shales. **b)** Speleothem-filled chamber inside Dino cave from where Dino-1 stalagmite was sampled over a boulder. **c)** Dino cave $\delta^{18}\text{O}$ dripwater point-event sampling from an active flowing stalactite. **d)** Temperature logger outside the entrance of Dino cave for hourly measurements protected by a radiation shield hanging on a trunk tree. Photographs (b-c) by Zane Libke and Alex Bentley.

The Dino cave temperature was monitored at an hourly rate with a DS1922L iButton temperature logger (± 0.5 °C accuracy, 0.0625 °C resolution) installed at ~2 m above the ground hanging in one of the cave walls avoiding the contact between the sensor and wall. Similarly, the air temperature outside the cave was recorded in the same manner, but the temperature monitor was placed in a tree trunk protected by a radiation shield (Figure 2.5d). The obtained data were validated with temperature records from Puyo and Shell instrumental stations and ERA5 reanalysis (2m temperature product) 0.25° x 0.25° horizontal resolution (Harris et al., 2020) (Figure 3.15).

2.3 Sample preparation

2.3.1 Dendrochronological work

All mounted cores were consecutively sanded from grain 60 to 4000 enhancing tree-ring visibility (Stokes and Smiley, 1968). Tree-ring width measurements were carried out using a LINTAB 6 measuring system (Rinntech, Heidelberg, Germany) with a 0.01 mm precision coupled with TSAP-Win software (Rinn, 2012). For cross-dating, a visual inspection of tree-ring patterns and standard statistical tests were performed (Cook et al., 1990). TRW series from stem disks were used to reference the synchronization of individual series from increment cores. Every tree-ring series was checked visually and statistically for cross-dating quality. Some series were excluded from the chronology based on ring-boundary visibility, wood damage, the occurrence of missing or wedging rings, and recurrent cross-dating problems, leaving 24 trees for subsequent work from the original 33 sampled on the field (Table 2). All individual tree-ring series were grouped and saved in Heidelberg format (.fh), then imported to the R statistical programming environment (R Core Team, 2020). To analyze and evaluate the statistical quality of the cross-dated TRW series, the “Dendrochronology program library in R (dplR)” was used (Bunn, 2008). Individual growth tendencies related to age and natural effects were removed through a “detrending” procedure. Preliminary interactive assessment utilized the “detrendR” package (Campelo et al., 2012), and the following work employed a non-interactive detrending in the “dplR” package with the “detrender ()” routine. From obtained detrended series, chronologies were built with the “chron ()” function (“dplR” package), from which standard and residual chronologies were obtained. In this work, both chronologies were evaluated, but standard chronology was used for seasonal correlation with climate variable (Meko et al., 2011). In addition, the chronology was built with pre-whitening and biweight to have a robust mean using the dplR package. The Expressed Population Signal (EPS) was calculated to obtain the similarity or common signal between several trees of the population, and it ranged from 0 to 1. Generally, an EPS of 0.85 is suggested to capture a common signal, while the remaining 0.15 is a residual chronological variance (Wigley et al., 1984). EPS was computed using the chronology Stripping “strip.rwl ()” function, which selects the best time-series with the

most similarity in each site (Bunn, 2010). In this study, the EPS was calculated using 24 trees for the TRW chronology.

2.3.2 Speleothems slabs

The sampled Dino-1 speleothem was cut using an Intec-G2 waterjet cutter along the central axis in two locations obtaining two lateral halves with a middle plaque (Figure 2.6). Halves were used for stable isotopes ($\delta^{18}\text{O}_{\text{cc}}$ and $\delta^{13}\text{C}_{\text{cc}}$), preliminary U content for U-Th dating, and Hendy test (Hendy, 1971). The central plaque was used exclusively for U-Th dating. All the speleothem slabs surfaces were consecutively grinded and polished up to 600 grit enhancing the visibility of laminae.

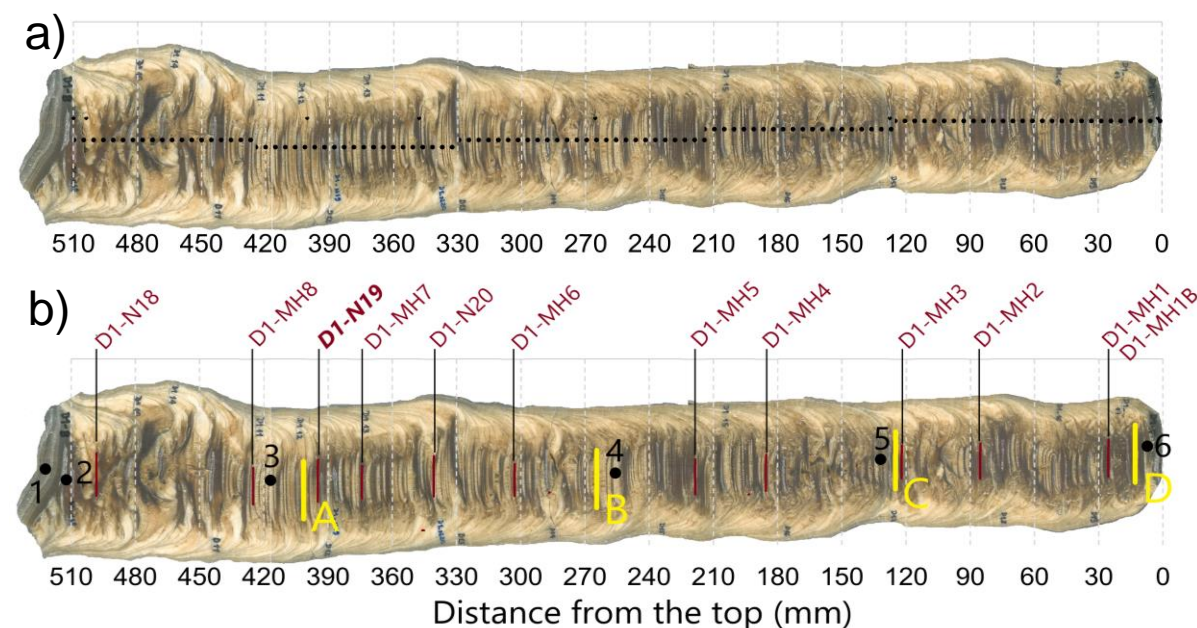


Figure 2.6 Stalagmite Dino-1 analyzed in this study with a total length from bottom to top of 519 mm. **a)** Sampling points across the central axis (black spots) at 5 mm resolution for $\delta^{18}\text{O}_{\text{cc}}$ and $\delta^{13}\text{C}_{\text{cc}}$ ($n = 110$). **b)** Slab showing the positions of preliminary U content test (black dots with numbers; 1=1.41 ppm, 2=3.07 ppm, 3=1.68 ppm, 4=1.93 ppm, 5=2.35 ppm and 6=1.38 ppm). The mean U content is 1.97 ppm. Selected layers for U-Th dating ($n = 12$, red lines) are indicated with their associated laboratory code. Layer D1-N19 (bold) was excluded from the final Age-Depth model. The layers for the Hendy test (yellow lines) are labeled from A to D. The distance from the top for the position of each letter are: A = 401 mm, B = 266 mm, C = 128 mm and D = 14 mm.

Furthermore, two selected speleothem layers were drilled (~ 200 mg) for mineral determination carried out by X-ray diffraction (XRD) on a Bruker D2 PHASER diffractometer at the Karst Research Institute ZRC SAZU, Slovenia. Recording conditions were: Anode - CuK α , el. voltage - 40 kV, el. current - 30 mA, Ni filter and proportional counter and automatic divergence valve. The recording was performed

continuously, at a rate of 2° $2\Theta/\text{min}$ in the range of a 2Θ angle from 2° to 70° (Otoničar, 2021).

2.4 Analytical measurements

2.4.1 Stable isotopes

2.4.1.1 Water stable isotopes in precipitation

The monthly rainwater samples were measured by Los Gatos Research, Liquid Water Isotope Analyzer (LGR LWIA-24i, ABB-Los Gatos Research, San Jose, California, United States. The internal laboratory standards were calibrated against international water standards, V-SMOW, GISP, and SLAP. The reproducibility was better than 0.16‰ for $\delta^{18}\text{O}_p$ and better than 1.04‰ for $\delta^2\text{H}_p$, based on repetitions of laboratory standards.

2.4.1.2 Cellulose-based tree-ring oxygen and carbon isotopes

Among the cross-dated cores, four dominant, long-lived tree cores were selected. I visually separated 1-year samples assisted by a Zeiss SteREO Discovery.V20 stereo microscope, and a scalpel. I measured $\delta^{18}\text{O}_{\text{TR}}$ and $\delta^{13}\text{C}_{\text{TR}}$ from each tree ($n = 4$) separately and averaged the results afterward, allowing us to account for intrasite variability and minimizing isotopic changes due to considerable growth variations in ring width (Borella et al., 1998). However, when rings were excessively narrow to separate conveniently, 2-3 consecutive rings were taken as one averaged sample to provide enough material for isotopic analysis. The isotopic value obtained in these sections was replicated in the neighboring rings to construct the individual chronology for each particular tree (Appendix D). The preparation of α -cellulose was based on the method described by Túri et al. (2021), modified to suit tree-ring samples, and is briefly summarized here. Resin and other soluble materials from individual tree-rings were removed by solvent extraction using a mixture of chloroform and ethanol (2:1 ratio) for approximately 6 hours. Then, lignin was oxidized using an acidified sodium chlorite solution in an ultrasonic bath at 70°C , followed by the removal of hemicellulose in sodium hydroxide in an ultrasonic bath at 80°C . Finally, samples were rinsed using deionized water and freeze-dried. Carbon and oxygen stable isotope ratio measurements were then carried out on the extracted cellulose samples. The stable isotopes were measured on a Thermo Scientific™ EA IsoLink™ IRMS System for CNSOH known as Flash EA, which is an enhanced elemental analyzer for oxygen and carbon isotope analyses as well. It is equipped with an automatic switching valve that allows fast switching from carbon analysis (Combustion) to oxygen analysis (Pyrolysis). Cellulose (0.25 ± 0.04 mg) was weighed into silver capsules for oxygen analysis and aluminium capsules for carbon analysis, then dropped into the autosampler of the elemental analyzer. The instrument is coupled to a Thermo Finnigan Delta^{PLUS} XP

continuous-flow isotope ratio mass spectrometer. Results are expressed in conventional delta notation as follows, δ (%) = $(R_{\text{sample}}/R_{\text{reference}} - 1) * 1000$, where R is the $^{18}\text{O}/^{16}\text{O}$ or $^{13}\text{C}/^{12}\text{C}$ ratio of the sample or reference standard. The $\delta^{18}\text{O}$ and $\delta^{13}\text{C}$ values are relative to VSMOW and VPDB standards, respectively. For $\delta^{18}\text{O}$, the used standard materials were celluloses IAEA-C3 (+32.14 ‰, VSMOW) and Merck (+28.67 ‰, VSMOW), then benzoic acid IAEA-601 (+23.14 ‰, VSMOW) (Kéri et al., 2015; Saurer et al., 1998). For $\delta^{13}\text{C}$, the used reference materials were IAEA-C3 cellulose (-24.91 ‰, VPDB) and IAEA C-5 wood (-25.49 ‰, VPDB) then an in-house sulfanilamide standard (-26.69 ‰, VPDB). Every cellulose sample was measured at least twice for each stable isotope, and standard deviations of individual $\delta^{13}\text{C}_{\text{TR}}$ and $\delta^{18}\text{O}_{\text{TR}}$ measurements were $\pm 0.1 \text{ ‰}$ and $\pm 0.35 \text{ ‰}$, respectively.

In the case of combustion, the analytical method is based on the complete and instantaneous oxidation of the sample by flash combustion at 1020 °C, which converts all cellulose substances into combustion products. The resulting combustion gases (in this case CO₂) are swept into the chromatographic column by the carrier gas (helium). The gases are separated in the column and detected by the mass spectrometer. For Pyrolysis (high-temperature conversion), the samples are pyrolytically decomposed in a high-temperature pyrolysis system at a temperature exceeding 1450 °C in the presence of reactive carbon. The resulting gases (in this case CO) are swept into the chromatographic column by the carrier gas (helium). The gases are separated in the column and detected by the mass spectrometer. Lastly, each $\delta^{13}\text{C}_{\text{TR}}$ measured value was adjusted by adding a correction factor (Δ) necessary to quote $\delta^{13}\text{C}_{\text{TR}}$ values relative to a pre-industrial standard value of -6.4 ‰ as recommended by McCarroll and Loader (2004). This correction addresses the atmospheric decline in $\delta^{13}\text{C}$ signal due to an anthropogenic increase in the CO₂ concentration in the atmosphere. The estimated annual values of atmospheric CO₂ (ppm) were obtained from McCarroll and Loader (2004) (Table 2) from 1864 to 2003 and then extended until 2018 from the Mauna Loa CO₂ records (Tans and Keeling, 2020).

2.4.1.3 Carbon and oxygen isotopes in calcite speleothem and Hendy test

Subsamples for stable carbon and oxygen isotopes ($\delta^{13}\text{C}_{\text{cc}}$ and $\delta^{18}\text{O}_{\text{cc}}$) were hand drilled at 5 mm spatial resolution along the central axis of Dino-1 stalagmite (n = 110). The drilled material was weighted in Labco 12 ml glassvials for subsequent conventional analysis after digestion with H₃PO₄ using an automated GasBench II sample preparation device connected to Thermo Finnigan Delta Plus XP or Thermo Scientific Delta V Plus isotope ratio mass spectrometer (Temovski et al., 2022). The obtained isotopic compositions are given as $\delta^{13}\text{C}$ and $\delta^{18}\text{O}$ values relative to Vienna Pee-Dee Belemnite (VPDB) reference, with a precision better than $\pm 0.1 \text{ ‰}$. In addition, a total of 28 samples were also drilled along individual growth layers at four locations as indicated in Figure

2.6b (letters A to D) to test for possible kinetic effects during calcite precipitation (Hendy test; Hendy, 1971).

2.4.2 Radioisotopes

2.4.2.1 Radiocarbon and annual ring validation

The annual formation of rings in tropical species has been debated in the research community in the last decades, because it has often been assumed that the cambium is active during the whole year in tropical species (Gourlay, 1995; Worbes, 2002). The accepted standard procedure for conducting tropical dendrochronological research consists of the independent validation of annual ring formation in the studied species by ^{14}C (Baker et al., 2017; Poussart et al., 2006; Santos et al., 2020; Siegwolf et al., 2022; Speer, 2010; van der Sleen et al., 2017; Worbes, 2002). Hence, initially wood thin sections of 10 to 20- μm thickness were prepared with a microtome, stained with safranin and astra blue solutions, and washed with ethanol (Gärtner and Schweingruber, 2013). Then, microscopic images were taken for ring boundary identification, vessel numbers, and diameter measurements. Useful for the delimitation of rings was the presence of a band of marginal parenchyma at the end of the growing season which is a peculiar feature among tropical species (see Figure 3.8). The functional significance of this parenchyma seems to be its starch storage role, supporting rapid flushes of growth (Gourlay, 1995 and references therein).

After measuring the ring widths of all wood cores with subsequent cross-dating, 18 rings were selected in the region of the “bomb-peak” for ^{14}C measurements. Samples were prepared using a standard BABAB (basic-acid-basic-acid bleaching) α -cellulose method (Molnár et al., 2013a). Then, cellulose was combusted to CO_2 ($550\text{ }^\circ\text{C}$, 12 hrs.) with MnO_2 as a reagent (Janovics et al., 2018). The resulting gas was purified on a vacuum line with a dry ice-isopropyl alcohol mixture and a liquid nitrogen trap. Finally, graphite was obtained through a sealed tube graphitization method (Rinyu et al., 2013) and ^{14}C measured by a MICADAS (mini carbon dating system) type AMS (Molnár et al., 2013b). The resulting percent modern carbon (pMC) values were isotope-fractionation corrected, expressed to fraction modern ($F^{14}\text{C}$), and compared with the post-bomb calibration curves for the Southern Hemisphere (SH Zone 1-2 and SH Zone 3) (Hua et al., 2013; Reimer and Reimer, 2004).

2.4.2.2 U-Th dating

Subsamples for U-Th dating were drilled in the central slab using Dremel 4000 handheld drill. About 10 mg of carbonate powder was first collected for determination of U concentration on an Agilent 8800 Triple Quadrupole ICP-MS (Figure 2.6b). The average U concentration of all these points was 1.97 ppm. Hence, about 10 mg of sampled carbonate powder was then collected in Eppendorf vials for U-Th dating. Chemical preparation to separate U and Th fractions from the carbonate matrix was

carried out in a Class 1000 clean laboratory, with procedures similar to those described in Edwards et al. (1987). Briefly, samples were first dissolved in concentrated nitric acid and spiked with a ^{229}Th - ^{233}U - ^{236}U tracer (a mixture of the IRMM-3636a and the SRM 4328C reference materials), with an amount based on pre-determined U concentration. Separation of U and Th fractions was done in a column filled with UTEVA resin. The thorium fraction was collected with 4 M hydrochloric acid, and the uranium fraction with 0.1 M hydrochloric acid, evaporated to dryness and followed by several cycles of digestion in concentrated nitric acid and evaporation to dryness, after which U fraction was collected in 3% nitric acid and Th fraction in a mixture of 3% nitric acid and 0.05 M hydrofluoric acid. The isotope ratio measurements were carried out on a Neptune PLUS multicollector ICP mass spectrometer equipped with an Aridus 3 desolvating system. For the measurement of uranium isotopes (^{233}U , ^{234}U , ^{235}U , ^{236}U , ^{238}U), only Faraday-cups were used to determine the ion beam intensities. For thorium isotopes (^{229}Th , ^{230}Th , ^{232}Th), the uranium detector configuration was used in a way that thorium ion beams were aligned to the detectors with the dispersion quadrupole of the MC-ICPMS. The secondary electron multiplier in the central position was used for the ^{230}Th , and with a magnet jump, for the ^{229}Th isotopes. A laboratory standard solution (StalMix) prepared from the CRM 112-A reference material and the IRMM-3636a double uranium spike ($^{233}\text{U}/^{236}\text{U} = 1.01906 \pm 0.00016$) was used during the isotope ratio measurements for the standard-sample bracketing. The mass bias correction for U and Th in each sample solution was determined based on the uranium isotope measurement run using the known $^{235}\text{U}/^{238}\text{U}$ isotopic ratio of CRM 112-A. All preparation procedures and analyses were carried out at the Isotope Climatology and Environmental Research Centre, Institute for Nuclear Research (ATOMKI) (Palcsu et al., 2022).

The U-Th ages were calculated by iteration using the standard $^{230}\text{Th}/^{238}\text{U}$ equation (Edwards et al., 1987; Kaufman and Broecker, 1965):

$$\left[\frac{^{230}\text{Th}}{^{238}\text{U}} \right] = 1 - e^{-\lambda_{230}T} + \left(\frac{\delta^{234}\text{U}_m}{1000} \right) \times \left(\frac{\lambda_{230}}{\lambda_{230} - \lambda_{234}} \right) \times (1 - e^{(\lambda_{230} - \lambda_{234})T}) \quad (5)$$

where the values in square brackets are activities, $\delta^{234}\text{U}_m$ is the measured $^{234}\text{U}/^{238}\text{U}$ ratio expressed as $\delta^{234}\text{U}_m = ([^{234}\text{U}/^{238}\text{U}] - 1) \times 1000$, T is the age and λ 's are the decay constants: $\lambda_{238} = 1.55125 \times 10^{-10}$ (Jaffey et al., 1971), $\lambda_{234} = 2.82206 \times 10^{-6}$ (Cheng et al., 2013a), $\lambda_{230} = 9.1705 \times 10^{-6}$ (Cheng et al., 2013a). The initial $^{234}\text{U}/^{238}\text{U}$ ratio ($\delta^{234}\text{U}_i$) is calculated from:

$$\delta^{234}\text{U}_i = \delta^{234}\text{U}_m e^{\lambda_{234}T} \quad (6)$$

Detrital Th-corrected ages are calculated by correcting the measured $^{230}\text{Th}/^{238}\text{U}$ ratios based on ^{232}Th as an index of the initial ^{230}Th contamination using the following equation (Richards and Dorale, 2003):

$$\left[\frac{^{230}Th}{^{238}U} \right]_{corr} = \left[\frac{^{230}Th}{^{238}U} \right] - \left[\frac{^{232}Th}{^{238}U} \right] \times \left[\frac{^{230}Th}{^{232}Th} \right]_i \times (e^{-\lambda_{230}T}) \quad (7)$$

where $[^{230}Th/^{232}Th]_i$ is the activity ratio of the detritus at the time of formation, for which bulk earth $^{230}Th/^{232}Th$ atomic ratio of $4.4 \pm 2.2 \times 10^{-6}$ was used. Calculated U-Th ages are reported in thousand years Before Present (ka BP), with Present defined as the year 1950 A.D. Age errors are given at 2σ , and incorporate analytical uncertainties and uncertainties in ratios of reference materials. Finally, an age-depth model was created using the open R-package “StalAge” (Scholz and Hoffmann, 2011) as shown in Figure 3.18. One sampled layer, with an age out of stratigraphic order was excluded (D1-N19 in Figure 2.6). Once the model was created, each age was matched with their respective $\delta^{18}O_{cc}$ forming the final Dino-1 record.

2.5 Climate datasets and gridded products

2.5.1 Stable isotopes of water

2.5.1.1 Stable isotopes database

The δ^2H_p and $\delta^{18}O_p$ from stations located in the Ecuadorian Amazon lowlands and inter-Andean highlands were primarily obtained from the IAEA Global Network of Isotopes in Precipitation (GNIP) database (IAEA/WMO, 2020), except for Estación Científica San Francisco (ECSF) obtained from Goller et al. (2005) and Timbe et al. (2014). Similarly, the isotopic values for Zhurucay basin correspond to Mosquera et al. (2016) and for Cajas station from Esquivel-Hernández et al. (2019). In the case of Nuevo Rocafuerte, the values were acquired from the isoscape model proposed by Bowen (2022). Although isoscapes models can be coarse at unmonitored sites, the obtained values for Nuevo Rocafuerte compared well with those monitored in the 2001-2002 period by Villacís et al. (2008) ($r = 0.89$, $p < 0.01$). When the precipitation values were missing from the corresponding stations, they were acquired from the Global Historical Climatology Network (GHCN) version 4 (NOAA, 2022).

Present-day gridded stable isotopologues of water were obtained from the ECHAM5 atmospheric general circulation model enhanced by stable water isotope diagnostics (ECHAM5-wiso; Werner, 2019; Werner et al., 2011) available at the PANGAEA website <https://doi.pangaea.de/10.1594/PANGAEA.902347>. The model resolution varies from $3.8^\circ \times 3.8^\circ$ to $0.75^\circ \times 0.75^\circ$ finer grid. Precipitable water was retrieved from a Weather Research and Forecasting (WRF) simulation with a domain of 50 km horizontal resolution (100 x 100 grid cells, centered at $1.77^\circ S - 78.10^\circ W$) and 51 levels in the vertical with a top pressure of 10 hPa. The WRF experiment was forced by the Community Climate System Model version 4, satisfactorily employed in South America and recently in Ecuador (Chimborazo and Vuille, 2021). Precipitable water is an absolute measure of the total water of the air, and equals the amount of water if all the water vapor was condensed (Arraut et al., 2012; EUMetraint, 2014).

2.5.1.2 Lagrangian back trajectories

The HYSPLIT model (HYbrid Single-Parcel Lagrangian Integrated Trajectory; Stein et al., 2015), successfully used in past investigations in Ecuador (e.g., Jiménez-Iñiguez et al., 2022; Trachte, 2018), was utilized to identify the sources of moisture employing the PySplit package (Warner, 2018). The trajectories originating at the Mera site in Central Ecuador were calculated at 1500 m. At this altitude broad precipitation encompasses most of the shallow and deep convection in the tropical Andes (Anders and Nesbitt, 2015). The meteorological data were obtained from the GDAS (Global Data Assimilation System) at $1^{\circ} \times 1^{\circ}$ spatial and 3-h time resolution. Trajectories were calculated from 2014 to 2019 for 240 hours (10 days) every two days. In order to refine the analysis, the calculation of moisture uptake was carried out following the methodology described in Sodemann et al. (2008), which utilizes a Lagrangian framework tracking moisture changes inside the atmospheric boundary layer and marking them as uptake points along the back trajectories path. For calculating the moisture uptake, values of precipitation=-0.2 and evaporation=0.2 at 6 hours intervals were used. The analysis and visualization used Python version 3.9.10 in the Scientific Python Development Environment (Spyder) 5.0. (Figure 3.2).

2.5.1.3 Cross-equatorial flow over western Amazon and gridded precipitation

The V-Index region was identified using the set of coordinates detailed in Wang and Fu (2002) which are: $5^{\circ}\text{S}-5^{\circ}\text{N}$, $65^{\circ}\text{W}-75^{\circ}\text{W}$ (black boxes in Figure 1.9). In order to verify the presence of this convective area in South America, I carried out an Empirical Orthogonal Function (EOF) analysis of the OLR product following the method of Garcia and Kayano (2010), except that monthly OLR data was used instead of pentad means. The OLR data was acquired from the NOAA/OAR/ESRL PSL at $2.5^{\circ} \times 2.5^{\circ}$ resolution (Liebmann and Smith, 1996) (Figure 3.1). Once the presence of the V-index region was verified, monthly precipitation time-series were obtained at the V-Index region from the European Centre for Medium-Range Weather Forecasts (ECMWF) ERA5 (Hersbach et al., 2020), The Climate Hazard group Infrared Precipitation with Stations (CHIRPS) (Funk et al., 2015), and the Climate Research Unit (CRU TS4.05) (Harris et al., 2020). In the case of the ERA5, the total precipitation NetCDF product on single levels from 1979 to 2021 ($0.25^{\circ} \times 0.25^{\circ}$ resolution) was used. This product is expressed in m (of water equivalent) day $^{-1}$; hence the conversion to mm month $^{-1}$ used the formula $\text{tp [mm]} = \text{tp [m day}^{-1}\text{]} \times 1000 \times N$, where N is the number of days in the month. Regarding CRU, the horizontal resolution for the precipitation product was $0.5^{\circ} \times 0.5^{\circ}$, whereas, for CHIRPS, the resolution was $0.05^{\circ} \times 0.05^{\circ}$, making it an appropriate product for capturing the rainfall variability of the Andes (Segura et al., 2020). The Pearson correlation coefficient was used to evaluate the monthly $\delta^{18}\text{O}_p$ variation regionally at the Mera site. The $\delta^{18}\text{O}_p$ time-series were compared with the gridded ERA5, CRU, CHIRPS precipitation, and the OLR datasets from February 2019 to January 2023 at $p < 0.05$. Initially, it was carried out

for Mera and then for the rest of the stations in the 1992-1996 and 1998-2018 periods (see Table 3).

2.5.2 Statistical analysis

2.5.2.1 *Cedrela nebulosa* tree-rings and regional records

The trend in the $\delta^{18}\text{O}_{\text{TR}}$ and $\delta^{13}\text{C}_{\text{TR}}$ records were fit using a break and ramp regression curves according to Mudelsee (2019) (Figure 3.10). I computed Pearson's correlation between the $\delta^{18}\text{O}_{\text{TR}}$ and $\delta^{13}\text{C}_{\text{TR}}$ with the corresponding local and regional climate variables to quantify the statistical relationship. The local precipitation and temperature were averaged from Puyo (1965-2018) and Shell (1981-2018) instrumental stations. The cloud cover time-series was acquired from the CRU TS4.04 from 1930 to 2018 (Harris et al., 2020) for the Mera site. In the case of monthly temperature anomalies for Ecuador, these corresponded to the Berkeley Earth Land/Ocean Temperature Record and spanned from 1901-2018 (Rohde and Hausfather, 2020). Daily datasets (1980-2018) for insolation, sunshine duration, and low cloud cover were acquired from the National Aeronautics and Space Administration website (<https://data.giss.nasa.gov/modelE/ar5plots/srlocat.html>) and ERA-Interim reanalysis at $0.75^\circ \times 0.75^\circ$ grid resolution (Dee et al., 2011). Datasets for decadal comparison between the Mera $\delta^{18}\text{O}_{\text{TR}}$ record with *Cedrela montana* forest for the common period 1864-2012, and Chimborazo ice cap for the period 1881-2000 were retrieved from Baker et al. (2018) and Ramirez (2003). Spatial correlations were conducted using the KNMI explorer (Trouet and Van Oldenborgh, 2013).

2.5.2.2 Dino-1 speleothems and regional records

The Dino-1 chronology was compared with other local and regional records downloaded from the National Centers for Environmental Information NOAA, paleoclimatological section <https://www.ncdc.noaa.gov/data-access/paleoclimatology-data>. The Cariaco basin record comes from Haug et al. (2001), Pallcacocha lake from Rodbell et al. (1999), Santiago cave from Mosblech et al. (2012), Tigre cave was obtained from van Breukelen et al. (2008), and Condor record is from Cheng et al. (2013). On the other hand, Shatuca speleothem record (Bustamante et al., 2016) was downloaded from the SISAL-Speleothem Isotopes Synthesis and Analysis database (Comas-Bru et al., 2020). The values for the Colombian Caracol speleothem was acquired from Gelvez (2019). Finally, the amounts of solar insolation at 10°N - 10°S during the mid-Holocene were obtained from Laskar et al. (2004) through the Matlab package “acycle” (Li et al., 2019).

2.5.2.3 Spectral analysis

The *Cedrela nebulosa* oxygen and carbon records are evenly spaced (annual resolution) from 1860 to 2018. Hence the cross wavelet analysis was carried out without

interpolation or alteration of the Probability Density Function using the open-source Cross wavelet and wavelet coherence MATLAB package from Grinsted et al. (2004). Coherence is a frequency based measure of the correlation between two time-series at a given frequency (Shumway and Stoffer, 2017). On the contrary, the unevenly spaced time domain of Dino-1 speleothem (Figure 2.6) restricted the use of the classical Blackman-Tukey approach, the Multitaper Method or the Singular Spectrum Analysis (Li et al., 2019; Mann and Lees, 1996; Trauth, 2021). Furthermore, interpolation to generate uniformly spaced time-series was circumvented because of the high probability of altering the spectrum by underestimating the high frequency components or the inclusion of artifacts into the data (Björg Ólafsdóttir et al., 2016; Mudelsee, 2014; Schulz and Mudelsee, 2002; Schulz and Stattegger, 1997; Trauth, 2021). Therefore, the obtention of periodic or quasi-periodic components in the record different to the red noise background was carried out by the use of the REDFIT package (Schulz and Mudelsee, 2002) included in the statistical software Past version 4.12b (Hammer et al., 2001), and the Lomb-Scargle periodogram analysis using the “acycle” Matlab package (Li et al., 2019). The spectral analysis was carried out without preceding interpolation, avoiding spectral distortion (Schulz and Stattegger, 1997). For analysis of the time-frequency domain, this study employs the Weighted Wavelet z-transform (WWZ) (Foster, 1996). A major advantage of this method is that the calculation is similar to the Wavelet transform (Torrence and Compo, 1998) but accepts unequally spaced data. The calculation was carried out using the software STAR and Past (Benn, 2012; Hammer et al., 2001; Templeton, 2004) (Appendix B.2).

2.5.2.4 Mid-Holocene Earth System model

The isotope-enabled version of the Max Planck Institute for Meteorology – Earth System Model (MPI-ESM-wiso; Cauquoin et al., 2020, 2019) was utilized for retrieving global water isotopes and precipitation datasets for the mid-Holocene during austral summer (DJF). The MPI-ESM-wiso is available at the PANGAEA website <https://doi.pangaea.de/10.1594/PANGAEA.912258>.

2.6 Reproducibility

For transparency and replicability of results, this work has been publicly archived according to the FAIR principles: Findable, Accessible, Interoperable and Reusable (Irving et al., 2021; Wilkinson et al., 2016) and is available at the author’s GitHub repository <https://github.com/vargasdanny/paleothesis>. The directories in the repository are organized according to their purpose following the guidelines of Noble (2009). Therefore, runnable programs and scripts (command-line workflows) are found in bin/, raw data in data/, results in results/ and all the documentation in the docs/ folder.

CHAPTER 3

RESULTS

3.1 Water stable isotopes

3.1.1 OLR decomposition and moisture trajectories

The OLR decomposition in the first three EOF modes in South America shows three main systems in Figure 3.1. The EOF1 corresponds to SAMS, the EOF2 to the convergence zones in the Atlantic ITCZ and in the continent the South Atlantic Convergence Zone (SACZ). The EOF3 represents the symmetric mode with the largest convective activity in the NOSA, ORIC and NAMZ (Figure 1.8) as previously indicated by Garcia and Kayano (2010). In particular, the EOF3 stands out for its location at the equator, spanning the northern and southern hemispheres and is particularly more enhanced at the western than at the eastern side of the continent.

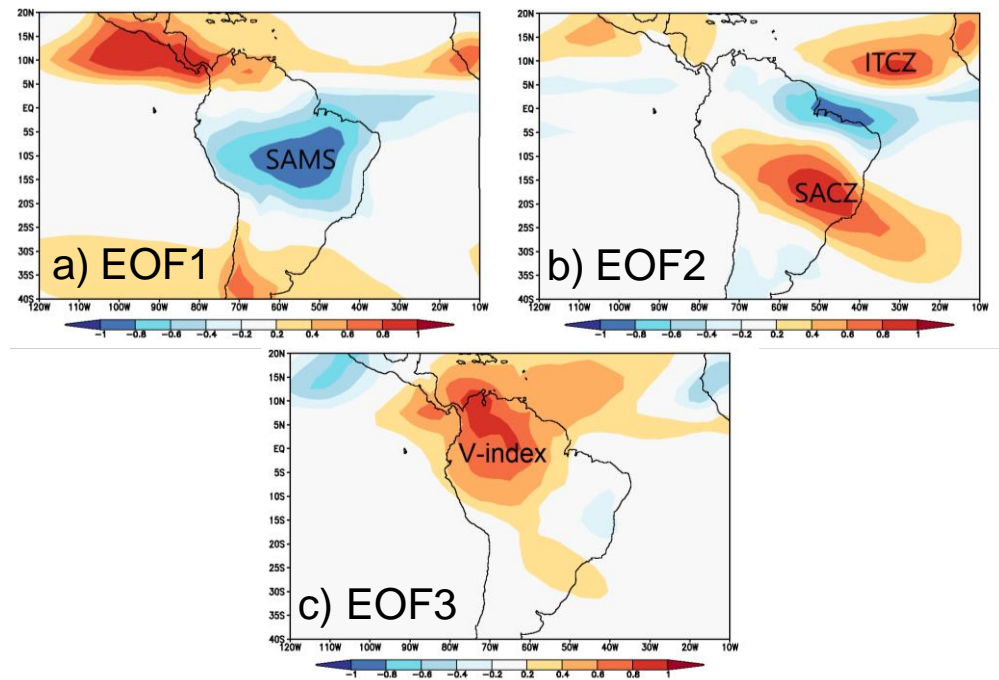


Figure 3.1 The first three EOF mode patterns of the OLR in tropical South America as described by Garcia and Kayano (2010). **a)** EOF1 corresponds to the SAMS, **b)** EOF2 corresponds to the Atlantic ITCZ and SACZ, and **c)** EOF3 is associated to the equatorially symmetric mode (V-index; Figure 1.9) which is the response of tropical convection to annual insolation on the equator and is the focus of this dissertation.

Remarkably, this area (V-index; Figure 3.1c) is again noticeable after running moisture back trajectories due to their confluence in this region (5°S - 5°N , 65°W - 75°W). Back trajectories show that during summer (DJF), northeast trajectories from the

tropical north Atlantic crossing Venezuela, Colombia (Orinoco plains) and finally Ecuador are dominant. Here the moisture flux upstream contributes to most of the flow arriving in Ecuador, with a lower amount being uptake in the vicinity of the Mera site (Figures 3.2a and e). A second trajectory from the South Pacific is also evident in this season in a "bow-shape" configuration. The average $\delta^{18}\text{O}_p$ value for this season is -5.27‰.

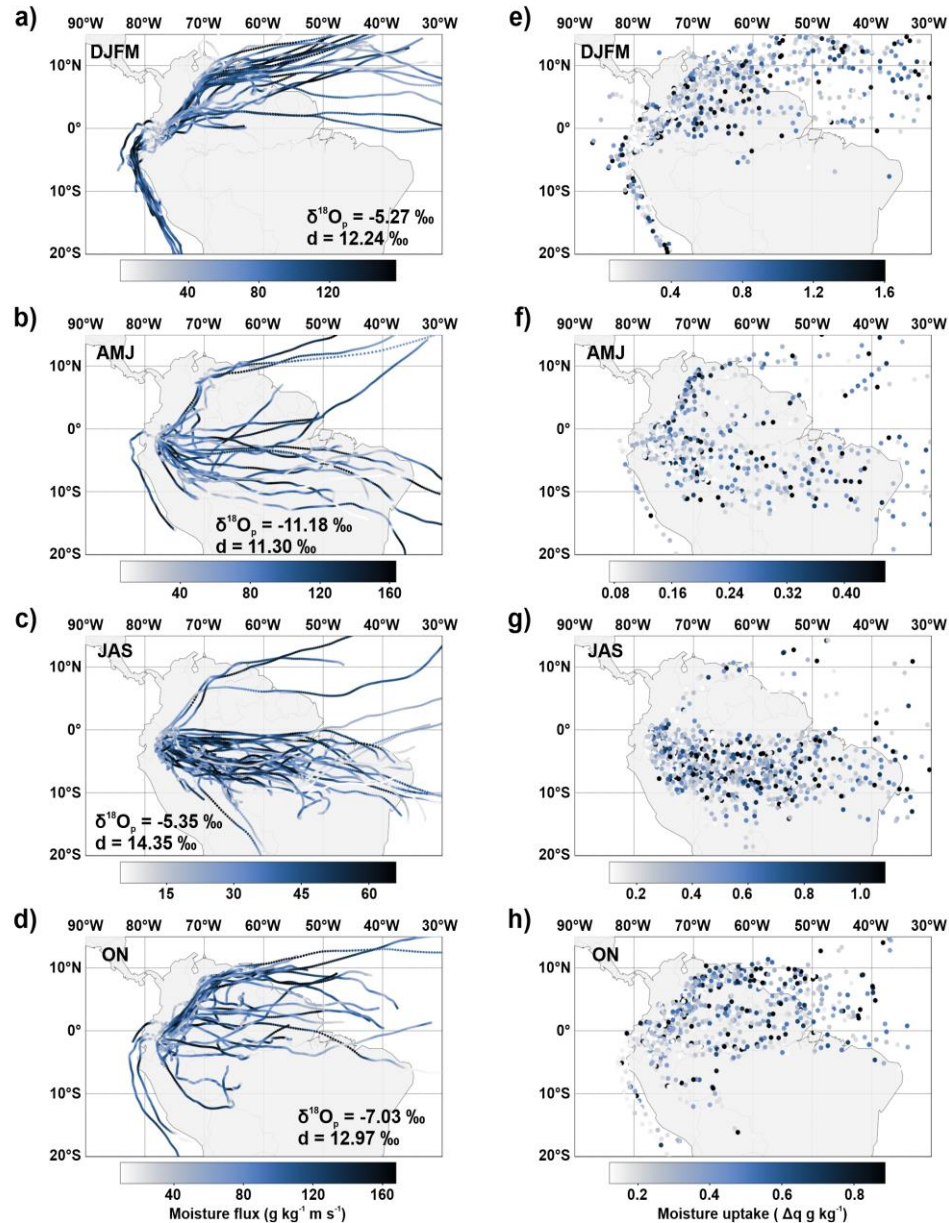


Figure 3.2 Seasonal moisture flux and uptake for the Mera site, Central Ecuador, calculated from 2014 to 2019 at 1500 m following the method of Sodemann et al. (2008) using the PySplit package (Warner, 2018) (a-e) Dec-Mar (b-f) Apr-Jun (c-g) Jul-Sep (d-h) Oct-Nov. The seasonal $\delta^{18}\text{O}_p$ and d-excess values are indicated at the bottom of each map.

Bulk trajectories also reveals that in austral autumn (AMJ), Atlantic northeasterlies and Pacific south trajectories along the coast of Peru and Ecuador are less prevalent, while easterly continental paths crossing over the Amazon basin become more distinct. In particular they move close and parallel to the geographical equator Figures 3.2b and f show a combined continental signal coming from the northeastern and eastern parts of the continent resulting in the most depleted $\delta^{18}\text{O}_p$ values (-11.18‰) during the year. In austral winter (JAS), the mean average value of $\delta^{18}\text{O}_p$ is -5.35‰, which is surprisingly high (without much depletion) as most of the trajectories have to cross the entire continent from east to west. In fact, during this season the moisture uptake signal is almost entirely coming through the Amazon basin (Figure 3.2c and g). Finally, in a similar configuration to autumn but reverse, the bulk trajectories for spring (ON) depict a steady decline in the number of eastern trajectories and a gradual increase in the ones with a northeastern signature (Figure 3.2d and h). The moisture flux is shared by the two source regions, although most of the moisture uptake is northeasterly biased. Analogous to AMJ, the $\delta^{18}\text{O}_p$ values (-7.03‰) are also lower.

The d-excess values present comparable values to $\delta^{18}\text{O}_p$. During austral summer and spring, the values are 12.24‰ in DJFM and 11.30‰ AMJ. Nevertheless, the higher values correspond to the second half of the year (i.e., 14.35‰ in JAS and 12.97‰ in ON) where the trajectories cross completely the Amazon basin suggesting that recycling may play a role in the enrichment.

3.1.2 Local Meteoric Water Line (LMWL) and “amount” effect

The relationship of $\delta^{18}\text{O}_p$ and $\delta^2\text{H}_p$ at the Mera site is closely aligned to the Global Meteoric Water Line (GMWL). Their linear relationship (LMWL) is $\delta^2\text{H}_p = 8.33 \delta^{18}\text{O}_p + 14.99$ ($n = 48$), showing an ~5‰ higher deuterium intercept (Figure 3.3a). The total mean $\delta^{18}\text{O}_p$ value is -7.1‰ which is higher than the weighted mean (-7.8‰). A closer inspection of the figure shows the intra-annual seasonality in $\delta^{18}\text{O}_p$, where AMJ months cluster completely separated from the rest of the months by having the lowest values during the 4 years of monitoring (-11.18‰). In a similar manner, but presenting the highest isotopic values are the seasons DJFM and JAS. Grouped closed to the weighted mean is the ON season, except for one enriched value (-3.40‰ in October 2020) plotted near to the highest $\delta^{18}\text{O}_p$ values. The $\delta^2\text{H}_p$ and $\delta^{18}\text{O}_p$ values are well correlated, hence the subsequent discussion primarily focuses on the $\delta^{18}\text{O}_p$.

Comparing the $\delta^{18}\text{O}_p$ with the local amount of rainfall gave a low negative correlation of $r = -0.47$ ($p < 0.01$). It can be seen from Figure 3.3b that a marked decrease in $\delta^{18}\text{O}_p$ occurs during Apr-May and Oct-Nov. In contrast, during austral winter (JAS), the highest $\delta^{18}\text{O}_p$ values are anti-correlated with the less-humid months. The monitored temperature on the site (February 2019 to May 2021) shows a low monthly seasonal amplitude with a mean of 18.98 °C (min. 18.18 °C and max. 19.72 °C) observable in Figure 3.3b. The monthly temperature fluctuations for the Shell station demonstrate

higher values by reaching a mean of 22.9 °C (min 20.5 °C and max 25.6 °C) with a decline in temperature during the JA, responsible for the wavy pattern observed in this time-series (red dashed line). In general, there is a weak correlation between the $\delta^{18}\text{O}_p$ and Shell instrumental temperature ($r = 0.12$; $p < 0.05$).

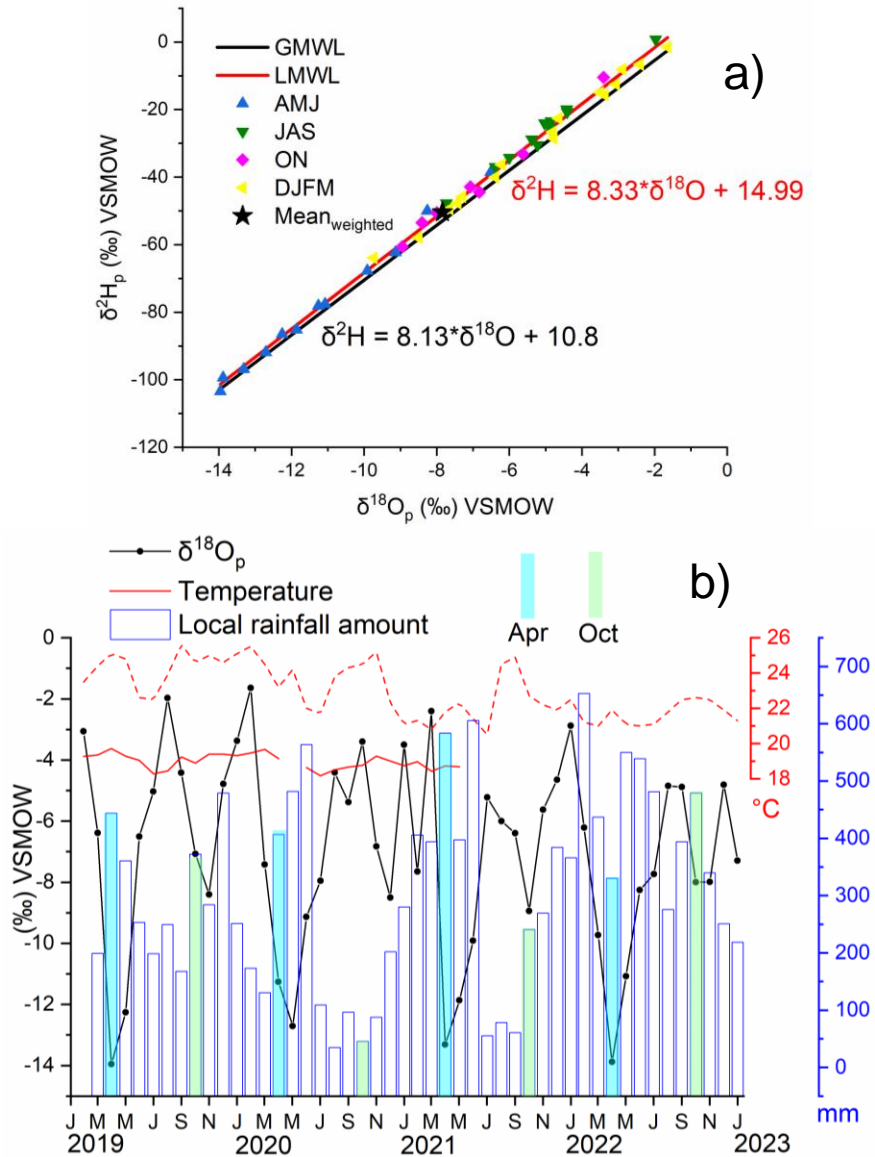


Figure 3.3 Monitoring campaign at the Mera site, Central Ecuador, from February 2019 to January 2023 ($n = 48$) showing **a)** Meteoric relationship for ^{18}O and ^2H in precipitation. The weighted mean value for $\delta^{18}\text{O}_p$ is -7.8‰ and for $\delta^2\text{H}_p$ is -50.4‰ (black star). **b)** Comparison between the local amount of rainfall (blue bars) with $\delta^{18}\text{O}_p$ (black line), local monitored temperature (red line) and Shell instrumental station (red dashed line). The months with higher precipitation and therefore lower isotopic values are highlighted by the colored bars (Apr and Oct).

3.1.3 Local “altitude” effect

Due to the complex Andes orography, the decrease of temperature with altitude is by far the dominant factor controlling subsequent changes in the $\delta^{18}\text{O}_\text{p}$ values after the transport from the Atlantic moisture source (Figure 3.2). Hence, the mean annual $\delta^{18}\text{O}_\text{p}$ against the altitudinal gradient was calculated giving a value of $-0.15\text{\textperthousand}$ $\delta^{18}\text{O}_\text{p}$ per 100-m rise (Figure 3.4). This points out the contribution of the Andes cordillera in modulating the local isotopic imprint.

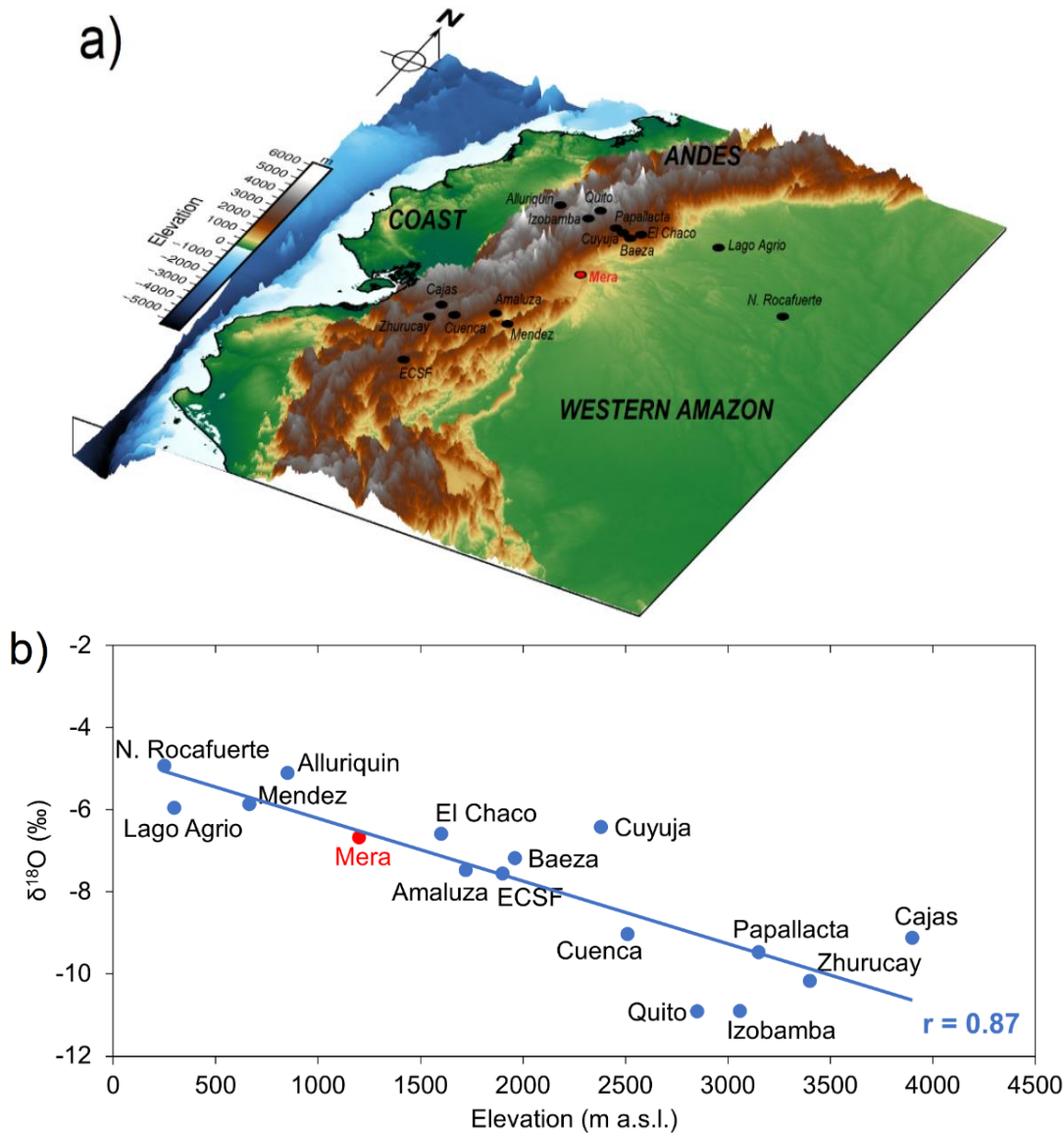


Figure 3.4 The altitude effect for $\delta^{18}\text{O}_\text{p}$ at the Andean and western Amazonian stations in Ecuador. **a)** 3-D perspective map indicating the location of the stations with $\delta^{18}\text{O}_\text{p}$ values (black dots) in the north and south. The Mera site (red dot) bridges the spatial gap due to its location in central Ecuador. **b)** Mean annual $\delta^{18}\text{O}_\text{p}$ values for the stations displayed in a) presenting an altitude gradient of $-0.15\text{\textperthousand}$ per 100 m.

3.1.4 Regional “amount” effect at the V-index

As shown in the previous sections (3.1.1 and 3.1.2), the V-Index region (5°S - 5°N , 65°W - 75°W) is the area in northwestern Amazon that encompasses the cross-equatorial flow coming from the eastern tropical Atlantic (TNA and TSA; Figure 1.8) and is highly convective. Pearson correlation coefficient between the monitored $\delta^{18}\text{O}_p$ at the Mera site with precipitation averaged at the V-Index region from February 2019 to January 2023 showed higher correlations with the ERA5 total Precipitation ($r = -0.72$, $p < 0.05$) and OLR ($r = 0.50$, $p < 0.05$) gridded products (Figure 3.5). A closer inspection of Table 3 indicates that a similar higher correlations were obtained for the CRU ($r = -0.66$, $p < 0.05$) and CHIRPS ($r = -0.68$, $p < 0.05$) rainfall products. However, for the rest of the analysis only ERA5 will be employed as it gave the highest values. The correlation is also significant by comparing it with the OLR product, giving a positive $r = 0.50$ ($p < 0.05$). Remarkably, the Mera $\delta^{18}\text{O}_p$ time-series follows the general pattern of regional precipitation at the V-Index region. Figure 3.5a reveals the marked decrease of $\delta^{18}\text{O}_p$ during AMJ and ON, coinciding with the bimodal zenithal rain peak in the region (low OLR values; Figure 3.5b). On the contrary, higher $\delta^{18}\text{O}_p$ values are visualized during the less-wetter periods in DJFM and JAS along with higher OLR values. Although the OLR correlation is lower than the ERA5 precipitation (due to the coarser resolution), the general trend during humid and less humid months is preserved. The OLR values decline during AMJ and ON ($<220 \text{ W m}^{-2}$) indicating deep convective activity (cold and high clouds) during these months over the equator, after the equinoxes, known as zenithal rain (Matsumoto and Murakami, 2000; Villacís et al., 2008). Conversely, OLR values $>220 \text{ W m}^{-2}$ indicate a reduced convection.

Given that the Mera $\delta^{18}\text{O}_p$ values closely follow the rainfall and convection patterns at the V-Index region, I extend the analysis to evaluate the $\delta^{18}\text{O}_p$ variability over the rest of stations distributed along the highlands, eastern slope, and Amazon lowlands (Figure 1.10). As shown in Table 3, there is a tight relationship between the V-index region and the stations in the Ecuadorian Andes and Amazon, which in some cases could reach remarkable high values like in the case of the Zhurucay station (2017-2018; $r = -0.90$, $p < 0.05$). Although, in El Chaco ($n=8$) and Cuyuja ($n=15$) stations I found the lowest correlation (-0.34 and -0.42 respectively, $p < 0.05$), most likely related to the short dataset. On average, the V-ERA5 precipitation gives a significant $r = -0.61$ and $r = -0.74$ ($p < 0.05$) correlation for the 1992-1996 and 1998-2018 periods with the $\delta^{18}\text{O}_p$, respectively. On the contrary, correlations with the local precipitation amount reveals a poor relationship with an $r = -0.26$ and $r = -0.52$ respectively for the same periods. The most remarkable relationship is with the Zhurucay station (2017-2018; $r = 0.90$). In all cases, independently of the precipitation product used, the average precipitation at the V-index region outperforms the relationship with the local precipitation in all the evaluated periods. These correlations are better observed in Figure 3.6 which clearly shows that the $\delta^{18}\text{O}_p$ values reflect the seasonal changes in

precipitation and convection at the V-Index region during the wettest periods and most convective months in AMJ and ON.

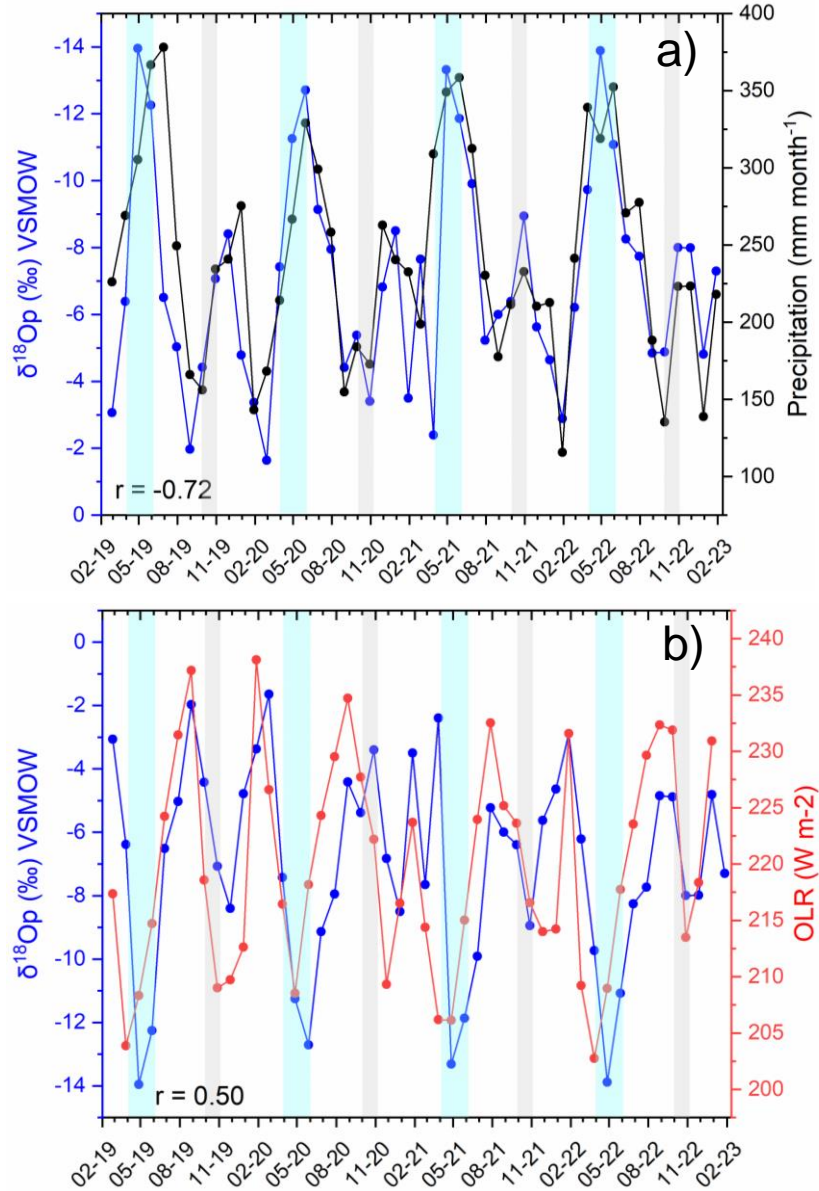


Figure 3.5 Monitoring of $\delta^{18}\text{Op}$ in the Mera site, central Ecuador, from February 2019 to January 2023 and comparison with **a)** amount of precipitation and **b)** Outgoing Longwave Radiation (OLR) averaged at the northwestern V-Index region in both cases. The blue and gray stripes highlight the bimodal peak in precipitation during AMJ and ON. The left y-axis is reversed in a) for direct comparison.

Table 3 Comparison between gridded precipitation at northwestern V-Index region from CRU, CHIRPS, and ERA5 with observed $\delta^{18}\text{O}_\text{p}$ across the Andes and western Amazon from previous studies in Figure 1.10 and the monitored Mera site.

Site	Lat	Lon	Elev. m. asl	Period	Local amount	V-CRU	V-CHIRPS	V-ERA5	V-OLR	Reference
Baeza	-0.46	-77.89	1960	1992-1993	-0.50	-0.85	-0.91	-0.77	0.62	
El Chaco	-0.33	-77.81	1600	1993-1996	0.20	-0.67	-0.56	-0.34	0.29	
Cuyuja	-0.41	-78.02	2380	1992-1993	0.29	-0.13	-0.40	-0.42	0.20	
Mendez	-2.71	-78.33	665	1992-1994	-0.62	-0.55	-0.74	-0.66	0.65	
Cuenca	-2.88	-78.98	2510	1992-1996	-0.67	-0.26	-0.47	-0.60	0.76	(Garcia et al., 1998)
Papallacta	-0.37	-78.14	3150	1992-1994	-0.10	-0.56	-0.70	-0.68	0.68	
Lago Agrio	-0.08	-76.86	297	1992-1996	-0.33	-0.74	-0.74	-0.61	0.31	
Amaluza	-2.60	-78.56	1720	1992-1994	-0.14	-0.65	-0.81	-0.78	0.59	
Alluriquin	-0.31	-78.96	850	1992-1996	-0.47	-0.44	-0.54	-0.64	0.46	
				Mean	-0.26	-0.54	-0.65	-0.61	0.51	
Izobamba	-0.37	-78.53	3058	1998-2008	-0.48	-0.47	-0.47	-0.57	0.38	
Quito	-0.16	-78.48	2850	1998-2014	-0.54	-0.64	-0.64	-0.69	0.38	(IAEA/WMO, 2020)
Bogota	4.7	-74.12	2547	1998-2016	-0.39	-0.52	-0.56	-0.50	0.12	
N. Rocafuerte	-0.89	-75.49	250	2001-2002	-0.49	-0.78	-0.85	-0.86	0.48	(Villacís et al., 2008)
Loja ECSF	-3.97	-79.07	1900	2000-2001	-0.35	-0.74	-0.63	-0.68	0.60	(Goller et al., 2005)
				2010-2012	-0.47	-0.50	-0.50	-0.70	0.70	(Timbe et al., 2014)
Zhurucay	-3.06	-79.23	3400	2011-2014	-0.57	-0.54	-0.57	-0.69	0.54	(Mosquera et al., 2016)
				2017-2018	-0.73	-0.78	-0.78	-0.90	0.74	(Zhiña et al., 2022)
Cajas	-2.78	-79.22	3900	2015-2016	-0.52	-0.77	-0.84	-0.82	0.66	(Esquivel-Hernández et al., 2019)
				†Mean	-0.52	-0.64	-0.65	-0.72	0.53	
Mera	-1.40	-78.05	1200	2019-2023	-0.47	-0.66	-0.68	-0.72	0.50	This study

Note: All the correlations are significant at $p<0.05$. †Calculated mean excluding the Bogota station.

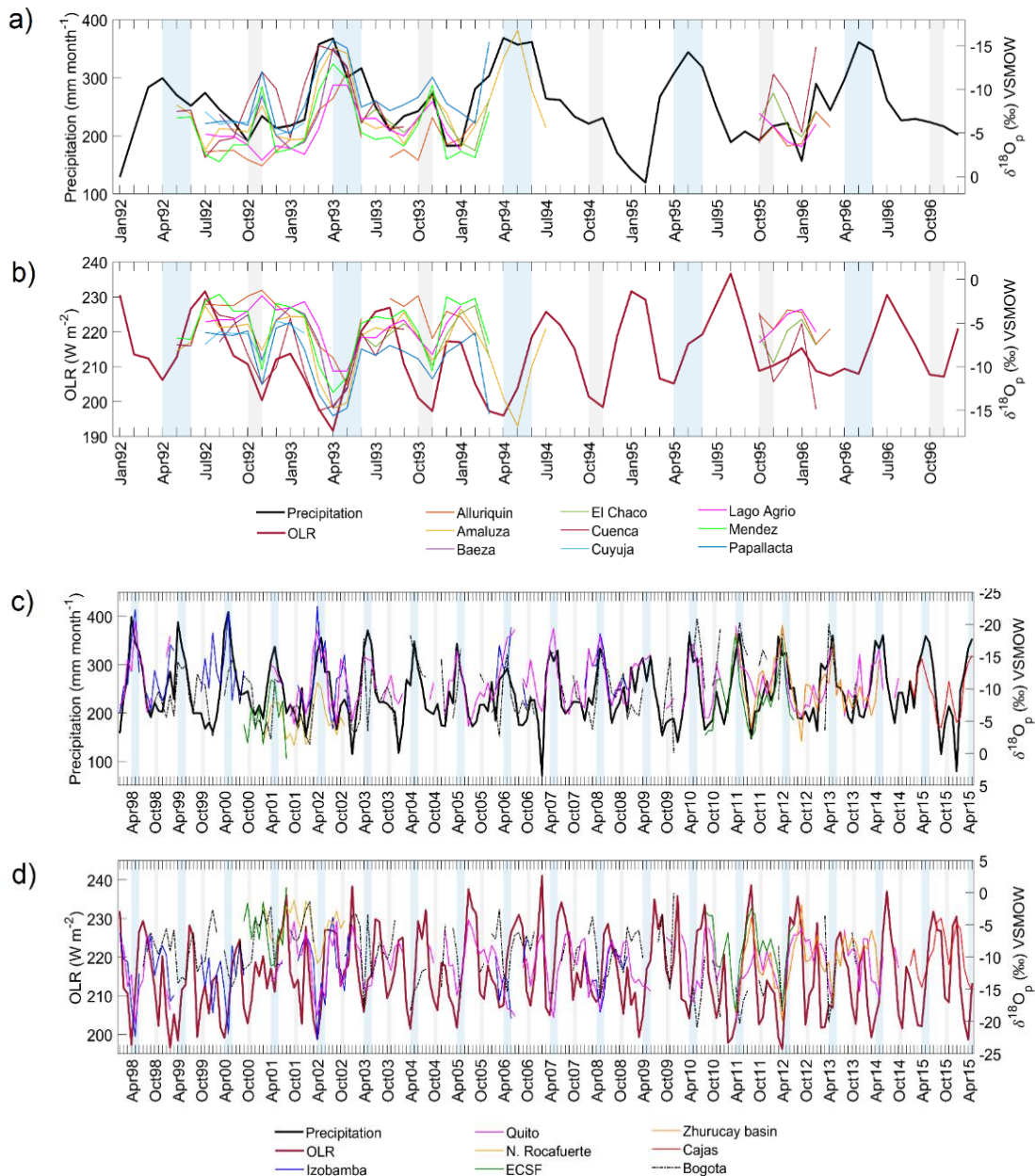


Figure 3.6 Comparison between $\delta^{18}\text{O}_p$ from inter-Andean and western Amazonian stations in Ecuador (Figure 1.10) with **a)** ERA5 precipitation 1992-1996, **b)** OLR 1992-1996, **c)** ERA5 precipitation 1998-2015, and **d)** OLR 1998-2015. Data from Zhurucay station during the period 2017-2018 is not included in **c)** and **d)**. As in Figure 3.5, the blue and gray stripes highlight the bimodal peak in precipitation during AMJ and ON rainfall. For direct comparison, the right y-axis is reversed in **a)** and **c)**.

After observing the tight correspondence between the $\delta^{18}\text{O}_p$ with the V-index region, I now evaluate independently the spatial seasonality of $\delta^{18}\text{O}_p$ in South America utilizing the ECHAM5 ESM (Werner, 2019; Werner et al., 2011) depicted in Figure 3.7. The most positive values are found from June to October with values ~ -1 to 0 ‰ , whereas the most depleted oxygen-18 values spatially shifts northwards from the SAMS region to the North, feeding the V-index region from January to

May. It is also remarkable to observe the fast flux of easterlies during austral summer (DJF) and winter (JAS) that dampens during the peak months of precipitation (i.e., April and October) especially in the V-index region. Together these results provide important insights on the precipitation dynamics establishing April/May and October/November as the onset months of the wettest seasons on NAMZ.

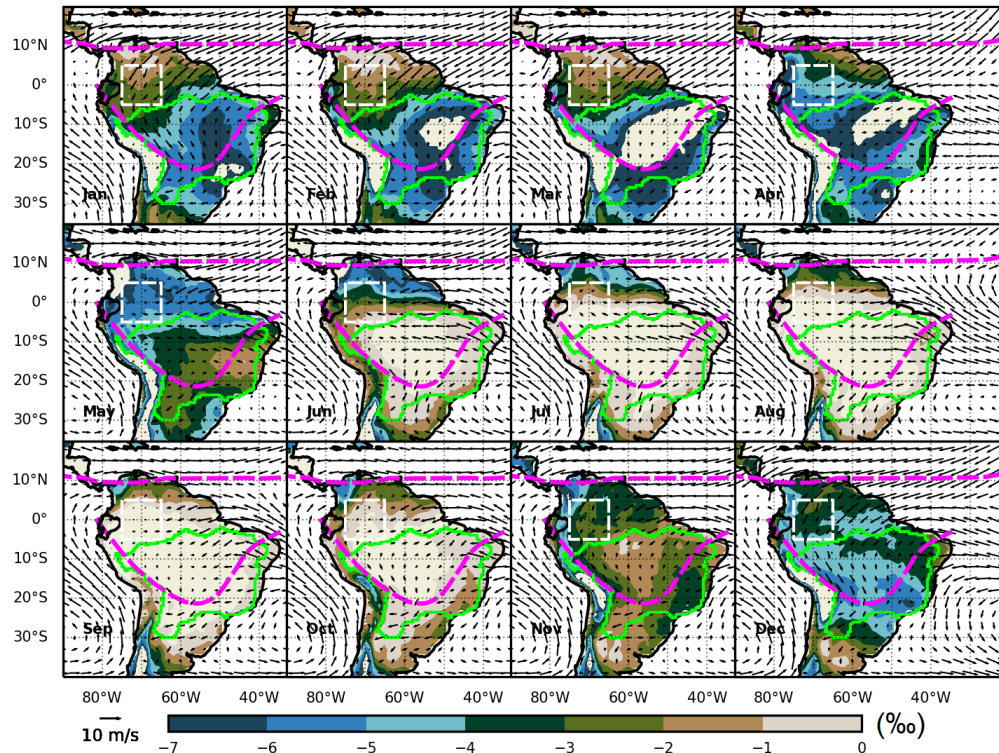


Figure 3.7 Monthly spatial distribution of $\delta^{18}\text{O}_p$ in South America (‰) using ECHAM5 model. The SAMS boundaries are drawn in green, the ITCZ excursions in magenta and wind speed by the black arrows. Similar to previous plots, the V-index region is drawn by the white dashed squared at the equator.

3.2 Tree-rings and modern climate

3.2.1 Annual ring periodicity

The wood anatomical analysis in *C. nebulosa* showed a well-defined demarcation of rings due to the presence of a marginal band of parenchyma indicating the onset of the growing season (Figure 3.8a). The vessels were arranged in radial and diagonal patterns with a diameter $\leq 350 \mu\text{m}$ and density $\leq 5 \text{ vessels/mm}^2$. In addition, larger vessels were clustered at the beginning of a new growing season (earlywood) in the parenchyma band with the presence of common tylosis and gums (Figure 3.8b and c). Moreover, the annual formation of rings in *C. nebulosa* was successfully validated using radiocarbon (^{14}C) taking advantage of the post-1955AD ‘bomb-pulse’, and the best fit was to the Southern Hemisphere Zone 3 (SHZ3) calibration curve (Hua et al., 2013) (Figure 3.8d and Appendix A.3).

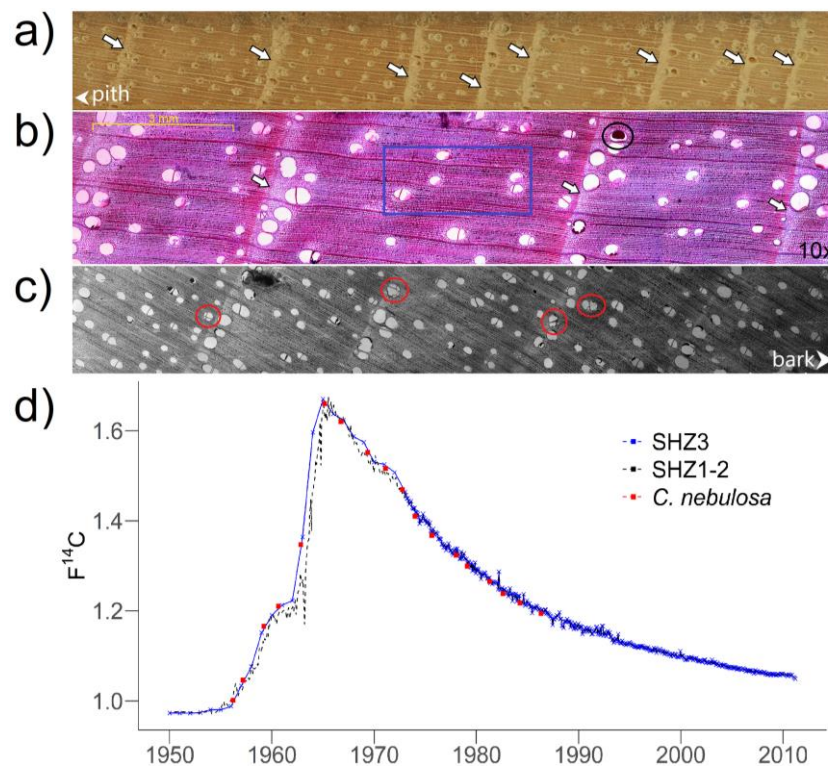


Figure 3.8 a) Wood cross-section of *C. nebulosa* showing the limits of growth rings defined by a thin band of marginal parenchyma (white arrows). b) Microscopic structure of growth rings with the presence of gums in a vessel (black circle). Wide vessels are embedded in marginal parenchyma (white arrows), whereas wood formed later during cambial growth presents narrower vessels (blue rectangle). c) Small to medium-sized vessels with the presence of tylosis (red circles). d) Individual tree-rings measured by ^{14}C (red dots) over the bomb-spike for independent validation of ring annuity. The $F^{14}\text{C}$ calibration curves for Southern Hemisphere correspond to SHZ1-2 (in black) and SHZ3 (in blue) (Hua et al., 2013).

3.2.2 Tree-ring chronologies

The *C. nebulosa* trees showed an initial slow growth with a subsequent increase at intermediate years to finally stabilize at maturity, forming a sigmoidal-type growth curve (Figure 3.9a). The first century of growth (1860-1960) did not vary considerably, and it is only from 1960 onwards that higher peaks are observed. Tree-rings were dated between the period 1860-2019. Most of the sampled trees were relatively young, with a mean of 46 years and an average ring-width of 4.38 mm. The maximum age was found in a tree growing for 160 years from 1860 to 2019, whereas the minimum registered age was 31 years from 1989 to 2019. The mean growth in diameter was $8.76 \text{ mm year}^{-1}$. The calculated EPS for the complete TRW chronology gave a value of 0.46 (1860-2019), increasing to 0.65 when considering a shorter period with higher sample replication (1960-2019) (see Appendix A.4). Each averaged detrended individual allowed the construction of a mean standard chronology whose robustness increased after 1920 (Figure 3.9b).

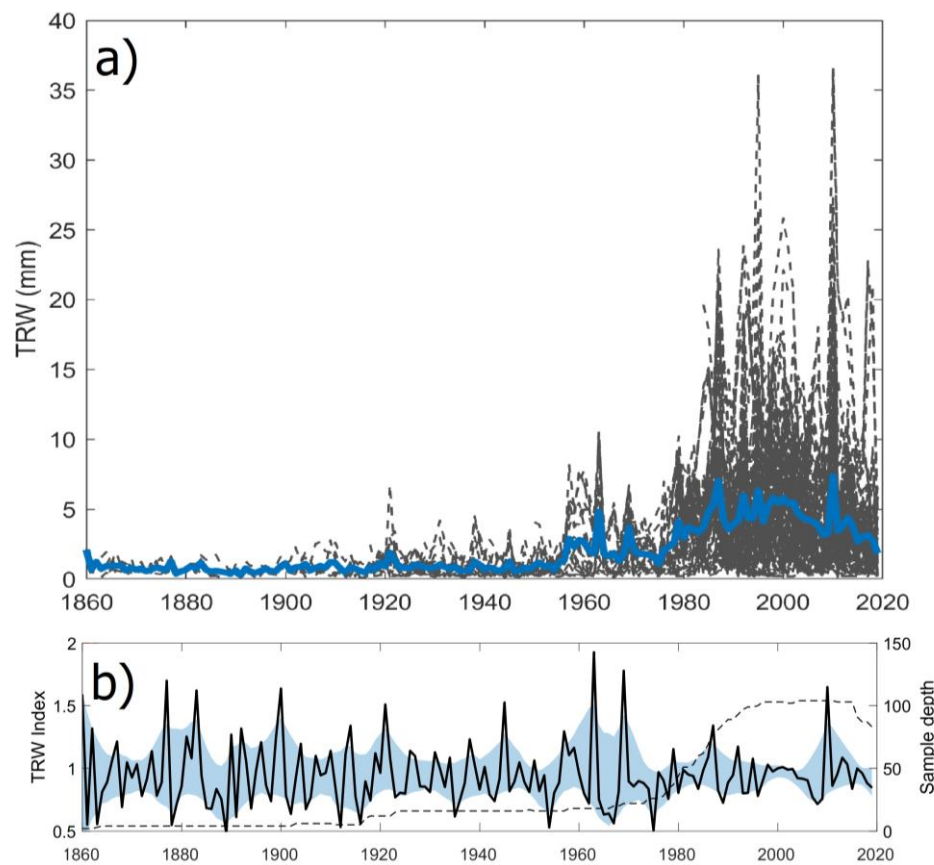


Figure 3.9 Built tree-ring chronologies of *C. nebulosa* for Mera, Ecuador **a)** Tree-ring raw measurements (mm) of 24 crossdated *C. nebulosa* trees from a total number of 33 collected trees. The individual tree-ring time-series show a slow initial growth, increase at intermediate years, and decrease at the end, forming a sigmoidal growth curve. **b)** TRW standard chronology and 95% confidence intervals (CI) (blue stripe). The superimposed black dashed line corresponds to the number of individuals (sample depth) used for its construction. For details on the number of employed trees per interval, the reader is referred to Appendix A.4, or the complete list at <https://github.com/vargasdanny/paleothesis>.

Regarding $\delta^{18}\text{O}_{\text{TR}}$ and $\delta^{13}\text{C}_{\text{TR}}$, their constructed chronologies covered the period between 1864 to 2018 (154 years). The mean isotopic value for the composite $\delta^{18}\text{O}_{\text{TR}}$ chronology (Fig. 3.10a black curve) was $23.9 \pm 1.2\text{\textperthousand}$, with a minimum of $20.7\text{\textperthousand}$ and a maximum of $26.8\text{\textperthousand}$. There is a evident trend towards more positive values with a short decline between 1920-1940 captured by the ramp regression curve. Further spectral analysis of the data reveals the existence of a significant periodicity of $\sim 14\text{-}16$ years and ~ 32 years in the record (Figure 3.10b). In the case of $\delta^{13}\text{C}_{\text{TR}}$ record (Fig. 3.10c blue curve), the mean value was $-27.7 \pm 1.4\text{\textperthousand}$ with values ranging from $-29.9\text{\textperthousand}$ (minimum) to $-24.8\text{\textperthousand}$ (maximum). Similar to the $\delta^{18}\text{O}_{\text{TR}}$ record, the $\delta^{13}\text{C}_{\text{TR}}$ revealed an upward trend towards more positive values from 1920 onwards, although with an initial decline to more negative values from 1860 to 1920. The noise distribution after fitting the trend (bottom left in Figure 3.10a and c) shows a close fitting to a normal distribution. In other words, it indicates that the

estimation of the trend component is well captured by the ramp and break nonlinear regression models.

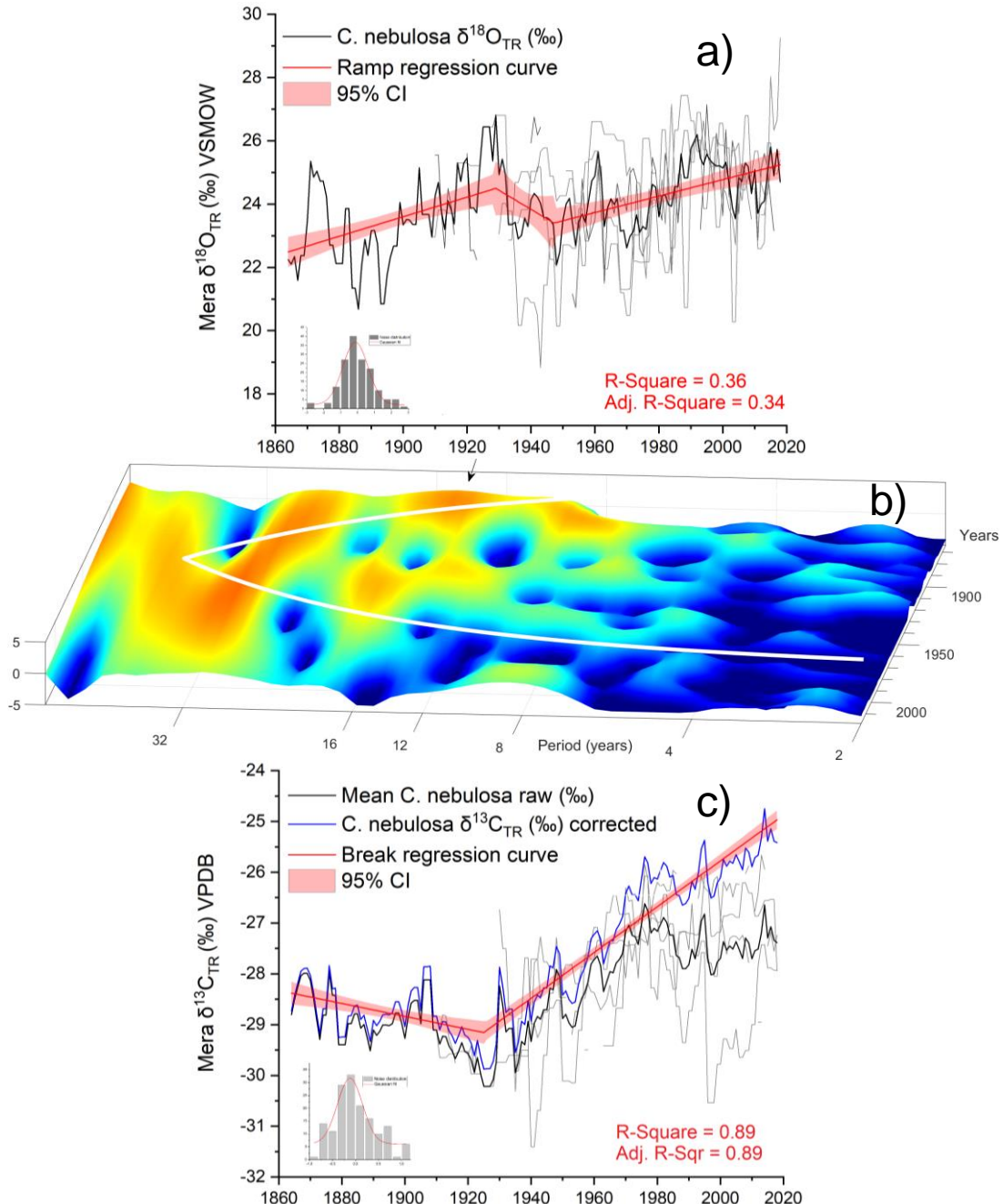


Figure 3.10 a) The newly constructed $\delta^{18}\text{O}_{\text{TR}}$ record (1864–2018) and its b) Morlet wavelet ($\sigma = 9$). The arrow marks the ~14 years periodicity. c) Similar to a) but for $\delta^{13}\text{C}_{\text{TR}}$ values. Both records in a) and c) come from 4 individual trees (gray lines). Their mean composite chronologies are superimposed (black curves) and fitted with a ramp and break regression curves respectively (red lines with 95% confidence intervals) with their respective R-Square and Adjusted R-Square for the evaluation of goodness of fit at the bottom right. The statistical distribution of residuals after the fitting the regression curves are shown at the bottom left in c) and e). The additional blue chronology in e) corresponds to the corrected $\delta^{13}\text{C}_{\text{TR}}$ relative to pre-industrial standard values, according to McCarroll and Loader (2004).

3.2.3 Oxygen isotopes and western Amazon precipitation

In our field observations of *C. nebulosa* phenology, I found that new leaves are formed from February to April and reach maturity during May to July. Leaf senescence starts from mid-August/September (see % foliage on Table 2), to finally give onset of the cambial season (no growth) from October to December/January (Figure 2.3). The traditional method of obtaining partial correlations between the TRW chronology with local temperature and precipitation climatology for the evaluation of possible climate relationships (Meko et al., 2011), did not provide a statistical significant climate signal (not shown). Hence, the subsequent analysis focus solely on stable isotopes. Pearson's correlation coefficient between $\delta^{18}\text{O}_{\text{TR}}$ chronology and local Mera CRU precipitation (1921-2018) during the wettest period March to June gave an $r = 0.07$ ($p < 0.05$). The correlation increased when employing the instrumental Puyo and Shell precipitation (1965-2018), obtaining an $r = 0.24$ ($p < 0.05$). Presumably, the low correlations with local CRU precipitation obey to the small number of stations that conformed the gridded data at this latitude. Therefore, a spatial analysis at a regional scale in the same humid months (Mar-Jun) between $\delta^{18}\text{O}_{\text{TR}}$ and the CRU rainfall product significantly improved the correlations to $r = -0.50$ (1921-2018, $p < 0.01$) in the northwestern area of the Amazon Basin (Figure 3.11a). Interestingly, this spatial correlation is also present at this latitude when using OLR, although evaluated for a shorter period (1985-2018, $p < 0.05$, Figure 3.11b). Taken together, these results suggest that there is an association between $\delta^{18}\text{O}_{\text{TR}}$ from the Mera site and the V-index region (Section 3.1). A wavelet coherence analysis between CRU precipitation over the V-index area and the $\delta^{18}\text{O}_{\text{TR}}$ (Figure 3.11c) shows a significant coherence in most of the records, especially from 1920 to mid-1970 ($\alpha < 0.05$), indicating a periodicity between 4 to 8 years. In contrast, associations are not significant from 1980 onwards, although few small regions displaying anti-phase angle (arrows pointing left) are observed. Similarly, the time-series in Figure 3.11d have an analogous interdecadal variation which even captures the apparent drop in precipitation at the end of 1970, followed by an increase at the beginning of 1990, which suggests a common regional controller in their moisture source. It is apparent from these results that $\delta^{18}\text{O}_{\text{TR}}$ does not correlate well with a local rainout, but it is regulated by Amazon basin-intrinsic processes. As can be seen from Figure 3.11e, it is clear that the most convective months with values $< 220 \text{ W m}^{-2}$ (higher rainfall) occur during Mar-May and Oct-Nov in the Mera site and the V-index region, in agreement with the previous findings.

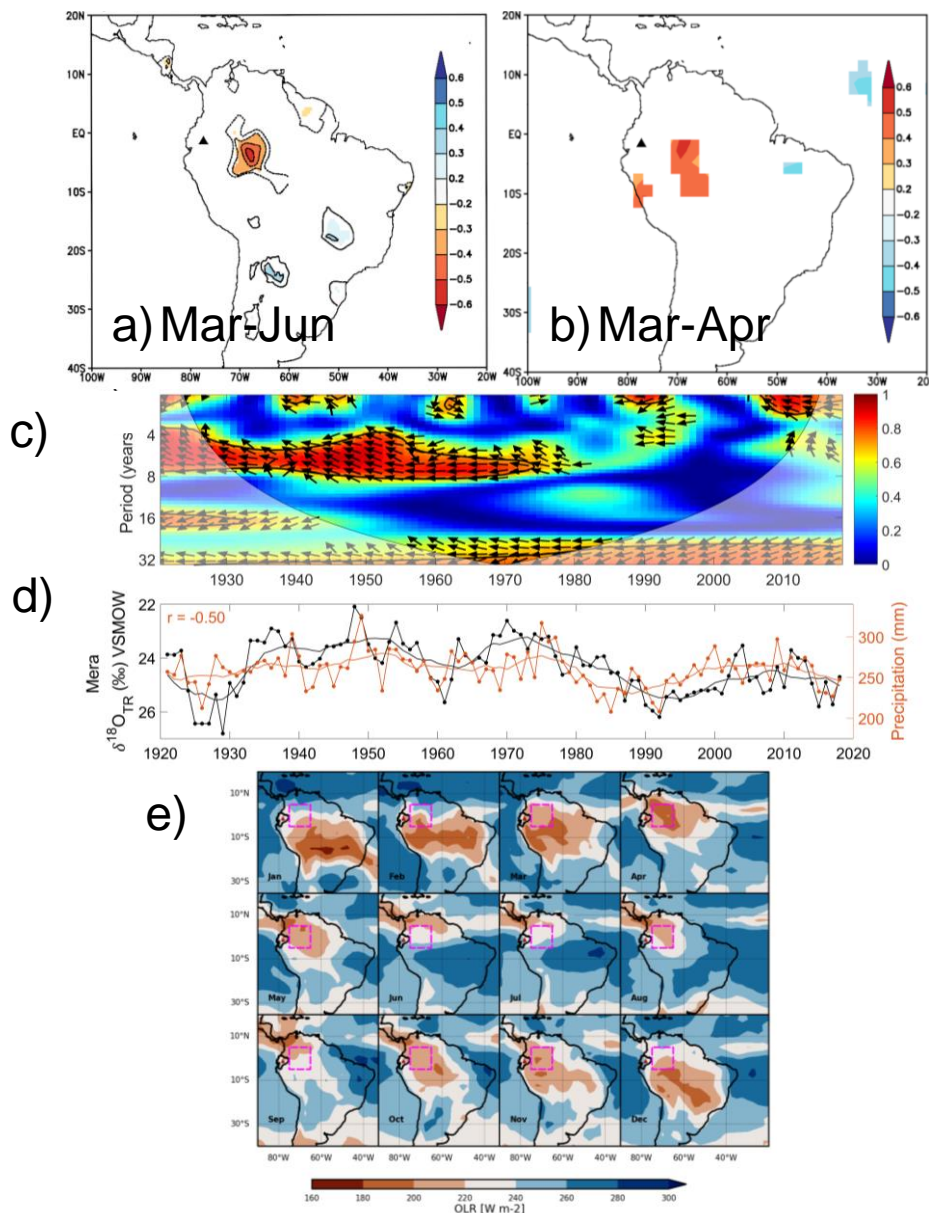


Figure 3.11 **a)** Spatial correlation fields between Mera $\delta^{18}\text{O}_{\text{TR}}$ with regional March-June CRU precipitation (1921-2018). The color bar indicates the strength of the correlation coefficients significant at $p < 0.01$. **b)** Spatial correlation between Mera $\delta^{18}\text{O}_{\text{TR}}$ with regional March-April OLR (1985-2018; $p < 0.05$). In all graphs, the location of the Mera site is indicated by a black triangle. **c)** Wavelet coherence between the Mera $\delta^{18}\text{O}_{\text{TR}}$ and CRU precipitation (Mar-Jun) at the V-index region (orange region). Red areas bordered by black contour lines indicate significant coherence ($\alpha < 0.05$), whereas arrows pointing left indicate anti-phase angle. The shading indicates areas outside the cone of influence. **d)** Similar to c) but depicting their time-series. Each record is superimposed with a 10-year Moving Average with a correlation ($r = -0.50$) significant at $p < 0.05$. The scale is reversed for $\delta^{18}\text{O}_{\text{TR}}$ (black curve). **e)** Mean monthly interpolated OLR derived from NOAA (1979-2020) in South America. The location of the Mera study site is indicated by a red triangle in all insets along with the V-index region (fuchsia dashed rectangle). Lower values ($< 220 \text{ W m}^{-2}$) correspond to higher precipitation, higher clouds, and deeper convection.

Finally, a visual comparison between our $\delta^{18}\text{O}_{\text{TR}}$ record with two independent local archives: *C. montana* from Cuyuja and the Chimborazo glacier (see locations in Figure 1.11) from 1864-onwards (Figure 3.12), found a correlation for both of $r = 0.35$ ($p < 0.05$). There are noticeable differences at an interannual scale in the records due to sampling resolution, forest type, altitude, and latitude effect. For instance, from 1860 to 1920 the signal is anticorrelated with the Chimborazo record (dashed black lines). Nevertheless, a common long-term variability seems to be preserved overall and become more alike when observed at decadal scales (see section 4.2.1 for further discussion).

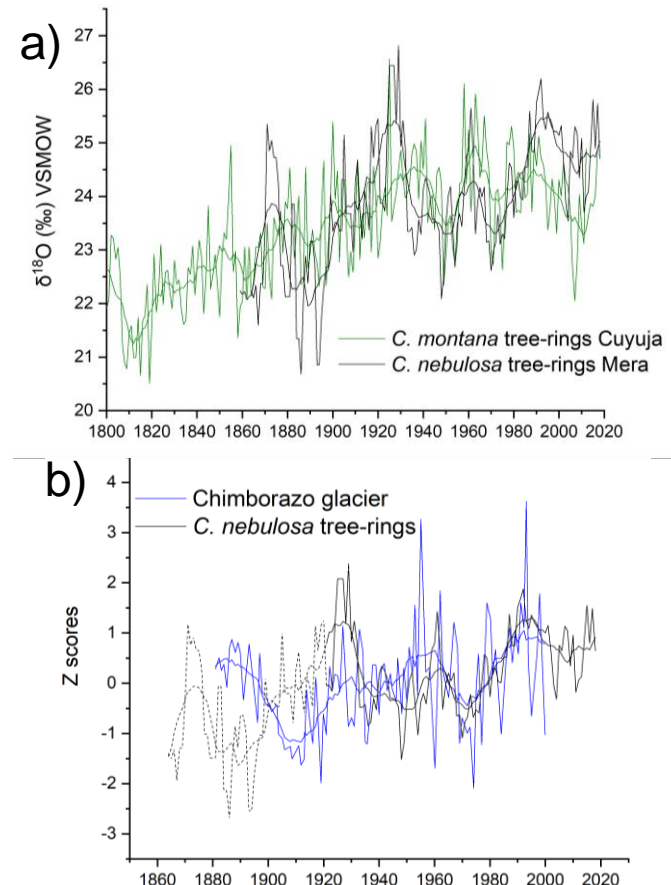


Figure 3.12 Interdecadal comparison with other local paleorecords indicated in Figure 1.11. **a)** Comparison between the $\delta^{18}\text{O}_{\text{TR}}$ records from *C. nebulosa* and *C. montana* (~105 km apart from *C. nebulosa* forest) for the common period 1864–2012 (Baker et al., 2018). **b)** Comparison with the Chimborazo glacier record (~85 km further from *C. nebulosa* forest) for the period 1881–2000 (Ramirez, 2003). In both cases, a 5-year Moving Average smoothing curve is overlaid for better visualization of the analogous pattern.

3.2.4 Carbon isotopes and temperature controls

The carbon isotopes for the Mera site showed a significant correlation ($r = 0.51$, $p < 0.05$) with CRU cloud cover (1930–2018) (Figure 3.13). Similarly, the $\delta^{13}\text{C}_{\text{TR}}$ correlations with the averaged Puyo and Shell temperature (1965–2018) gave a value of $r = 0.53$ ($p < 0.05$), and an even higher correlation $r = 0.67$ ($p < 0.05$) was

obtained with the temperature anomalies for Ecuador (1901-2018). The evaluated period was July-August in all cases, which corresponded to the lower temperature season (Figure 2.1c). There is a consistent upward trend between $\delta^{13}\text{C}_{\text{TR}}$ with all the assessed climatic factors. In contrast, correlations with the averaged Puyo and Shell relative humidity gave a negative correlation of -0.53 ($p<0.05$) (not shown).

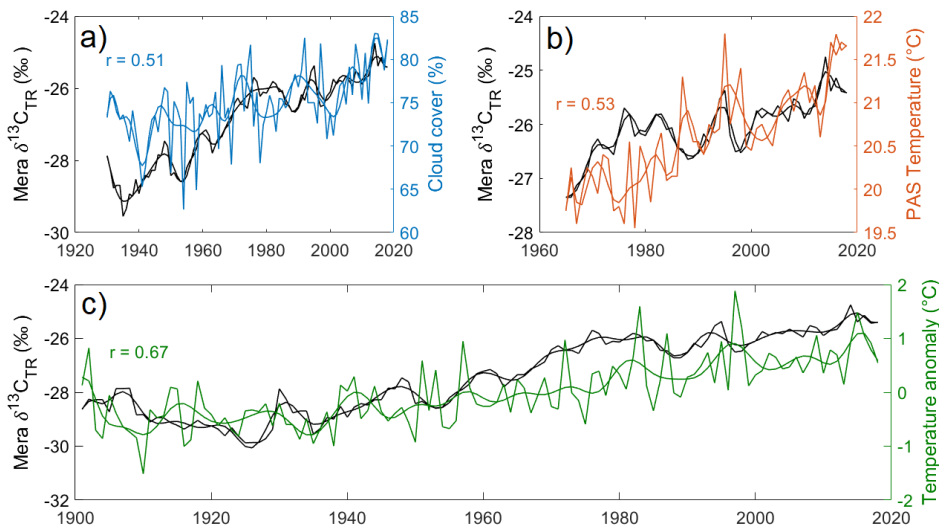


Figure 3.13 Carbon isotopes $\delta^{13}\text{C}_{\text{TR}}$ (black curve) correlated with (a) CRU cloud cover (1930-2018), (b) Puyo and Shell (PAS) temperature (1965-2018), and (c) Temperature anomalies (1901-2018) relative to the period of January 1951-December 1980 average for Ecuador from the Berkeley Land/Ocean Temperature Record (<http://berkeleyearth.org/data/>). In all the graphs, the analyzed interval corresponds to July-August. A cubic spline was superimposed to each time-series to visualize long-term variability.

These high positive correlated results with temperature (anomalies) and cloud cover suggest that photosynthetic rate is the primary control in the $\delta^{13}\text{C}_{\text{TR}}$ record. Therefore, two key climatic elements that regulate this process indirectly are sunshine duration (sunshine hours) and cloud cover. The former, based on the ERA-Interim dataset (1980-2018) indicates a sunshine duration in the Mera site of 274 hours month⁻¹ / 9 hours 7 min day⁻¹ (Jan-Mar), 282 hours month⁻¹ / 9 hours 24 min day⁻¹ (Apr-Jun), 314 hours month⁻¹ / 10 hours 27 min day⁻¹ (Jul-Sep), and 287 hours month⁻¹ / 9 hours 34 min day⁻¹ (Oct-Dec). Hence, it is clear that austral winter/spring (JAS) is the season with the most available sunlight disponibility across the calendar year (Figure 3.14a). Regarding cloud cover, a greater percentage is seen at the onset of the year (Jan to May), which diminishes towards austral winter/spring (Jun-Sep), and again a moderate uptick in the trend is evident for the austral summer (Oct-Dec). Therefore, during the season of lower precipitation from July to September, cloud cover has a significantly reduced percentage compared to the other seasons (Figure 3.13a). It is noteworthy to mention that sunshine duration is different to insolation, which, as depicted in Figure 3.14b, moves coeval to the mean air temperature. Equinoxes happen on the 22 of March and 22 of September approximately. Conversely, the solstice occurs around June 20th and fit into the temperature-insolation curves (lowest temperature), contrary to the sunshine duration plot.

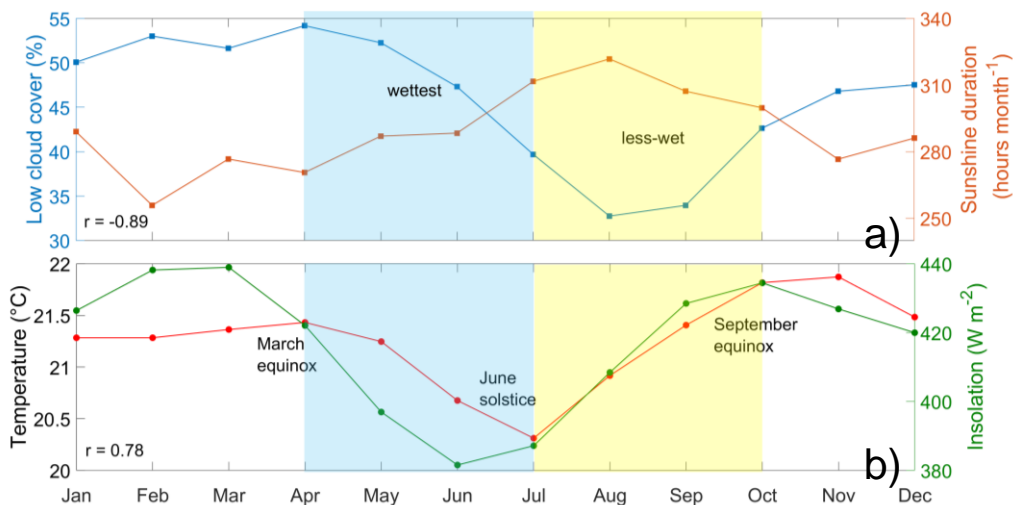


Figure 3.14 Seasonal patterns of the principal climate variables associated with changes in temperature and photosynthesis in the Mera site. **a)** Low cloud cover (from surface to 2 km) and sunshine duration from the ERA-Interim for 1980-2018. **b)** Combined Puyo and Shell temperature (1965-2018) and monthly insolation (1980-2018) from the National Aeronautics and Space Administration (<https://data.giss.nasa.gov/modelE/ar5plots/srlocat.html>). Pearson's correlation coefficient between the variables in each inset is shown at the bottom left and are significant at $p < 0.05$.

3.3 Dino-1 stalagmite and mid-Holocene climate

3.3.1 Cave monitoring

3.3.1.1 Temperature

The air temperature monitoring campaign (hourly) established outside the Dino cave can be analyzed into three periods. The first one from February 2019 to April 2020 (14 months), the second from June 2020 to May 2021 (11 months) and the final one from January to February 2022 (1 month) (Figure 3.15a). The first period was characterized by high peaks in temperature, especially during austral winter (JAS) (Figure 3.15b) with some values even reaching 48 °C. The mean temperature for this period was 19.19 °C (median 18.86 °C, minimum 13.66 °C and maximum 48.63 °C). In the case of the second period, it shows a more homogenous pattern and lack of extremely high values. The mean temperature for these months was 18.70 °C (median 18.42 °C, minimum 14.29 °C and maximum 27.43 °C). Finally, the third period from January to February 2022 shows a mean of 18.64 °C (median 18.53 °C, minimum 14.89 °C and maximum 23.03 °C) with no significant outliers. Overall, the mean temperature for the whole monitored period (Feb 2019-Feb 2022) was 18.97 °C, with a median of 18.67 °C, a minimum of 13.67 °C, and a maximum of 48.63 °C.

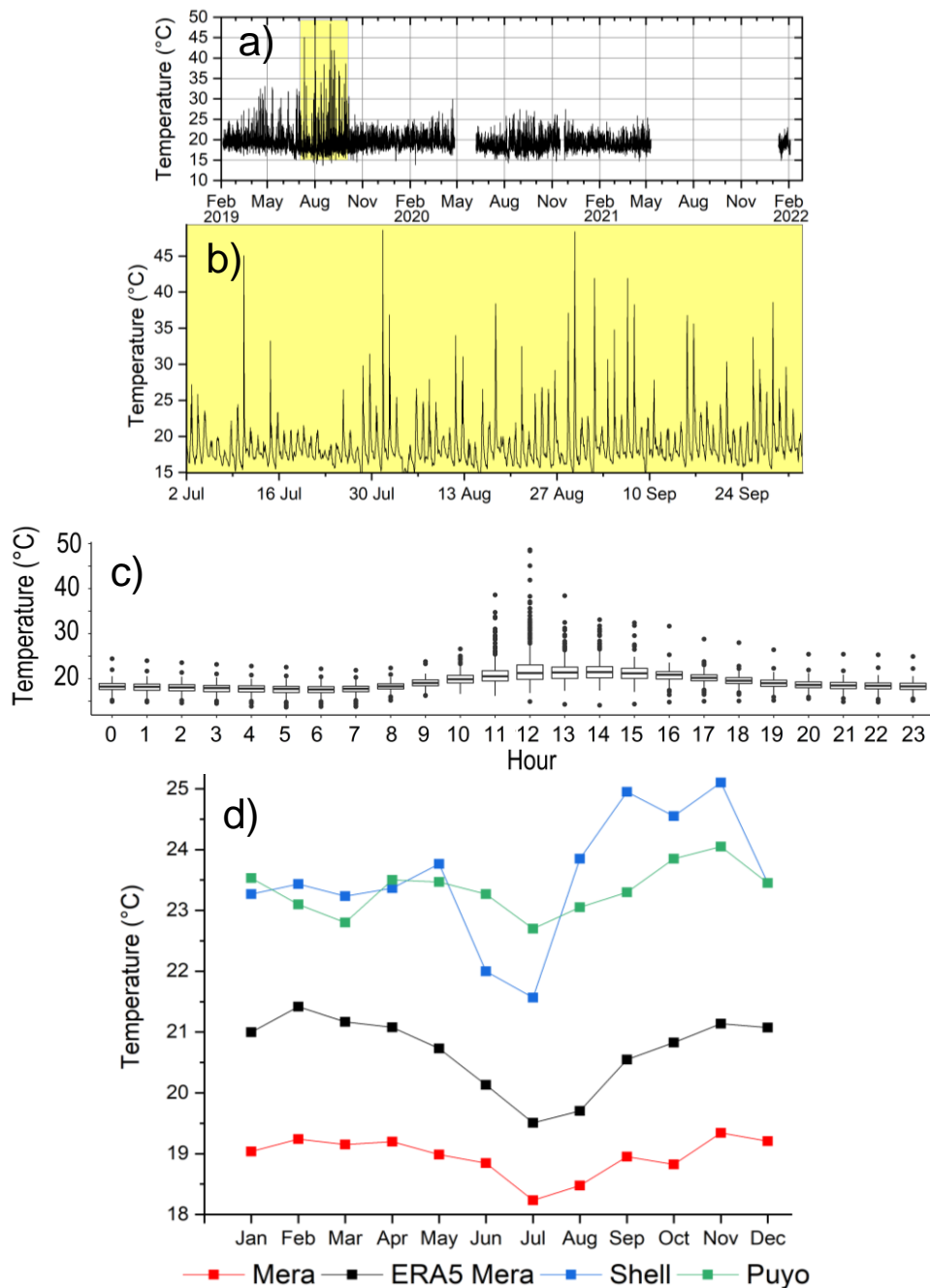


Figure 3.15 Seasonal temperature fluctuations outside the Dino cave. **a)** Temperature time-series at hourly resolution from February 2019 to February 2022. **b)** Enlarged austral winter months (Jul-Sep; yellow box) depicting high temperature peaks above 40 $^{\circ}\text{C}$. **c)** Temperature boxplot showing daily fluctuations. The time interval from 10 am to 4 pm is the warmest during the day, with temperatures above 30 $^{\circ}\text{C}$. Minimum temperatures are found in early mornings and late nights. **d)** Comparison between the monitored temperature at monthly scale (red line) with ERA5 reanalysis interpolated for Mera (black line) and Shell (blue line) and Puyo (green line) meteorological stations. The common period 2019 to 2022 was used in all cases.

The highest temperatures were reached between 10 am to 3 pm which is the peak of insolation. Early mornings and late nights were the coldest periods of the day outside the cave (Figure 3.15c). From these statistics, is it clear that there is an

approximately 1 °C difference between the mean and minimum values, but more than 20 °C comparing the maximums. Hence, for further analysis our statistics rely on the median, which is more robust and resistant to outliers, giving a <0.50 °C difference between the evaluated periods. What is interesting about the high peaks during Jul-Sep (Figure 3.15b) is that despite presenting high temperature values, it is also the season with an approximately 1 °C drop with a gradual increase in the following months (Sep-Apr) clearly seen at monthly resolution (Figure 3.15d). This pattern is also observed in the instrumental Puyo, Shell and ERA5 reanalysis at monthly scale for the monitored period 2019-2022. The ERA5 mean temperature interpolated for Mera was 20.7 °C (minimum 19.3 °C and maximum 21.8 °C). In addition, the comparison with Puyo and Shell instrumental stations gave a mean of 23.3 °C (minimum 21.5 °C and maximum 25.2 °C), and 23.4 °C (minimum 20.5 °C and maximum 25.6 °C), respectively. The temperature variability is higher in the Puyo and Shell stations (4-5 °C), whereas in the ERA5 reanalysis, the Mera variation is lower (2.5 °C) relative to our monitored values. This marked difference in employing instrumental stations is likely related to their location.

On the other hand, monitored temperature for a similar period (Feb 2019-Feb 2022) but inside the cave showed a stable pattern, with minimal fluctuations (mean 19.24 °C, median 19.23 °C, minimum 19.15 °C and maximum 19.36 °C). In fact, the difference between the lowest and highest value during the 3 years of monitoring was ≤0.21 °C (Figure 3.16). Any apparent trend, like the drop during wettest months (Feb-May and Oct-Nov) is within the error of the iButton logger (± 0.5 °C accuracy, Section 2.2.3), and not a fluctuation of the meteorology outside. Nevertheless, there is strong evidence to conclude that the cave has an almost steady temperature throughout the year.

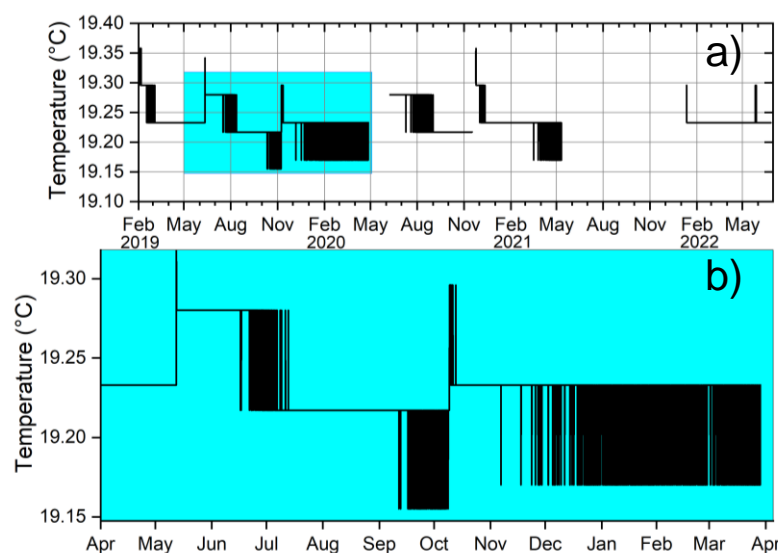


Figure 3.16 Temperature monitoring inside Dino cave from February 2019 to February 2022. **a)** Scatter plot of temperatures showing minimal changes in the air temperature inside the monitored chamber. **b)** Enlarged blue box in a) showing an uninterrupted year of monitoring (Apr 2019-Apr 2020).

3.3.1.2 Dripwater

The Dino and the nearby caves Copa and Union are ponor caves of two separate karst systems (Figure 2.4). Nevertheless, their $\delta^{18}\text{O}_{\text{drip}}$ values fit close to the Mera LMWL. The total mean of $\delta^{18}\text{O}_{\text{drip}}$ for Copa cave was $-6.40 \pm 0.5\text{\textperthousand}$, for Union cave $-7.04 \pm 1.3\text{\textperthousand}$, and $-7.57 \pm 0.9\text{\textperthousand}$ for Dino cave as shown below in Figure 3.17a. Two samples from December 2021 and January 2022 from Union cave follow an evaporative line on the $\delta^{18}\text{O}$ - $\delta^2\text{H}$ plot, deviating from the LMWL. As the rest of the data are falling closely to the LMWL, and considering the high precipitation amount in the area and constant dripping in the cave, in-cave evaporative effect is highly unlikely and these samples were most likely affected by evaporation during transportation to the laboratory. Therefore, these data are excluded as outliers from further discussion.

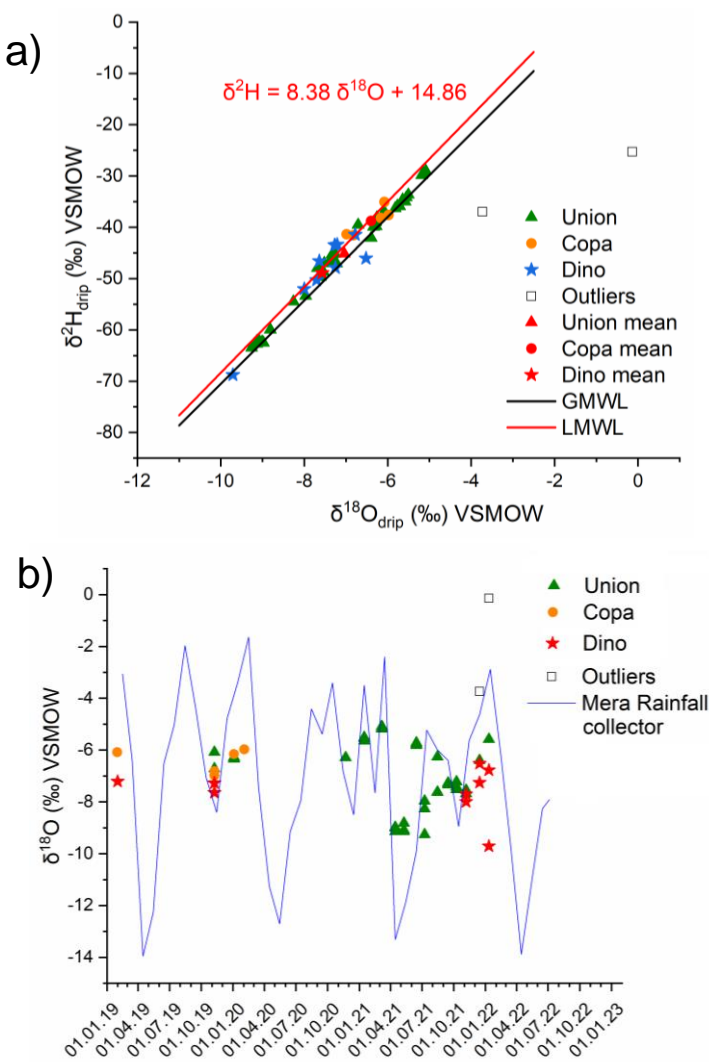


Figure 3.17 Point-event cave dripwater monitoring in Dino, Copa and Union caves in Mera, Central Ecuador from January 2019 until January 2022. **a)** Copa and Union caves (triangle and point symbols) are separated 245 m from each other and ~ 2.5 km from the Dino cave (star symbol). Their mean values (calculated without outliers) are indicated by the red symbols for each cave. **b)** Dripwater monitoring time-series for each cave along with the Mera monthly precipitation values. In both figures, outliers are denoted by white rectangles.

Figure 3.17b reveals that in general, the point-event samples time-series follow the Mera $\delta^{18}\text{O}_p$ curve. The general pattern of a marked decrease in $\delta^{18}\text{O}_p$ in 2019-ON, 2021-AMJ and 2021-ON is followed by the $\delta^{18}\text{O}_{\text{drip}}$ values. Similarly, the steep rise towards more positive $\delta^{18}\text{O}_p$ values can be observed in 2021-JF, 2021-JA and 2022-JF. Although valuable, these findings must be approached with some caution because of the lack of continuous monitoring at a higher frequency of sampling. This might have missed the sampling of important rainfall events. Nevertheless, these results are a good reference point and bring about good possibilities for the preservation of the isotopic signal.

3.3.2 Dino-1 speleothem

3.3.2.1 Mineralogy, U-Th dating and spectral analysis

X-ray diffraction of powdered samples showed that the Dino-1 stalagmite is principally composed of calcite (CaCO_3) (Figure 3.18a). Visually, the fabric indicates fast growth with non-visible hiatuses. In fact, the presence of hiatuses in Dino-1 is unlikely due to its fast growth rate in a short period 0.35 mm yr^{-1} ($519 \text{ mm} / 1492 \text{ yr}$), or the other way around 2.87 yr mm^{-1} suggesting a continuous growth. This provides a mean temporal $\delta^{18}\text{O}_{\text{drip}}$ sampling resolution of 14.4 years (drilled at 5 mm). This condition was also observed in the Dino cave chamber characterized by irregular tall speleothems with a changeable axis.

Eleven U-Th ages: D1-N18 (6849 ± 51 a), D1-N20 (6673 ± 50 a), D1-MH1 (5469 ± 62 a), D1-MH2 (5638 ± 38 a), D1-MH3 (5614 ± 39 a), D1-MH4 (5951 ± 53 a), D1-MH5 (6150 ± 51 a), D1-MH6 (6363 ± 52 a), D1-MH7 (6502 ± 49 a), D1-MH8 (6689 ± 63 a) and D1-MH1B (5357 ± 47 a) were employed in the construction of the Age-Depth profile. During the iteration process, D1-N19 (7515 ± 53 a) was considered an outlier and was removed from the final calculation (Figure 3.18b). These results place Dino-1 stalagmite in the mid-Holocene period starting at 6856 a until 5313 a (approximately 7 to 5 ka). The values of $\delta^{18}\text{O}_{\text{cc}}$ in the record (Figure 3.18c, black curve) varied from -6.02 to $-4.53\text{\textperthousand}$ VPDB ($n=107$), with a mean of $-5.43 \pm 0.32\text{\textperthousand}$. Using the monitored temperature of the cave (Section 3.3.1.1), and the mean $\delta^{18}\text{O}_{\text{drip}}$ (Section 3.3.1.2), I proceed to calculate the recent equilibrium values on calcite deposition according to Daëron et al. (2019) considered close to equilibrium conditions:

$$10^3 \ln(^{18}\alpha_{cc/w}) = 17.57 \times 10^3 / T - 29.13 \quad (8)$$

where $T = 19.24 \text{ }^\circ\text{C}$ (292.4 K) and $\delta^{18}\text{O}_{\text{drip}} = -7.57\text{\textperthousand}$. This calculation gives us a result of $-7.3\text{\textperthousand}$ VPDB (after conversion from VSMOW to VPDB using Gonfiantini et al., 1995 formula), which is lower than the minimum value of $-6.02\text{\textperthousand}$ measured in the stalagmite. A possible explanation for this might be that the isotopic composition changed in modern climate towards more negative values, suggesting present more humid conditions. Another alternative could be that the dripwater does not represent the mean values in the cave, because mean values might be biased

towards seasons with more data. A third option might be the presence of kinetic fractionation effects, making the isotopic composition distorted or biased towards higher values than what was expected from present day equilibrium. These alternatives are further evaluated in the Discussion section (Section 4.3.1).

Regarding the spacing (Figure 3.18c, red curve), the time-series show intervals of steady calcite accumulation such as the periods from 6800-6600 a (~13 years), 6500-6200 a (~18 years) and 6000-5700 a (~27 years) which are in their majority periods of lower $\delta^{18}\text{O}_{\text{cc}}$ values (wetter episodes). On the other hand, two sharp shifts towards intervals of reduced growth are visible, and correspond to 6600-6500 a and 5700-5600 a associated with more positive $\delta^{18}\text{O}_{\text{cc}}$ values (drier episodes).

If we now turn to the evaluation of significant spectral peaks against red-noise background, I found that the Dino-1 record presents two significant peaks with a periodicity approximately of 495 and 30 years (Figure 3.18d). These values are significant at the 95 and 99% confidence level. The 30-year period is also confirmed in the Lomb-Scargle periodogram (Figure 3.18e) and the Weighted Wavelet z-Transform (Appendix B2). However, no significant peak at the 495 years was detected in the subsequent spectral analysis.

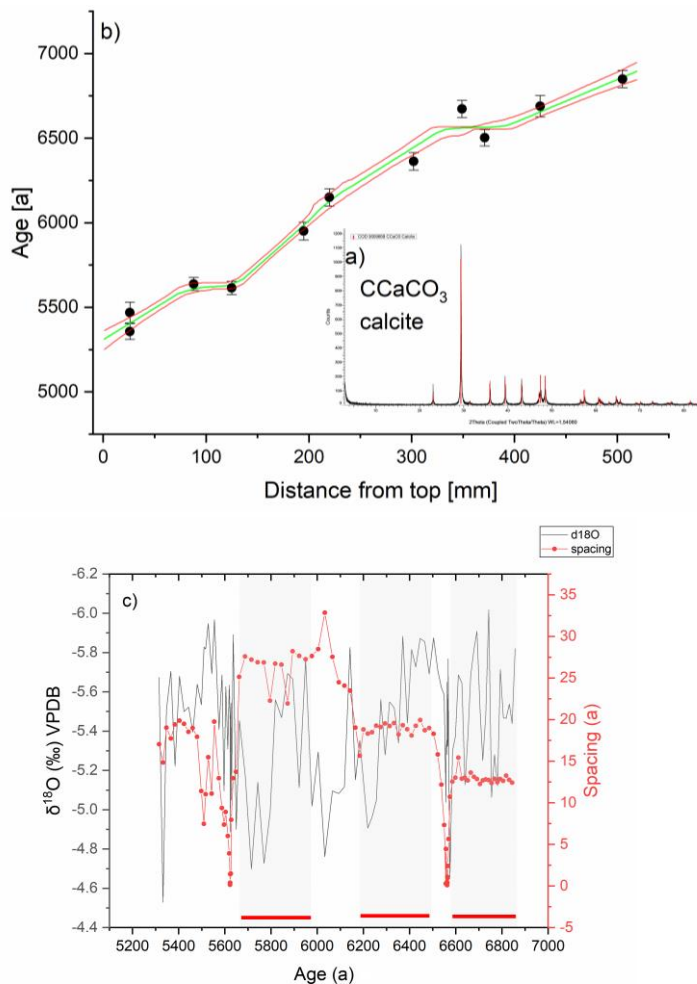


Figure 3.18 Dino-1 speleothem features **a)** XRD mineral composition in the speleothem slab showing calcite (CaCO_3) mineralogy (red peak). **b)** Age-depth model fitted for the U-Th ages dated from layers in Figure 2.6 using StalAge.

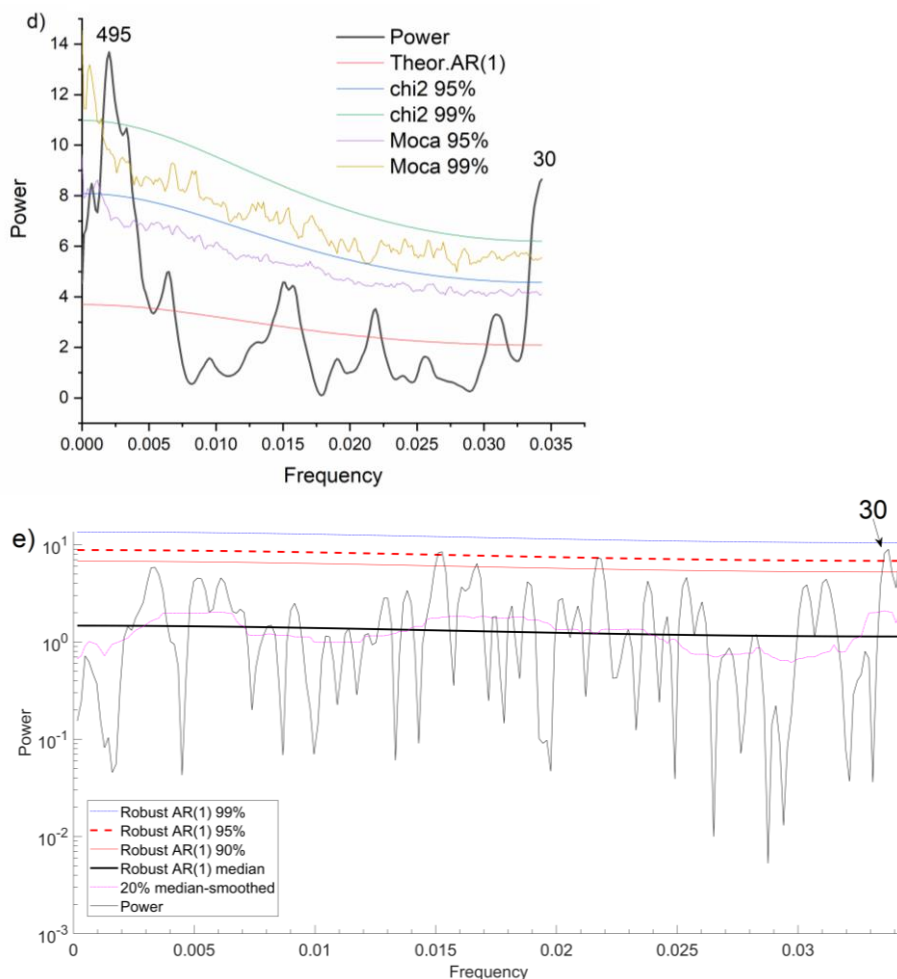


Figure 3.18 (continued) c) $\delta^{18}\text{O}_{\text{cc}}$ record from Dino cave Mera, Central Ecuador at 5 mm resolution. From bottom to top, the record covers the mid-Holocene from 6849 ± 51 to 5357 ± 47 a (1492 years). Additionally, the red curve shows the spacing time-series (accumulation rate) in the record. Lower red bars indicate periods of accumulation at near constant rate. **d)** Dino-1 spectrogram for the evaluation of spectral peaks above a red noise background. The Welch window parameters for REDFIT analysis were: oversample = 9 and segments = 3. AR(1), Chi-square (chi2) and Montecarlo (Moca) significance lines at 95 and 99% confidence are marked along with the spectrum (black line). The Power at the left-y axis corresponds to the square of the amplitude. **e)** Lomb-Scargle periodogram for Dino-1 record. The analysis was carried out after detrending using a local regression smoothing rLOESS regression.

3.3.2.2 Mid-Holocene climate

Precipitation simulations

Climate simulations of total precipitation change (%) during the mid-Holocene (6.5-5.5 ka) relative to pre-industrial period (1850 CE) reveals a progression from drier to wetter conditions in South America. Indeed, the brown areas in Figure 3.19 illustrate these differences for the austral summer period (DJF). In central and southern South America (10°N - 40°S), more humid conditions are noticeable especially over the SAMS domain. At the equatorial latitudes, the change

seems minimal at land but enhanced at the equatorial Atlantic Ocean, in the boundaries of the modern ITCZ. On the contrary, Northern Africa was most likely wetter than modern times in the monsoonal region (cyan regions)

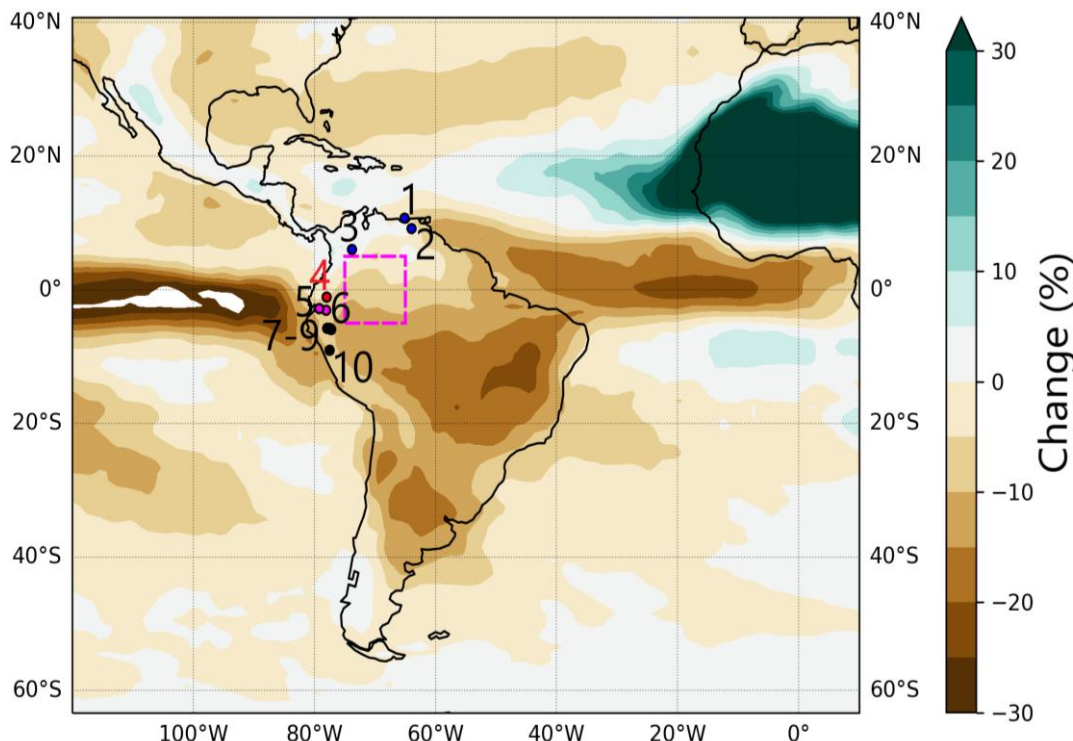


Figure 3.19 Total precipitation change during Mid-Holocene (6.5 – 5.5 ka) relative to pre-Industrial (1850 CE) precipitation during austral summer (DJF). Northern South American records are indicated by closed circles: 1-Cariaco Basin (Ven) (Haug et al., 2001); 2-Alfredo Jahn cave (Veaj; Ven) (Medina et al., 2023); 3-Caracol cave (Col) (Gelvez, 2019); 4-Dino cave (Ecu) (this study); 5-Pallcacocha lake (Ecu), (Rodbell et al., 1999); 6-Santiago cave (Ecu) (Mosblech et al., 2012); 7-Shatuca cave (Per) (Bustamante et al., 2016); 8-Condor cave (Per) (Cheng et al., 2013b); 9-Tigre cave (Per) (van Breukelen et al., 2008); 10-Huascaran glacier (Per) (Thompson et al., 2000, 1995; Thompson and Davis, 2007). Brownish color indicates dryness whereas cyan color represents wetter conditions during the mid-Holocene in reference towards pre-Industrial values. Dataset correspond to an ensemble of simulations (16 models) from the PMIP4-CMIP6 obtained through the IPCC Atlas (Douville et al., 2021).

Water isotopes in the MPI-ESM model

If I now evaluate the water isotopic values for the mid-Holocene from the MPI-ESM-wiso, a coherent variability among the records towards wetter conditions from the mid-Holocene to the pre-Industrial period is corroborated (Figure 3.20). What can be clearly seen in this figure is the dramatic decrease in $\delta^{18}\text{O}_\text{p}$ in the subtropics, especially in the monsoonal areas in Africa and Asia (blue colors, numbers 3 and 4 in Figure 3.20), signaling a wetter mid-Holocene than the drier pre-Industrial. Conversely, South America shows patches of more positive isotopic areas at the North, the Andes and the central-southern part of the SAMS region (number 2 in Figure 3.20), suggesting drier conditions in the mid-Holocene compared to the

more humid pre-industrial. Interestingly, the V-index region also shows a more humid pattern than at mid-Holocene. Northeastern Brazil seems to have an opposite trend, but this is consistent with the literature of the existence of a climate dipole in South America (Cheng et al., 2013b; Cruz et al., 2009).

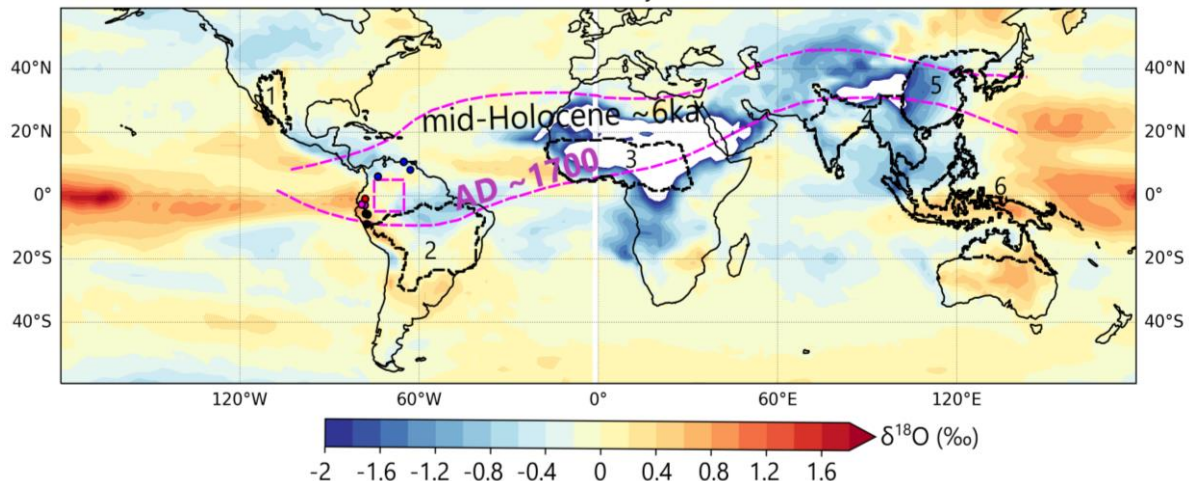


Figure 3.20 Global difference between mid-Holocene (6 ka) and pre-Industrial period (1850 CE) using the simulated water isotopes by the MPI-ESM-wiso (Cauquoin et al., 2019). The mean ITCZ boundaries for the mid-Holocene and pre-Industrial (AD ~1700) obtained from Wanner et al. (2008) (magenta dashed lines). The V-index region is indicated by the magenta box. Numbers from 1 to 6 are monsoonal areas: 1-North American Monsoon, 2-South American Monsoon, 3-West African Monsoon, 4-South and Southeast Asian Monsoon, 5-East Asian Monsoon, 6-Australian and Maritime Continent Monsoon. The location of the records is identical to Figure 3.19.

Holocene regional paleoclimate records

The insolation in the early to mid-Holocene (10-4 ka) in northern South America (10°N-10°S) shows a steady increase from ~390 to 410 W m⁻² (Figure 3.21a). The Venezuelan records (i.e., Cariaco and Veaj; Figure 3.21b-c) does not show a synchronic trend. Cariaco shows a clear tendency towards dryness (low Ti % due to less runoff material), whereas Veaj speleothem record only shows clear trends to dryness in the period ~6 to 5.2 ka, and then after 5.2 ka resumes the upward trend. What is striking about the Figure 3.21d-i, is that the rest of South American records located in Colombia, Ecuador and Peru covering the same period show comparable trends towards more humid conditions, observed by the linear trend towards more negative $\delta^{18}\text{O}$ values in the speleothems and Huascaran glacier record. Nonetheless, the Dino-1 linear trend towards more humid conditions (Figure 3.21f) is not able to capture the high variability of the record, noted by the small dependence from previous values based on Lag-1 scatterplot (Appendix B-2). To put it succinctly, there is no tendency of the values to cluster along the line, meaning that current values do not follow previous values (low serial dependence). In addition, the short length of the Dino-1 record makes it difficult to determine if the record has a more humid trend from early to mid-Holocene.

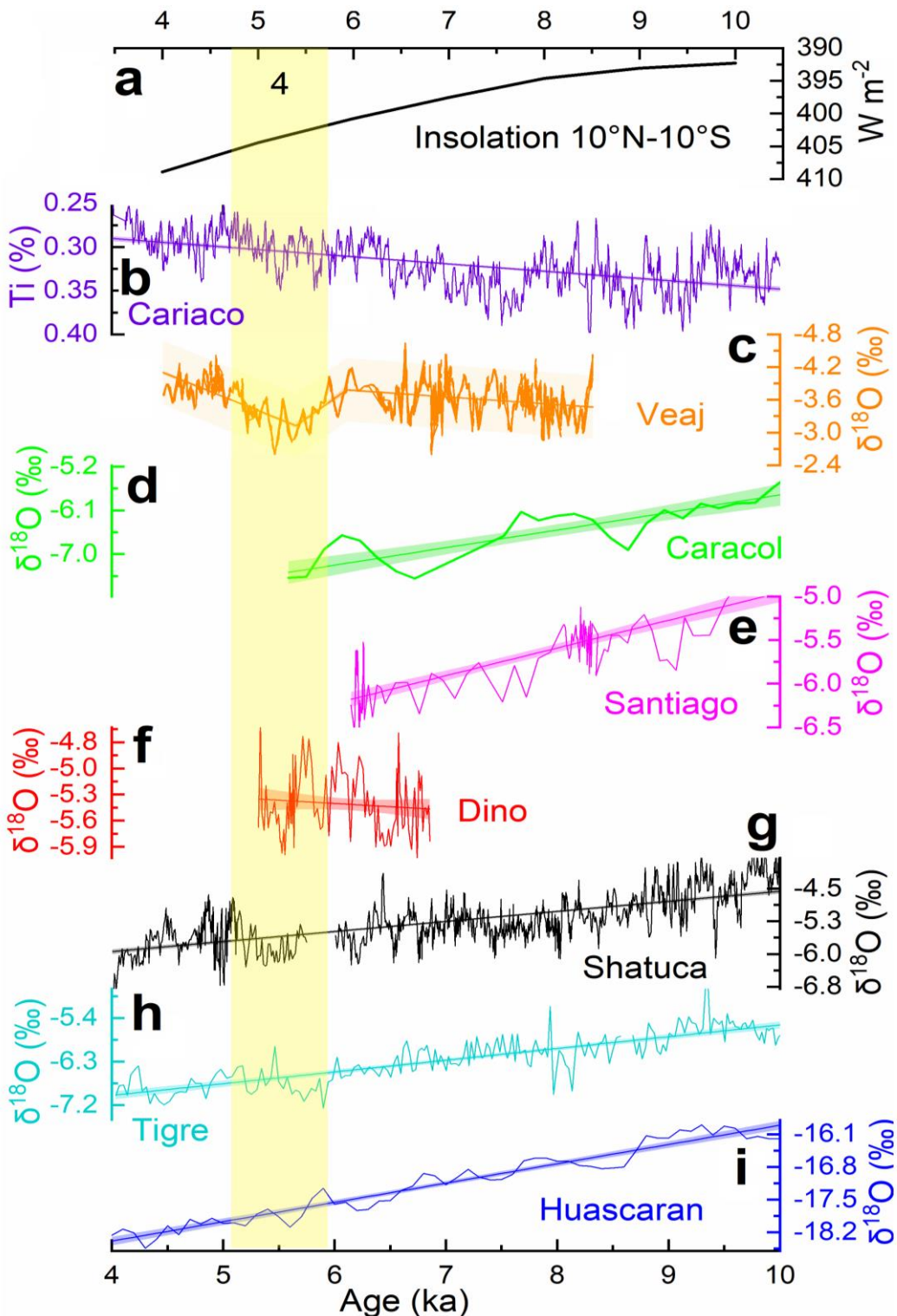


Figure 3.21 Holocene insolation and raw paleoclimate records in Northern South America from Figure 3.19. **a)** Summer (DJF) insolation at 10°N - 10°S (Laskar et al., 2004) **b)** Cariaco Basin (Ven); **c)** Alfredo Jahn cave (Veaj; Ven); **d)** Caracol cave (Col); **e)** Santiago cave (Ecu); **f)** Dino cave (Ecu, this study); **g)** Shatuca cave (Per); **h)** Tigre cave (Per); **i)** Huascaran glacier (Per). The y-axis in a), b) and c) are shifted for visualization. In all the records, the shaded area parallel to the linear trend corresponds to the 95% confidence interval. The vertical yellow shading shows periods of anomalous increase in $\delta^{18}\text{O}$ values (see in depth discussion in section 4.3.3).

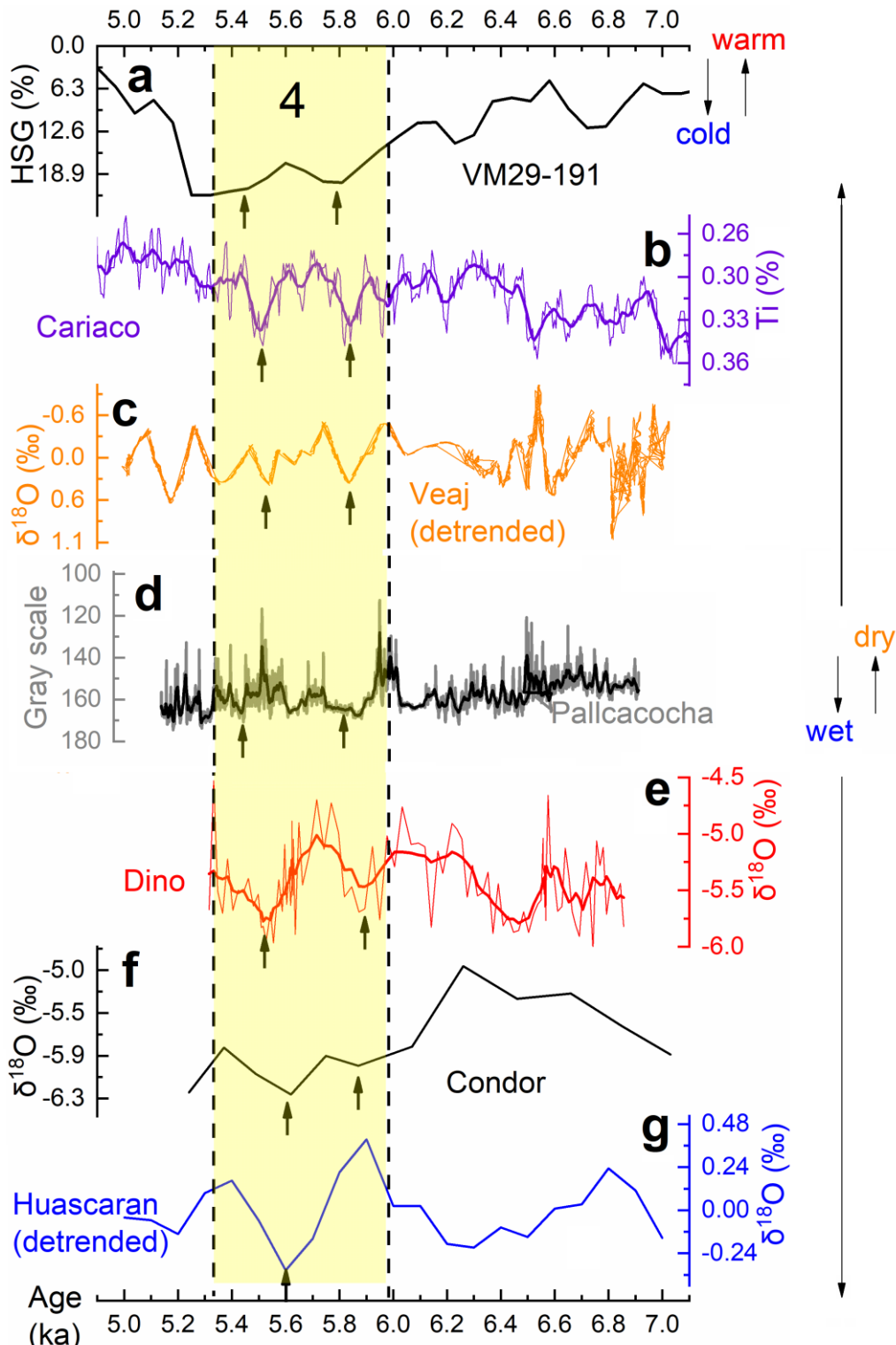


Figure 3.22 Comparison of mid-Holocene records spanning the period 7 to 5 ka: **a**) VM29-191 ice-rafter debris (hematite-stained grains HSG) as proxy for Bond events (Bond et al., 2001); **b**) Cariaco basin (Ven); **c**) Alfredo Jahn cave (Veaj; Ven); **d**) Pallcacocha lake sediment (Ecu) (Rodbell et al., 1999); **e**) Dino cave (Ecu, this study); **f**) Condor cave (Per); **g**) Huascaran glacier (Per). The c) Veaj and g) Huascaran records were detrended using a rLOESS regression. A 3, 5 and 10-year Moving average was fitted to e) Dino, b) Cariaco and d) Pallcacocha records. The strong cold event (drift ice input, Bond 4) is highlighted by the yellow shading, and the anomalous shift in values within by the black arrows.

Focusing on the time span between 5 to 7 ka, what emerges from the visual inspection of Dino-1 speleothem record is the rapid decrease in $\delta^{18}\text{O}_{\text{cc}}$ values at ~ 6.5 ka, and twice between the period 6-5 ka (Figure 3.22). Expanding the visual analysis to the other records displayed in Figure 3.19 reveals a common pulse towards wetter conditions (low $\delta^{18}\text{O}$, higher gray scale and Ti content), apparently responding to the cold Bond 4 event in the North Atlantic Ocean. This is a significant outcome, especially because the forcing is observed on the different archives (speleothems, lake sediment and ice cap), and the event has not been previously described to affect the western part of South America during the mid-Holocene. Overall, the presented results from climate models and records present a coherent and robust signal indicating more wetter condition at the mid-Holocene than at its onset (10 ka).

CHAPTER 4

DISCUSSION

4.1 Rainwater stable isotopes

4.1.1 Local temperature and precipitation amount

Our monitoring campaign showed a substantial difference between the monitored temperature and the registered at the Puyo and Shell stations. A possible explanation for this seems to be related to their location (Figures 2.1a and 2.2a). For instance, the Shell station is located at the Rio Amazonas airport, where the potential urban heat island effect might play a role and influence the measurements. Nevertheless, the temperature seasonal variation is coherent among the records and might be related to the solar insolation having peaks during Vernal and Autumnal equinoxes (Mar 20 and Sep 22). Conversely, the approximately 1 °C decrease in our monitoring during July-August could be attributed to the June solstice, where the Mera site receives the lowest insolation (<400 W m⁻²) compared to the equinoxes (>430 W m⁻²). This might explain the distinctive “V” pattern observed in the instrumental, reanalysis, and monitored temperature in Figure 3.15d. On the contrary, the hourly temperature data observed in Figure 3.15a-c showed higher variability, fluctuating from 15 to over 40 °C in a few hours. These results are likely to reflect the normal high diurnal variations in temperature, characteristic of tropical climates (Hastenrath, 1991).

The results from our monitoring campaign are consistent with the obtained by Jiménez-Iñiguez et al. (2022). The authors also carried out a monitoring work (April 2019-February 2020) at Jumandy cave (location in Figure 1.11c), a location with similar settings to Mera (same Napo formation). Ambient temperature and precipitation amount data were collected in the cave site at the eastern slope of the Andes, allowing a direct comparison and independent validation to our findings. Similar to our results, they showed a low correlation between the local air temperature ($r = -0.02$, $p < 0.05$) and the most depleted $\delta^{18}\text{O}_p$ were measured during Mar-Jun and Oct-Dec ($r = -0.39$, $p < 0.05$), coinciding with our findings and highlighting the key role that rainout upstream plays. This low correlation between local precipitation and $\delta^{18}\text{O}_p$ can be partly explained by the location of both sites, being a transition zone between the Amazon lowlands and the Andes cordillera (Figure 1.11c). The high development of clouds at the eastern Andean slope has been reported in the literature due to the barrage effect that the Andes play against incoming northeasterlies (Bendix et al., 2006, Figure 3.2). The Andes' interaction with prevailing wind flow triggers convection and the development of rapidly organized convective storms called Mesoscale convective systems (Campozano et al., 2018). This continuous input of convective cloudiness significantly increases the precipitation at the

eastern Andean slopes and Amazon foothills, altering the correlation with the locally monitored $\delta^{18}\text{O}_\text{p}$ at the sites.

4.1.2 Altitude effect

As discussed in the previous section, this study could not demonstrate a direct relationship between the rainwater stable isotopic composition and air temperature. Nevertheless, this link exists indirectly through the presence of the Andes, where isotopic moisture values from the Amazon lowlands might differ towards the Andes. Indeed, the calculated annually averaged $-0.15\text{\textperthousand}$ per 100 m (Figure 3.4) is in good agreement with the previous $-0.17\text{\textperthousand}$ shown in two latitudinal transects in Ecuador (Garcia et al., 1998) and the $-0.22\text{\textperthousand}$ per 100 m in a southern tropical montane forest during September to December 2010 in the country (Windhorst et al., 2013). Consequently, topographic relief plays a vital role in the spatial variability of $\delta^{18}\text{O}_\text{p}$, particularly at montane sites (Gonfiantini et al., 2001) (Figure 3.4b).

4.1.3 Low Level-Jets (LLJs)

The back trajectories of Figures 3.2a and 3.2e indicated that during austral summer (DJFM), there is a characteristic flow from the TNA, which crosses northern South America from east to west. This fast-flowing flow is likely related to the Orinoco LLJ, a low-level nocturnal wind occurring during austral summer at 950-800 hPa with mean wind speeds of 8 m s^{-1} over Colombia and Venezuela (Jiménez-Sánchez et al., 2020) (Figure 1.9a). It has been recently reported that the Orinoco LLJ influences the northeastern part of Ecuador (jet exit region) based on the transport of air pollutants moving from the Orinoco river basin towards Ecuador (Bendix and Lauer, 1992; Rodríguez-Gómez et al., 2021). On the other hand, the water vapor moving from the South Pacific in the same season corresponds to the cold Humboldt current, characteristic of the wind system at the coast (Emck, 2007; Makowski Giannoni et al., 2016). The other distinctive moisture pattern observed in the trajectories is the flow crossing the Amazon basin, onsetting at the TSA during austral autumn (MAM; Figures 3.2b,f, and 1.9b). This equatorial Amazon flow could be attributed to the equatorial mid-tropospheric easterly jet (EMTEJ). The EMTEJ is an easterly jet at 700-600 hPa ($\sim 3000\text{-}4000 \text{ m a.s.l.}$) centered on the equator with a maximum wind speed of 10 m s^{-1} from March to August that travels from the Atlantic Ocean to the Andes and is weakened during ENSO years (Poveda et al., 2014; Poveda and Mesa, 1999). The EMTEJ has been reported by Hastenrath (1999) along the eastern equatorial Pacific using upper-wind radiosoundings measurements over Galapagos (1967-1971). Similarly, Poveda et al. (2014) and Poveda and Mesa (1999) have also described the occurrence of the EMTEJ over the continent. Indeed, the trajectories during austral winter (JJA) are characterized by easterly paths crossing the Amazon basin from east to west, where northeasterly paths have minimal influence. The EMTEJ dynamics are stronger, and most of the uptake moisture at the Mera site has an

eastern and southeastern provenance (Figure 3.2c and 3.2g). In general, the Orinoco and EMTEJ are the primary LLJs involved in transporting moisture converging at the V-Index region (Figure 1.9) with direct influence over the Ecuadorian territory.

4.1.4 V-index and monsoon trough

An initial objective of this dissertation was to identify the primary rainfall system influencing the Ecuadorian Andes and Amazon. From the previous discussion and as shown in section 3.1, the V-index region identified by decomposing the OLR into its three main EOF modes (Figure 3.1) reveals that this is a highly convective region ($\text{OLR} < 240 \text{ W m}^{-2}$; Figure 3.11). Convection occurs when a fluid under gravity is heated rapidly from below or cooled from the top. Therefore, molecular diffusion cannot redistribute the altered density field fast enough to maintain the equilibrium, bringing about buoyancy (Houze, 1997). In other words, convection is the vertical transport of heat and moisture occurring by temperature fluctuations triggering density differences and stabilizing the atmosphere (Houze, 1997; North et al., 2014). This process usually produce cumulonimbus clouds whose precipitation is partly convective and partly stratiform (Houze, 1997). In fact, the physical interpretation of the V-index region given by Garcia and Kayano (2010) is that it represents convection occurring during the transition seasons from dry to wet and vice-versa in the western equatorial Amazon. Similarly, the close resemblance with the $\delta^{18}\text{O}_\text{p}$ is due to its particular location, entirely on the path of moisture-laden trade winds receiving the flow from their confluence and capturing the interhemispheric hydrology (Figure 3.2). This framework adequately explains the typical $\delta^{18}\text{O}_\text{p}$ seasonality in Ecuadorian Amazon and Andes, pointing to a common regional controller imprinting the observed "W" shape pattern, with the yearly two peaks (DJFM, JAS) and drops (AMJ, ON) in $\delta^{18}\text{O}_\text{p}$ independently of the amount of precipitation (Figure 1.10; Table 3). Another independent confirmation of the V-index as a regional hydrological center emerges by looking at the "Aerial lake" concept over the Amazon, a new framework for considering large-scale moisture transport proposed by Arraut et al. (2012) (see their Figure 3). Aerial lakes are sections of moisture pathways where the flow slows down and broadens, due to diffusione, presenting a high amount of precipitable water. This latter is clearly visible in Figure 4.1, where higher precipitable water values are observed in MAM, ON, and shifted southwards in DJF at the SAMS region. Conversely, the lowest values are registered in JJA. This aerial lake of moisture is most profound in the west (V-Index region). It plays a vital role as a reservoir distributing moisture toward Central America in the dry season (JJA) and towards the South American subtropics in the wet (DJF), following the cross-equatorial southerly and northerly flows developed during the ITCZ excursions.

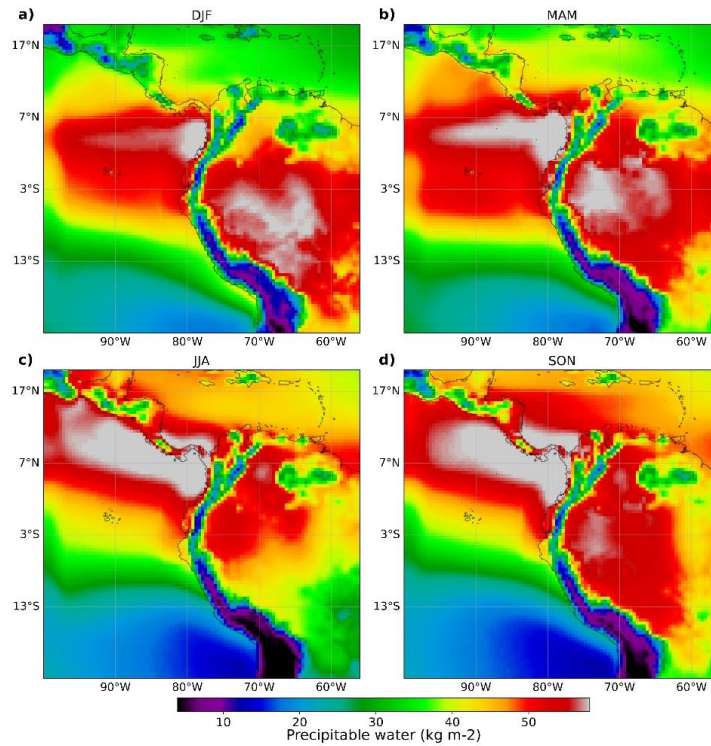


Figure 4.1. Precipitable water from a WRF simulation for 18Z (1 p.m. Ecuador continental time) with a horizontal resolution of 50 km over northern South America for austral: **a)** summer, **b)** autumn, **c)** winter, **d)** spring.

These findings raise intriguing questions regarding the nature and extent of the V-index region, which can be completed by looking at our findings. First, the coexistence of northeast and southeast flows (TNA and TSA) during the transition between seasons (DJF-MAM and SON-DJF; Figure 3.2). Second is the significant and in phase correlation between $\delta^{18}\text{OTR}$ and rainfall from March to June (Figure 3.11c-d). Third, the seasonal movement of convection (OLR) from southeast to northwest (Figure 3.11e) and its increase in convection in April and October. Fourth, the consistency between the ECHAM5 and our monitored monthly $\delta^{18}\text{O}_p$ ($n=48$) (Figures 3.5 and 3.7) shows that the lowest $\delta^{18}\text{O}_p$ values occur during austral autumn and spring (AMJ, ON).

In all of these results, there is a constant overlap of months where the demise of one system is the onset of the other at the V-index region. Specifically, the SAMS demise in March follows the ITCZ onset, and the other way around, the ITCZ southward excursion from Central America in October triggers the beginning of the SAMZ. Hence, it could conceivably be hypothesized that a clear demarcation of both rainfall systems at the equator is complex, and this region should be considered a transition area. Therefore, these findings are consistent with those of Wang et al. (2017), who have meteorologically defined this transition area as a Monsoon trough. The origin of the term comes from the more detailed classification of the ITCZ into two types: monsoon trough and trade wind

convergence zone (Ramage, 1971; Wang et al., 2017). The section of the ITCZ embedded in the monsoon trough shows larger meridional migrations of precipitation and reversal of the winds (Wang and Fu, 2002; Wang et al., 2017), as previously revealed in Figures 1.2 and 1.9, and is now summarized in Figure 4.2. On the contrary, the ITCZ trade wind regions span the oceans and present small annual latitudinal displacement with a lack of change in the wind direction and the absence of the monsoon (Wang et al., 2017).

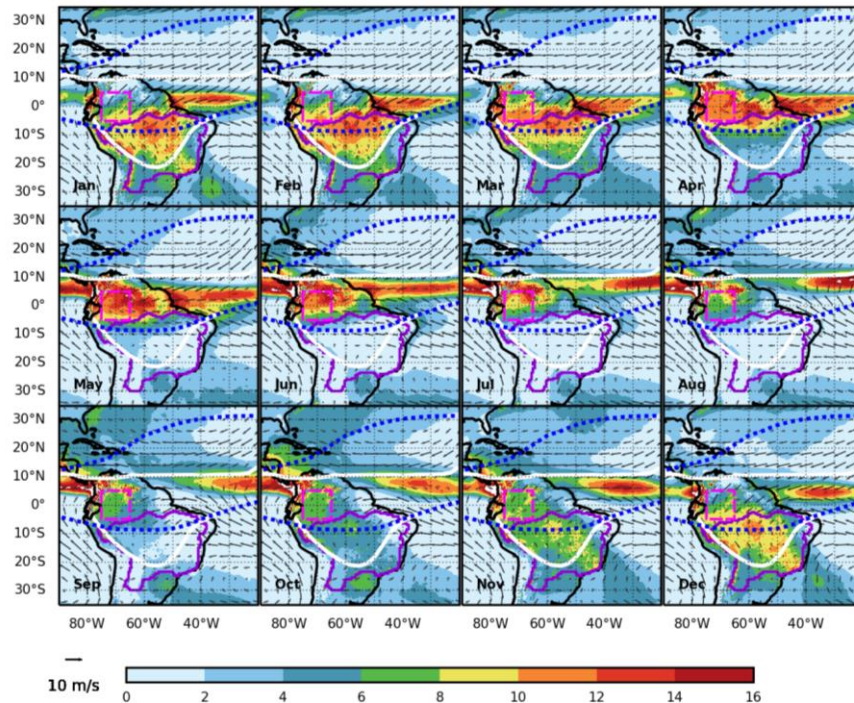


Figure 4.2. Monthly variation of total precipitation (ERA5 1959–2021; mm day⁻¹) in South America, along with its wind speed (black arrows). Similar to previous plots, the V-index region is drawn by the magenta dashed squared at the equator. The white dashed line indicates the modern ITCZ boundaries, whereas the blue dashed line reveals the mid-Holocene (top) and pre-Industrial (bottom) positions in the continent (similar to Figure 3.20). For the past and recent ITCZ boundaries, the V-index region is embedded in the Monsoon trough.

Addressing this V-index region as a monsoon trough that harbors South America's two chief rainfall systems (i.e., ITCZ and SAMS) is twofold. First, it may help us to understand and reconcile the idea of having LLJs (Orinoco, EMTEJ) within the ITCZ borders. Secondly, it supports the concept that the two systems are not separated but interconnected, allowing the transport of moisture from the TNA to the La Plata river basin (Garreaud et al., 2009; Raia and Cavalcanti, 2008; Rojas et al., 2016; Zhou and Lau, 1998). Various studies have assessed the efficacy of the OLR for identifying areas of strong convection in South America, which showed to be strongly correlated with $\delta^{18}\text{O}_\text{p}$ (Villacís et al., 2008; Vimeux et al., 2005). However, this methodology seems

inadequate for Ecuador due to the short $\delta^{18}\text{O}_p$ available records (Table 3), low sampling frequency (e.g., monthly), and the coarse resolution of the OLR products. Moreover, this last method brings spatially extended correlations, especially over the Atlantic ocean, where surface heating becomes insignificant (Matsumoto and Murakami, 2000) (not shown). On the contrary, the $\delta^{18}\text{O}_p$ relationship in the Monsoon through, spatially constrained at the V-Index region, is a more robust approach that avoids potential spurious correlations (Figures 3.5 and 3.6).

4.2 Modern climate (centennial-scale)

4.2.1 *Cedrela nebulosa* growth

Studies on dendroclimatology in Ecuador are scarce. The available literature has focused on dry forests and their possible teleconnections with ENSO, especially in the south of the country (Pucha-Cofrep et al., 2015; Figure 1.11a). Previous studies employing the genus *Cedrela* have been carried out mainly with *C. odorata* (Nacimba, 2015) and *C. montana* (Baker, 2017; Volland et al., 2015). For *C. nebulosa*, this study is the first investigation that addresses its dendroclimatic potential in Ecuador in a pre-montane forest and the second in South America. Prior research using *C. nebulosa* was recently conducted in the montane Andean forest of Peru in the Junin Department (Layme-Huaman et al., 2018) and served as a reference to compare some of our findings. The Mera TRW chronology (1860-2019) shows a low EPS of 0.46 due to the small sample replication of individuals before 1920 (Figure 3.9). The period from 1960 to 2019 covers the largest number of trees and provides a significant increment in EPS to 0.65, but still lower when compared to the *C. nebulosa* in the Peruvian Andes, which gave an EPS of 0.91 (23 series-13 trees) (Layme-Huaman et al., 2018). A similar situation of a less than 0.85 EPS threshold was recently encountered in another newly constructed chronology from a tropical montane forest in Cajas National Park, Ecuador using *Polylepis reticulata* (Figure 1.11a). The EPS values above 0.85 in the chronologies (1821-2015) were reached only after 1990 (Alvites et al., 2019), suggesting that only ~14% of the constructed chronology satisfied the established 0.85 cut-off. Hence, this only illustrates that low EPS values can be expected principally due to the lack of long-lived individuals when employing a new species in tropical dendrochronology. In my case, despite field exploration efforts (Appendix A.1), I only found a few long-lived *C. nebulosa* trees, which overall has contributed to a low sample replication and a subsequent low EPS in the final TRW chronology.

In general, the EPS estimates the variance fraction of an infinite hypothetical population expressed by the chronology, and a general 0.85 in EPS is considered a robust chronology for climate studies (Wigley et al., 1984). Nevertheless, there is an ongoing debate about applying EPS to evaluate the suitability of tree-ring data for climate reconstruction purposes. The assigned 0.85 threshold originally appeared as an example

of another statistical parameter used for dendrochronological studies (Subsample Signal Strength) and is advised not to be taken as a rule for accepting or rejecting chronologies (Buras, 2017; Wigley et al., 1984). Although this low EPS value might affect the local strength of the correlations obtained between TRW and local climate parameters, this shortcoming affected neither the results nor the main conclusions of this study, mainly based on the use of oxygen and carbon stable isotopes. However, this does not mean that the dendrochronological part was undertaken lightly. On the contrary, a proper tree-ring delimitation and cross-dating were successfully achieved by two independent and complementary tools, wood anatomy and radiocarbon (Figure 3.8), accomplishing this initial task before undertaking subsequent isotopic analysis in the tree-rings (van der Sleen et al., 2017). A caveat in the constructed $\delta^{18}\text{O}_{\text{TR}}$ and $\delta^{13}\text{C}_{\text{TR}}$ is the low number of samples from 1864-1920. In fact, the chronologies were built with only one core from 1864 to 1909. Two cores conformed the period 1910-1920 (gray time-series in Figures 3.10c and e). Hence, the synchronized uptick in trend in both records captured by the piecewise regressions (ramp and break) is not robust and should be taken with caution when interpreting them during this period (1864-1920). The chronologies are more robust from 1921 to the end.

Annual validation of growth rings in tropical trees is not always straightforward. Despite the extensive evidence of annual ring formation in *Cedrela*, there is an indication that this genus may form more than one ring per year, especially in aseasonal climates (Baker et al., 2017). Hence, independent confirmation of the annual periodicity at a new site is always advisable at tropical latitudes, as was carried out in this dissertation (Appendix A.3). Concerning the *C. nebulosa* tree-phenology, it goes from Jan/Feb to Aug/Sep, encompassing the wettest (Apr-Jun) and less-wet (Jul-Sep) months at this latitude (Figure 2.3). These results match those observed in early studies in *Cedrela* in Central Amazon, which indicates that cambial growth is determined by the change from wet to dry season (Dünisch et al., 2002). In addition, this study supports evidence from previous observations in Ecuador using *C. montana* and *C. odorata* (Bendix et al., 2006a; Nacimba, 2015), who found that Cedrela trees were leafless from October to December/January (austral spring-summer).

4.2.2 Tree-ring oxygen isotopes and western Amazonian precipitation

The Mera $\delta^{18}\text{O}_{\text{TR}}$ record presents a ~14 years period observed in Figure 3.10d. This spectral peak likely corresponds to the pan-Atlantic decadal oscillation and corresponds to zonal bands of SST and wind anomalies (pulses) between the extratropical and tropical Atlantic (Mélice and Roucou, 1998; Xie and Tanimoto, 1998). In fact, Mélice and Roucou (1998) found similar periodicity in the Quelccaya glacier in Peru (~850 km South of Huascaran in Figure 3.19). The same climate dynamics apply to our record and the Peruvian glacier. There is an elicit water moisture advection during the rainy season from the TNA by northeast winds and precipitates at their respective

locations. This process is facilitated by the LLJs, starting with Orinoco, which feeds the South American LLJ and preserves its TNA isotopic signature (Garreaud and Aceituno, 2007; Jones and Carvalho, 2018; Veblen et al., 2015).

The $\delta^{18}\text{O}_{\text{TR}}$ record was not significantly correlated with local precipitation values. However, it gave better results comparing it with the rainfall at the monsoon trough region (V-index) at the western Amazon, capturing most of the interdecadal variability during the primary wet season (March to June) and showing an anticorrelation between $\delta^{18}\text{O}_{\text{TR}}$ with the rainfall in the zone (Figure 3.11). This robust relationship is consistent with previous observations indicating that rainout upstream in convective areas better explains the seasonal variations in $\delta^{18}\text{O}_{\text{p}}$ (Villacís et al., 2008; Vimeux et al., 2005). This isotope-climate relationship is characteristic of tropical precipitation, which is highly convective at low latitudes (Hastenrath, 1997; Kurita et al., 2009). Another important finding is the marked period of 4 to 8 years in the wavelet coherence analysis between the $\delta^{18}\text{O}_{\text{TR}}$ and western Amazon rainfall records (Figure 3.11c). These results are most likely related to variations in Sea Surface Temperature (SST) in the TNA, which is the primary moisture source to the continent and is responsible for the seasonal displacement of the ITCZ (Figure 3.7) (Baker, 2017; Yoon and Zeng, 2010). Although ENSO has a similar periodicity (3-7) years, a recent regionalization of precipitation in Ecuador showed a minor influence on our site (Ilbay-Yupa et al., 2021). In the same spectrum, the 0-4 years and short 16 years period (out of the cone of influence) might arise due to the low resolution of both the $\delta^{18}\text{O}_{\text{TR}}$ record and coarse-gridded CRU precipitation dataset. Finally, the 32 years periodicity requires further detailed investigation, as it might result from instationary couple mechanisms arising from a variety of physical phenomena (e.g., changes in pressure, temperature) (Maraun and Kurths, 2004).

In general, therefore, it seems that *C. nebulosa* tree-ring oxygen values are a good proxy for the western Amazon wettest rainfall season (Mar-Jun), responding to a convective regional hydroclimate process regulated by the ITCZ at the Monsoon trough. A note of caution is due here since other plant physiological effects may alter the isotopic signal of precipitation before its final fixation in the wood (i.e., leaf water enrichment) (Treydte et al., 2014). Nevertheless, our findings suggest that the $\delta^{18}\text{O}_{\text{TR}}$ variability is chiefly determined by those of meteoric rainwater. Previous studies on *Cedrela odorata* in Bolivia have shown that this genus has a superficial root-system, and water is uptake from the topsoil layer (Brienen et al., 2012). Furthermore, the leaf water enrichment effect is low as atmospheric humidity is high during most of the year in the Mera site (86% average: 1965-2018), reducing the transpiration rate. The general agreement in the long-term trend between the local independent archives (Cuyuja tree-ring and Chimborazo glacier; Figure 3.12) reveals something about the systematic preservation of the oxygen isotopic signal. Brienen et al. (2012) indicated that tree-rings preserve the signal of oxygen isotopes during the wet season, with a weaker influence on the temperature in Bolivia. In a follow-up study, Baker (2017) compared the strength of the

$\delta^{18}\text{O}_{\text{TR}}$ signal from *C. montana* trees in Cuyuja (Ecu, Figure 1.11a), and *C. odorata* forests (Bol) from Purisima (11.40°S, 68.72°W, 170 m a.s.l.), Selva Negra (10.10°S, 66.31°W, 160 m a.s.l.), and El Tigre (10.98°S, 65.72°W, 165 m a.s.l.) forests. The results showed that the Ecuadorian and Bolivian $\delta^{18}\text{O}_{\text{TR}}$ chronologies correlated well with each other despite their altitude and distance (~1500 km), showing that a similar mechanism of water-vapor transport controls their isotopic imprint. Along the same lines, the Orinoco and EMTEJ LLJs seem to be the wind corridors carrying the atmospheric moisture towards the Ecuadorian Andes and Amazon from the TNA and TSA to the Cuyuja, Mera and Chimborazo sites.

4.2.3 Tree-ring carbon isotopes and the role of cloud cover

The cloud cover seasonality is strongly associated with the movement of the ITCZ and therefore mirrors the reduction in rainfall during austral winter (JAS) observed in Figure 3.14. Indeed, Bendix et al. (2006) found that the seasonal cycle of cloudiness was significantly correlated with the spatial occurrence of the rainy seasons in Ecuador. Based on our analysis in Figures 4.1 and 4.2, it is evident that July to September are the months with a significant decrease in the amount of precipitation (and precipitable water), suggesting that deep organized tropical convection and cloud cover is reduced (“M-shape” in Figure 3.14a) owing to the northernmost position of the ITCZ in these months (Garcia et al., 1998; Hastenrath, 1997; Managave and Ramesh, 2012). Cloud cover and sunshine duration are strongly anticorrelated ($r = -0.89$, Figure 3.14a). Lower cloudiness reduces albedo but increases sunshine duration, enhancing the photosynthetic rate during the less-wet season from July to September. Higher cloud fraction in the wet season absorbs Photosynthetically Active Radiation, affecting photosynthesis and flowering (Bendix et al., 2008; Günter et al., 2008). Flowering and fruit production are synchronized with drought periods and sunny conditions and are indicators of reduced cloud cover percentage. Therefore, this may also be the case for *C. nebulosa* trees. Prior studies on *Cedrela* and field observations confirm that fruiting starts during the season of lower precipitation (Aug-Sep) (Nacimba, 2015; Pennington and Muellner, 2010), where sunshine duration contrasts with low cloud cover (Figure 3.14a). Several reports have shown that *C. montana*, which shares part of *C. nebulosa* geographical range and occupies a similar ecological niche (Pennington and Muellner, 2010), can be considered a light-demanding species (Bräuning et al., 2008). These findings show that lower precipitations from July until September enhance the rate of photosynthesis, where the photosynthetic rate (increasing temperature, higher photon flux/low cloud cover) outweighs stomatal conductance (lower relative humidity and soil moisture lead by precipitation). This results in a decrease in the internal concentration of CO₂ and a more significant proportion of atmospheric ¹³CO₂ (during CO₂ assimilation) moving through the pathway as carbohydrates, then being transported to the cambium to be finally incorporated into the wood (Gagen et al., 2011; van der Sleen et al., 2017). Therefore, I

interpret the $\delta^{13}\text{C}_{\text{TR}}$ as a rise in photosynthetic rate during the less-wet season (Jul-Sep) characterized by higher sunshine duration (>300 hours month $^{-1}$ / 10 hours day $^{-1}$), regulated by cloud amount and ultimately driven by ITCZ excursions (Figure 3.10e). Admittedly, the ITCZ dynamics in November involve another second rainfall maxima, but it has a lower intensity. I assume this does not significantly influence the $\delta^{13}\text{C}_{\text{TR}}$ because this peak does not occur during the growing season of Jan/Feb-September, but during the dormancy period in Oct-Dec/Jan (Figure 2.3). Although I acknowledge the potential of having a signal for the entire year in tropical trees because growth does not necessarily cease (Gagen et al., 2011), the synchronous shifts in the meteorological parameters are especially predominant and stronger during July-September, and *C. nebulosa* trees are actively synchronized with them.

4.3 Mid-Holocene climate (millennial-scale)

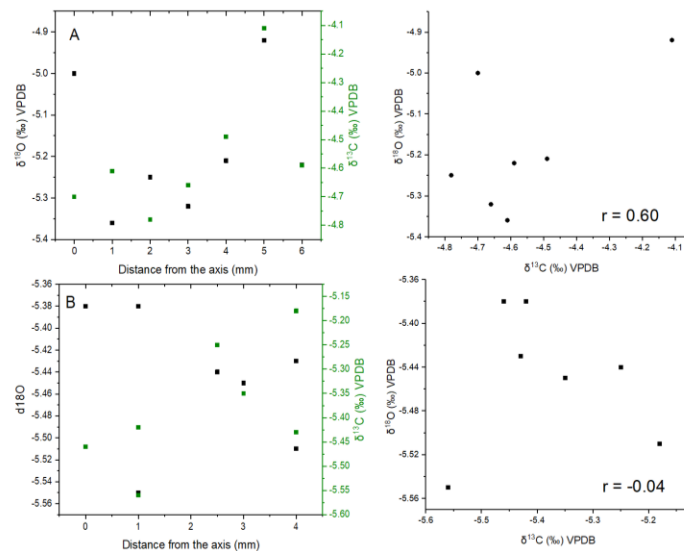
4.3.1 $\delta^{18}\text{O}$ values in the cave system

Carbonate rocks and high precipitation levels have led to the ubiquitous formation of karstic caves in the Ecuadorian Amazon representing 5 to 10% of the country's total surface, although most of it is still unexplored (Constantin et al., 2019). In this tropical karst, the dissolution process is very aggressive and contributes to the caves' short life cycle and length (Constantin et al., 2019; Toulkeridis et al., 2015). One of the most developed karst landscapes corresponds to the Napo Formation in Central Ecuador, where the limestone is frequently fossiliferous and typically presents shells and or large ammonites (Chamba Vásquez, 2020; Constantin et al., 2019). Surprisingly, despite having vast karst areas extending the whole western Amazon region, only one speleothem record has been studied from southeastern Ecuador and corresponds to the Santiago cave (Figure 1.11c) (Mosblech et al., 2012). Although the composite record was precisely dated, the study lacks cave monitoring to support the interpretation of the isotopic signal in the speleothem. In fact, very little was found in the literature on the question of $\delta^{18}\text{O}$ values of cave drip waters in the Ecuadorian karst systems. The first monitoring of $\delta^{18}\text{O}_{\text{drip}}$ in Ecuador comes from Jumandy cave in north-central Ecuador (Figure 1.11c) (Jiménez-Iñiguez et al., 2022). The authors, after 10-month monitoring, concluded that the system has an Atlantic signal whose infiltrated rainwater resides nearly three weeks in the epikarst. The dripping rate obeys the cave morphology, but the $\delta^{18}\text{O}_{\text{drip}}$ signature reflects the mixing of short-term individual rainfall events buffered within the karst system giving a lagged common signal. Our point-event $\delta^{18}\text{O}_{\text{drip}}$ monitoring ($n=50$ without outliers; Figure 3.17), although not evenly spaced, seem to indicate different but short residence times with some evaporative effect controlled by the characteristics of the local epikarst system for Copa, Union and Dino caves. This is concluded based on the close display of values following the monthly precipitation trend (Figure 3.17b).

In particular, the monitored temperature values showed minimal fluctuations at Dino cave. The temperature inside the chamber remained stable during the 48-month observation period, with an average value of 19.24 °C suggesting poorly ventilated conditions in this sampled-monitored chamber. The annual relative humidity is high in the area (average 85%; Appendix B.3). There is also continuous rainfall input, with no dry season *per se* (Figure 3.3b). Therefore, these statements offer a good basis for assuming vapor saturation in the cave with little evaporation of dripwater, maximizing the chances of signal preservation.

4.3.2 Kinetic fractionation between water and carbonate

The expected recent equilibrium values based on $\delta^{18}\text{O}_{\text{drip}}$ and temperature at Dino cave is -7.3‰ VPDB, much lower than the minimum -6.02‰ measured from $\delta^{18}\text{O}_{\text{cc}}$ (Section 3.3.2.1). Despite the unlikely drip water evaporation previously discussed, potential non-equilibrium (kinetic) effects might have altered the past $\delta^{18}\text{O}_{\text{cc}}$. This option was evaluated using the Hendy test. The correlation between $\delta^{18}\text{O}_{\text{cc}}$ and $\delta^{13}\text{C}_{\text{cc}}$ values from the adjacent points in layers A, B, C, and D depicted in Figure 2.6b is variable. The highest correlation was obtained at layer D ($0.98 \text{ p}<0.05$; DFT 14 mm), whereas the lowest correlation was obtained at layer B ($-0.04 \text{ p}<0.05$; DFT 266 mm). In the case of layers A (DFT 401 mm) and C (DFT 128 mm), their correlation was 0.60 and 0.69 ($\text{p}<0.05$), respectively. Overall, these results for the Hendy test showed no evidence of significant kinetic fractionation during calcite deposition during the growth of Dino-1 stalagmite (Figure 4.3).



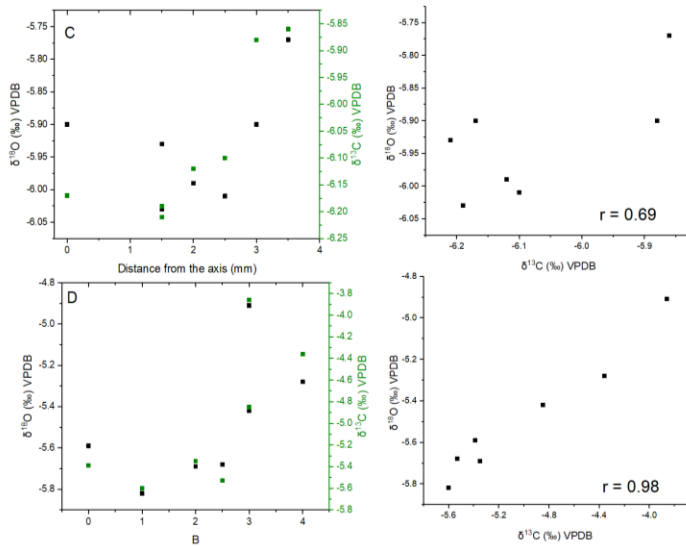


Figure 4.3 Hendy test results for Dino-1 stalagmite. The location of the sampled layers (A, B, C, D) are indicated in Figure 2.6b (yellow vertical lines).

Another possible explanation for this shifted $\delta^{18}\text{O}_{\text{cc}}$ value from modern equilibrium might be that dripwater data doesn't represent the mean values in the cave. Previous studies evaluating the Napo karst (Figures 1.11c and 2.1a) observed that the morphology is largely controlled by the mixed geology (thin-bedded limestones with frequent occurrence of shale beds; sub-horizontal or monoclinic structures) and the precipitation regime showing daily episodes of heavy rain (Constantin et al., 2019). In other words, the Napo karst can be described as shallow, fragmentary and immature, mostly conformed by two main geological layers of 2-9 m thick limestone and 2-4 m marlstone (Chamba Vásquez, 2020; Constantin et al., 2019). Hence, it could conceivably be hypothesized that our dripwater data clusters close to the monthly precipitation values due to the shallow thickness of the epikarst, reduced residence times and active response to rainfall events. Nevertheless, further work at increased resolution is needed to ascertain whether this affirmation is valid through long-term dripping water monitoring on Dino cave, which is currently ongoing. The final and most plausible alternative is that the cave's climate setting was different. It implies that the $\delta^{18}\text{O}_{\text{drip}}$ values were higher during speleothem growth, most likely due to drier conditions in the past (mid-Holocene) than the modern ones being monitored.

4.3.3 Holocene rainfall changes

At first, using three spectral analyses (i.e., REDFIT, Lomb-Scargle, and Wavelets) seems excessive in the Dino-1 $\delta^{18}\text{O}_{\text{cc}}$ record (Figure 3.18), but it is not unsystematic. The apparent 495-year significant peak seems robust but did not pass the Lomb-Scargle test, and only the 30-year peak was consistent. The importance of a robust spectral analysis lies in the fact that artifact periodicities might emerge if the series does

not have a good resolution or is short. To illustrate, many modern and past records have linked their 50-70 year periodicity to the Atlantic Multidecadal Oscillation (Apaéstegui et al., 2014; Mann et al., 1995; Mann and Park, 1994), which the same author has recently reported to be an artifact. This signal (50-70 period) is bolstered due to the use of short climate records, added to anthropogenic greenhouse gases and sulfate aerosols emissions, intermingled with natural pulses of volcanic activity (Mann et al., 2021, 2020). In other words, the Atlantic Multidecadal Oscillation does not exist. In the Dino-1 record, I interpret the consistent 30-year periodicity as related to the Atlantic Meridional Overturning Circulation (AMOC). AMOC carries warm waters north and returns cold deep waters across the Equator with a quasi-30-year oscillation (Huang et al., 2012; Kwon and Frankignoul, 2012). On the other hand, the ~500-year oscillation should be confirmed with an increase in resolution in the Dino-1 slab to avoid the occurrence of the aliasing phenomenon (Trauth, 2021).

Comparing the regional records with the Dino-1 speleothem indicates a consistent pattern towards more humid conditions from the early to mid-Holocene (Figure 3.21). This change is coeval with the increase in insolation during austral summer (DJF). Most are stalagmite-based records except for the Cariaco basin sediment (Ven) and the Huascaran glacier (Per) records. This clarification is essential, especially for the Venezuelan archives Cariaco sediment and Veaj speleothem, as they seem to show contradictory patterns. The Cariaco record has been ubiquitously used in South America as a direct proxy for precipitation and ITCZ position (Haug et al., 2001; McGee et al., 2014; Schneider et al., 2014). The increment in the amount of Ti (%) has been interpreted as a rise in the runoff amount due to heavy rainfall, and its lowering implies drier conditions, as observed in Figure 3.21b (Haug et al., 2001). However, despite their close distance, the Veaj record (Figure 3.21c) presents initial wetter conditions (low $\delta^{18}\text{O}_{\text{cc}}$ values) from 8 to 6 ka, and only drier patterns are observed from ~6-5 ka (higher $\delta^{18}\text{O}_{\text{cc}}$ values). This discrepancy has been explained by Medina et al. (2023) to be related to the manner in which the archives deposited and accrue material. For instance, the Veaj record shows high-frequency variability not captured by the Cariaco chronology, which is influenced by ocean circulation and sea level besides precipitation. It is feasible, therefore, that the expected pattern towards dryness in the Veaj stalagmite (as in Cariaco) is dampened due to the proximity of the cave to the coast, where the ^{18}O depleted water through Rayleigh distillation would be more dominant and amplified only further inland (Medina et al., 2023). In fact, previous studies have observed that changes in tropical precipitation tend to be zonally heterogeneous among paleo-records (McGee et al., 2014). Nonetheless, the steep and continued lower $\delta^{18}\text{O}$ values from early to mid-Holocene (10-4 ka) in the rest of the western records show a gradual transition towards a more humid climate coherent with the rise in insolation. In addition, these regional patterns toward wetness are corroborated by the climate simulations for this period (Figures 3.19 and 3.20). Although the use of climate models has successfully aided in validating the

observed trends with the terrestrial archives, it has certain limitations. A major problem with the currently available mid-Holocene simulations is that although the initial conditions are given for the comparison among modeling groups (e.g., CMIP6), they are not overlapping continuous time (e.g., from 8 to 4 ka). They currently offer periods (between 100 to 700 years) where the most common period is the last 3 ka. Only the MIROC-ES2L covered the early Holocene (8000-8099) (Brierley et al., 2020). Hence, the PMI-CMIP6 presented in Figure 3.19 only provides a rough average of the mid-Holocene patterns but not a clear regional trend as with regional speleothem archives.

There is a broad agreement in the literature that there were pronounced changes in the seasonal cycle of insolation over the last 7 ka, especially in the region of the tropics (0-10°N) (Lorenz et al., 2006). The distribution of Earth's top-of-atmosphere insolation changed due to precession (λ = longitude of perihelion at vernal equinox) and obliquity cycles. These values varied from September ($\lambda=164^\circ$) to January ($\lambda=282^\circ$) and lowering of the Earth's tilt from 24.2° to 23.4° (Lorenz et al., 2006). In the tropics, the impact was reflected as an increment in the September insolation of 30 W m^{-2} more than during March, making equinoxes unbalanced to what is currently observed (almost symmetric values) (see their Figure 2). Previous studies showed that this increment in the austral spring insolation (SON) brought about a stronger SAMS in these months than during the pre-Industrial summer (DJF) (Shimizu et al., 2020). At the same time, the ITCZ shifted south, leaving a cooling trend in the NH boreal summer (Arbuszewski et al., 2013; Wanner et al., 2008). In other words, the extra-tropics of the NH cooled while the tropics warmed, and the ITCZ is closely tied to heat transport (McGee et al., 2014). Although out of the scope of this dissertation, it is noteworthy to mention the existing of apparent discrepancies between the climate at the northern against the southern parts of South America. In a paper analyzing the ITCZ changes related to heat transport, McGee et al. (2014) indicate that mean ITCZ shifts are likely less than 1° and if bigger, respond to regional but not global zonal extensions. In addition, it is stated that there are reduced precipitations and weaker SAMS south of the equator. While it is true that not systematic analysis of the real boundaries of the past ITCZ has been thoroughly done, and some authors tend to "stretch" its limits, it does not necessarily follow that drier conditions are ubiquitous south of the equator. This contrasting pattern can be reconciled due to the existence of the South American dipole. It shows that the variations of eastern tropical precipitation are antiphased with the western on orbital timescales, even registered by paleoclimate records (Cruz et al., 2009; Deininger et al., 2019). In other words, records from the western might show a wetter pattern, whereas the ones located in the southeastern part may display drier trends. This occurs because those records are chiefly controlled by the South Atlantic Converge Zone (SACZ, Figure 3.1b and 3.20), a large cloud system bringing precipitation during austral summer to central and southeastern Brazil (Deininger et al., 2019; Della Libera et al., 2022; Luciene Dias de Melo and Marengo, 2008; Prado et al., 2013; Silva Dias et al., 2009).

Admittedly, the period covered by the Dino-1 record is short (6.8-5.3 ka), and does not allow to observe a downward trend towards wetness (Figure 3.21). However, it presents a higher resolution than the northwestern Caracol and Santiago records, filling this mid-Holocene time gap. By harnessing this attribute, I observe two clear drops between ~6.0 to 5.3 ka. They are well replicated by other regional records besides speleothems, the Cariaco and Pallcacocha sediments, and Huascaran ice cap (Figure 3.22). This observation matches those in earlier studies of the influence of cold Bond episodic events over South America (Deininger et al., 2019; Fernández Sánchez, 2016; Medina et al., 2023; Strikis et al., 2011; Wanner et al., 2008). Ice rafted debris in the form of hematite-stained grains (HSG, Figure 3.22a yellow beam) over the North Atlantic has been used as a proxy for cooler periods during the Holocene and was postulated by Bond et al. (2001). At least nine cold relapses (numbered from 0 to 8) have been identified and peaked around 0.4, 1.4, 2.8, 4.3, 5.9, 8.1, 9.4, 10.3, and 11.1 ka. The Bond cycle number 4 (6.0 to 5.3 ka) triggered changes in the North Atlantic meridional overturning circulation (AMOC) related to the thermohaline circulation. It is possible, therefore that, this caused abrupt precipitation changes at low-latitudes, producing stronger trade winds and ITCZ displacement to the south (Fernández Sánchez, 2016; Medina et al., 2023; Strikis et al., 2011). This hydrological change-point in the western region was likely the reason for the $\delta^{18}\text{O}$ valued to be changed towards more negative in the Veaj, Dino and Condor stalagmites along with the Huascaran glacier. Moreover, higher runoff sediments in the Cariaco and Pallcacocha were also registered.

Overall, the ITCZ southward excursion during more humid interglacials in Ecuador seems to be a consistent pattern since the last 500 ka (Rincón-Martínez et al., 2010). Hence, considering the Holocene epoch as the recent interglacial (Wanner and Buetikofer, 2008) gives us an important insight into its dynamics towards a more humid tropics enhanced by its migration towards the south, where more positive isotopic values imply a modern wetter climate (Figure 3.20). These findings have important implications for the calibration of millennial to centennial-scale paleorecords in northern South America. The ITCZ is a permanent feature of atmospheric circulation moving along the equator and shifts in response to zonal SST. The SAMS reflects a land-sea thermal gradient and depends on land topography and northeasterlies flux regulated by the ITCZ position (Prado et al., 2013; Vuille et al., 2012). The apparent overlap of boundaries between the ITCZ and SAMS (Monsoon through) seems to be an issue only from the late Holocene to recent times, after the ITCZ has shifted towards warmer conditions in the tropical Atlantic, allowing the SAMS features to be strengthened such as LLJs. During the early Holocene, African and Asian monsoons were wetter than SAMS (ITCZ northward) (Cauquoin et al., 2020; Fairchild and Baker, 2012; Lorenz et al., 2006). Afterwards, in the mid-Holocene, the southward ITCZ relocation amplified the SAMS hydrology but reduced the African and Asian monsoons altering their isotopic composition (blue/white patches in Figure 3.20). In the modern climate, the Monsoon

through region stands out, receiving an equal amount of radiation during the equinoxes (March and September), increasing convection and establishing clear SAMS onsets (DJF) and demise (March) (Vuille et al., 2012; Wanner et al., 2008). This is evidence of the coherent tree-ring isotopic signature tied to the average rainfall at the Monsoon through (V-index) (Figure 3.11d). I argue that for the calibration of modern archives close to the equator (5°N to 5°S), each rainfall system's contribution has to be considered as it might play a decisive role.

CHAPTER 5

SUMMARY AND CONCLUSIONS

Northwestern South America has a low number of records contributing to substantial-high uncertainty in the study of past tropical precipitation. Most records come from areas directly influenced by the South American Monsoon System (SAMS), and only a few focus on the Intertropical Convergence Zone (ITCZ) domain. This dissertation set out to investigate the past climate patterns employing terrestrial archives: tree-rings and speleothems from the western Amazon Basin in the Mera site, Central Ecuador, a region currently influenced by the SAMS and ITCZ domains. The methodology used during the research consisted principally in identifying suitable tropical karst and forest areas with appropriate specimens for paleoclimatological studies. In the study site, a forty-eight-month monitoring campaign was established for monthly rainfall collection. Mean annual temperature and tree species phenology was also observed. Moreover, cave temperature and dripwater were also monitored for calibration of the archives. The stable ($\delta^2\text{H}$, $\delta^{18}\text{O}$, $\delta^{13}\text{C}$) and radioisotopes (^{14}C , $^{234}\text{U}/^{230}\text{Th}$) were measured in the collected specimens. Furthermore, using observations, reanalysis, and climate modeling for rainfall and isoscapes products contributed to bridging the regional and local climatology gap.

The first aim of this study was to evaluate the amount effect and identify the local or regional controller of the rainwater stable isotopic composition in the Ecuadorian Andes and Amazon. Based on back trajectory analysis, the results demonstrated that moisture arrives from two primary sources: the Tropical North Atlantic (DJFM) and the South Atlantic crossing the Amazon Basin (JAS). Nevertheless, their convergence in autumn and spring (AMJ and ON) is crucial for modulating the lowest isotopic values. Precisely, this convergence is stronger at the V-Index region (5°S – 5°N , 65° – 75°W), where the wind seasonality and reversal at low levels are enhanced, allowing the inter-hemispheric moisture flux transport. This V-index area is embedded within the ITCZ and SAMS boundaries and is called a monsoon trough globally. I propose that the amount of rainfall located at the monsoon trough, constrained at the V-Index, is a more robust approach for explaining the $\delta^2\text{H}_p$ and $\delta^{18}\text{O}_p$ variability rather than the local amount observed downstream.

The second objective was to reconstruct modern centennial hydrology using oxygen and carbon isotopes in cellulose from tree species. This study successfully constructed $\delta^{18}\text{O}_{\text{TR}}$ and $\delta^{13}\text{C}_{\text{TR}}$ records of *Cedrela nebulosa* spanning 155 years (1864–2018). The annuity of rings was visually identified by wood anatomy and independently confirmed with radiocarbon (^{14}C) using the “bomb-pulse” (1955–2000). Spatial correlations revealed that $\delta^{18}\text{O}_{\text{TR}}$ better reflects months of higher precipitation (March–June) in the western Amazon than local rainout processes at the decadal time scale. Two chief processes are pivotal for this climate relationship, the northward ITCZ excursion and the strong convection in the basin at this time of the year (low OLR). Similarly, this study identifies cloud cover as an essential controller of sunshine duration, which influences the phenology of *Cedrela nebulosa*. I interpreted the variability of the $\delta^{13}\text{C}_{\text{TR}}$ as changes in the photosynthetic rate during light-increased months (July–September), regulated by cloudiness driven by the southward ITCZ passage. False and small rings are the norm rather than

the exception in the tropics. Hence, the manual slicing of tree-rings is a laborious and time-consuming activity. A natural progression of this work in the future is to carry out high-resolution intra-annual tree-ring measurements of $\delta^{13}\text{C}$ using Laser Ablation LA-IRMS.

Finally, the third aim focused on reconstructing past millennial hydrology using $\delta^{18}\text{O}$ from Dino-1 speleothem. Long-term temperature and dripwater monitoring campaigns were established in the Dino, Copa, and Union caves in Central Ecuador. Although not continuous, the dripwater oxygen-18 values tend to follow the established LMWL offering good likelihood for a robust transfer of the climatic signal. The temperature at the Dino cave is steady, with a mean of 19.24 °C in almost 4 years of monitoring. The results of this study indicate that North Atlantic climate anomalies are rapidly transmitted to the tropics. In fact, Dino-1 record, although short (1.5 ka) depicts Bond event 4, one of the cold pulses that took place in the North Atlantic during mid-Holocene. The spectral analysis of Dino-1 record also shows a significant 30-year period which I interpret as a reflection of the Atlantic Multidecadal Oscillation signal part of its time-series variability. In a regional scale, a consistent pattern of wetness developed from early, mid-Holocene, and pre-Industrial times observed in climate models and northeastern and northwestern regional speleothem, sediments, and glacier records. Taken together, these results suggest that the monsoon trough concept valid for modern conditions is not appropriate at the millennial scale. At the early to mid-Holocene, the ITCZ latitudinal boundary was limited in its southern extension; hence SAMS was weaker, not allowing a border overlap as noted nowadays. In other words, ITCZ and SAMS systems are associated in the last millennia but dissociated during the mid-Holocene. The present work is limited in that it only considers one speleothem for the paleoclimate reconstruction of the mid-Holocene, and one of the best practices in speleothem science is the replication with coeval stalagmites (Fairchild and Baker, 2012; Lachniet, 2009). However, a key strength is the multiproxy approach to its scheme. The cave monitoring (dripwater and temperature) along with the precipitation collection (4 years) with moisture back trajectories, complemented with the work carried out with another terrestrial archive (tree-rings) and use of climate modeling encompassing precipitation and stable isotopes, gives us a robust image of the climate features controlling the northwestern Amazon in present and past conditions.

The present thesis offers valuable insights into our understanding of the seasonal extension of the SAMS domain and the influence of the ITCZ in tropical northwestern South America, especially observed during the months of monsoon withdrawal and the onset of the ITCZ. In addition, it provides a framework for calibration of other terrestrial archives, especially ice cores from Ecuadorian glaciers, which could not be interpreted appropriately (Villacís et al., 2008), and sheds light on recalibrating the few available records in the country under the ITCZ mode.

NEW SCIENTIFIC FINDINGS

Rainwater stable isotopes

- The validation of the existence of a regional convection hub at 5°S-5°N, 65°W-75°W (V-index, Wang and Fu, 2002) located in the monsoon trough that controls the main isotopic signal in precipitation through the amount effect. This V-index region can be considered as an aerial lake containing high precipitable water (Arraut et al., 2012).
- The North and South Atlantic moisture source, and the altitude effect due to the Andes orography are the complementary effects tuning the local isotopic signal.
- The moisture arriving to the western Ecuadorian Amazon and Andes is carried by two low-level jets: Orinoco (950–800 hPa) and the Equatorial mid-tropospheric easterly jet (700–600 hPa), which are SAMS features.
- The new local meteoric water line for the Mera site (western Amazon) is $\delta^2\text{H} = 8.33\delta^{18}\text{O} + 14.99$.
- Mean annual temperature is 18.97 °C in the study site, except for an ~1° drop in July-August related to the reduced insolation (June solstice).

Tree-rings and modern climate

- First dendroclimatological study in Ecuador and Northern South America to show the ITCZ imprint in a tree-ring archive.
- The key feature for identification of *Cedrela nebulosa* rings is the embedding of big pores and vessels in marginal parenchyma at the beginning of the growing season.
- $\delta^{18}\text{O}_{\text{TR}}$ reflect the ITCZ passage during the wettest months (March–June) over the western Amazon.
- $\delta^{13}\text{C}_{\text{TR}}$ reflect changes in the photosynthetic rate during light-increased months (July–September) with low cloudiness.
- *C. nebulosa* is well-adapted to wet environments presenting one distinct season of higher precipitation during the year.

Speleothem and mid-Holocene climate

- Mid-Holocene climate was wetter than early Holocene, but drier than pre-Industrial at northwestern South America due to ITCZ latitudinal southward shift.
- Dino-1 speleothem record presents a significant 30-year periodicity, associated with the Atlantic Meridional Overturning Circulation (AMOC).
- Dino-1 speleothem record is a good proxy for mid-Holocene hydrology and seems to register Bond event 4, a strong cold pulse over the North Atlantic observed in northwestern tropical records.

REFERENCES

- Ahrens, C.D., 2019. Meteorology today: an introduction to weather, climate, and the environment. Cengage Learning Canada Inc.
- Alley, R.B., Andrews, J.T., Brigham-Grette, J., Clarke, G.K.C., Cuffey, K.M., Fitzpatrick, J.J., Funder, S., Marshall, S.J., Miller, G.H., Mitrovica, J.X., Muhs, D.R., Otto-Bliesner, B.L., Polyak, L., White, J.W.C., 2010. History of the Greenland Ice Sheet: paleoclimatic insights. *Quat. Sci. Rev.* 29, 1728–1756. <https://doi.org/https://doi.org/10.1016/j.quascirev.2010.02.007>
- Alvites, C., Battipaglia, G., Santopuoli, G., Hampel, H., Vázquez, R.F., Matteucci, G., Tognetti, R., 2019. Dendrochronological analysis and growth patterns of *Polylepis reticulata* (Rosaceae) in the Ecuadorian Andes. *IAWA J.* 40, 331–S5. <https://doi.org/10.1163/22941932-40190240>
- Ancapichún, S., De Pol-Holz, R., Christie, D.A., Santos, G.M., Collado-Fabbri, S., Garreaud, R., Lambert, F., Orfanoz-Chequela, A., Rojas, M., Southon, J., Turnbull, J.C., Creasman, P.P., 2021. Radiocarbon bomb-peak signal in tree-rings from the tropical Andes register low latitude atmospheric dynamics in the Southern Hemisphere. *Sci. Total Environ.* 774, 145126. <https://doi.org/10.1016/j.scitotenv.2021.145126>
- Ancapichún, S., Pawlyta, J., Rakowski, A.Z., Sieczkowska, D., 2022. Influence of air parcels from Northern and Southern Hemispheres on Radiocarbon-based Inca chronology. *Radiocarbon* 1–16. <https://doi.org/DOI: 10.1017/RDC.2022.87>
- Anders, A.M., Nesbitt, S.W., 2015. Altitudinal Precipitation Gradients in the Tropics from Tropical Rainfall Measuring Mission (TRMM) Precipitation Radar. *J. Hydrometeorol.* 16, 441–448. <https://doi.org/10.1175/JHM-D-14-0178.1>
- Apaéstegui, J., Cruz, F.W., Sifeddine, A., Vuille, M., Espinoza, J.C., Guyot, J.L., Khodri, M., Strikis, N., Santos, R.V., Cheng, H., Edwards, L., Carvalho, E., Santini, W., 2014. Hydroclimate variability of the northwestern Amazon Basin near the Andean foothills of Peru related to the South American Monsoon System during the last 1600 years. *Clim. Past* 10, 1967–1981. <https://doi.org/10.5194/cp-10-1967-2014>
- Araguás-Araguás, L., Froehlich, K., Rozanski, K., 2000. Deuterium and oxygen-18 isotope composition of precipitation and atmospheric moisture. *Hydrol. Process.* 14, 1341–1355. [https://doi.org/10.1002/1099-1085\(20000615\)14:8<1341::AID-HYP983>3.0.CO;2-Z](https://doi.org/10.1002/1099-1085(20000615)14:8<1341::AID-HYP983>3.0.CO;2-Z)
- Araguas, L.A., Danesi, P., Froehlich, K., Rozanski, K., 1996. Global monitoring of the isotopic composition of precipitation. *J. Radioanal. Nucl. Chem. Artic.* 205, 189–200. <https://doi.org/10.1007/BF02039404>
- Arbuszewski, J.A., DeMenocal, P.B., Cléroux, C., Bradtmiller, L., Mix, A., 2013. Meridional shifts of the Atlantic intertropical convergence zone since the Last Glacial Maximum. *Nat. Geosci.* 6, 959–962. <https://doi.org/10.1038/ngeo1961>
- Arias, P.A., Fu, R., Vera, C., Rojas, M., 2015. A correlated shortening of the North and South American monsoon seasons in the past few decades. *Clim. Dyn.* 45, 3183–3203. <https://doi.org/10.1007/s00382-015-2533-1>
- Arraut, J.M., Nobre, C., Barbosa, H.M.J., Obregon, G., Marengo, J., 2012. Aerial Rivers and Lakes: Looking at Large-Scale Moisture Transport and Its Relation to Amazonia and to Subtropical Rainfall in South America. *J. Clim.* 25, 543–556.

- https://doi.org/10.1175/2011JCLI4189.1
- Baker, A., Hartmann, A., Duan, W., Hankin, S., Comas-Bru, L., Cuthbert, M.O., Treble, P.C., Banner, J., Genty, D., Baldini, L.M., Bartolomé, M., Moreno, A., Pérez-Mejías, C., Werner, M., 2019. Global analysis reveals climatic controls on the oxygen isotope composition of cave drip water. *Nat. Commun.* 10, 2984. <https://doi.org/10.1038/s41467-019-11027-w>
- Baker, J.C.A., 2017. Unravelling the drivers of short- and long-term variability in the Amazon hydrological cycle using tree-ring oxygen isotopes. *Unravelling drivers short-and long-term Var. Amaz. Hydrol. cycle using tree-ring Oxyg. Isot.*
- Baker, J.C.A., Gloor, M., Boom, A., Neill, D.A., Cintra, B.B.L., Clerici, S.J., Brienen, R.J.W., 2018. Questioning the Influence of Sunspots on Amazon Hydrology: Even a Broken Clock Tells the Right Time Twice a Day. *Geophys. Res. Lett.* 45, 1419–1422. <https://doi.org/10.1002/2017GL076889>
- Baker, J.C.A., Gloor, M., Spracklen, D. V., Arnold, S.R., Tindall, J.C., Clerici, S.J., Leng, M.J., Brienen, R.J.W., 2016. What drives interannual variation in tree ring oxygen isotopes in the Amazon? *Geophys. Res. Lett.* 43, 11–831. <https://doi.org/10.1002/2016GL071507>
- Baker, J.C.A., Santos, G.M., Gloor, M., Brienen, R.J.W., 2017. Does Cedrela always form annual rings? Testing ring periodicity across South America using radiocarbon dating. *Trees* 31, 1999–2009. <https://doi.org/10.1007/s00468-017-1604-9>
- Baker, P.A., Fritz, S.C., 2015. Nature and causes of Quaternary climate variation of tropical South America. *Quat. Sci. Rev.* 124, 31–47. <https://doi.org/10.1016/j.quascirev.2015.06.011>
- Beck, H.E., Zimmermann, N.E., McVicar, T.R., Vergopolan, N., Berg, A., Wood, E.F., 2018. Present and future Köppen-Geiger climate classification maps at 1-km resolution. *Sci. Data* 5, 180214. <https://doi.org/10.1038/sdata.2018.214>
- Bendix, J., Homeier, J., Cueva Ortiz, E., Emck, P., Breckle, S.-W., Richter, M., Beck, E., 2006a. Seasonality of weather and tree phenology in a tropical evergreen mountain rain forest. *Int. J. Biometeorol.* 50, 370–384. <https://doi.org/10.1007/s00484-006-0029-8>
- Bendix, J., Lauer, W., 1992. Die Niederschlagsjahreszeiten in Ecuador und ihre klimadynamische Interpretation (Rainy seasons in Ecuador and their climate-dynamic interpretation). *Erdkunde* 118–134.
- Bendix, J., Rollenbeck, R., Fabian, P., Emck, P., Richter, M., Beck, E., 2008. Climate Variability, in: Gradients in a Tropical Mountain Ecosystem of Ecuador. Springer, pp. 281–290. https://doi.org/10.1007/978-3-540-73526-7_27
- Bendix, J., Rollenbeck, R., Göttlicher, D., Cermak, J., 2006b. Cloud occurrence and cloud properties in Ecuador. *Clim. Res.* 30, 133–147. <https://doi.org/10.3354/cr030133>
- Benn, D., 2012. Algorithms+ Observations= VStar. *J. Am. Assoc. Var. Star Obs.* 40, 852.
- Bés de Berc, S., Baby, P., Soula, J.-C., Rosero, J., Souris, M., Christophoul, F., Vega, J., 2004. La superficie mera-upano: marcador geomorfológico de la incisión fluvial y del levantamiento tectónico de la zona subandina ecuatoriana, in: La Cuenca Oriente: Geología y Petróleo. Institut français d'études andines, pp. 153–167.
- Betancourt, J.L., Grissino-Mayer, H.D., Salzer, M.W., Swetnam, T.W., 2002. A test of “Annual resolution” in stalagmites using tree rings. *Quat. Res.* 58, 197–199.

- https://doi.org/10.1006/qres.2002.2354
- Bisgaard, S., Kulahci, M., 2011. Time series analysis and forecasting by example. John Wiley & Sons.
- Björg Ólafsdóttir, K., Schulz, M., Mudelsee, M., 2016. REDFIT-X: Cross-spectral analysis of unevenly spaced paleoclimate time series. *Comput. Geosci.* 91, 11–18. <https://doi.org/https://doi.org/10.1016/j.cageo.2016.03.001>
- Bond, G., Kromer, B., Beer, J., Muscheler, R., Evans, M.N., Showers, W., Hoffmann, S., Lotti-Bond, R., Hajdas, I., Bonani, G., 2001. Persistent solar influence on north atlantic climate during the Holocene. *Science (80-.).* 294, 2130 – 2136. <https://doi.org/10.1126/science.1065680>
- Bony, S., Risi, C., Vimeux, F., 2008. Influence of convective processes on the isotopic composition (δ 18 O and δ D) of precipitation and water vapor in the tropics: 1. Radiative-convective equilibrium and Tropical Ocean–Global Atmosphere–Coupled Ocean-Atmosphere Response Experiment (TOGA-CO). *J. Geophys. Res.* 113, D19305. <https://doi.org/10.1029/2008JD009942>
- Bony, S., Stevens, B., Frierson, D.M.W., Jakob, C., Kageyama, M., Pincus, R., Shepherd, T.G., Sherwood, S.C., Siebesma, A.P., Sobel, A.H., Watanabe, M., Webb, M.J., 2015. Clouds, circulation and climate sensitivity. *Nat. Geosci.* 8, 261–268. <https://doi.org/10.1038/ngeo2398>
- Borella, S., Leuenberger, M., Saurer, M., Siegwolf, R., 1998. Reducing uncertainties in δ 13 C analysis of tree rings: Pooling, milling, and cellulose extraction. *J. Geophys. Res. Atmos.* 103, 19519–19526. <https://doi.org/10.1029/98JD01169>
- Bowen, G.J., 2022. The Online Isotopes in Precipitation Calculator [WWW Document]. URL https://wateriso.utah.edu/waterisotopes/pages/data_access/oipc.html
- Bowen, G.J., 2010. Isoscapes: Spatial Pattern in Isotopic Biogeochemistry. *Annu. Rev. Earth Planet. Sci.* 38, 161–187. <https://doi.org/10.1146/annurev-earth-040809-152429>
- Bradley, R.S., 2015. Paleoclimatology. Elsevier. <https://doi.org/10.1016/C2009-0-18310-1>
- Bräuning, A., Homeier, J., Cueva, E., Beck, E., Günter, S., 2008. Growth Dynamics of Trees in Tropical Mountain Ecosystems, in: Gradients in a Tropical Mountain Ecosystem of Ecuador. Springer, pp. 291–302. https://doi.org/10.1007/978-3-540-73526-7_28
- Brienen, R.J.W., Helle, G., Pons, T.L., Guyot, J.-L., Gloor, M., 2012. Oxygen isotopes in tree rings are a good proxy for Amazon precipitation and El Nino-Southern Oscillation variability. *Proc. Natl. Acad. Sci.* 109, 16957–16962. <https://doi.org/10.1073/pnas.1205977109>
- Brierley, C.M., Zhao, A., Harrison, S.P., Braconnot, P., Williams, C.J.R., Thornalley, D.J.R., Shi, X., Peterschmitt, J.-Y., Ohgaito, R., Kaufman, D.S., Kageyama, M., Hargreaves, J.C., Erb, M.P., Emile-Geay, J., D'Agostino, R., Chandan, D., Carré, M., Bartlein, P.J., Zheng, W., Zhang, Z., Zhang, Q., Yang, H., Volodin, E.M., Tomas, R.A., Routson, C., Peltier, W.R., Otto-Bliesner, B., Morozova, P.A., McKay, N.P., Lohmann, G., Legrande, A.N., Guo, C., Cao, J., Brady, E., Annan, J.D., Abe-Ouchi, A., 2020. Large-scale features and evaluation of the PMIP4-CMIP6 midHolocene simulations. *Clim. Past* 16, 1847–1872. <https://doi.org/10.5194/cp-16-1847-2020>

- Builes-Jaramillo, A., Yepes, J., Salas, H.D., 2021. The Orinoco Low-Level Jet and its association with the hydroclimatology of northern South America. *J. Hydrometeorol.* <https://doi.org/10.1175/JHM-D-21-0073.1>
- Bunn, A.G., 2010. Statistical and visual crossdating in R using the dplR library. *Dendrochronologia* 28, 251–258. <https://doi.org/10.1016/j.dendro.2009.12.001>
- Bunn, A.G., 2008. A dendrochronology program library in R (dplR). *Dendrochronologia* 26, 115–124. <https://doi.org/10.1016/j.dendro.2008.01.002>
- Buras, A., 2017. A comment on the expressed population signal. *Dendrochronologia* 44, 130–132. <https://doi.org/10.1016/j.dendro.2017.03.005>
- Bustamante, M.G., Cruz, F.W., Vuille, M., Apaéstegui, J., Strikis, N., Panizo, G., Novello, F. V., Deininger, M., Sifeddine, A., Cheng, H., Moquet, J.S., Guyot, J.L., Santos, R. V., Segura, H., Edwards, R.L., 2016. Holocene changes in monsoon precipitation in the Andes of NE Peru based on $\delta^{18}\text{O}$ speleothem records. *Quat. Sci. Rev.* 146, 274–287. <https://doi.org/https://doi.org/10.1016/j.quascirev.2016.05.023>
- Campelo, F., García-González, I., Nabais, C., 2012. detrendeR – A Graphical User Interface to process and visualize tree-ring data using R. *Dendrochronologia* 30, 57–60. <https://doi.org/10.1016/j.dendro.2011.01.010>
- Campozano, L., Céller, R., Trachte, K., Bendix, J., Samaniego, E., 2016. Rainfall and Cloud Dynamics in the Andes: A Southern Ecuador Case Study. *Adv. Meteorol.* 2016, 1–15. <https://doi.org/10.1155/2016/3192765>
- Campozano, L., Trachte, K., Céller, R., Samaniego, E., Bendix, J., Albuja, C., Mejia, J.F., 2018. Climatology and Teleconnections of Mesoscale Convective Systems in an Andean Basin in Southern Ecuador: The Case of the Paute Basin. *Adv. Meteorol.* 2018, 1–13. <https://doi.org/10.1155/2018/4259191>
- Capello, E., 2018. From imperial pyramids to anticolonial sundials: commemorating and contesting French geodesy in Ecuador. *J. Hist. Geogr.* 62, 37–50. <https://doi.org/https://doi.org/10.1016/j.jhg.2018.04.008>
- Cauquoin, A., Werner, M., Lohmann, G., 2020. MPI-ESM-wiso simulations data for preindustrial and mid-Holocene conditions. <https://doi.org/10.1594/PANGAEA.912258>
- Cauquoin, A., Werner, M., Lohmann, G., 2019. Water isotopes -- climate relationships for the mid-Holocene and preindustrial period simulated with an isotope-enabled version of MPI-ESM. *Clim. Past* 15, 1913–1937. <https://doi.org/10.5194/cp-15-1913-2019>
- Chalán, M., 2019. Influencia de las precipitaciones sobre el crecimiento anual de *Acacia macracantha* Humb. & Bonpl. ex Willd, en dos sitios de la Provincia de Loja. Universidad Nacional de Loja.
- Challoner, J., 2018. The Atom: A Visual Tour. MIT Press.
- Chamba Vásquez, B.A., 2020. The First Electrical Resistivity Tomography Study Applied to an Ecuadorian Cave (Uctu Iji Changa, Tena): Insights into Amazonian Karst Systems.
- Chao, W.C., Chen, B., 2001. The Origin of Monsoons. *J. Atmos. Sci.* 58, 3497–3507. [https://doi.org/10.1175/1520-0469\(2001\)058<3497:TOOM>2.0.CO;2](https://doi.org/10.1175/1520-0469(2001)058<3497:TOOM>2.0.CO;2)
- Cheng, H., Lawrence Edwards, R., Shen, C.-C., Polyak, V.J., Asmerom, Y., Woodhead, J., Hellstrom, J., Wang, Y., Kong, X., Spötl, C., Wang, X., Calvin Alexander, E., 2013a. Improvements in ^{230}Th dating, ^{230}Th and ^{234}U half-life values, and U–Th

- isotopic measurements by multi-collector inductively coupled plasma mass spectrometry. *Earth Planet. Sci. Lett.* 371–372, 82–91.
<https://doi.org/https://doi.org/10.1016/j.epsl.2013.04.006>
- Cheng, H., Sinha, A., Cruz, F.W., Wang, X., Edwards, R.L., D’Horta, F.M., Ribas, C.C., Vuille, M., Stott, L.D., Auler, A.S., 2013b. Climate change patterns in Amazonia and biodiversity. *Nat. Commun.* 4, 1411. <https://doi.org/10.1038/ncomms2415>
- Chiang, J.C.H., 2009. The Tropics in Paleoclimate. *Annu. Rev. Earth Planet. Sci.* 37, 263–297. <https://doi.org/10.1146/annurev.earth.031208.100217>
- Chimborazo, O., Vuille, M., 2021. Present-day climate and projected future temperature and precipitation changes in Ecuador. *Theor. Appl. Climatol.* 143, 1581–1597.
<https://doi.org/10.1007/s00704-020-03483-y>
- CITES, (Convention on International Trade in Endangered Species of Wild Fauna and Flora), 2021. Appendices I, II and III.
- Clark, I., 2015. Groundwater Geochemistry and Isotopes. CRC Press.
<https://doi.org/10.1201/b18347>
- Comas-Bru, L., Rehfeld, K., Roesch, C., Amirnezhad-Mozhdehi, S., Harrison, S.P., Atsawawaranunt, K., Ahmad, S.M., Brahim, Y.A., Baker, A., Bosomworth, M., Breitenbach, S.F.M., Burstyn, Y., Columbu, A., Deininger, M., Demény, A., Dixon, B., Fohlmeister, J., Hatvani, I.G., Hu, J., Kaushal, N., Kern, Z., Labuhn, I., Lechleitner, F.A., Lorrey, A., Martrat, B., Novello, V.F., Oster, J., Pérez-Mejías, C., Scholz, D., Scroxton, N., Sinha, N., Ward, B.M., Warken, S., Zhang, H., 2020. SISALv2: a comprehensive speleothem isotope database with multiple age–depth models. *Earth Syst. Sci. Data* 12, 2579–2606. <https://doi.org/10.5194/essd-12-2579-2020>
- Constantin, S., Toulkeridis, T., Moldovan, O.T., Villacís, M., Addison, A., 2019. Caves and karst of Ecuador – state-of-the-art and research perspectives. *Phys. Geogr.* 40, 28–51. <https://doi.org/10.1080/02723646.2018.1461496>
- Cook, E., Briffa, K., Shiyatov, S., Mazepa, V., Jones, P.D., 1990. Data Analysis, in: Methods of Dendrochronology. Springer Netherlands, Dordrecht, pp. 97–162.
https://doi.org/10.1007/978-94-015-7879-0_3
- Cook, E.R., Kairiukstis, L.A., 1990. Methods of dendrochronology: applications in the environmental sciences. Springer Science & Business Media.
- Cook, K.H., 2009. South American Climate Variability and Change: Remote and Regional Forcing Processes BT - Past Climate Variability in South America and Surrounding Regions: From the Last Glacial Maximum to the Holocene, in: Vimeux, F., Sylvestre, F., Khodri, M. (Eds.), . Springer Netherlands, Dordrecht, pp. 193–212. https://doi.org/10.1007/978-90-481-2672-9_8
- Cruz, F.W., Vuille, M., Burns, S.J., Wang, X., Cheng, H., Werner, M., Lawrence Edwards, R., Karmann, I., Auler, A.S., Nguyen, H., 2009. Orbitally driven east–west antiphasing of South American precipitation. *Nat. Geosci.* 2, 210–214.
<https://doi.org/10.1038/ngeo444>
- Daëron, M., Drysdale, R.N., Peral, M., Huyghe, D., Blamart, D., Coplen, T.B., Lartaud, F., Zanchetta, G., 2019. Most Earth-surface calcites precipitate out of isotopic equilibrium. *Nat. Commun.* 10, 429. <https://doi.org/10.1038/s41467-019-08336-5>
- Dansgaard, W., 1964. Stable isotopes in precipitation. *Tellus* 16, 436–468.
<https://doi.org/10.3402/tellusa.v16i4.8993>

- Dee, D.P., Uppala, S.M., Simmons, A.J., Berrisford, P., Poli, P., Kobayashi, S., Andrae, U., Balmaseda, M.A., Balsamo, G., Bauer, P., Bechtold, P., Beljaars, A.C.M., van de Berg, L., Bidlot, J., Bormann, N., Delsol, C., Dragani, R., Fuentes, M., Geer, A.J., Haimberger, L., Healy, S.B., Hersbach, H., Hólm, E. V., Isaksen, L., Kållberg, P., Köhler, M., Matricardi, M., McNally, A.P., Monge-Sanz, B.M., Morcrette, J.-J., Park, B.-K., Peubey, C., de Rosnay, P., Tavolato, C., Thépaut, J.-N., Vitart, F., 2011. The ERA-Interim reanalysis: configuration and performance of the data assimilation system. *Q. J. R. Meteorol. Soc.* 137, 553–597. <https://doi.org/10.1002/qj.828>
- Dee, S., Emile-Geay, J., Evans, M.N., Allam, A., Steig, E.J., Thompson, D.M., 2015. PRYSM: An open-source framework for PROX System Modeling, with applications to oxygen-isotope systems. *J. Adv. Model. Earth Syst.* 7, 1220–1247. <https://doi.org/10.1002/2015MS000447>
- Deininger, M., Ward, B.M., Novello, V.F., Cruz, F.W., 2019. Late Quaternary Variations in the South American Monsoon System as Inferred by Speleothems—New Perspectives using the SISAL Database. *Quaternary* 2, 6. <https://doi.org/10.3390/quat2010006>
- Della Libera, M.E., Novello, V.F., Cruz, F.W., Orrison, R., Vuille, M., Maezumi, S.Y., de Souza, J., Cauhy, J., Campos, J.L.P.S., Ampuero, A., Utida, G., Stríkis, N.M., Stumpf, C.F., Azevedo, V., Zhang, H., Edwards, R.L., Cheng, H., 2022. Paleoclimatic and paleoenvironmental changes in Amazonian lowlands over the last three millennia. *Quat. Sci. Rev.* 279, 107383. <https://doi.org/10.1016/j.quascirev.2022.107383>
- Dorale, J.A., Edwards, R.L., Jr, E.C.A., Shen, C.-C., Richards, D.A., Cheng, H., 2007. Uranium-Series Dating Of Speleothemes: current techniques, limits and; applications, in: *Studies of Cave Sediments*. Springer Netherlands, Dordrecht, pp. 177–197. https://doi.org/10.1007/978-1-4020-5766-3_10
- Dorale, J.A., Liu, Z., 2009. Limitations of Hendy test criteria in judging the paleoclimatic suitability of speleothems and the need for replication. *J. Cave Karst Stud* 71, 73–80.
- Douville, H., Raghavan, K., Renwick, J., Allan, R.P., Arias, P.A., Barlow, M., Cerezo-Mota, R., Cherchi, A., Gan, T.Y., Gergis, J., Jiang, D., Khan, A., Pokam Mbá, W., Rosenfeld, D., Tierney, J., Zolina, O., 2021. Water Cycle Changes. In *Climate Change 2021: The Physical Science Basis. Contribution of Working Group I to the Sixth Assessment Report of the Intergovernmental Panel on Climate Change*.
- Dreybrodt, W., Gabrovsek, F., 2003. Basic processes and mechanisms governing the evolution of karst. *Speleogenes. Evol. karst aquifers* 1, 115–154.
- Dreybrodt, W., Gabrovšek, F., Romanov, D., 2005. Processes of Speleogenesis: A Modeling Approach. *Založba ZRC*.
- Dünisch, O., Bauch, J., Gasparotto, L., 2002. Formation of increment zones and intraannual growth dynamics in the xylem of *Swietenia macrophylla*, *Carapa guianensis*, and *Cedrela odorata* (Meliaceae). *IAWA J.* 23, 101–119. <https://doi.org/10.1163/22941932-90000292>
- Edwards, L., Chen, J.H., Wasserburg, G.J., 1987. ^{238}U - ^{234}U - ^{230}Th - ^{232}Th systematics and the precise measurement of time over the past 500,000 years. *Earth Planet. Sci. Lett.* 81, 175–192. [https://doi.org/10.1016/0012-821X\(87\)90154-3](https://doi.org/10.1016/0012-821X(87)90154-3)
- Emck, P., 2007. A climatology of south Ecuador-with special focus on the major Andean ridge as Atlantic-Pacific climate divide.

- Espinosa, C.I., Camarero, J.J., Gusmán, A.A., 2018. Site-dependent growth responses to climate in two major tree species from tropical dry forests of southwest Ecuador. *Dendrochronologia* 52, 11–19. <https://doi.org/10.1016/j.dendro.2018.09.004>
- Esquivel-Hernández, G., Mosquera, G.M., Sánchez-Murillo, R., Quesada-Román, A., Birkel, C., Crespo, P., Céller, R., Windhorst, D., Breuer, L., Boll, J., 2019. Moisture transport and seasonal variations in the stable isotopic composition of rainfall in Central American and Andean Páramo during El Niño conditions (2015–2016). *Hydrol. Process.* 33, hyp.13438. <https://doi.org/10.1002/hyp.13438>
- EUMetraIn, 2014. Product Tutorial on TPW Content Products [WWW Document]. URL <http://www.eumetrain.org>
- Evans, M.N., Tolwinski-Ward, S.E., Thompson, D.M., Anchukaitis, K.J., 2013. Applications of proxy system modeling in high resolution paleoclimatology. *Quat. Sci. Rev.* 76, 16–28.
- Fairchild, I.J., Baker, A., 2012. Speleothem science: from process to past environments. John Wiley & Sons.
- Fairchild, I.J., Smith, C.L., Baker, A., Fuller, L., Spötl, C., Matthey, D., McDermott, F., E.I.M.F., 2006. Modification and preservation of environmental signals in speleothems. *Earth-Science Rev.* 75, 105–153. <https://doi.org/10.1016/j.earscirev.2005.08.003>
- Fernández Sánchez, A., 2016. Revisión de la estratigrafía del d₁₈O en sondeos de hielo de glaciares en los Andes Centrales: Implicaciones para la variabilidad climática del Holoceno. *Rev. Geotemas* 16, 565–568.
- Ferreiro, L.D., 2011. Measure of the Earth: the enlightenment expedition that reshaped our world. Basic Books (AZ), New York.
- Foster, G., 1996. Wavelets for period analysis of unevenly sampled time series. *Astron. J.* 112, 1709. <https://doi.org/10.1086/118137>
- Fu, R., Arias, P.A., Wang, H., 2016. The Connection Between the North and South American Monsoons BT - The Monsoons and Climate Change: Observations and Modeling, in: de Carvalho, L.M.V., Jones, C. (Eds.), . Springer International Publishing, Cham, pp. 187–206. https://doi.org/10.1007/978-3-319-21650-8_9
- Funk, C., Peterson, P., Landsfeld, M., Pedreros, D., Verdin, J., Shukla, S., Husak, G., Rowland, J., Harrison, L., Hoell, A., Michaelsen, J., 2015. The climate hazards infrared precipitation with stations—a new environmental record for monitoring extremes. *Sci. Data* 2, 150066. <https://doi.org/10.1038/sdata.2015.66>
- Gadgil, S., 2018. The monsoon system: Land–sea breeze or the ITCZ? *J. Earth Syst. Sci.* 127, 1. <https://doi.org/10.1007/s12040-017-0916-x>
- Gagen, M., McCarroll, D., Loader, N.J., Robertson, I., 2011. Stable Isotopes in Dendroclimatology: Moving Beyond ‘Potential,’ in: Dendroclimatology. Springer, pp. 147–172. https://doi.org/10.1007/978-1-4020-5725-0_6
- Garcia, M., Villalba, F., Araguas-Araguas, L., Rozanski, K., 1998. The role of atmospheric circulation patterns in controlling the regional distribution of stable isotope contents in precipitation: Preliminary results from two transects in the Ecuadorian Andes, in: Isotope Techniques in the Study of Environmental Change. International Atomic Energy Agency, Vienna (Austria).
- Garcia, S.R., Kayano, M.T., 2010. Some evidence on the relationship between the South American monsoon and the Atlantic ITCZ. *Theor. Appl. Climatol.* 99, 29–38.

- https://doi.org/10.1007/s00704-009-0107-z
- Garreaud, R.D., Aceituno, P., 2007. Atmospheric Circulation and Climatic Variability, in: The Physical Geography of South America. Oxford University Press.
- https://doi.org/10.1093/oso/9780195313413.003.0010
- Garreaud, R.D., Vuille, M., Compagnucci, R., Marengo, J., 2009. Present-day South American climate. *Palaeogeogr. Palaeoclimatol. Palaeoecol.* 281, 180–195.
- https://doi.org/10.1016/j.palaeo.2007.10.032
- Gärtner, H., Schweingruber, F.H., 2013. Microscopic preparation techniques for plant stem analysis. Remagen: Kessel Publishing House.
- Gelvez, J.C.R., 2019. A 50 kyr rainfall record derived from Colombian stalagmites: Insights on intertropical convergence zone dynamics and the role of ocean circulation. Iowa State University.
- Ghil, M., 1997. The SSA-MTM Toolkit: Applications to analysis and prediction of time series, in: Applications of Soft Computing. International Society for Optics and Photonics, pp. 216–230.
- Ghil, M., Allen, M.R., Dettinger, M.D., Ide, K., Kondrashov, D., Mann, M.E., Robertson, A.W., Saunders, A., Tian, Y., Varadi, F., 2002. Advanced spectral methods for climatic time series. *Rev. Geophys.* 40, 1–3. https://doi.org/10.1029/2001RG000092
- Gilman, D.L., Fuglister, F.J., Mitchell, J.M., 1963. On the Power Spectrum of “Red Noise.” *J. Atmos. Sci.* 20, 182–184. https://doi.org/https://doi.org/10.1175/1520-0469(1963)020<0182:OTPSON>2.0.CO;2
- Gimeno, L., Dominguez, F., Nieto, R., Trigo, R., Drumond, A., Reason, C.J.C., Taschetto, A.S., Ramos, A.M., Kumar, R., Marengo, J., 2016. Major Mechanisms of Atmospheric Moisture Transport and Their Role in Extreme Precipitation Events. *Annu. Rev. Environ. Resour.* 41, 117–141. https://doi.org/10.1146/annurev-environ-110615-085558
- Goller, R., Wilcke, W., Leng, M.J., Tobschall, H.J., Wagner, K., Valarezo, C., Zech, W., 2005. Tracing water paths through small catchments under a tropical montane rain forest in south Ecuador by an oxygen isotope approach. *J. Hydrol.* 308, 67–80. https://doi.org/10.1016/j.jhydrol.2004.10.022
- Gonfiantini, R., Roche, M.-A., Olivry, J.-C., Fontes, J.-C., Zuppi, G.M., 2001. The altitude effect on the isotopic composition of tropical rains. *Chem. Geol.* 181, 147–167. https://doi.org/10.1016/S0009-2541(01)00279-0
- Gonfiantini, R., Stichler, W., Rozanski, K., 1995. Standards and intercomparison materials distributed by the International Atomic Energy Agency for stable isotope measurements.
- Goosse, H., 2015. Climate system dynamics and modeling. Cambridge University Press.
- Gourlay, I.D., 1995. Growth ring characteristics of some African Acacia species. *J. Trop. Ecol.* 11, 121–140. https://doi.org/DOI: 10.1017/S0266467400008488
- Grinsted, A., Moore, J.C., Jevrejeva, S., 2004. Application of the cross wavelet transform and wavelet coherence to geophysical time series. *Nonlinear Process. Geophys.* 11, 561–566. https://doi.org/10.5194/npg-11-561-2004
- Grissino-Mayer, H., 2001. Evaluating Crossdating Accuracy: A Manual and Tutorial for the Computer Program COFECHA 57, 205–221.
- Gunn, J., 2004. Encyclopedia of caves and karst science. Taylor & Francis.
- Günter, S., Stimm, B., Cabrera, M., Diaz, M.L., Lojan, M., Ordoñez, E., Richter, M.,

- Weber, M., 2008. Tree phenology in montane forests of southern Ecuador can be explained by precipitation, radiation and photoperiodic control. *J. Trop. Ecol.* 24, 247–258. <https://doi.org/10.1017/S0266467408005063>
- Guy, H., Seimon, A., Perry, L.B., Konecky, B.L., Rado, M., Andrade, M., Potocki, M., Mayewski, P.A., 2019. Subseasonal Variations of Stable Isotopes in Tropical Andean Precipitation. *J. Hydrometeorol.* 20, 915–933. <https://doi.org/10.1175/JHM-D-18-0163.1>
- Hammer, Ø., Harper, D., Ryan, P., 2001. PAST: Paleontological Statistics Software package for Education and Data Analysis. *Palaeontol. Electron.* 4, 1–9.
- Harris, I., Osborn, T.J., Jones, P., Lister, D., 2020. Version 4 of the CRU TS monthly high-resolution gridded multivariate climate dataset. *Sci. Data* 7, 109. <https://doi.org/10.1038/s41597-020-0453-3>
- Hastenrath, S., 1999. Equatorial mid-tropospheric easterly jet over the eastern Pacific. *J. Meteorol. Soc. Japan. Ser. II* 77, 701–709.
- Hastenrath, S., 1997. Annual cycle of upper air circulation and convective activity over the tropical Americas. *J. Geophys. Res. Atmos.* 102, 4267–4274. <https://doi.org/10.1029/96JD03122>
- Hastenrath, S., 1991. Climate Dynamics of the Tropics. Springer Netherlands, Dordrecht. <https://doi.org/10.1007/978-94-011-3156-8>
- Haug, G.H., Hughen, K.A., Sigman, D.M., Peterson, L.C., Röhl, U., 2001. Southward migration of the intertropical convergence zone through the Holocene. *Science* (80-). 293, 1304–1308.
- Hendy, C.H., 1971. The isotopic geochemistry of speleothems—I. The calculation of the effects of different modes of formation on the isotopic composition of speleothems and their applicability as palaeoclimatic indicators. *Geochim. Cosmochim. Acta* 35, 801–824. [https://doi.org/https://doi.org/10.1016/0016-7037\(71\)90127-X](https://doi.org/https://doi.org/10.1016/0016-7037(71)90127-X)
- Hersbach, H., Bell, B., Berrisford, P., Biavati, G., Horányi, A., Muñoz Sabater, J., Nicolas, J., Peubey, C., Radu, R., Rozum, I., Schepers, D., Simmons, A., Soci, C., Dee, D., Thépaut, J.-N., 2019. ERA5 monthly averaged data on single levels from 1979 to present. Copernicus Climate Change Service (C3S) Climate Data Store (CDS) [WWW Document]. <https://doi.org/10.24381/cds.f17050d7>
- Hersbach, H., Bell, B., Berrisford, P., Hirahara, S., Horányi, A., Muñoz-Sabater, J., Nicolas, J., Peubey, C., Radu, R., Schepers, D., Simmons, A., Soci, C., Abdalla, S., Abellán, X., Balsamo, G., Bechtold, P., Biavati, G., Bidlot, J., Bonavita, M., Chiara, G., Dahlgren, P., Dee, D., Diamantakis, M., Dragani, R., Flemming, J., Forbes, R., Fuentes, M., Geer, A., Haimberger, L., Healy, S., Hogan, R.J., Hólm, E., Janisková, M., Keeley, S., Laloyaux, P., Lopez, P., Lupu, C., Radnoti, G., Rosnay, P., Rozum, I., Vamborg, F., Villaume, S., Thépaut, J., 2020. The ERA5 global reanalysis. *Q. J. R. Meteorol. Soc.* 146, 1999–2049. <https://doi.org/10.1002/qj.3803>
- Hogg, A.G., Heaton, T.J., Hua, Q., Palmer, J.G., Turney, C.S.M., Southon, J., Bayliss, A., Blackwell, P.G., Boswijk, G., Bronk Ramsey, C., Pearson, C., Petchey, F., Reimer, P., Reimer, R., Wacker, L., 2020. SHCal20 Southern Hemisphere Calibration, 0–55,000 Years cal BP. *Radiocarbon* 62, 759–778. <https://doi.org/DOI: 10.1017/RDC.2020.59>
- Holmes, R., 1983. Computer-Assisted Quality Control in Tree-Ring Dating and Measurement.

- Houze, R.A., 1997. Stratiform Precipitation in Regions of Convection: A Meteorological Paradox? *Bull. Am. Meteorol. Soc.* 78, 2179–2196. [https://doi.org/10.1175/1520-0477\(1997\)078<2179:SPIROC>2.0.CO;2](https://doi.org/10.1175/1520-0477(1997)078<2179:SPIROC>2.0.CO;2)
- Hu, P., Chen, W., Huang, R., Nath, D., 2018. On the weakening relationship between the South China Sea summer monsoon onset and cross-equatorial flow after the late 1990s. *Int. J. Climatol.* 38, 3202–3208. <https://doi.org/10.1002/joc.5472>
- Hua, Q., Barbetti, M., Rakowski, A.Z., 2013. Atmospheric Radiocarbon for the Period 1950–2010. *Radiocarbon* 55, 2059–2072. https://doi.org/10.2458/azu_js_rc.v55i2.16177
- Hua, Q., Turnbull, J.C., Santos, G.M., Rakowski, A.Z., Ancapichún, S., De Pol-Holz, R., Hammer, S., Lehman, S.J., Levin, I., Miller, J.B., Palmer, J.G., Turney, C.S.M., 2022. Atmospheric Radicarbon for the period 1950–2019. *Radiocarbon* 64, 723–745. <https://doi.org/DOI: 10.1017/RDC.2021.95>
- Huang, B., Hu, Z.-Z., Schneider, E.K., Wu, Z., Xue, Y., Klinger, B., 2012. Influences of tropical–extratropical interaction on the multidecadal AMOC variability in the NCEP climate forecast system. *Clim. Dyn.* 39, 531–555. <https://doi.org/10.1007/s00382-011-1258-z>
- Hwang, Y.-T., Frierson, D.M.W., 2013. Link between the double-Intertropical Convergence Zone problem and cloud biases over the Southern Ocean. *Proc. Natl. Acad. Sci.* 110, 4935–4940. <https://doi.org/10.1073/pnas.1213302110>
- IAEA/WMO, 2020. Global Network of Isotopes in Precipitation. The GNIP Database. Accessible at: <https://nucleus.iaea.org/wiser>.
- IAEA/WMO, 2014. Precipitation Sampling guide V2. 02 September 2014.
- Ilbay-Yupa, M., Lavado-Casimiro, W., Rau, P., Zubieto, R., Castillón, F., 2021. Updating regionalization of precipitation in Ecuador. *Theor. Appl. Climatol.* 143, 1513–1528. <https://doi.org/10.1007/s00704-020-03476-x>
- Insel, N., Poulsen, C.J., Ehlers, T.A., 2010. Influence of the Andes Mountains on South American moisture transport, convection, and precipitation. *Clim. Dyn.* 35, 1477–1492. <https://doi.org/10.1007/s00382-009-0637-1>
- IPCC, 2021. Annex V: Monsoons [Cherchi, A., A. Turner (eds.)], in: Masson-Delmotte, V., Zhai, P., Pirani, A., Connors, S.L., Péan, C., Berger, S., Caud, N., Chen, Y., Goldfarb, L., Gomis, M.I., Huang, M., Leitzell, K., Lonnoy, E., Matthews, J.B.R., Maycock, T.K., Waterfield, T., Yelekçi, O., Yu, R., Zhou, B. (Eds.), *Climate Change 2021: The Physical Science Basis. Contribution of Working Group I to the Sixth Assessment Report of the Intergovernmental Panel on Climate Change*. Cambridge University Press, Cambridge, United Kingdom and New York, NY, USA, pp. 2193–2204. <https://doi.org/10.1017/9781009157896.019>
- Irving, D., Hertweck, K., Johnston, L., Ostblom, J., Wickham, C., Wilson, G., 2021. Research Software Engineering with Python: Building software that makes research possible. Chapman and Hall/CRC.
- Jaffey, A.H., Flynn, K.F., Glendenin, L.E., Bentley, W.C., Essling, A.M., 1971. Precision Measurement of Half-Lives and Specific Activities of ^{235}U and ^{238}U . *Phys. Rev. C* 4, 1889–1906. <https://doi.org/10.1103/PhysRevC.4.1889>
- Janovics, R., Futó, I., Molnár, M., 2018. Sealed Tube Combustion Method with MnO_2 for AMS ^{14}C Measurement. *Radiocarbon* 60, 1347–1355. <https://doi.org/10.1017/RDC.2018.110>

- Jiménez-Iñiguez, A., Ampuero, A., Valencia, B.G., Mayta, V.C., Cruz, F.W., Vuille, M., Novello, V.F., Misailidis Stríkis, N., Aranda, N., Conicelli, B., 2022. Stable isotope variability of precipitation and cave drip-water at Jumandy cave, western Amazon River basin (Ecuador). *J. Hydrol.* 610, 127848.
<https://doi.org/10.1016/j.jhydrol.2022.127848>
- Jiménez-Sánchez, G., Markowski, P.M., Young, G.S., Stensrud, D.J., 2020. The Orinoco Low-Level Jet: An Investigation of Its Mechanisms of Formation Using the WRF Model. *J. Geophys. Res. Atmos.* 125, e2020JD032810.
<https://doi.org/10.1029/2020JD032810>
- Jones, C., Carvalho, L.M. V, 2018. The influence of the Atlantic multidecadal oscillation on the eastern Andes low-level jet and precipitation in South America. *npj Clim. Atmos. Sci.* 1, 40. <https://doi.org/10.1038/s41612-018-0050-8>
- Kanner, L.C., Burns, S.J., Cheng, H., Edwards, R.L., Vuille, M., 2013. High-resolution variability of the South American summer monsoon over the last seven millennia: insights from a speleothem record from the central Peruvian Andes. *Quat. Sci. Rev.* 75, 1–10. <https://doi.org/10.1016/j.quascirev.2013.05.008>
- Kaufman, A., Broecker, W., 1965. Comparison of Th230 and C14 ages for carbonate materials from lakes Lahontan and Bonneville. *J. Geophys. Res.* 70, 4039–4054.
<https://doi.org/https://doi.org/10.1029/JZ070i016p04039>
- Kéri, M., Palcsu, L., Túri, M., Heim, E., Czébely, A., Novák, L., Bánya, I., 2015. ¹³C NMR analysis of cellulose samples from different preparation methods. *Cellulose* 22, 2211–2220. <https://doi.org/10.1007/s10570-015-0642-y>
- Kogovšek, J., 2010. Characteristics of percolation through the karst vadose zone. *Založba ZRC*.
- Kuitems, M., Wallace, B.L., Lindsay, C., Scifo, A., Doeve, P., Jenkins, K., Lindauer, S., Erdil, P., Ledger, P.M., Forbes, V., Vermeeren, C., Friedrich, R., Dee, M.W., 2022. Evidence for European presence in the Americas in ad 1021. *Nature* 601, 388–391.
<https://doi.org/10.1038/s41586-021-03972-8>
- Kurita, N., Ichiyangi, K., Matsumoto, J., Yamanaka, M.D., Ohata, T., 2009. The relationship between the isotopic content of precipitation and the precipitation amount in tropical regions. *J. Geochemical Explor.* 102, 113–122.
<https://doi.org/10.1016/j.gexplo.2009.03.002>
- Kwiecien, O., Braun, T., Brunello, C.F., Faulkner, P., Hausmann, N., Helle, G., Hoggarth, J.A., Ionita, M., Jazwa, C., Kelmelis, S., Marwan, N., Nava-Fernandez, C., Nehme, C., Opel, T., Oster, J.L., Perșoiu, A., Petrie, C., Pruffer, K., Saarni, S.M., Wolf, A., Breitenbach, S.F.M., 2021. What we talk about when we talk about seasonality – A transdisciplinary review. *Earth-Science Rev.* 103843.
<https://doi.org/10.1016/j.earscirev.2021.103843>
- Kwon, Y.-O., Frankignoul, C., 2012. Stochastically-driven multidecadal variability of the Atlantic meridional overturning circulation in CCSM3. *Clim. Dyn.* 38, 859–876.
<https://doi.org/10.1007/s00382-011-1040-2>
- Lachniet, M.S., 2009. Climatic and environmental controls on speleothem oxygen-isotope values. *Quat. Sci. Rev.* 28, 412–432.
<https://doi.org/10.1016/j.quascirev.2008.10.021>
- Lambert, F., Delmonte, B., Petit, J.R., Bigler, M., Kaufmann, P.R., Hutterli, M.A., Stocker, T.F., Ruth, U., Steffensen, J.P., Maggi, V., 2008. Dust-climate couplings

- over the past 800,000 years from the EPICA Dome C ice core. *Nature* 452, 616–619. <https://doi.org/10.1038/nature06763>
- Larsson, L.-Å., 2016. CDendro & CooRecorder Program Package for Tree Ring Measurements and Crossdating of the Data, Version 8.1. 1.
- Laskar, J., Robutel, P., Joutel, F., Gastineau, M., Correia, A.C.M., Levrard, B., 2004. A long-term numerical solution for the insolation quantities of the Earth. *Astron. Astrophys.* 428, 261–285. <https://doi.org/10.1051/0004-6361:20041335>
- Layme-Huaman, E.T., Ferrero, M.E., Palacios-Lazaro, K.S., Requena-Rojas, E.J., 2018. Cedrela nebulosa: A novel species for dendroclimatological studies in the montane tropics of South America. *Dendrochronologia* 50, 105–112. <https://doi.org/10.1016/j.dendro.2018.06.004>
- Li, M., Hinnov, L., Kump, L., 2019. Acycle: Time-series analysis software for paleoclimate research and education. *Comput. Geosci.* 127, 12–22. <https://doi.org/10.1016/j.cageo.2019.02.011>
- Liebmann, B., Smith, C.A., 1996. Description of complete (interpolated) outgoing longwave radiation data set. *Bull. Amer. Meteor. Soc.* 77.
- Lima, P., 2019. Uso de Isotopos Estables para el Estudio de las Fuentes de Agua Superficiales en el Ecuador y sus Implicaciones para la Gestión de los Recursos Hídricos. INGENIO 2, 38–45. <https://doi.org/10.29166/ingenio.v2i2.1701>
- Lisiecki, L.E., Raymo, M.E., 2005. A Pliocene-Pleistocene stack of 57 globally distributed benthic $\delta^{18}\text{O}$ records. *Paleoceanography* 20, n/a-n/a. <https://doi.org/10.1029/2004PA001071>
- Lisztes-Szabó, Z., Braun, M., Csík, A., Pető, Á., 2019. Phytoliths of six woody species important in the Carpathians: characteristic phytoliths in Norway spruce needles. *Veg. Hist. Archaeobot.* 28, 649–662. <https://doi.org/10.1007/s00334-019-00720-x>
- Loader, N.J., McCarroll, D., Gagen, M., Robertson, I., Jalkanen, R., 2007. Extracting Climatic Information from Stable Isotopes in Tree Rings, in: *Terrestrial Ecology*. Elsevier, pp. 25–48. [https://doi.org/10.1016/S1936-7961\(07\)01003-2](https://doi.org/10.1016/S1936-7961(07)01003-2)
- Lorenz, S.J., Kim, J.-H., Rimbu, N., Schneider, R.R., Lohmann, G., 2006. Orbitally driven insolation forcing on Holocene climate trends: Evidence from alkenone data and climate modeling. *Paleoceanography* 21. <https://doi.org/https://doi.org/10.1029/2005PA001152>
- Lu, J., Vecchi, G.A., 2015. *TROPICAL METEOROLOGY & Climate: Hadley Circulation*. J Pyle and F Zhang; Elsevier Ltd., Waltham, MA, United States(US).., United States.
- Luciene Dias de Melo, M., Marengo, J.A., 2008. The influence of changes in orbital parameters over South American climate using the CPTEC AGCM: simulation of climate during the mid Holocene. *The Holocene* 18, 501–516. <https://doi.org/10.1177/0959683608089205>
- Magurran, A.E., 2013. *Measuring biological diversity*. John Wiley & Sons, Oxford, United Kingdom.
- Makowski Giannoni, S., Trachte, K., Rollenbeck, R., Lehnert, L., Fuchs, J., Bendix, J., 2016. Atmospheric salt deposition in a tropical mountain rainforest at the eastern Andean slopes of south Ecuador – Pacific or Atlantic origin? *Atmos. Chem. Phys.* 16, 10241–10261. <https://doi.org/10.5194/acp-16-10241-2016>
- Mallapaty, S., 2022. Why are Pakistan's floods so extreme this year? *Nature*.

- https://doi.org/10.1038/d41586-022-02813-6
- Managave, S.R., Ramesh, R., 2012. Isotope Dendroclimatology: A Review with a Special Emphasis on Tropics, in: Earth System Science Data Discussions. Copernicus GmbH, pp. 811–833. https://doi.org/10.1007/978-3-642-10637-8_38
- Mann, M.E., Lees, J.M., 1996. Robust estimation of background noise and signal detection in climatic time series. *Clim. Change* 33, 409–445.
https://doi.org/10.1007/BF00142586
- Mann, M.E., Park, J., 1994. Global-scale modes of surface temperature variability on interannual to century timescales. *J. Geophys. Res. Atmos.* 99, 25819–25833.
https://doi.org/https://doi.org/10.1029/94JD02396
- Mann, M.E., Park, J., Bradley, R.S., 1995. Global interdecadal and century-scale climate oscillations during the past five centuries. *Nature* 378, 266–270.
https://doi.org/10.1038/378266a0
- Mann, M.E., Steinman, B.A., Brouillette, D.J., Miller, S.K., 2021. Multidecadal climate oscillations during the past millennium driven by volcanic forcing. *Science* (80-.). 371, 1014–1019. https://doi.org/10.1126/science.abc5810
- Mann, M.E., Steinman, B.A., Miller, S.K., 2020. Absence of internal multidecadal and interdecadal oscillations in climate model simulations. *Nat. Commun.* 11, 49.
https://doi.org/10.1038/s41467-019-13823-w
- Maraun, D., Kurths, J., 2004. Cross wavelet analysis: significance testing and pitfalls. *Nonlinear Process. Geophys.* 11, 505–514. https://doi.org/10.5194/npg-11-505-2004
- Marsh, E.J., Bruno, M.C., Fritz, S.C., Baker, P., Capriles, J.M., Hastorf, C.A., 2018. IntCal, SHCal, or a Mixed Curve? Choosing a 14C Calibration Curve for Archaeological and Paleoenvironmental Records from Tropical South America. *Radiocarbon* 60, 925–940. https://doi.org/DOI: 10.1017/RDC.2018.16
- Marsh, E.J., Kidd, R., Ogburn, D., Durán, V., 2017. Dating the Expansion of the Inca Empire: Bayesian Models from Ecuador and Argentina. *Radiocarbon* 59, 117–140.
https://doi.org/DOI: 10.1017/RDC.2016.118
- Martinez, J.A., Arias, P.A., Junquas, C., Espinoza, J.C., Condom, T., Dominguez, F., Morales, J.S., 2022. The Orinoco Low-level Jet and the Cross-Equatorial Moisture Transport over tropical South America: lessons from seasonal WRF simulations. *J. Geophys. Res. Atmos.* e2021JD035603. https://doi.org/10.1029/2021JD035603
- Matsumoto, J., Murakami, T., 2000. Annual Changes of Tropical Convective Activities as Revealed from Equatorially Symmetric OLR Data. *J. Meteorol. Soc. Japan. Ser. II* 78, 543–561. https://doi.org/10.2151/jmsj1965.78.5_543
- McCarroll, D., Loader, N.J., 2004. Stable isotopes in tree rings. *Quat. Sci. Rev.* 23, 771–801. https://doi.org/10.1016/j.quascirev.2003.06.017
- McGee, D., Donohoe, A., Marshall, J., Ferreira, D., 2014. Changes in ITCZ location and cross-equatorial heat transport at the Last Glacial Maximum, Heinrich Stadial 1, and the mid-Holocene. *Earth Planet. Sci. Lett.* 390, 69–79.
https://doi.org/https://doi.org/10.1016/j.epsl.2013.12.043
- Medina, N.M.M., Cruz, F.W., Winter, A., Zhang, H., Ampuero, A., Vuille, M., Mayta, V.C., Campos, M.C., Rámirez, V.M., Utida, G., Zúñiga, A.C., Cheng, H., 2023. Atlantic ITCZ variability during the Holocene based on high-resolution speleothem isotope records from northern Venezuela. *Quat. Sci. Rev.* 307, 108056.
https://doi.org/https://doi.org/10.1016/j.quascirev.2023.108056

- Meko, D.M., Touchan, R., Anchukaitis, K.J., 2011. Seascorr: A MATLAB program for identifying the seasonal climate signal in an annual tree-ring time series. *Comput. Geosci.* 37, 1234–1241. <https://doi.org/10.1016/j.cageo.2011.01.013>
- Mélice, J.L., Roucou, P., 1998. Decadal time scale variability recorded in the Quelccaya summit ice core $\delta^{18}\text{O}$ isotopic ratio series and its relation with the sea surface temperature. *Clim. Dyn.* 14, 117–132. <https://doi.org/10.1007/s003820050213>
- Molnár, M., Janovics, R., Major, I., Orsovszki, J., Gönczi, R., Veres, M., Leonard, A.G., Castle, S.M., Lange, T.E., Wacker, L., Hajdas, I., Julll, A.J.T., 2013a. Status Report of the New AMS ^{14}C Sample Preparation Lab of the Hertelendi Laboratory of Environmental Studies (Debrecen, Hungary). *Radiocarbon* 55, 665–676. https://doi.org/10.2458/azu_js_rc.55.16394
- Molnár, M., Rinyu, L., Veres, M., Seiler, M., Wacker, L., Synal, H.-A., 2013b. EnvironMICADAS: A Mini ^{14}C AMS with Enhanced Gas Ion Source Interface in the Hertelendi Laboratory of Environmental Studies (HEKAL), Hungary. *Radiocarbon* 55, 338–344. <https://doi.org/10.1017/S0033822200057453>
- Mosblech, N.A.S., Bush, M.B., Gosling, W.D., Hodell, D., Thomas, L., van Calsteren, P., Correa-Metrio, A., Valencia, B.G., Curtis, J., van Woesik, R., 2012. North Atlantic forcing of Amazonian precipitation during the last ice age. *Nat. Geosci.* 5, 817–820. <https://doi.org/10.1038/ngeo1588>
- Mosquera, G.M., Segura, C., Vaché, K.B., Windhorst, D., Breuer, L., Crespo, P., 2016. Insights into the water mean transit time in a high-elevation tropical ecosystem. *Hydrol. Earth Syst. Sci.* 20, 2987–3004. <https://doi.org/10.5194/hess-20-2987-2016>
- Mudelsee, M., 2019. Trend analysis of climate time series: A review of methods. *Earth-Science Rev.* 190, 310–322. <https://doi.org/https://doi.org/10.1016/j.earscirev.2018.12.005>
- Mudelsee, M., 2014. Climate time series analysis, in: *Climate Time Series Analysis*. Springer, pp. 217–267.
- Mudelsee, M., 2002. TAUEST: A computer program for estimating persistence in unevenly spaced weather/climate time series. *Comput. Geosci.* 28, 69–72.
- Mudelsee, M., 2001. Statistical Analysis in Climate Research-Hans von Storch and Francis W. Zwiers; Cambridge University Press, Cambridge, 1999, x+ 484pp., US \$110, ISBN 0-521-45071-3 (hardback). *Comput. Geosci.* 27, 371–373.
- Murakami, T., Nakazawa, T., 1985. Transition from the Southern to Northern Hemisphere Summer Monsoon. *Mon. Weather Rev.* 113, 1470–1486. [https://doi.org/10.1175/1520-0493\(1985\)113<1470:TFTSTN>2.0.CO;2](https://doi.org/10.1175/1520-0493(1985)113<1470:TFTSTN>2.0.CO;2)
- Nacimba, M., 2015. Crecimiento y dendrocronología de Cedrela Odorata en un bosque de la Amazonía ecuatoriana. Pontificia Universidad Católica del Ecuador.
- Nissen, J.A., 2018. High-resolution speleothem record of climate variability during the late Pleistocene from Spring Valley Caverns, Minnesota. University of Minnesota.
- NOAA, 2022. National Centers for Environmental Information: Global Historical Climatology Network (GHCN) [WWW Document]. URL <https://www.ncei.noaa.gov/products/land-based-station/global-historical-climatology-network-monthly> (accessed 4.11.22).
- Noble, W.S., 2009. A Quick Guide to Organizing Computational Biology Projects. *PLoS Comput. Biol.* 5, e1000424. <https://doi.org/10.1371/journal.pcbi.1000424>
- North, G.R., Pyle, J.A., Zhang, F., 2014. *Encyclopedia of atmospheric sciences*. Elsevier.

- Ogburn, D.E., 2012. Reconceiving the Chronology of Inca Imperial Expansion. *Radiocarbon* 54, 219–237. https://doi.org/10.2458/azu_js_rc.v54i2.16014
- Otoničar, B., 2021. Speleogenesis and depositional history of paleokarst phreatic caves/cavities; Podgrad, SW Slovenia. *Acta Carsologica* 50. <https://doi.org/10.3986/ac.vi.9945>
- Palacios, W.A., 2016. Árboles del Ecuador: Familias y Géneros. Editorial UTN.
- Palacios, W.A., 2007. Flora of Ecuador, Volume 82: Meliaceae. Göteborg: Department of Plant and Environmental Sciences.
- Palacios, W.A., Santiana, J., Iglesias, J., 2019. A new species of Cedrela (Meliaceae) from the eastern flanks of Ecuador. *Phytotaxa* 393, 84. <https://doi.org/10.11646/phytotaxa.393.1.8>
- Palcsu, L., Temovski, M., Vargas, D., Kiss, G.I., Surányi, G., 2022. A new U-Th laboratory for dating speleothems, in: Climate Change: The Karst Record IX (KR9). p. 120.
- Pennington, T.D., Muellner, A.N., 2010. A monograph of Cedrela (Meliaceae). DH Books, Sherborne, UK.
- Percival, D.B., Walden, A.T., 1993. Spectral Analysis for Physical Applications. Cambridge University Press. <https://doi.org/10.1017/CBO9780511622762>
- Petit, J.R., Jouzel, J., Raynaud, D., Barkov, N.I., Barnola, J.-M., Basile, I., Bender, M., Chappellaz, J., Davis, M., Delaygue, G., Delmotte, M., Kotlyakov, V.M., Legrand, M., Lipenkov, V.Y., Lorius, C., PÉpin, L., Ritz, C., Saltzman, E., Steinenard, M., 1999. Climate and atmospheric history of the past 420,000 years from the Vostok ice core, Antarctica. *Nature* 399, 429–436. <https://doi.org/10.1038/20859>
- Phipps, R.L., 1985. Collecting, Preparing, Crossdating, and Measuring Tree Increment Cores. US Geol. Surv. Water Resour. Investig. Rep. 85-4148 48.
- Poussait, P.M., Myneni, S.C.B., Lanzirotti, A., 2006. Tropical dendrochemistry: A novel approach to estimate age and growth from ringless trees. *Geophys. Res. Lett.* 33, 1–5. <https://doi.org/10.1029/2006GL026929>
- Poveda, G., Jaramillo, L., Vallejo, L.F., 2014. Seasonal precipitation patterns along pathways of South American low-level jets and aerial rivers. *Water Resour. Res.* 50, 98–118. <https://doi.org/10.1002/2013WR014087>
- Poveda, G., Mesa, O., 1999. La corriente de chorro superficial del Oeste (“del Chocó”) y otras dos corrientes de chorro en Colombia: climatología y variabilidad durante las fases del ENSO. *Rev. Académica Colomb. Cienc.* 23, 517–528.
- Poveda, G., Waylen, P.R., Pulwarty, R.S., 2006. Annual and inter-annual variability of the present climate in northern South America and southern Mesoamerica. *Palaeogeogr. Palaeoclimatol. Palaeoecol.* 234, 3–27. <https://doi.org/10.1016/j.palaeo.2005.10.031>
- Prado, L.F., Wainer, I., Chiessi, C.M., Ledru, M.-P., Turcq, B., 2013. A mid-Holocene climate reconstruction for eastern South America. *Clim. Past* 9, 2117–2133. <https://doi.org/10.5194/cp-9-2117-2013>
- Pucha-Cofrep, D., Peters, T., Bräuning, A., 2015. Wet season precipitation during the past century reconstructed from tree-rings of a tropical dry forest in Southern Ecuador. *Glob. Planet. Change* 133, 65–78. <https://doi.org/10.1016/j.gloplacha.2015.08.003>
- R Core Team, 2020. R: A language and environment for statistical computing.

- Raia, A., Cavalcanti, I.F.A., 2008. The Life Cycle of the South American Monsoon System. *J. Clim.* 21, 6227–6246. <https://doi.org/10.1175/2008JCLI2249.1>
- Railsback, L.B., Gibbard, P.L., Head, M.J., Voarintsoa, N.R.G., Toucanne, S., 2015. An optimized scheme of lettered marine isotope substages for the last 1.0 million years, and the climatostratigraphic nature of isotope stages and substages. *Quat. Sci. Rev.* 111, 94–106. <https://doi.org/10.1016/j.quascirev.2015.01.012>
- Ramage, C.S., 1971. Monsoon meteorology.
- Ramirez, E., 2003. Interprétation de la variaibilité climatique enregistrée dans les carottes de glace à partir des isotopes stables de l'eau: cas des Andes tropicales. Paris 6.
- Reimer, P.J., Brown, T.A., Reimer, R.W., 2004. Discussion: Reporting and Calibration of Post-Bomb ^{14}C Data. *Radiocarbon* 46, 1299–1304. <https://doi.org/10.1017/S0033822200033154>
- Reimer, P.J., Reimer, R., 2004. CALIBomb radiocarbon calibration. *Interact. Progr.* available on-line <http://intcal.qub.ac.uk/CALIBomb/frameset.html>.
- Richards, D.A., Dorale, J.A., 2003. Uranium-series Chronology and Environmental Applications of Speleothems. *Rev. Mineral. Geochemistry* 52, 407–460. <https://doi.org/10.2113/0520407>
- Rincón-Martínez, D., Lamy, F., Contreras, S., Leduc, G., Bard, E., Saukel, C., Blanz, T., Mackensen, A., Tiedemann, R., 2010. More humid interglacials in Ecuador during the past 500 kyr linked to latitudinal shifts of the equatorial front and the Intertropical Convergence Zone in the eastern tropical Pacific. *Paleoceanography* 25. <https://doi.org/10.1029/2009PA001868>
- Rinn, F., 2012. TSAPWin scientific: time series analysis and presentation for dendrochronology and related applications.
- Rinyu, L., Molnár, M., Major, I., Nagy, T., Veres, M., Kimák, Á., Wacker, L., Synal, H.-A., 2013. Optimization of Sealed Tube Graphitization Method for Environmental ^{14}C Studies Using MICADAS. *Nucl. Instruments Methods Phys. Res. Sect. B Beam Interact. with Mater. Atoms* 294, 270–275. <https://doi.org/10.1016/j.nimb.2012.08.042>
- Risi, C., Bony, S., Vimeux, F., Jouzel, J., 2010. Water-stable isotopes in the LMDZ4 general circulation model: Model evaluation for present-day and past climates and applications to climatic interpretations of tropical isotopic records. *J. Geophys. Res.* 115, D12118. <https://doi.org/10.1029/2009JD013255>
- Robinson, A., 2011. History: How Earth shaped up. *Nature* 476, 149–150. <https://doi.org/10.1038/476149a>
- Rodbell, D.T., Seltzer, G.O., Anderson, D.M., Abbott, M.B., Enfield, D.B., Newman, J.H., 1999. An ~15,000-Year Record of El Niño-Driven Alluviation in Southwestern Ecuador. *Science* (80-.). 283, 516–520. <https://doi.org/10.1126/science.283.5401.516>
- Rodríguez-Gómez, C., Echeverry, G., Jaramillo, A., Ladino, L.A., 2021. The Negative Impact of Biomass Burning and the Orinoco Low-Level Jet on the Air Quality of the Orinoco River Basin. *Atmósfera*. <https://doi.org/10.20937/ATM.52979>
- Rohde, R.A., Hausfather, Z., 2020. The Berkeley Earth Land/Ocean Temperature Record. *Earth Syst. Sci. Data* 12, 3469–3479. <https://doi.org/10.5194/essd-12-3469-2020>
- Rojas, M., Arias, P.A., Flores-Aqueveque, V., Seth, A., Vuille, M., 2016. The South American monsoon variability over the last millennium in climate models. *Clim.*

- Past 12, 1681–1691. <https://doi.org/10.5194/cp-12-1681-2016>
- Rozanski, K., Araguás-Araguás, L., 1995. Spatial and temporal variability of stable isotope composition of precipitation over the South American continent. Bull. l’Institut Français d’études Andin. 24, 379–390.
- Ruiz-Vásquez, M., Arias, P.A., Martínez, J.A., Espinoza, J.C., 2020. Effects of Amazon basin deforestation on regional atmospheric circulation and water vapor transport towards tropical South America. Clim. Dyn. 54, 4169–4189. <https://doi.org/10.1007/s00382-020-05223-4>
- Salati, E., Dall’Olio, A., Matsui, E., Gat, J.R., 1979. Recycling of water in the Amazon basin: an isotopic study. Water Resour. Res. 15, 1250–1258.
- Santos, G.M., Granato-Souza, D., Barbosa, A.C., Oelkers, R., Andreu-Hayles, L., 2020. Radiocarbon analysis confirms annual periodicity in *Cedrela odorata* tree rings from the equatorial Amazon. Quat. Geochronol. 58, 101079. <https://doi.org/10.1016/j.quageo.2020.101079>
- Saurer, M., Borella, S., Schweingruber, F., Siegwolf, R., 1997. Stable carbon isotopes in tree rings of beech: climatic versus site-related influences. Trees 11, 291. <https://doi.org/10.1007/s004680050087>
- Saurer, M., Robertson, I., Siegwolf, R., Leuenberger, M., 1998. Oxygen Isotope Analysis of Cellulose: An Interlaboratory Comparison. Anal. Chem. 70, 2074–2080. <https://doi.org/10.1021/ac971022f>
- Saurer, M., Sahlstedt, E., Rinne-Garmston, K.T., Lehmann, M.M., Oettli, M., Gessler, A., Treydte, K., 2022. Progress in high-resolution isotope-ratio analysis of tree rings using laser ablation. Tree Physiol. <https://doi.org/10.1093/treephys/tpac141>
- Schneider, T., Bischoff, T., Haug, G.H., 2014. Migrations and dynamics of the intertropical convergence zone. Nature 513, 45–53. <https://doi.org/10.1038/nature13636>
- Scholz, D., Hoffmann, D., 2008. 230Th/U-dating of fossil corals and speleothems. E&G Quat. Sci. J. 57, 52–76.
- Scholz, D., Hoffmann, D.L., 2011. StalAge – An algorithm designed for construction of speleothem age models. Quat. Geochronol. 6, 369–382. <https://doi.org/10.1016/j.quageo.2011.02.002>
- Schulz, M., Mudelsee, M., 2002. REDFIT: estimating red-noise spectra directly from unevenly spaced paleoclimatic time series. Comput. Geosci. 28, 421–426. [https://doi.org/https://doi.org/10.1016/S0098-3004\(01\)00044-9](https://doi.org/https://doi.org/10.1016/S0098-3004(01)00044-9)
- Schulz, M., Stattegger, K., 1997. Spectrum: spectral analysis of unevenly spaced paleoclimatic time series. Comput. Geosci. 23, 929–945. [https://doi.org/https://doi.org/10.1016/S0098-3004\(97\)00087-3](https://doi.org/https://doi.org/10.1016/S0098-3004(97)00087-3)
- Schwarcz, H., 2013. Carbonate Stable Isotopes | Speleothems, in: Encyclopedia of Quaternary Science. Elsevier, pp. 294–303. <https://doi.org/10.1016/B978-0-444-53643-3.00339-3>
- Segura, H., Espinoza, J.C., Junquas, C., Lebel, T., Vuille, M., Garreaud, R., 2020. Recent changes in the precipitation-driving processes over the southern tropical Andes/western Amazon. Clim. Dyn. 54, 2613–2631. <https://doi.org/10.1007/s00382-020-05132-6>
- Seidel, D.J., Fu, Q., Randel, W.J., Reichler, T.J., 2008. Widening of the tropical belt in a changing climate. Nat. Geosci. 1, 21–24. <https://doi.org/10.1038/ngeo.2007.38>

- Sharp, Z., 2017. Principles of stable isotope geochemistry.
<https://doi.org/doi.org/10.25844/h9q1-0p82>
- Shimizu, M.H., Sampaio, G., Venancio, I.M., Maksic, J., 2020. Seasonal changes of the South American monsoon system during the Mid-Holocene in the CMIP5 simulations. *Clim. Dyn.* 54, 2697–2712. <https://doi.org/10.1007/s00382-020-05137-1>
- Shumway, R.H., Stoffer, D.S., 2017. Time Series Analysis and Its Applications, Springer Texts in Statistics. Springer International Publishing, Cham.
<https://doi.org/10.1007/978-3-319-52452-8>
- Siegwolf, R.T.W., Brooks, J.R., Roden, J., Saurer, M., 2022. Stable Isotopes in Tree Rings, Tree Physiology. Springer International Publishing, Cham.
<https://doi.org/10.1007/978-3-030-92698-4>
- Silva Dias, P.L., Turcq, B., Silva Dias, M.A.F., Braconnot, P., Jorgetti, T., 2009. Mid-Holocene Climate of Tropical South America: A Model-Data Approach BT - Past Climate Variability in South America and Surrounding Regions: From the Last Glacial Maximum to the Holocene, in: Vimeux, F., Sylvestre, F., Khodri, M. (Eds.), Springer Netherlands, Dordrecht, pp. 259–281. https://doi.org/10.1007/978-90-481-2672-9_11
- Simpson, E.H., 1949. Measurement of Diversity. *Nature* 163, 688–688.
<https://doi.org/10.1038/163688a0>
- Slingo, J., 2015. Tropical Meteorology and Climate | Monsoon: Overview, in: North, G.R., Pyle, J., Zhang, F. (Eds.), Encyclopedia of Atmospheric Sciences (Second Edition). Academic Press, Oxford, pp. 146–150.
<https://doi.org/https://doi.org/10.1016/B978-0-12-382225-3.00235-8>
- Sodemann, H., 2006. Tropospheric transport of water vapour: Lagrangian and Eulerian perspectives. ETH Zurich.
- Sodemann, H., Schwierz, C., Wernli, H., 2008. Interannual variability of Greenland winter precipitation sources: Lagrangian moisture diagnostic and North Atlantic Oscillation influence. *J. Geophys. Res.* 113, D03107.
<https://doi.org/10.1029/2007JD008503>
- Speer, J.H., 2010. Fundamentals of tree-ring research. University of Arizona Press.
- Stein, A.F., Draxler, R.R., Rolph, G.D., Stunder, B.J.B., Cohen, M.D., Ngan, F., 2015. NOAA's HYSPLIT Atmospheric Transport and Dispersion Modeling System. *Bull. Am. Meteorol. Soc.* 96, 2059–2077. <https://doi.org/10.1175/BAMS-D-14-00110.1>
- Stokes, M.A., Smiley, T.L., 1968. An introduction to tree-ring dating. University of Chicago Press, Chicago, IL.
- Storch, H. von, Zwiers, F.W., 1999. Statistical Analysis in Climate Research. Cambridge University Press. <https://doi.org/10.1017/CBO9780511612336>
- Strikis, N.M., Cruz, F.W., Cheng, H., Karmann, I., Edwards, R.L., Vuille, M., Wang, X., de Paula, M.S., Novello, V.F., Auler, A.S., 2011. Abrupt variations in South American monsoon rainfall during the Holocene based on a speleothem record from central-eastern Brazil. *Geology* 39, 1075–1078. <https://doi.org/10.1130/G32098.1>
- Stull, R.B., 2020. A Simplified Description of the Global Circulation.
- Sturm, C., Hoffmann, G., Langmann, B., 2007a. Simulation of the Stable Water Isotopes in Precipitation over South America: Comparing Regional to Global Circulation Models. *J. Clim.* 20, 3730–3750. <https://doi.org/10.1175/JCLI4194.1>

- Sturm, C., Vimeux, F., Krinner, G., 2007b. Intraseasonal variability in South America recorded in stable water isotopes. *J. Geophys. Res.* 112, D20118. <https://doi.org/10.1029/2006JD008298>
- Suntaxi, F., Jiménez, E., 2011. Aproximación dendroclimatológica, en un Bosque Seco utilizando la Especie Guasmo (*Guazuma ulmifolia*) y su Relación con la Precipitación y la Temperatura en el Período 1974-2007. *Rev. Tecnológica-ESPOL* 24.
- Tada, M., Yoshimura, K., Toride, K., 2021. Improving weather forecasting by assimilation of water vapor isotopes. *Sci. Rep.* 11, 18067. <https://doi.org/10.1038/s41598-021-97476-0>
- Tans, P., Keeling, R., 2020. NOAA/GML Trends in Atmospheric Carbon Dioxide [WWW Document]. URL <https://www.esrl.noaa.gov/gmd/ccgg/trends/data.html> (accessed 3.15.21).
- Temovski, M., Rinyu, L., Futó, I., Molnár, K., Túri, M., Demény, A., Otoničar, B., Dublyansky, Y., Audra, P., Polyak, V., Asmerom, Y., Palcsu, L., 2022. Combined use of conventional and clumped carbonate stable isotopes to identify hydrothermal isotopic alteration in cave walls. *Sci. Rep.* 12, 9202. <https://doi.org/10.1038/s41598-022-12929-4>
- Templeton, M., 2004. Time-series analysis of variable star data. *J. Am. Assoc. Var. Star Obs.* vol. 32, no. 1, p. 41-54 32, 41–54.
- Thompson, L.G., Davis, M.E., 2007. ICE CORE RECORDS | South America, in: Encyclopedia of Quaternary Science. Elsevier, pp. 1233–1242. <https://doi.org/https://doi.org/10.1016/B0-44-452747-8/00349-5>
- Thompson, L.G., Mosley-Thompson, E., Davis, M.E., Lin, P.-N., Henderson, K.A., Cole-Dai, J., Bolzan, J.F., Liu, K., 1995. Late Glacial Stage and Holocene Tropical Ice Core Records from Huascarán, Peru. *Science* (80-.). 269, 46–50. <https://doi.org/10.1126/science.269.5220.46>
- Thompson, L.G., Mosley-Thompson, E., Henderson, K.A., 2000. Ice-core palaeoclimate records in tropical South America since the Last Glacial Maximum. *J. Quat. Sci.* 15, 377–394. [https://doi.org/https://doi.org/10.1002/1099-1417\(200005\)15:4<377::AID-JQS542>3.0.CO;2-L](https://doi.org/https://doi.org/10.1002/1099-1417(200005)15:4<377::AID-JQS542>3.0.CO;2-L)
- Timbe, E., Windhorst, D., Crespo, P., Frede, H.-G., Feyen, J., Breuer, L., 2014. Understanding uncertainties when inferring mean transit times of water trough tracer-based lumped-parameter models in Andean tropical montane cloud forest catchments. *Hydrol. Earth Syst. Sci.* 18, 1503–1523. <https://doi.org/10.5194/hess-18-1503-2014>
- Torrence, C., Compo, G.P., 1998. A Practical Guide to Wavelet Analysis. *Bull. Am. Meteorol. Soc.* 79, 61–78. [https://doi.org/10.1175/1520-0477\(1998\)079<0061:APGTWA>2.0.CO;2](https://doi.org/10.1175/1520-0477(1998)079<0061:APGTWA>2.0.CO;2)
- Toulkeridis, Theofilos, Addison, Aaron, Constantin, Silviu, Winkler, E., Toomey III, R., Osburn, R., Simón Baile, D., Toulkeridis, T, Constantin, S, Addison, A, 2015. Espeleología en Tena, Napo. Un breve inventario geológico y cartográfico, in: 3er Simposio Internacional de Espeleología En El Ecuador-Tena. Boletín Científico. Imprenta de La Universidad de Las Fuerzas Armadas-ESPE, Sangolquí. pp. 26–67.
- Trachte, K., 2018. Atmospheric Moisture Pathways to the Highlands of the Tropical Andes: Analyzing the Effects of Spectral Nudging on Different Driving Fields for

- Regional Climate Modeling. *Atmosphere* (Basel). 9, 456.
<https://doi.org/10.3390/atmos9110456>
- Trauth, M.H., 2021. Spectral analysis in Quaternary sciences. *Quat. Sci. Rev.* 270, 107157. <https://doi.org/10.1016/j.quascirev.2021.107157>
- Treydte, K., Boda, S., Graf Pannatier, E., Fonti, P., Frank, D., Ullrich, B., Saurer, M., Siegwolf, R., Battipaglia, G., Werner, W., Gessler, A., 2014. Seasonal transfer of oxygen isotopes from precipitation and soil to the tree ring: source water versus needle water enrichment. *New Phytol.* 202, 772–783.
<https://doi.org/10.1111/nph.12741>
- Tropicos.org, 2020. Accessible at: www.tropicos.org/home.
- Trouet, V., Van Oldenborgh, G.J., 2013. KNMI Climate Explorer: A Web-Based Research Tool for High-Resolution Paleoclimatology. *Tree-Ring Res.* 69, 3–13.
<https://doi.org/10.3959/1536-1098-69.1.3>
- Túri, M., Hubay, K., Molnár, M., Braun, M., László, E., Futó, I., Palcsu, L., 2021. Holocene paleoclimate reconstruction based on stable isotope results of Sphagnum cellulose, Mohos peat bog, Romania. *J. Paleolimnol.*
- Valdes, P., Braconnot, P., Meissner, K., Eggleston, S., 2021. 29 (2): Paleoclimate Modelling Intercomparison Project (PMIP): 30th anniversary. *Past Glob. Chang. Mag.* 29(2) 61–108. <https://doi.org/https://doi.org/10.22498/pages.29.2>
- van Breukelen, M.R., Vonhof, H.B., Hellstrom, J.C., Wester, W.C.G., Kroon, D., 2008. Fossil dripwater in stalagmites reveals Holocene temperature and rainfall variation in Amazonia. *Earth Planet. Sci. Lett.* 275, 54–60.
<https://doi.org/10.1016/j.epsl.2008.07.060>
- van der Sleen, P., Zuidema, P.A., Pons, T.L., 2017. Stable isotopes in tropical tree rings: theory, methods and applications. *Funct. Ecol.* 31, 1674–1689.
<https://doi.org/10.1111/1365-2435.12889>
- Veblen, T.T., Young, K.R., Orme, A.R., 2015. The physical geography of South America. Oxford University Press.
- Villacís, M., Vimeux, F., Taupin, J.D., 2008. Analysis of the climate controls on the isotopic composition of precipitation ($\delta^{18}\text{O}$) at Nuevo Rocafuerte, 74.5°W, 0.9°S, 250 m, Ecuador. *Comptes Rendus Geosci.* 340, 1–9.
<https://doi.org/10.1016/j.crte.2007.11.003>
- Vimeux, F., Gallaire, R., Bony, S., Hoffmann, G., Chiang, J.C.H., 2005. What are the climate controls on δD in precipitation in the Zongo Valley (Bolivia)? Implications for the Illimani ice core interpretation. *Earth Planet. Sci. Lett.* 240, 205–220.
<https://doi.org/10.1016/j.epsl.2005.09.031>
- Volland, F., Pucha, D., Bräuning, A., 2015. Hydro-climatic variability in southern Ecuador reflected by tree-ring oxygen isotopes. *Erdkunde* 70, 69–82.
<https://doi.org/10.3112/erdkunde.2016.01.05>
- Vuille, M., Bradley, R.S., Werner, M., Healy, R., Keimig, F., 2003. Modeling $\delta^{18}\text{O}$ in precipitation over the tropical Americas: 1. Interannual variability and climatic controls. *J. Geophys. Res. Atmos.* 108.
<https://doi.org/doi.org/10.1029/2001JD002038>
- Vuille, M., Burns, S.J., Taylor, B.L., Cruz, F.W., Bird, B.W., Abbott, M.B., Kanner, L.C., Cheng, H., Novello, V.F., 2012. A review of the South American monsoon history as recorded in stable isotopic proxies over the past two millennia. *Clim. Past*

- 8, 1309–1321. <https://doi.org/10.5194/cp-8-1309-2012>
- Waliser, D.E., Jiang, X., 2015. Intertropical Convergence Zone, in: Encyclopedia of Atmospheric Sciences. Elsevier, pp. 121–131. <https://doi.org/10.1016/B978-0-12-382225-3.00417-5>
- Wang, B., Ding, Q., 2008. Global monsoon: Dominant mode of annual variation in the tropics. *Dyn. Atmos. Ocean.* 44, 165–183.
<https://doi.org/10.1016/j.dynatmoce.2007.05.002>
- Wang, H., Fu, R., 2002. Cross-Equatorial Flow and Seasonal Cycle of Precipitation over South America. *J. Clim.* 15, 1591–1608. [https://doi.org/10.1175/1520-0442\(2002\)015<1591:CEFASC>2.0.CO;2](https://doi.org/10.1175/1520-0442(2002)015<1591:CEFASC>2.0.CO;2)
- Wang, P.X., Wang, B., Cheng, H., Fasullo, J., Guo, Z., Kiefer, T., Liu, Z., 2017. The global monsoon across time scales: Mechanisms and outstanding issues. *Earth-Science Rev.* 174, 84–121. <https://doi.org/10.1016/j.earscirev.2017.07.006>
- Wang, P.X., Wang, B., Cheng, H., Fasullo, J., Guo, Z.T., Kiefer, T., Liu, Z.Y., 2014. The global monsoon across timescales: coherent variability of regional monsoons. *Clim. Past* 10, 2007–2052. <https://doi.org/10.5194/cp-10-2007-2014>
- Wanner, H., Beer, J., Bütkofer, J., Crowley, T.J., Cubasch, U., Flückiger, J., Goosse, H., Grosjean, M., Joos, F., Kaplan, J.O., Küttel, M., Müller, S.A., Prentice, I.C., Solomina, O., Stocker, T.F., Tarasov, P., Wagner, M., Widmann, M., 2008. Mid- to Late Holocene climate change: an overview. *Quat. Sci. Rev.* 27, 1791–1828.
<https://doi.org/https://doi.org/10.1016/j.quascirev.2008.06.013>
- Wanner, H., Buetikofer, J., 2008. Holocene Bond Cycles: real or imaginary. *Geografie* 113, 338–349.
- Warner, M.S.C., 2018. Introduction to PySPLIT: A Python Toolkit for NOAA ARL's HYSPLIT Model. *Comput. Sci. Eng.* 20, 47–62.
<https://doi.org/10.1109/MCSE.2017.3301549>
- Webster, P.J., Fasullo, J., 2015. Tropical Meteorology and Climate | Monsoon: Dynamical Theory, in: Encyclopedia of Atmospheric Sciences. Elsevier, pp. 151–164. <https://doi.org/10.1016/B978-0-12-382225-3.00236-X>
- Wendt, K.A., Li, X., Edwards, R.L., Cheng, H., Spötl, C., 2021. Precise timing of MIS 7 substages from the Austrian Alps. *Clim. Past* 17, 1443–1454.
<https://doi.org/10.5194/cp-17-1443-2021>
- Werner, M., 2019. ECHAM5-wiso simulation data - present-day, mid-Holocene, and Last Glacial Maximum. <https://doi.org/10.1594/PANGAEA.902347>
- Werner, M., Langebroek, P.M., Carlsen, T., Herold, M., Lohmann, G., 2011. Stable water isotopes in the ECHAM5 general circulation model: Toward high-resolution isotope modeling on a global scale. *J. Geophys. Res.* 116, D15109.
<https://doi.org/10.1029/2011JD015681>
- White, W.B., 2019. Chapter 117 - Speleothems, in: White, W.B., Culver, D.C., Pipan, T. (Eds.), Encyclopedia of Caves (Third Edition). Academic Press, pp. 1006–1017.
<https://doi.org/https://doi.org/10.1016/B978-0-12-814124-3.00117-5>
- Wigley, T.M.L., Briffa, K.R., Jones, P.D., 1984. On the average value of correlated time series with applications in dendroclimatology and hydrometeorology. *J. Clim. Appl. Meteorol.* [https://doi.org/10.1175/1520-0450\(1984\)023<0201:OTAVOC>2.0.CO;2](https://doi.org/10.1175/1520-0450(1984)023<0201:OTAVOC>2.0.CO;2)
- Wilkinson, M.D., Dumontier, M., Aalbersberg, IJ.J., Appleton, G., Axton, M., Baak, A., Blomberg, N., Boiten, J.-W., da Silva Santos, L.B., Bourne, P.E., Bouwman, J.,

- Brookes, A.J., Clark, T., Crosas, M., Dillo, I., Dumon, O., Edmunds, S., Evelo, C.T., Finkers, R., Gonzalez-Beltran, A., Gray, A.J.G., Groth, P., Goble, C., Grethe, J.S., Heringa, J., 't Hoen, P.A.C., Hooft, R., Kuhn, T., Kok, R., Kok, J., Lusher, S.J., Martone, M.E., Mons, A., Packer, A.L., Persson, B., Rocca-Serra, P., Roos, M., van Schaik, R., Sansone, S.-A., Schultes, E., Sengstag, T., Slater, T., Strawn, G., Swertz, M.A., Thompson, M., van der Lei, J., van Mulligen, E., Velterop, J., Waagmeester, A., Wittenburg, P., Wolstencroft, K., Zhao, J., Mons, B., 2016. The FAIR Guiding Principles for scientific data management and stewardship. *Sci. Data* 3, 160018. <https://doi.org/10.1038/sdata.2016.18>
- Wilks, D.S., 2019. Statistical methods in the atmospheric sciences. Academic press.
- Windhorst, D., Waltz, T., Timbe, E., Frede, H.-G., Breuer, L., 2013. Impact of elevation and weather patterns on the isotopic composition of precipitation in a tropical montane rainforest. *Hydrol. Earth Syst. Sci.* 17, 409–419. <https://doi.org/10.5194/hess-17-409-2013>
- Wolf, A., Roberts, W.H.G., Ersek, V., Johnson, K.R., Griffiths, M.L., 2020. Rainwater isotopes in central Vietnam controlled by two oceanic moisture sources and rainout effects. *Sci. Rep.* 10, 16482. <https://doi.org/10.1038/s41598-020-73508-z>
- Worbes, M., 2002. One hundred years of tree-ring research in the tropics - A brief history and an outlook to future challenges. *Dendrochronologia* 20, 217–231. <https://doi.org/10.1078/1125-7865-00018>
- Xie, P., Arkin, P.A., 1997. Global Precipitation: A 17-Year Monthly Analysis Based on Gauge Observations, Satellite Estimates, and Numerical Model Outputs. *Bull. Am. Meteorol. Soc.* 78, 2539–2558. [https://doi.org/10.1175/1520-0477\(1997\)078<2539:GPAYMA>2.0.CO;2](https://doi.org/10.1175/1520-0477(1997)078<2539:GPAYMA>2.0.CO;2)
- Xie, S., Tanimoto, Y., 1998. A pan-Atlantic decadal climate oscillation. *Geophys. Res. Lett.* 25, 2185–2188. <https://doi.org/10.1029/98GL01525>
- Yoon, J.-H., Zeng, N., 2010. An Atlantic influence on Amazon rainfall. *Clim. Dyn.* 34, 249–264. <https://doi.org/10.1007/s00382-009-0551-6>
- Yoshimura, K., Kanamitsu, M., Noone, D., Oki, T., 2008. Historical isotope simulation using Reanalysis atmospheric data. *J. Geophys. Res.* 113, D19108. <https://doi.org/10.1029/2008JD010074>
- Zhang, C., 2001. Double ITCZs. *J. Geophys. Res. Atmos.* 106, 11785–11792. <https://doi.org/10.1029/2001JD900046>
- Zhang, G.J., Song, X., Wang, Y., 2019. The double ITCZ syndrome in GCMs: A coupled feedback problem among convection, clouds, atmospheric and ocean circulations. *Atmos. Res.* 229, 255–268. <https://doi.org/https://doi.org/10.1016/j.atmosres.2019.06.023>
- Zhang, R., Delworth, T.L., 2005. Simulated Tropical Response to a Substantial Weakening of the Atlantic Thermohaline Circulation. *J. Clim.* 18, 1853–1860. <https://doi.org/10.1175/JCLI3460.1>
- Zhiña, D.X., Mosquera, G.M., Esquivel-Hernández, G., Córdova, M., Sánchez-Murillo, R., Orellana-Alvear, J., Crespo, P., 2022. Hydrometeorological factors controlling the stable isotopic composition of precipitation in the highlands of south Ecuador. *J. Hydrometeorol.* <https://doi.org/10.1175/JHM-D-21-0180.1>
- Zhisheng, A., Guoxiong, W., Jianping, L., Youbin, S., Yimin, L., Weijian, Z., Yanjun, C., Anmin, D., Li, L., Jiangyu, M., Hai, C., Zhengguo, S., Liangcheng, T., Hong, Y.,

- Hong, A., Hong, C., Juan, F., 2015. Global Monsoon Dynamics and Climate Change. *Annu. Rev. Earth Planet. Sci.* 43, 29–77. <https://doi.org/10.1146/annurev-earth-060313-054623>
- Zhou, J., Lau, K.-M., 1998. Does a Monsoon Climate Exist over South America? *J. Clim.* 11, 1020–1040. [https://doi.org/10.1175/1520-0442\(1998\)011<1020:DAMCEO>2.0.CO;2](https://doi.org/10.1175/1520-0442(1998)011<1020:DAMCEO>2.0.CO;2)
- Zuidema, P.A., Babst, F., Groenendijk, P., Trouet, V., Abiyu, A., Acuña-Soto, R., Adenesky-Filho, E., Alfaro-Sánchez, R., Aragão, J.R.V., Assis-Pereira, G., Bai, X., Barbosa, A.C., Battipaglia, G., Beeckman, H., Botosso, P.C., Bradley, T., Bräuning, A., Brienen, R., Buckley, B.M., Camarero, J.J., Carvalho, A., Ceccantini, G., Centeno-Erguera, L.R., Cerano-Paredes, J., Chávez-Durán, Á.A., Cintra, B.B.L., Cleaveland, M.K., Couralet, C., D'Arrigo, R., del Valle, J.I., Dünisch, O., Enquist, B.J., Esemann-Quadros, K., Eshetu, Z., Fan, Z.-X., Ferrero, M.E., Fichtler, E., Fontana, C., Francisco, K.S., Gebrekirstos, A., Gloor, E., Granato-Souza, D., Haneca, K., Harley, G.L., Heinrich, I., Helle, G., Inga, J.G., Islam, M., Jiang, Y., Kaib, M., Khamisi, Z.H., Koprowski, M., Kruijt, B., Layme, E., Leemans, R., Leffler, A.J., Lisi, C.S., Loader, N.J., Locosselli, G.M., Lopez, L., López-Hernández, M.I., Lousada, J.L.P.C., Mendivelso, H.A., Mokria, M., Montóia, V.R., Moors, E., Nabais, C., Ngoma, J., Nogueira Júnior, F. de C., Oliveira, J.M., Olmedo, G.M., Pagotto, M.A., Panthi, S., Pérez-De-Lis, G., Pucha-Cofrep, D., Pumijumnong, N., Rahman, M., Ramirez, J.A., Requena-Rojas, E.J., Ribeiro, A. de S., Robertson, I., Roig, F.A., Rubio-Camacho, E.A., Sass-Klaassen, U., Schöngart, J., Sheppard, P.R., Slotta, F., Speer, J.H., Therrell, M.D., Toirambe, B., Tomazello-Filho, M., Torbenson, M.C.A., Touchan, R., Venegas-González, A., Villalba, R., Villanueva-Díaz, J., Vinya, R., Vlam, M., Wils, T., Zhou, Z.-K., 2022. Tropical tree growth driven by dry-season climate variability. *Nat. Geosci.* 15, 269–276. <https://doi.org/10.1038/s41561-022-00911-8>



Registry number: DEENK/109/2023.PL
Subject: PhD Publication List

Candidate: Danny Fernando Vargas Espin
Doctoral School: Doctoral School of Physics
MTMT ID: 10080878

List of publications related to the dissertation

Foreign language scientific articles in international journals (2)

1. **Vargas Espin, D. F.**, Pucha-Cofrep, D., Serrano-Vincenti, S., Burneo, A., Carlosama, L., Herrera, M., Cerna, M., Molnár, M., Jull, A. J. T., Temovski, M., László, E., Futó, I., Horváth, A., Palcsu, L.: ITCZ precipitation and cloud cover excursions control Cedrela nebulosa tree-ring oxygen and carbon isotopes in the northwestern Amazon.

Glob. Planet. Change. 211, 1-15, 2022. ISSN: 0921-8181.

DOI: <http://dx.doi.org/10.1016/j.gloplacha.2022.103791>

IF: 4.956 (2021)

2. **Vargas Espin, D. F.**, Chimborazo, O., László, E., Temovski, M., Palcsu, L.: Rainwater Isotopic Composition in the Ecuadorian Andes and Amazon Reflects Cross-Equatorial Flow Seasonality.

Water. 14 (13), 1-22, 2022. EISSN: 2073-4441.

DOI: <https://doi.org/10.3390/w14132121>

IF: 3.53 (2021)

Foreign language abstracts (4)

3. **Vargas Espin, D. F.**, Temovski, M., László, E., Kiss, G. I., Palcsu, L.: Middle Holocene ITCZ shifts: Evidence from Central Ecuador.

In: Climate Change : The Karst Record IX (KR9): Programme and abstract. Eds.: Gina Moseley, Linda Partl, Paul Töchterle, Gabriella Kolai, Mojgan Soleimani, Jonathan Baker, Christoph Spötl, University of Innsbruck, Innsbruck, 102, 2022.

4. **Vargas Espin, D. F.**, Temovski, M., Kiss, G. I., László, E., Surányi, G., Palcsu, L.: Preliminary results of speleothem U-Th dating and paleoclimate reconstruction from Garganta del Dino Cave (Ecuador).

In: 28th International Karstological School "Classical karst" Regional karstology - local and general aspects. Ed.: Matej Blatník, Franci Gabrovšek, Cyril Mayaud, Andrej Mihevc, Metka Petrič, Nataša Ravbar, Nadja Zupan Hajna, Založba ZRC, Ljubljana, 133, 2021. ISBN: 9789610505617





5. **Vargas Espin, D. F.**, Pucha-Cofrep, D., Burneo, A., Carlosama, L., Herrera, M., Serrano, S., Cerna, M., Jull, A. J. T., Molnár, M., Futó, I., Horváth, A., Temovski, M., Palcsu, L.: Impact of cloud coverage on growth dynamics of *Cedrela nebulosa* from an Amazonian pre-montane forest in Central Ecuador.
In: CL1.24 Interdisciplinary Tree-ring research. Ed.: Kerstin Treydte, Flurin Babst, Giovanna Battipaglia, Jan Esper, EGU General Assembly, [Vienna], 1, 2020.
6. **Vargas Espin, D. F.**, Temovski, M., László, E., Palcsu, L.: Paleoclimate reconstruction based on speleothems from Ecuadorian caves.
In: 27th International Karstological School "Classical karst" Karst hydrogeology - research trends and applications : Abstracts & Guide Book. Ed.: Matej Blatník, Franci Gabrovšek, Blaž Kogovšek, Cyril Mayaud, Metka Petrič, Nataša Ravbar, Založba ZRC, Ljubljana, 133-134, 2019. ISBN: 9789610501961

List of other publications

Foreign language abstracts (2)

7. Palcsu, L., Temovski, M., **Vargas Espin, D. F.**, Kiss, G. I., Surányi, G.: A new U-Th laboratory for dating speleothems.
In: Climate Change : The Karst Record IX (KR9): Programme and abstract. Eds.: Gina Moseley, Linda Partl, Paul Töchterle, Gabriella Kolai, Mojgan Soleimani, Jonathan Baker, Christoph Spötl, University of Innsbruck, Innsbruck, 120, 2022.
8. Temovski, M., Molnár, K., **Vargas Espin, D. F.**, Kiss, G. I., Palcsu, L.: Petrographic and geochemical properties of a subaqueous speleothem from a Macedonian cave-preliminary results and insight into MIS 7 paleoclimate record of the Balkan Peninsula.
In: Climate Change : The Karst Record IX (KR9): Programme and abstract. Eds.: Gina Moseley, Linda Partl, Paul Töchterle, Gabriella Kolai, Mojgan Soleimani, Jonathan Baker, Christoph Spötl, University of Innsbruck, Innsbruck, 106-107, 2022.

Total IF of journals (all publications): 8,486

Total IF of journals (publications related to the dissertation): 8,486

The Candidate's publication data submitted to the iDEa Tudóstér have been validated by DEENK on the basis of the Journal Citation Report (Impact Factor) database.

13 April, 2023



ACKNOWLEDGMENTS

Firstly, I would like to thank for the opportunity to my supervisor Dr. Palcsu László. I do appreciate his patience, support and leadership.

I would like to thank for their great collaboration to my colleagues at the project: Dr. Temovski Marjan, Dr. László Elemér, Dr. Temovski-Molnár Kata, Dr. Arató Róbert, Dr. Molnár Mihály, Dr. A.J. Timothy Jull, Dr. Veres Mihály, Dr. Benkó Zsolt, Dr. Futó István, Dr. Rinyu László, Dr. Turi Marianna.

My gratitude to my colleagues Kiss Gabriella, Puskás-Preszner Anita, Dóra Réka, Horváth Anikó, Túri Marianna, Hornyákné Telki Andrea, Kállai Mariann, Orbánné Pető Etelka, Barta Judit, Orsovszki Judit, Varga Tamás, Karacs Norbert, Hajnal Andor, Fekete Gergő, Vasváry Gábor, Tóth István, Erzsébet Pájerné Sóki, Sóvágó Dávid and many other technicians, engineers, and colleagues at the Institute for Nuclear Research (Atomki) and the University of Debrecen.

This work was greatly enhanced by the valuable comments and discussions of Dr. Kázmér Miklós and Dr. Csige István, who dedicated their time and effort to complete this work.

I would like to express my appreciation for the continuous support of the Isotope Climatology and Environmental Research Centre (ICER), project leaders and the team.

The research was supported by the European Union and the State of Hungary, co-financed by the European Regional Development Fund in the project of GINOP-2.3.2-15-2016-00009 ‘ICER’.

I am also grateful for the support of the Doctoral School of Physics along the administrative steps of my PhD defense process: Dr. Kun Ferenc, Dr. Sohler Dóra and Dr. Oláh László.

Finally, but not least, I am grateful and blessed for my wife Timi and daughter Sárika Abigél. To my mom, who understood the importance of education in science and faith. To my father for instilling in me discipline and transparency. To my siblings, nieces and nephews. To my friends and brothers at IBCD, who supported and deeply cared along the way, especially Jon and Amanda Good.

This thesis is specially dedicated to the memory of my beloved uncle Walter Ramos[†].

APPENDIX A – MERA STUDY SITE SURVEY

Appendix A.1 – Forest taxa survey

A total of 50 tree cores from the marked transects were classified into 16 families and 21 species. Cores from tree species that could not be identified despite having their vegetative and reproductive parts (leaves, fruits and flowers) were grouped and labelled as “Unknown”. The most abundant taxonomic families were Fabaceae ($n = 20$), Meliaceae ($n = 8$) and Burseraceae ($n = 6$). At the species rank, *Inga* sp., *Protium* sp., and *Cedrela odorata* with 9, 5 and 4 trees respectively had the highest number of individuals on the 0.2 surveyed hectares. Within the 16 identified families, 9 species formed visible growth rings corresponding to the Bombacaceae, Burseraceae, Brunelliaceae, Fabaceae, Melastomataceae, Meliaceae and Rutaceae families. Among them, *Cedrela odorata* and *Cedrela nebulosa* stood out for their clarity in ring growth visibility. This last species was selected due to the presence of a well-preserved forest stand with enough individuals for sampling replication. Calculated Simpson's dominance (D), Simpson's diversity (1-D), and Shannon diversity (H) indices utilizing the program PAST were 0.05; 0.95 and 3.24, respectively (Hammer et al., 2001; Magurran, 2013; Simpson, 1949). According to these results, the Mera study site has extremely low dominance, but a very high diversity of species with different phenological rhythmicity clearly illustrated with a total of 14 forest species that could not be identified in the local Herbariums.

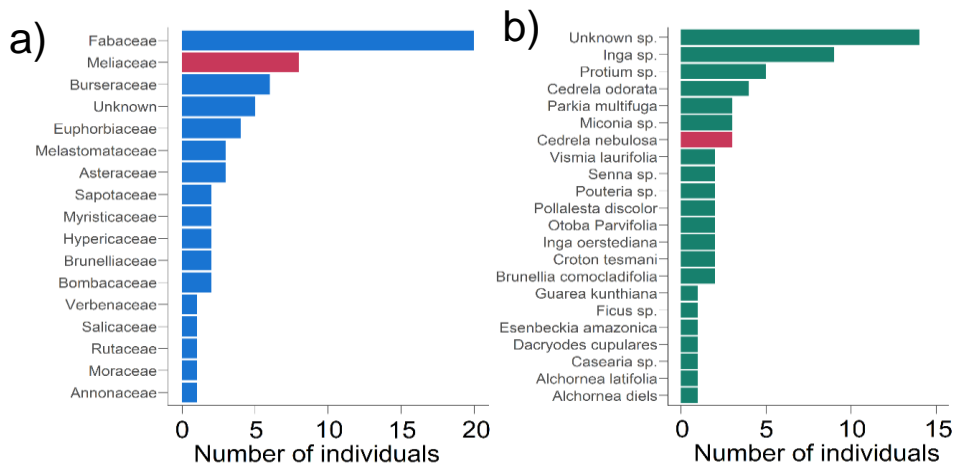


Figure A.1 a) Identified families and **b)** identified species in the forest field survey in 2019. In 2000 m² (0.2 ha), a total of 16 families and 21 species were catalogued at local Herbariums. For this study, *Cedrela nebulosa* (Meliaceae family, red bar) was selected.

Appendix A.2 – Example of two field notebooks filled during collection of wood samples and cross sections in Mera, Central Ecuador. The complete notebooks are available at <https://github.com/vargasdanny/paleothesis>

2. Tree number:	01	10. Elevation (m a.s.l.):	1211	16. Type of sample:	Nucleus
3. Tree ID:	MECE01	11. Slope (%)/direction:	5°/ W-E	17. CBH/DBH (cm):	129/ 41.38
6. Species:	Cedro	12. Foliage (%):	90	19. Light / canopy cover (%):	10/90
7. Location:	Mera	13. Fruit/Flowering:	NO	20. Tree comments:	Bromeliads
8. X Coordinates (lon):	827973	14. Tree condition:	Good	21. Tree crown (dom, inter, supp):	Dom
9. Y Coordinates (lat):	9844195	15. Trunk (inclination °):	0	22. Responsible:	Byron Cabrera

1. Date – Time	4. Sample ID	5. Sample direction	23. Sample comment
9:20/10 sep 2019	MECE01	N-S	Complete
9:35/10 sep 2019	MECE01	W-E	Complete

2. Tree number:	02	10. Elevation (m a.s.l.):	1195	16. Type of sample:	Nucleus
3. Tree ID:	MECE02	11. Slope (%)/direction:	40°/ N-S	17. CBH/DBH (cm):	163/ 51.38
6. Species:	Cedro	12. Foliage (%):	95	19. Light / canopy cover (%):	5/95
7. Location:	Mera	13. Fruit/Flowering:	NO	20. Tree comments:	Bromeliads, raíces tablares notorias
8. X Coordinates (lon):	828006	14. Tree condition:	Good	21. Tree crown (dom, inter, supp):	Dom
9. Y Coordinates (lat):	9844214	15. Trunk (inclination °):	0	22. Responsible:	Byron Cabrera Madison Herrera

1. Date – Time	4. Sample ID	5. Sample direction	23. Sample comment
9:52/10 sep 2019	MECE02	N-S	Complete, dark wood center
10:07/10 sep 2019	MECE02	W-E	Complete

Appendix A.2 – *Continued*

FIELD DATA SHEET FOR COLLECTION OF WOOD CROSS SECTIONS

Date - hour: 12-Sep-2019 - 10:05

Tree number: (or ID)	MECE31	Location:	Mera
Scientific name:	<i>Cedrela sp.</i>	X Coordinates (lon):	821165
Common name:	Cedro	Y Coordinates (lat):	9838349
CBH (cm):	107	Elevation (m a.s.l.):	1198
DBH (cm):	34.06	Land slope (°):	
TH (m):	13	Ground slope direction (Ex. N-S, E-W):	
CH (m):	10	Trunk (CH) (inclination °):	
Tree crown (dominant, intermediate, suppressed, relicts):	Relict	Direction of the inclination of the trunk (Ex. N-S):	
Fruit/Flowering status:	-	Name of collector(s):	Dayana Jiménez María Angélica Burneo Madison Herrera
Sapwood Color (green) Munsell Code and Color Name		Heartwood color (green) Munsell Code and Color Name	
Flavor (green) Sweet, Bitter, Acid, aAstringent, Absent, Characteristic (specify)		Odor (green) Aromatic, Unpleasant, Absent, Characteristic (specify)	
Tree condition: (Good, regular, poor)	Poor	Comments:	
Foliage (%): (percentage of leaves)	0	Comments:	Fallen tree

Date - hour: 12-Sep-2019 - 10:05

Tree number: (or ID)	MECE32	Location:	Mera
Scientific name:	<i>Cedrela sp.</i>	X Coordinates (lon):	821165
Common name:	Cedro	Y Coordinates (lat):	9838349
CBH (cm):	120	Elevation (m a.s.l.):	572
DBH (cm):	38.21	Land slope (°):	20
TH (m):	10	Ground slope direction (Ex. N-S, E-W):	W-E
CH (m):	7	Trunk (CH) (inclination °):	10
Tree crown (dominant, intermediate, suppressed, relicts):	Relict	Direction of the inclination of the trunk (Ex. N-S):	W-E
Fruit/Flowering status:	-	Name of collector(s):	Dayana Jiménez Maria Angélica Burneo Madison Herrera
Sapwood Color (verde) Munsell Code and Color Name		Heartwood color (verde) Munsell Code and Color Name	
Flavor (verde) Sweet, Bitter, Acid, Astringent, Absent, Characteristic (specify)		Odor (verde) Aromatic, Unpleasant, Absent, Characteristic (specify)	
Tree condition: (Good, regular, poor)	Good	Comments:	
Foliage (%): (percentage of leaves)	0	Comments:	Tree without leaves, with Bromeliads, leaning slightly

Appendix A.3 – C-14 measurements in tree-ring cellulose for *C. nebulosa* tree, Ecuador. Values are expressed in Fraction Modern Carbon (Fm) and years calculated using the Calibomb SHZ3 calibration curve (Reimer and Reimer, 2004).

No.	AMS Lab code	Year A.D. (dendro)	Fm ^{14}C mean	Fm (unc.) (1s)	Year A.D. (radiocarbon)
1	DeA-24139	1956	1.0015	0.0019	1956.21-1956.40
2	DeA-24140	1957	1.0460	0.0021	1957.18-1957.39
3	DeA-24141	1959	1.1655	0.0021	1959.21-1959.54
4	DeA-24142	1960	1.2099	0.0022	1960.64-1961.30
5	DeA-24143	1962	1.3466	0.0023	1962.83-1962.92
6	DeA-24144	1965	1.6599	0.0026	1965.14-1965.46
7	DeA-24145	1966	1.6198	0.0026	1966.76-1967.26
8	DeA-24146	1969	1.5513	0.0025	1969.38-1969.66
9	DeA-24147	1971	1.5158	0.0025	1971.12-1971.86
10	DeA-24148	1972	1.4690	0.0024	1972.76-1973.05
11	DeA-24149	1974	1.4099	0.0024	1974.01-1975.07
12	DeA-24150	1975	1.3676	0.0023	1975.65-1976.40
13	DeA-24151	1978	1.3233	0.0023	1978.01-1978.98
14	DeA-24152	1979	1.2993	0.0023	1979.10-1980.07
15	DeA-24153	1981	1.2652	0.0023	1981.30-1982.25
16	DeA-24154	1982	1.2379	0.0022	1982.59-1983.89
17	DeA-24155	1984	1.2174	0.0022	1984.26-1985.23
18	DeA-24156	1986	1.1939	0.0022	1986.32-1987.16

Appendix A.4 – Raw tree-ring width (TRW) data from 33 trees. The complete table is available at <https://github.com/vargasdanny/paleothesis>

Year	Number	Raw width chronology	Standard chronology	Raw TRW statistics	
2019	83	1.83	0.85	Parameter	Values
2018	87	2.77	0.88	No. of trees / radii	24 / 108
2017	87	3.13	0.96	Time period	1860-2019
2016	91	3.02	1.00	Average series length (years)	46
2015	103	2.70	0.84	Mean ring width (mm year ⁻¹)	0.10 to 36.74
2014	103	3.76	1.03	Mean sensitivity	0.37
2013	103	4.38	1.08	First order autocorrelation	0.51
2012	103	3.79	0.95	Rbar.wt ^a	2.34
2011	104	3.43	0.86	Mean EPS ^a (1860-2019)	0.46
2010	104	7.35	1.65	Mean EPS (1960-2019)	0.65
2009	104	3.28	0.76		
2008	104	3.18	0.72	Rbar.wt ^a : mean interseries	
2007	104	3.83	0.77	EPS: Expressed Population Signal	
2006	104	4.12	0.90		
2005	104	4.24	0.92		
2004	104	4.38	0.92		
2003	102	4.70	0.99		
2002	102	5.49	0.99		
2001	103	5.39	1.01		
2000	103	5.79	1.00		
1999	103	5.45	0.97		
---	---	---	---		
---	---	---	---		
---	---	---	---		
---	---	---	---		
1869	4	0.81	1.05		
1868	4	0.61	0.69		
1867	4	0.97	1.21		
1866	4	0.96	1.06		
1865	4	0.94	0.89		
1864	4	0.93	0.81		
1863	3	0.74	0.56		
1862	2	1.23	1.32		
1861	2	0.70	0.55		
1860	2	2.10	1.59		

Appendix A.5 – Raw tree-ring oxygen isotope ($\delta^{18}\text{O}_{\text{TR}}$) data from four *Cedrela nebulosa* trees from Mera, central Ecuador. The complete table is available at <https://github.com/vargasdanny/paleothesis>

year	MECE22	MECE24	MECE25	MECE26	Mean
2018	18.61	25.39	25.57	29.26	24.71
2017		24.96	25.57	26.66	25.73
2016	23.15	24.96	25.14	26.33	24.89
2015	24.10	25.93	25.14	28.04	25.80
2014	25.12	25.93	24.31	24.43	24.95
2013	25.60	22.79	24.31	23.66	24.09
2012	25.10	22.59	24.64	23.66	24.00
2011	22.86	22.59	25.68		23.71
2010	25.10	24.48	25.68		25.09
2009	24.47	24.48	24.89	23.52	24.34
2008	24.89	26.79	24.89	24.18	25.19
2007	24.98	26.79	24.45	24.99	25.30
2006	25.28	25.00	24.45	24.11	24.71
2005	23.70	25.00	25.93	24.74	24.84
2004	25.46	20.27	25.70	22.72	23.54
2003	26.01	20.27	25.70	23.56	23.88
2002	24.23	25.78	24.81	23.85	24.67
2001	26.35	25.78	24.81	24.36	25.32
2000	23.63	25.87	26.56	24.49	25.14
1999	25.16	25.87	26.56	23.27	25.21
---	--	--	--	--	--
---	--	--	--	--	--
---	--	--	--	--	--
---	--	--	--	--	--
1877				22.70	22.70
1876				24.23	24.23
1875				24.73	24.73
1874				24.73	24.73
1873				25.04	25.04
1872				24.85	24.85
1871				25.35	25.35
1870				23.49	23.49
1869				22.37	22.37
1868				22.37	22.37
1867				21.59	21.59
1866				22.34	22.34
1865				22.10	22.10
1864				22.24	22.24

Appendix A.6 – Raw tree-ring carbon isotope ($\delta^{13}\text{C}_{\text{TR}}$) data from four *Cedrela nebulosa* trees from Mera, central Ecuador. The complete table is available at <https://github.com/vargasdanny/paleothesis>

year	MECE22	MECE24	MECE25	MECE26	Mean	Δ	$\delta^{13}\text{C}$
2018	-26.43	-27.94	-27.93	-27.24	-27.39	1.97	-25.42
2017		-26.54	-27.93	-27.56	-27.34	1.95	-25.39
2016	-26.70	-26.54	-27.88	-27.18	-27.07	1.93	-25.14
2015		-26.56	-27.88	-27.45	-27.30	1.91	-25.39
2014	-25.94	-26.56	-27.42		-26.64	1.89	-24.75
2013	-25.66	-26.73	-27.42	-28.95	-27.19	1.87	-25.32
2012	-26.40	-26.86	-27.83	-28.95	-27.51	1.85	-25.66
2011	-26.77	-26.86	-29.00		-27.54	1.83	-25.71
2010		-26.41	-29.00		-27.70	1.81	-25.89
2009	-25.87	-26.41	-29.51	-27.78	-27.39	1.79	-25.60
2008	-26.03	-26.21	-29.51	-27.44	-27.30	1.77	-25.53
2007		-26.21	-29.65	-27.24	-27.70	1.75	-25.95
2006	-26.24	-26.89	-29.65	-27.33	-27.53	1.73	-25.80
2005	-26.23	-26.89	-29.09	-27.26	-27.37	1.71	-25.66
2004	-26.49	-26.83	-29.47	-27.26	-27.51	1.69	-25.82
2003	-26.22	-26.83	-29.47	-27.30	-27.45	1.67	-25.78
2002	-26.36	-26.86	-29.28	-27.62	-27.53	1.65	-25.88
2001	-26.18	-26.86	-29.28	-27.15	-27.37	1.62	-25.75
2000	-26.93	-27.18	-29.78	-26.88	-27.69	1.59	-26.10
1999	-26.08	-27.18	-29.78	-28.05	-27.77	1.56	-26.21
---	---	---	---	---	---	---	---
---	---	---	---	---	---	---	---
---	---	---	---	---	---	---	---
---	---	---	---	---	---	---	---
1877				-28.42	-28.42	0.13	-28.29
1876				-27.97	-27.97	0.13	-27.84
1875				-28.81	-28.81	0.12	-28.69
1874				-28.81	-28.81	0.12	-28.69
1873				-29.29	-29.29	0.11	-29.18
1872				-28.89	-28.89	0.11	-28.78
1871				-28.48	-28.48	0.11	-28.37
1870				-28.13	-28.13	0.10	-28.03
1869				-27.99	-27.99	0.10	-27.89
1868				-27.99	-27.99	0.09	-27.90
1867				-28.04	-28.04	0.09	-27.95
1866				-28.27	-28.27	0.08	-28.19
1865				-28.51	-28.51	0.08	-28.43
1864				-28.80	-28.80	0.07	-28.73

APPENDIX B – SPELEOTHEMS

Appendix B.1 – Rio Anzu caves – Mera, Central Ecuador

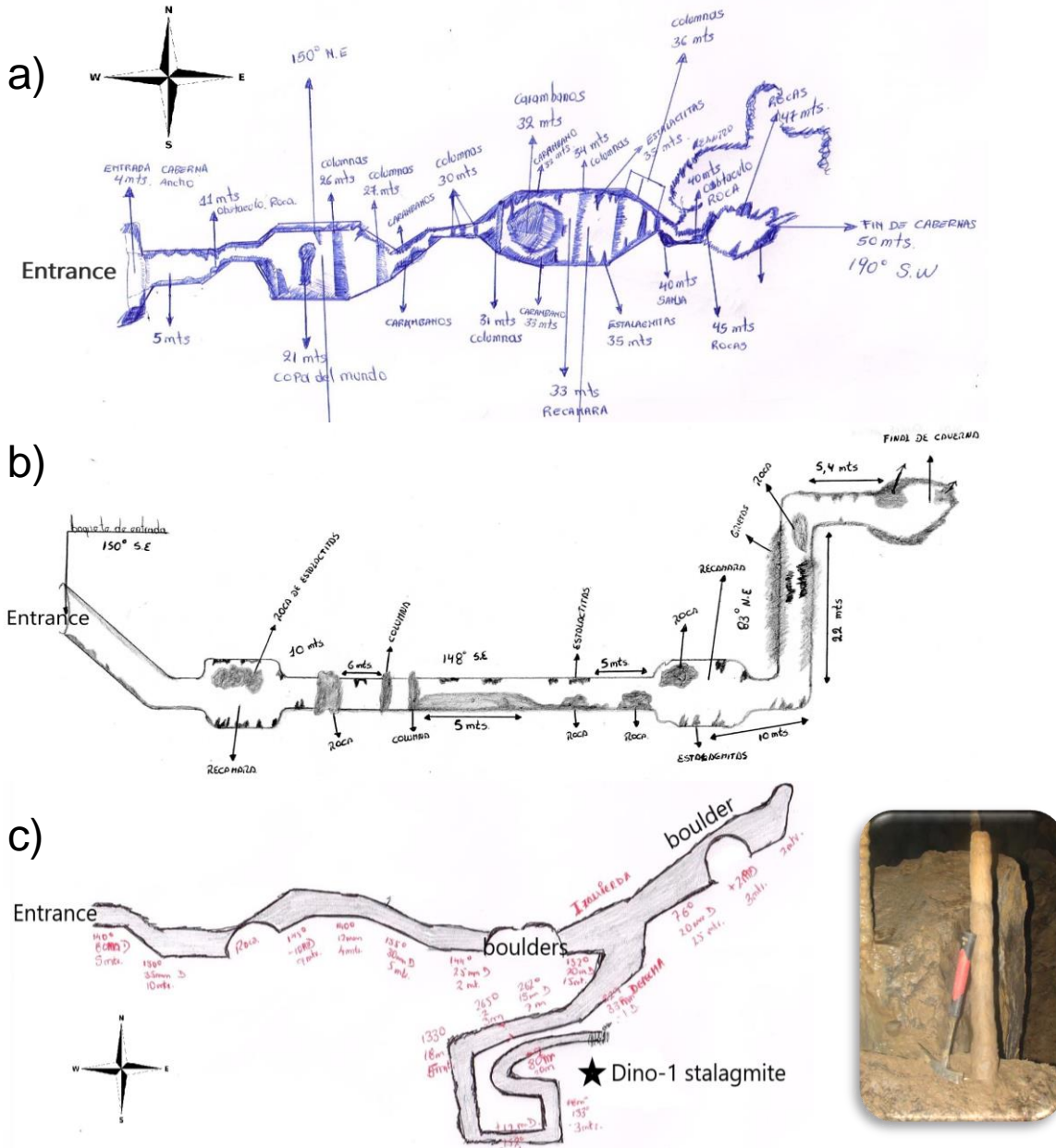
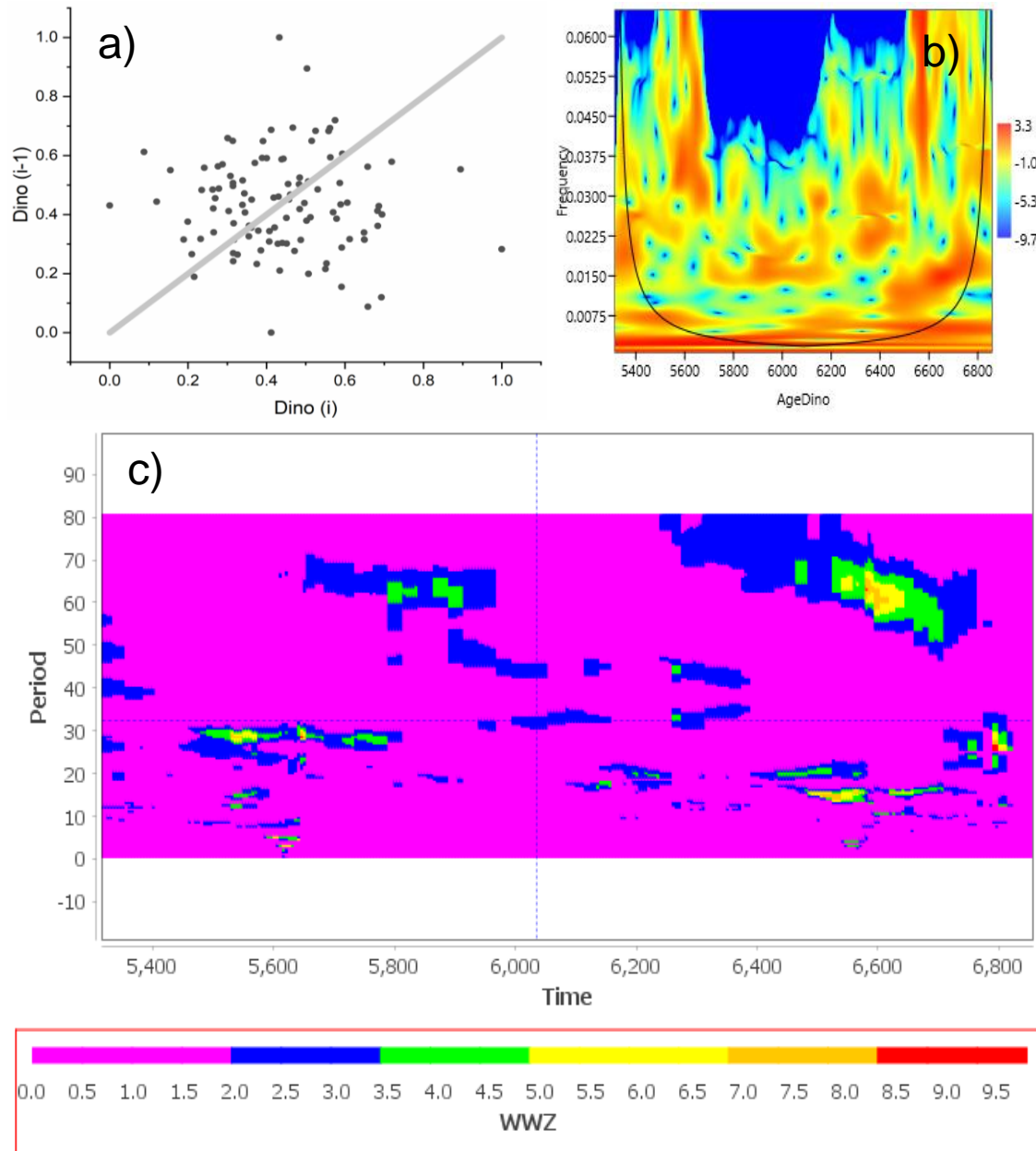


Figure B.1 Raw sketches of the morphology of the studied caves in this dissertation. **a)** Copa cave ($01^{\circ} 24.3' S$, $78^{\circ} 2.6' W$), **b)** Union cave ($01^{\circ} 24.4' S$, $78^{\circ} 2.7' W$), and **c)** Dino cave ($01^{\circ} 25.5' S$, $78^{\circ} 2.4' W$). Dripwater collection was carried out on Union and Dino caves. At the Dino cave, from the ponor to the entrance, more than 60 m of cave passages met the surface at few locations. At places, darker limestone layers can be seen (bituminous limestone). A main passage led to a dry, speleothem-filled room. Here, one complete and inactive stalagmite was found on a boulder in the middle of the room and was detached by hammering (Dino-1; black star in c). Drawings were generously provided by Franklin Villa.

Appendix B.2 – a) Dino-1 persistence and b-c) Weighted Wavelet z-Transform (WWZ)



Appendix B.3 –Hövmuller time-space plot of ERA5 relative humidity for longitude 80 to 75 °W (Ecuadorian territory) at 850 hPa (1.5 km height). The values (%) correspond to the monitoring period February 2019 to January 2023.

